

**Comprehensive,
Consistent and Systematic
Approach to the
Mathematical Modeling of
PEM Fuel Cells**

by
Jeffrey James Baschuk

A thesis presented to the
University of Waterloo
in fulfillment of the
thesis requirement
for the degree of
Doctor of Philosophy
in
Mechanical Engineering

Waterloo, Ontario, Canada, 2006
©Jeffrey James Baschuk 2006

I hereby declare that I am the sole author of this thesis. This is a true copy of the thesis, including any required revisions, as accepted by my examiners.

I understand that my thesis may be made electronically available to the public.

Jeffrey James Baschuk

Abstract

Polymer electrolyte membrane (PEM) fuel cells are a promising zero-emission power source for transportation applications. An important tool for advancing PEM fuel cell technology is mathematical modeling. Mathematical models can be used to provide insight on the physical phenomena occurring within a fuel cell, as well as aid in the design of fuel cells by simulating the effect of changes in design or operating conditions on performance.

A comprehensive, consistent and systematic general formulation for a mathematical PEM fuel cell model is presented in this thesis. The formulation is developed by considering the fuel cell to be composed of several, co-existing phases. The conservation of mass, momentum, species, and energy are applied to each phase in the fuel cell. The interactions between the phases are modeled by applying a volume-averaging procedure to the conservation equations in each phase.

The solution of the governing equations for the general formulation are beyond the scope of this thesis research. Instead, simplifying assumptions are applied to the general formulation in order to reduce the number of governing equations. The cell is assumed to be two-dimensional, steady state and isothermal. As well, the polymer electrolyte is assumed to be impervious to the gas phase and liquid water is assumed to exist only in the gas phase or polymer electrolyte.

The numerical solution of the simplified formulation is implemented using the computer language of C++ and the finite volume method. The numerical solution provides details of the transport phenomena within the anode and cathode gas flow channels, electrode backing layers, and catalyst layers, as well as the polymer electrolyte membrane layer. These details include the bulk velocity of the gas phase; the concentrations of the species within the gas phase; the potential and current density in the solid phase and polymer electrolyte; the water content in the polymer electrolyte; and the distribution of reaction rate within the catalyst layers.

Acknowledgments

This work was supported by the Natural Sciences and Engineering Research Council of Canada. I would also like to thank my supervisor, Dr. Xianguo Li, for his guidance in the production of this thesis.

Contents

1	Introduction	1
1.1	Background Information	2
1.2	Thesis Objectives and Outline	10
2	Literature Review	13
2.1	Empirical Models	14
2.2	Mathematical Models	15
2.2.1	MEA-Centered Approach	16
2.2.2	Channel-Centered Approach	24
2.3	Summary	28
3	General Formulation	30
3.1	Physical Structure	31
3.2	Assumptions	33
3.3	Volume-Averaging Method	33
3.4	Conservation of Momentum	36
3.5	Conservation of Mass and Species	43
3.5.1	Reaction	46
3.6	Conservation of Energy	55
3.6.1	Anode Heat of Reaction	59
3.6.2	Cathode Heat of Reaction	62
3.6.3	Reversible Heat Generation	62
3.6.4	Irreversible Heat Generation	64
3.7	Summary	64
4	Simplified Formulation for Numerical Implementation	67
4.1	Assumptions	68
4.2	Gas Phase	69
4.3	Solid Phase	71
4.4	Liquid Phase in the Electrolyte	73
4.5	Reaction	80
4.6	Boundary Conditions and Computational Domain	83
4.7	Summary	86

5	Numerical Implementation	89
5.1	Finite Volume Grid	91
5.2	General Discretization Methods	93
5.3	Conservation of Momentum	95
5.4	Conservation of Species in the Gas Phase: Excluding Water	102
5.5	Conservation of Species in the Electrolyte Pores: Hydronium	106
5.6	Conservation of Species: Water	108
5.7	Conservation of Species: Solid	114
5.8	Conservation of Mass	116
5.9	Boundary Conditions	119
5.9.1	Velocity Boundary Conditions	119
5.9.2	Pressure Boundary Conditions	123
5.9.3	Scalar Boundary Conditions	125
5.10	Numerical Procedure	128
5.11	Summary	132
6	Parameter Determination for the Electrolyte Model	136
6.1	Water Diffusion Coefficient	138
6.2	Hydronium Diffusion Coefficient	142
6.3	Electro-osmotic Drag	144
6.4	Comparison with Springer Model	146
6.5	Summary	152
7	Results and Discussion	154
7.1	Validation	155
7.2	Model Input Parameters	156
7.3	Grid Independent Solution	162
7.4	Convergence Criteria	166
7.5	Comparison to Experimental Data	168
7.6	Transport Phenomena Within the PEM Fuel Cell	169
7.6.1	Bulk Gas Phase Transport	169
7.6.2	Hydrogen Transport	173
7.6.3	Oxygen Transport	179
7.6.4	Water Transport	181
7.6.5	Electron Transport	189
7.6.6	Hydronium Transport	192
7.6.7	Catalyst Layer Reactions	196
7.6.8	Effect of Channel Length	200
7.7	Summary	207
8	Summary and Future Work	209
	References	222

List of Tables

1.1	The physical and chemical phenomena in each layer of a PEM fuel cell.	8
4.1	The exchange current density for oxygen reduction at the reference conditions corresponding to a fully hydrated electrolyte and oxygen partial pressure of 1 atm [104].	81
6.1	The polynomial constants for the experimental conductivity data of Sone <i>et al.</i> [124].	143
6.2	The values of \hat{D}_α^β for a fully hydrated membrane at a temperature of 353 K.	148
6.3	Comparison between the Thesis and Springer electrolyte models.	150
7.1	The comparison between the thesis research code and that of Ferziger and Perić [120] for lid driven cavity flow: x direction velocity.	156
7.2	The operating conditions for the high stoichiometry data from Mughal [127].	157
7.3	Catalyst surface area per unit mass of catalyst (A_s) as a function of mass ratio of platinum to carbon support (f_{Pt}) [128]	160
7.4	The design parameters used for comparing the mathematical model with experimental data.	161
7.5	The number of control volumes required for a grid independent solution.	166
7.6	The design parameters used for illustrating two-dimensional effects.	202
7.7	The number of control volumes used for illustrating two-dimensional effects.	203

List of Figures

1.1	Illustration of a polymer electrolyte membrane (PEM) fuel cell.	3
1.2	The components of a PEM fuel cell and the processes occurring within each component. The PEM fuel cell is composed of the (a) cathode bipolar plate, (b) cathode gas flow channel, (c) cathode electrode backing layer, (d) cathode catalyst layer, (e) polymer electrolyte membrane layer, (f) anode catalyst layer, (g) anode electrode backing layer, (h) anode gas flow channel, and (i) anode gas flow channel.	5
1.3	Polarization curve of a typical polymer electrolyte membrane fuel cell illustrating the activation, ohmic and concentration overpotential regions.	9
3.1	The structure of the layers within a PEM fuel cell.	31
3.2	Representative volume for volume-averaging the conservation equations.	34
3.3	Cylindrical pore having (a) hydrophilic and (b) hydrophobic characteristics.	40
3.4	Capillary pressure dependence on liquid water saturation for (a) hydrophilic quartz sand, (b) hydrophobic PTFE and (c) a 1:2 mixture of hydrophilic quartz sand and hydrophobic PTFE. The curves are from Ustohal <i>et al.</i> [90], and the pressure head difference is related to the capillary pressure by $P_{cgl} = (\rho_\ell)(g)(hd)$	41
4.1	The hydration of the polymer electrolyte membrane as a function of the activity of water in the gas phase for various temperatures.	78
4.2	The boundary conditions and computational domain of the PEM fuel cell model.	84
5.1	The sample grid used for the PEM fuel cell model. The grid is continuous and consists of 11 distinct regions: (a) anode minus extension, (b) anode gas flow channel, (c) anode plus extension, (d) anode electrode backing layer, (e) anode catalyst layer, (f) polymer electrolyte layer, (g) cathode catalyst layer, (h) cathode electrode backing layer, (i) cathode minus extension, (j) cathode gas flow channel, and (k) cathode plus extension. Note that the figure is not to scale, with the y direction being exaggerated in the figure.	92
5.2	The two types of fluxes encountered in the Finite Volume Method: F_c is the convective flux, while F_d is the diffusive flux.	94
5.3	The interpolation of scalar quantities to the face of the (a) scalar and (b) velocity control volumes.	96
5.4	The balance of momentum forces on (a) u and (b) v control volumes.	97
5.5	The conservation of species for the gas phase.	103
5.6	The conservation of species for the liquid in the electrolyte pores.	107

5.7	The partial density of water in the electrolyte as a function of membrane activity for the temperatures of 303 K, 333 K, and 353 K.	110
5.8	The conservation of species for the solid phase.	114
5.9	The conservation of mass for the gas phase.	116
5.10	The external boundary conditions for the velocity: (a) specified velocity and (b) fully developed.	120
5.11	Internal boundary condition for the velocity.	122
5.12	The external boundary conditions for the pressure: (a) specified velocity and (b) specified pressure.	124
5.13	Internal boundary condition for the pressure.	125
5.14	The conservation of a scalar quantity near the boundary.	126
5.15	The conservation of a scalar quantity near the a phase discontinuity.	128
5.16	The overall solution procedure.	129
5.17	The flowchart for the “Calculate Constants” procedure.	131
5.18	The flowchart for the “Calculate Species” procedure.	133
5.19	The flowchart for the “Calculate Flow” procedure.	134
6.1	The diffusion coefficient of water in the membrane as a function of hydration for temperatures of 303, 333, and 353 K.	140
6.2	The Darken factor based on the electrolyte hydration function of (a) Springer <i>et al.</i> [26] and (b) Futerko and Hsing [115]	141
6.3	The diffusion coefficient of water in the membrane as a function of hydration determined with (a) the Darken factor originally used by Motupally <i>et al.</i> [122] and (b) the Darken factor calculated with the hydration function of Futerko and Hsing [115]. The temperature is 353 K.	142
6.4	The diffusion coefficient for hydronium ions in the membrane as a function of membrane hydration for temperatures of 303, 333, and 353 K.	145
6.5	Electro-osmotic drag coefficient as a function of membrane hydration for temperature of 303, 333, and 353 K.	146
6.6	One-dimensional membrane simulation for comparing the Thesis and Springer models.	149
6.7	The membrane hydration predicted by the Thesis and Springer models for case 2.	151
7.1	Test case for validating the numerical procedure.	155
7.2	The boundary conditions used for comparing the mathematical model with experimental data.	158
7.3	The design parameters required for the PEM fuel cell model.	159
7.4	The mesh used for the comparison between the mathematical model and experimental data. The regions are the (a) anode gas flow channel, (b) anode plus extension, (c) anode electrode backing layer, (d) anode catalyst layer, (e) polymer electrolyte layer, (f) cathode catalyst layer, (g) cathode electrode backing layer, (h) cathode gas flow channel, (i) cathode plus extension. Note that the figure is not drawn to scale.	163
7.5	The effect of the number of control volumes on the error in the pressure drop.	164
7.6	The effect of the number of control volumes on the error in the current density.	165
7.7	The effect of convergence criteria on the error in the partial density of oxygen.	167
7.8	Current density as a function of ζ_{A_p}	168

7.9	The gas phase streamlines in the PEM fuel cell	170
7.10	The magnitude of the phase-averaged, bulk gas phase velocity the PEM fuel cell at $x/L_{ch} = 0.5$. The y direction has been normalized such that the cathode gas flow channel corresponds to $(0 \leq y \leq 1)$, the cathode electrode backing layer corresponds to $(1 \leq y \leq 2)$, the cathode catalyst layer corresponds to $(2 \leq y \leq 3)$, the polymer electrolyte layer corresponds to $(3 \leq y \leq 4)$, the anode catalyst layer corresponds to $(4 \leq y \leq 5)$, the anode electrode backing layer corresponds to $(5 \leq y \leq 6)$, and the anode gas flow channel corresponds to $(6 \leq y \leq 7)$	172
7.11	The streamlines for the total mass flux of hydrogen in the PEM fuel cell	174
7.12	The streamlines for the diffusional mass flux of hydrogen in the PEM fuel cell	174
7.13	The mass fraction of hydrogen in the anode gas flow channel, electrode backing layer and catalyst layer. The y direction has been normalized such that the anode catalyst layer corresponds to $(4 \leq y \leq 5)$, the anode electrode backing layer corresponds to $(5 \leq y \leq 6)$ and the anode gas flow channel corresponds to $(6 \leq y \leq 7)$. The (a) two-dimensional distribution and the (b) one-dimensional distribution at $x/L_{ch} = 0.5$ are shown.	176
7.14	The concentration of hydrogen in the anode gas flow channel, electrode backing layer and catalyst layer. The y direction has been normalized such that the anode catalyst layer corresponds to $(4 \leq y \leq 5)$, the anode electrode backing layer corresponds to $(5 \leq y \leq 6)$ and the anode gas flow channel corresponds to $(6 \leq y \leq 7)$. The (a) two-dimensional distribution and the (b) one-dimensional distribution at $x/L_{ch} = 0.5$ are shown.	177
7.15	Test problem for explaining the hydrogen mass fraction gradient in the anode catalyst layer.	178
7.16	The streamlines for the total mass flux of oxygen in the PEM fuel cell	179
7.17	The mass fraction of oxygen in the anode gas flow channel, electrode backing layer and catalyst layer. The y direction has been normalized such that the cathode gas flow channel corresponds to $(0 \leq y \leq 1)$, the cathode electrode backing layer corresponds to $(1 \leq y \leq 2)$ and the cathode catalyst layer corresponds to $(2 \leq y \leq 3)$. The (a) two-dimensional distribution and the (b) one-dimensional distribution at $x/L_{ch} = 0.5$ are shown.	180
7.18	The concentration of oxygen in the anode gas flow channel, electrode backing layer and catalyst layer. The y direction has been normalized such that the cathode gas flow channel corresponds to $(0 \leq y \leq 1)$, the cathode electrode backing layer corresponds to $(1 \leq y \leq 2)$ and the cathode catalyst layer corresponds to $(2 \leq y \leq 3)$. The (a) two-dimensional distribution and the (b) one-dimensional distribution at $x/L_{ch} = 0.5$ are shown.	182
7.19	The streamlines of total water mass flux in the PEM fuel cell.	183
7.20	The y direction water mass flux in the catalyst layers and polymer electrolyte layer at $x/L_{ch} = 0.5$. The y direction has been normalized such that the cathode catalyst layer corresponds to $(2 \leq y \leq 3)$, the polymer electrolyte layer corresponds to $(3 \leq y \leq 4)$, and the anode catalyst layer corresponds to $(4 \leq y \leq 5)$	184

7.21	The fraction of y direction water mass flux that is transported in the electrolyte at $x/L_{\text{ch}} = 0.5$. The y direction has been normalized such that the cathode catalyst layer corresponds to $(2 \leq y \leq 3)$, the polymer electrolyte layer corresponds to $(3 \leq y \leq 4)$, and the anode catalyst layer corresponds to $(4 \leq y \leq 5)$	185
7.22	Diagram of water transport in the MEA of a PEM fuel cell.	186
7.23	The membrane activity in the PEM fuel cell. The y direction has been normalized such that the cathode gas flow channel corresponds to $(0 \leq y \leq 1)$, the cathode electrode backing layer corresponds to $(1 \leq y \leq 2)$, the cathode catalyst layer corresponds to $(2 \leq y \leq 3)$, the polymer electrolyte layer corresponds to $(3 \leq y \leq 4)$, the anode catalyst layer corresponds to $(4 \leq y \leq 5)$, the anode electrode backing layer corresponds to $(5 \leq y \leq 6)$, and the anode gas flow channel corresponds to $(6 \leq y \leq 7)$. The (a) two-dimensional distribution and the (b) one-dimensional distribution at $x/L_{\text{ch}} = 0.5$ are shown.	188
7.24	The y -component of electronic current density in the PEM fuel cell. The y direction has been normalized such that the cathode gas flow channel corresponds to $(0 \leq y \leq 1)$, the cathode electrode backing layer corresponds to $(1 \leq y \leq 2)$, the cathode catalyst layer corresponds to $(2 \leq y \leq 3)$, the polymer electrolyte layer corresponds to $(3 \leq y \leq 4)$, the anode catalyst layer corresponds to $(4 \leq y \leq 5)$, the anode electrode backing layer corresponds to $(5 \leq y \leq 6)$, and the anode gas flow channel corresponds to $(6 \leq y \leq 7)$. The (a) two-dimensional distribution and the (b) one-dimensional distribution at $x/L_{\text{ch}} = 0.5$ are shown.	190
7.25	The solid phase potential in the PEM fuel cell. The y direction has been normalized such that the cathode gas flow channel corresponds to $(0 \leq y \leq 1)$, the cathode electrode backing layer corresponds to $(1 \leq y \leq 2)$, the cathode catalyst layer corresponds to $(2 \leq y \leq 3)$, the polymer electrolyte layer corresponds to $(3 \leq y \leq 4)$, the anode catalyst layer corresponds to $(4 \leq y \leq 5)$, the anode electrode backing layer corresponds to $(5 \leq y \leq 6)$, and the anode gas flow channel corresponds to $(6 \leq y \leq 7)$. The (a) two-dimensional distribution and the (b) one-dimensional distribution at $x/L_{\text{ch}} = 0.5$ are shown.	191
7.26	The y -component of ionic current density in the PEM fuel cell. The y direction has been normalized such that the cathode catalyst layer corresponds to $(2 \leq y \leq 3)$, the polymer electrolyte layer corresponds to $(3 \leq y \leq 4)$, and the anode catalyst layer corresponds to $(4 \leq y \leq 5)$. The (a) two-dimensional distribution and the (b) one-dimensional distribution at $x/L_{\text{ch}} = 0.5$ are shown.	193
7.27	The electrolyte potential in the catalyst and polymer electrolyte layers. The y direction has been normalized such that the cathode catalyst layer corresponds to $(2 \leq y \leq 3)$, the polymer electrolyte layer corresponds to $(3 \leq y \leq 4)$, and the anode catalyst layer corresponds to $(4 \leq y \leq 5)$. The (a) two-dimensional distribution and the (b) one-dimensional distribution at $x/L_{\text{ch}} = 0.5$ are shown.	194
7.28	The reaction rate in the cathode catalyst layer. The y direction has been normalized such that the cathode catalyst layer corresponds to $(2 \leq y \leq 3)$. The (a) two-dimensional distribution and the (b) one-dimensional distribution at $x/L_{\text{ch}} = 0.5$ are shown.	198

7.29	The reaction rate in the anode catalyst layer. The y direction has been normalized such that the anode catalyst layer corresponds to $(4 \leq y \leq 5)$. The (a) two-dimensional distribution and the (b) one-dimensional distribution at $x/L_{\text{ch}} = 0.5$ are shown.	199
7.30	The boundary conditions used for examining the effect of channel length.	201
7.31	The mesh used for the comparison between the mathematical model and experimental data. The regions are the (a) anode minus extension, (b) anode gas flow channel, (c) anode plus extension, (d) anode electrode backing layer, (e) anode catalyst layer, (f) polymer electrolyte layer, (g) cathode catalyst layer, (h) cathode electrode backing layer, (i) cathode minus extension, (j) cathode gas flow channel, (k) cathode plus extension. Note that the figure is not drawn to scale.	202
7.32	The membrane activity in the PEM fuel cell with a channel length of (a) 1×10^{-2} m and (b) 1×10^{-1} m. The y direction has been normalized such that the cathode gas flow channel corresponds to $(0 \leq y \leq 1)$, the cathode electrode backing layer corresponds to $(1 \leq y \leq 2)$, the cathode catalyst layer corresponds to $(2 \leq y \leq 3)$, the polymer electrolyte layer corresponds to $(3 \leq y \leq 4)$, the anode catalyst layer corresponds to $(4 \leq y \leq 5)$, the anode electrode backing layer corresponds to $(5 \leq y \leq 6)$, and the anode gas flow channel corresponds to $(6 \leq y \leq 7)$	204
7.33	The membrane activity in the PEM fuel cell with a channel length of (a) 1×10^{-2} m and (b) 1×10^{-1} m at $x/L_{\text{ch}} = 0, 0.5$ and 1. The y direction has been normalized such that the cathode gas flow channel corresponds to $(0 \leq y \leq 1)$, the cathode electrode backing layer corresponds to $(1 \leq y \leq 2)$, the cathode catalyst layer corresponds to $(2 \leq y \leq 3)$, the polymer electrolyte layer corresponds to $(3 \leq y \leq 4)$, the anode catalyst layer corresponds to $(4 \leq y \leq 5)$, the anode electrode backing layer corresponds to $(5 \leq y \leq 6)$, and the anode gas flow channel corresponds to $(6 \leq y \leq 7)$	205
7.34	The magnitude of the y -direction current density at the external boundary of the cathode bipolar plate ($y = 0$).	206

List of Symbols

A	Area, m^2 ; Numerical solution constant
\mathcal{A}_e	Dissociation of the polymer electrolyte membrane pore fluid
A_{kn}	Area of the interface between phases k and n , m^2
A_v	Reactive surface area per unit volume, m^{-1}
\tilde{a}	Membrane activity
B	Numerical solution constant
B^α	Tafel slope, V
\mathbf{b}	Momentum body force, N m^{-3}
b_i^α	Ratio of forward to backward reaction rate constant, mole m^{-3} or $\text{m}^3 \text{mole}^{-1}$
$C_{p,k}$	Constant pressure specific heat for phase k , $\text{J kg}^{-1} \text{K}^{-1}$
$C_{p,k}^\alpha$	Constant pressure specific heat for species α in phase k , $\text{J kg}^{-1} \text{K}^{-1}$
c	Concentration, mole m^{-3}
c_k^α	Concentration of species α in phase k , mole m^{-3}
\mathcal{D}_β^α	Overall diffusion coefficient of species α in the polymer electrolyte, $\text{kg m}^{-1} \text{s}^{-1}$ or $\text{kg m}^{-1} \text{V}^{-1} \text{s}^{-1}$
$D_{\alpha-k}$	Diffusion coefficient of species α in phase k , $\text{m}^2 \text{s}^{-1}$
$\mathcal{D}_{\alpha-\beta,k}$	Binary diffusion coefficient of species α and β in phase k , $\text{m}^2 \text{s}^{-1}$
E	Cell voltage, V
$E_J^{\text{H}_3\text{O}^+}$	Energy transfer due to ion migration, W m^{-3}
E_m	Energy transfer due to composition change, W m^{-3}
E_{react}	Energy transfer due to reactions, W m^{-3}

E_{rev}	Reversible cell voltage, V
E_W	Energy transfer due to phase change, W m^{-3}
\mathcal{F}	Faraday's constant, $9.6485309 \times 10^4 \text{ C mole}^{-1}$
g	Acceleration due to gravity, m s^{-2}
H	Enthalpy, J kg^{-1}
\hat{H}	Enthalpy, J mole^{-1}
H_k	Enthalpy of phase k , J kg^{-1}
H_k^α	Enthalpy of species α in phase k , J kg^{-1}
$\Delta \hat{H}_R$	Enthalpy of reaction, J mole^{-1}
I	Current, A
J	Current density, A m^{-2}
J_o	Exchange current density, A m^{-2}
\mathcal{J}_k^α	Mass flux of species α in phase k due to molecular diffusion, $\text{kg m}^{-2} \text{ s}^{-1}$
K	Permeability, m^2
\mathbb{K}_e	Equilibrium constant for the acid-base reaction in the polymer electrolyte membrane
k_{rk}	Relative permeability of phase k
k_i^α	Forward reaction rate constant, m s^{-1} or $\text{mole m}^{-2} \text{ s}^{-1}$
\mathcal{L}_e	Water content of the polymer electrolyte membrane
\hat{M}	Molecular weight, kg mole^{-1}
m''	Mass flux, $\text{kg m}^{-2} \text{ s}^{-1}$
\mathcal{N}_k^α	Molar flux due to diffusion of species α in phase k , $\text{mole m}^{-2} \text{ s}^{-1}$
N	Molar flux, $\text{mole m}^{-2} \text{ s}^{-1}$
$N_s^{e^-}$	Molar flux of electrons in the solid phase, $\text{mole m}^{-2} \text{ s}^{-1}$
\mathbf{n}_{kn}	Unit normal of the interface between phases k and n
P	Pressure, Pa
$\dot{\mathcal{P}}^\alpha$	Production of species α , $\text{mole m}^{-3} \text{ s}^{-1}$
P_{cgl}	Capillary pressure $P_g - P_\ell$, Pa
P_k	Pressure of phase k , Pa

\tilde{P}_k	Pressure deviation of phase k , Pa
P_{sat}	Saturation pressure, Pa
\mathbf{q}_k	Heat flux due to conduction in phase k , W m^{-2}
q_{react}	Heat of reaction, W m^{-2}
\mathcal{R}	Reaction rate, $\text{mole m}^{-2} \text{s}^{-1}$
\mathcal{R}	Universal gas constant, $8.31451 \text{ J mole}^{-1} \text{ K}^{-1}$
r	Interaction parameter for CO adsorption, J mole^{-1}
S	Entropy, $\text{J kg}^{-1} \text{ K}^{-1}$; Numerical solution source term
\hat{S}	Entropy, $\text{J mole}^{-1} \text{ K}^{-1}$
S_k	Entropy of phase k , $\text{J kg}^{-1} \text{ K}^{-1}$
S_k^α	Entropy of species α in phase k , $\text{J kg}^{-1} \text{ K}^{-1}$
$\Delta \hat{S}_R$	Entropy change due to reaction, $\text{J mole}^{-1} \text{ K}^{-1}$
s	Saturation
T	Temperature, K
T_k	Temperature of phase k , K
t	Time, s
U'	Reference potential, V
\mathbf{u}	Velocity, m s^{-1}
\mathbf{u}_k	Velocity of phase k , m s^{-1}
\mathbf{u}_k^α	Velocity of species α in phase k , m s^{-1}
V	Representative volume, m^3
V_k	Volume of phase k within the representative volume, m^3
V_{CV}	Volume of control volume
\mathbf{F}_k^α	Mass flux of species α in phase k , $\text{kg m}^{-2} \text{s}^{-1}$
\mathbf{w}_{kn}	Velocity of the interface between phases k and n , m s^{-1}
x	Rectangular coordinate, m
x_k^α	Mole fraction of species α in phase k
y	Rectangular coordinate, m

Z Capillary pressure correction factor that accounts for roughness

z Rectangular coordinate, m

z_α Charge of species α

Greek

α Relaxation factor

Γ Interfacial source term in the conservation equations

$\Gamma_{E,k}$ Interfacial source term representing the energy entering phase k , W m^{-3}

$\Gamma_{F,k}$ Interfacial source term representing the momentum change in phase k , N m^{-3}

$\Gamma_{M,k}$ Interfacial source term representing the mass entering phase k , $\text{kg m}^{-3} \text{s}^{-1}$

$\Gamma_{S,k}^\alpha$ Interfacial source term representing the mass of species α entering phase k , $\text{kg m}^{-3} \text{s}^{-1}$

$\Gamma_{S,k-n}^\alpha$ Interfacial source term representing the mass of species α entering phase k from phase n , $\text{kg m}^{-3} \text{s}^{-1}$

$\Gamma_{S,k-\text{react}}^\alpha$ Interfacial source term representing the mass of species α entering phase k due to reactions, $\text{kg m}^{-3} \text{s}^{-1}$

γ_k^α Activity coefficient of species α in phase k

Δ Distance in finite volume grid, m^{-1}

ϵ Volume fraction of the void region

ϵ_k Volume fraction of phase k

η Overpotential, V

η_{act} Activation overpotential, V

η_{cell} Cell overpotential, V

η_{ohmic} Ohmic overpotential, V

θ_c Contact angle

θ_s^α Fraction of reaction sites covered by species α

κ_k Electrical conductivity of phase k , S m^{-1}

λ_k Thermal conductivity of phase k , $\text{W m}^{-1} \text{K}^{-1}$

μ Viscosity, $\text{kg m}^{-1} \text{s}^{-1}$

$\hat{\mu}_k^\alpha$ Electro-chemical energy of species α in phase k , J mole^{-1}

μ_k	Viscosity of phase k , $\text{kg m}^{-1} \text{s}^{-1}$
ν	Kinematic viscosity, $\text{m}^2 \text{s}^{-1}$
ρ	Density, kg m^{-3}
ρ_k	Density of phase k , kg m^{-3}
σ	Surface tension, N m^{-1}
τ	Viscous stress, N m^{-2}
τ_k	Viscous stress in phase k , N m^{-2}
Φ	Potential, V
Φ_k	Potential of phase k , V
ω_k^α	Mass fraction of species α in phase k

Subscripts

a	Anode
act	Activation
BC	Boundary condition
bp	Bipolar plate
c	Cathode; convectonal component
cell	Cell
cl	Catalyst layer
d	Diffusional component
eb	Electrode backing layer
E	East control volume
e	Polymer electrolyte membrane; East face
fc	Gas flow channel
g	Gas
i	Index for the x -direction
j	Index for the y -direction
ℓ	Liquid
M	Polymer matrix of the polymer electrolyte membrane

m	Mixture
N	North control volume
NW	Non-wetting fluid
n	North face
ohmic	Ohmic
o	Reference value
P	Control volume center
ref	Reference value
rev	Reversible
S	South control volume
s	Solid; South face
sat	Saturation value
W	Wetting fluid; West control volume
w	West face

Superscripts

CDS	Central difference scheme
eff	Effective value
LDC	Linear deferred correction
old	Previous iteration value
UDS	Upwind difference scheme

Overbars

$\bar{}$	Equilibrium value
$\hat{}$	Molar units

Operators

$\langle \rangle$	Total-volume average
$\langle \rangle^*$	Phase-volume average

Chapter 1

Introduction

The transportation sector is a vital component of industrial societies, allowing for the movement of people and goods both nationally and internationally. Currently, the majority of transportation is accomplished with the use of fossil fuels and the internal combustion engine. However, due to the finite supply of fossil fuels and the environmental damage caused by combustion exhaust, such as global warming and air pollution, eliminating or reducing pollution from transportation sources is a major policy objective [1]. Currently, two possibilities exist for the power requirements of a zero-emission vehicle: batteries or fuel cells. Batteries are disadvantaged by long recharge times and limited driving range; only fuel cells have the potential of matching the convenience and range offered by the internal combustion engine, while emitting no pollutants, at least at the point of use [2].

Many different types of fuel cells exist, but the type most applicable for transportation applications is the polymer electrolyte membrane (PEM) fuel cell [3]. PEM fuel cells operate at a temperature of approximately 353 K (80°C), allowing for a start-up time comparable to the internal combustion engine. Since these fuel cells use a solid polymer as the electrolyte, the cell is mechanically robust: pressure differentials between the fuel and oxidant streams of up to 5.17 MPa are possible [4] and any environmental danger of electrolyte leakage is eliminated. With an attainable, net power density of over 1 kW/liter [5], PEM fuel cells are competitive with the internal com-

bustion engine in terms of power density for transportation applications [6]. Although PEM fuel cells have many advantages over the internal combustion engine in terms of environmental impact, there are several significant obstacles to their commercialization [1]. Many of the obstacles involve systems peripheral to the PEM fuel cells, such as a lack of hydrogen refueling infrastructure [7]. However, many challenges are specific to the PEM fuel cells, such as improving the durability, increasing the performance and reducing cost [1].

Overcoming these challenges can be aided through the use of mathematical modeling studies. Because of the small size of PEM fuel cells, particularly the thin catalyst layers where the reactions occur, local values of physically significant properties, such as concentration and current density, can not be directly measured. Through simulation, mathematical models can supply information about local phenomena that can be used to provide a better understanding on the processes occurring within the fuel cell. Additionally, mathematical models can be used as a replacement for time-consuming experimental investigations, allowing for the optimization of design parameters and operating conditions.

In order for a mathematical model to be useful, it must capture the physically relevant processes within a PEM fuel cell. Therefore, the goal of this thesis is to develop a comprehensive, consistent and systematic mathematical model of a PEM fuel cell. This chapter elaborates on the goals of the thesis research and provides an outline for the organization of this thesis. First, background information, that describes the structure and operation of a PEM fuel cell, is presented.

1.1 Background Information

Typical PEM fuel cells operate at a voltage ranging from 0.7 to 0.8 V, and produce a current per active area, or current density, of 0.2 to 0.6 A/cm² [3]. Most applications have voltage or power requirements that can not be satisfied by a single cell; thus, single cells are connected in series, forming a PEM fuel cell stack. For example, the Mark 902 fuel cell stack, manufactured by Ballard Power Systems, supplies 85 kW at a voltage of 284 V, and the Mark 902 single cells can be combined

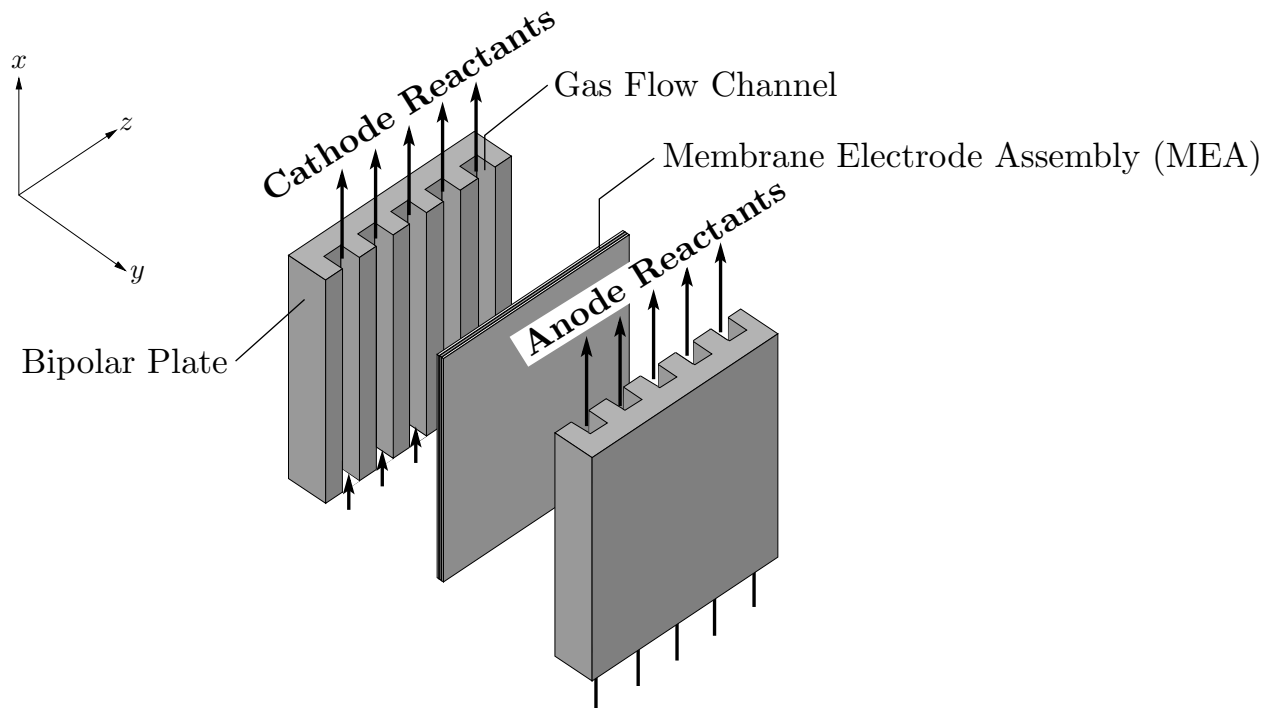


Figure 1.1: Illustration of a polymer electrolyte membrane (PEM) fuel cell.

to form stacks with power outputs of 10 to 300 kW [5]. Because the single PEM fuel cell is the basic unit of a stack, the thesis research concentrates on modeling the single PEM fuel cell as a first step, or building block.

A single PEM fuel cell consists of two bipolar plates and the membrane electrode assembly (MEA), as illustrated in Figure 1.1. The bipolar plates are constructed of graphite or metal. The anode and cathode reactants flow through the gas flow channels, which are grooved into the bipolar plates. The width and depth of the gas flow channels are typically about 1 mm or smaller, and the total thickness of a bipolar plate is 2 to 4 mm. Figure 1.1 illustrates the parallel gas flow channel configuration; other configurations are possible, such as serpentine or interdigitated [3, 8]. The gas flow channels allow the anode and cathode reactants to enter the MEA, where the electro-chemical reactions that convert the chemical energy of hydrogen and oxygen into water occur. Thus, the active area of the PEM fuel cell is the surface of the MEA, in Figure 1.1, that is normal to the y -direction. The MEA typically has a thickness of approximately $600 \mu\text{m}$ and consists of five distinct

CHAPTER 1. INTRODUCTION

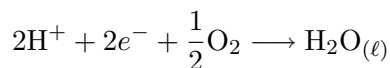
layers: the anode and cathode electrode backing layers; the anode and cathode catalyst layers; and the polymer electrolyte membrane layer, as illustrated in Figure 1.2.

Figure 1.2 illustrates each layer of the MEA and represents the xy plane of Figure 1.1. The PEM fuel cell is divided into an anode and cathode side by the polymer electrolyte membrane layer. The polymer electrolyte membrane layer consists of a sulfonated fluoropolymer, which is similar to Teflon, and acts as a conductor of positive ions that travel from the anode to the cathode catalyst layers. Electrons can not be transported in the membrane, and are forced to travel through the external circuit. As well, the permeability of the membrane to reactant gases is low; reactant cross-over is minimal. However, the membrane is permeable to water, and depending on the local operating conditions, water can be transported from either the anode to the cathode, or from the cathode to the anode sides of the PEM fuel cell [9]. The thickness of the polymer electrolyte membrane layer ranges from 50 to 250 μm [10] and the most popular polymer electrolyte membrane employed for PEM fuel cells is Nafion, manufactured by DuPont.

The conversion of the chemical energy of the reactants to electrical energy, heat, and liquid water occurs in the catalyst layers, which have thicknesses of approximately 5 μm [11]. The catalyst layers are a porous media; reactant gas, liquid water, and polymer electrolyte occupy the void space of a solid matrix that consists of carbon supported platinum catalyst. If the fuel is CO-free, the overall reaction in the anode catalyst layer is hydrogen oxidation:



In the cathode catalyst layer, the proton and electron produced by hydrogen oxidation participate in the reduction of oxygen:



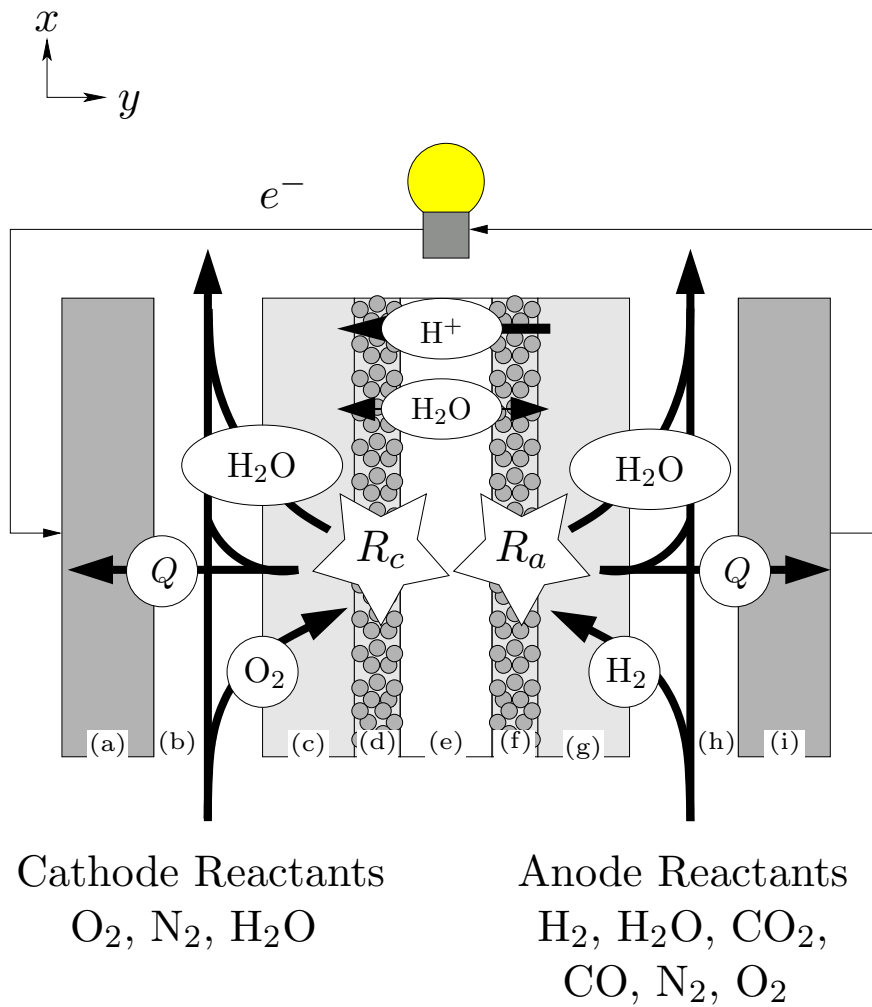
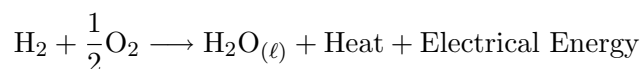


Figure 1.2: The components of a PEM fuel cell and the processes occurring within each component. The PEM fuel cell is composed of the (a) cathode bipolar plate, (b) cathode gas flow channel, (c) cathode electrode backing layer, (d) cathode catalyst layer, (e) polymer electrolyte membrane layer, (f) anode catalyst layer, (g) anode electrode backing layer, (h) anode gas flow channel, and (i) anode gas flow channel.

CHAPTER 1. INTRODUCTION

The combination of the two half cell reactions results in the overall PEM fuel cell reaction:



The anode and cathode electrode backing layers are typically composed of a porous, carbon paper, or cloth, and are approximately 200 μm in thickness [11]. The electrode backing layers allow reactant transport from the gas flow channels to the catalyst layers, and also allow the product, water, to be transported out of the MEA and into the gas flow channels. Electrons are transported in the solid matrix.

Figure 1.2 also illustrates the compositions of the anode and cathode gas streams. The reactant in the cathode side of the MEA is oxygen, with nitrogen being present if air is used as the fuel cell oxidant. Hydrogen is the main reactant in a PEM fuel cell, but carbon monoxide and carbon dioxide can be present if a reformed hydrocarbon is used as the fuel. The presence of carbon monoxide, even with concentration levels in the order of a few parts per million, poisons the hydrogen oxidation reaction; carbon monoxide inhibits the hydrogen oxidation reaction by adsorbing to the platinum catalyst [12]. Several methods of mitigating CO poisoning have been attempted, such as the use of an alloy catalyst, increasing the cell temperature, and introducing 2 to 5% oxygen into the anode gas stream, referred to as oxygen (O_2) bleeding [13]. Therefore, both oxygen and nitrogen can be present in the anode fuel stream. Humidification of the polymer electrolyte membrane is necessary for ion conduction and liquid water is produced by oxygen reduction; hence water, in both liquid and gas phases, is present in both the anode and cathode gas flow channels.

The reactions in the catalyst layers are exothermic; hence, heat must be transported out of the fuel cell. The heat can be removed via convection in the gas flow channels, conduction in the solid matrix of the catalyst and electrode backing layers, as well as conduction in the solid portion of the bipolar plates. Since liquid water is produced by the PEM fuel cell, the condensation and evaporation of water affects the heat transfer in a PEM fuel cell. Thus, the water and heat management in a fuel cell are closely linked.

CHAPTER 1. INTRODUCTION

Therefore, many physical and chemical phenomena occur within the layers of a fuel cell and these processes are summarized in Table 1.1. Electrons and heat are transported in the solid phase of the anode and cathode bipolar plates. The electron transport also generates heat within the bipolar plates through Joule heating. In the gas flow channels, both a liquid and gas phase exist. Thus, both mass and energy transport occurs with each fluid phase, as well as interfacial mass and energy transport due to the evaporation and condensation of water. The phenomena occurring within the electrode backing layers are a combination of the phenomena in the bipolar plates and gas flow channels. Hence, electron and heat transport occur in the solid phase, while mass and energy transport occur in the gas and liquid phases. Additionally, since the gas and liquid phases are in contact with the solid phase, the phenomena associated with porous media flow is present in the electrode backing layers. Like the electrode backing layer, the polymer electrolyte layer is also composed of a gas, liquid and solid phase; thus, many of the same phenomena are present. Unlike the electrode backing layers, however, the polymer electrolyte layer contains ions in the liquid phase. Therefore, liquid phase ionic transport and acid-base equilibrium between the ionic compounds in the liquid phase occur within this layer in addition to the phenomena occurring within the electrode backing layers. The phenomena in the catalyst layers include those occurring in both the electrode backing and polymer electrolyte layers. Unique to the catalyst layers are reactions which produce electrons and ions, as well as gas phase and liquid phase species.

These phenomena affect the performance of a PEM fuel cell, which is characterized by a voltage versus current density plot, or polarization curve. The cell voltage, in general, can be expressed as

$$E = E_{\text{rev}} - \eta_{\text{cell}}, \quad (1.1)$$

where E_{rev} represents the reversible, thermodynamically determined cell voltage and η_{cell} is the voltage loss, or overpotential of the PEM fuel cell. Under typical operating conditions, the reversible cell voltage is approximately 1.2 V. The overpotential arises from irreversibilities within the PEM fuel cell and there are three types of overpotential: activation, ohmic, and concentration [14].

Table 1.1: The physical and chemical phenomena in each layer of a PEM fuel cell.

Layer	Phenomena
Anode/cathode bipolar plate	<ul style="list-style-type: none"> • Electron transport • Solid phase heat conduction
Anode/cathode gas flow channel	<ul style="list-style-type: none"> • Gas phase mass and energy transport • Liquid phase mass and energy transport • Water evaporation and condensation
Anode/cathode electrode backing layer	<ul style="list-style-type: none"> • Gas phase mass and energy transport • Liquid phase mass and energy transport • Water evaporation and condensation • Electron transport • Solid phase heat conduction • Porous media flow
Anode/cathode catalyst layer	<ul style="list-style-type: none"> • Gas phase mass and energy transport • Liquid phase mass and energy transport • Water evaporation and condensation • Electron transport • Solid phase heat conduction • Ionic transport in solid electrolyte • Production and consumption of electrons, ions, gas and liquid species • Porous media flow
Polymer electrolyte membrane layer	<ul style="list-style-type: none"> • Gas phase mass and energy transport • Liquid phase mass and energy transport • Ionic and liquid transport in the polymer electrolyte • Solid phase heat conduction • Acid-base equilibrium • Porous media flow

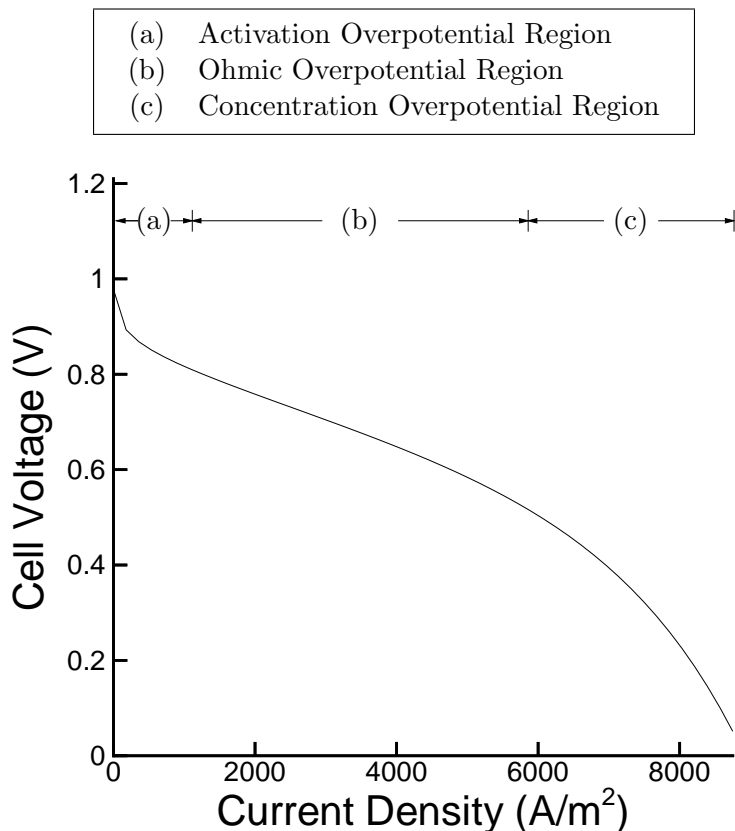


Figure 1.3: Polarization curve of a typical polymer electrolyte membrane fuel cell illustrating the activation, ohmic and concentration overpotential regions.

The polarization curve of a PEM fuel cell can be divided into three regions, with one type of overpotential dominating each region, although all three types of overpotential occur in each region simultaneously.

A typical polarization curve, illustrating the effect of the three types of overpotential, is shown in Figure 1.3. As current is drawn from the cell, the initial drop in cell voltage is mainly due to activation overpotential. In the activation overpotential region, voltage losses occur when slow electro-chemical reactions are driven from equilibrium to produce electric current. The electro-chemical reaction that is responsible for the majority of the activation overpotential is the reduction of oxygen in the cathode catalyst layer, although if CO is present in the anode, the voltage loss due to hydrogen electro-oxidation is also significant.

As the PEM fuel cell produces more electrical current, the activation losses increase at a slower

rate than the ohmic losses, and the polarization curve enters the region characterized by ohmic overpotential. The ohmic overpotential arises from the transport of charged species; resistance to electron migration in the bipolar plates, electrode backing layers, and catalyst layers, as well as hydronium ion transport in the polymer electrolyte membrane and catalyst layers contribute to the ohmic overpotential.

Further increases in current density result in the polarization curve entering the concentration overpotential region. The concentration overpotential is caused by mass transport limitations; the rates of the electro-chemical reactions within the catalyst layers are hindered by a lack of reactants. The mass transport limitations are due to diffusional limitations in the electrode backing and catalyst layers, and the phenomena of water flooding. At high current densities, the amount of liquid water produced in the cathode catalyst layer becomes greater than the amount of water that can be removed by the flow in the gas flow channels; the liquid water accumulates in the electrode backing layer and severely hinders the transport of oxygen to the cathode catalyst layer. The lack of oxygen hinders the oxygen reduction reaction in the cathode catalyst layer and increases the overpotential; this is referred to as water flooding. Therefore, the performance of a PEM fuel cell is affected by the electro-chemical kinetics in the catalyst layers, electron migration in the bipolar plates, electrode backing layers and catalyst layers, hydronium ion migration in the catalyst layers and polymer electrolyte membrane layer, and the mass transport of the reactants and water in each component of the MEA and gas flow channels.

1.2 Thesis Objectives and Outline

The performance of a PEM fuel cell is affected by the processes occurring within each layer of the cell, which include the simultaneous transport of neutral and charged species, as well as heat. In-situ measurements are difficult, due to the thinness of the layers, and thus mathematical modeling and simulation has become the predominant tool for better understanding and optimization of PEM fuel cells. Therefore, the objective of this thesis is to develop a mathematical PEM fuel cell

model.

Specifically, the thesis objectives are to

- develop a comprehensive, consistent, and systematic general formulation that can be used as a starting point for all mathematical models of practical PEM fuel cells,
- develop a simplified version of the general formulation that can be implemented and solved numerically within the time period of this thesis research,
- develop a novel model for water and ion transport which is consistent with the formulation for other transport phenomena,
- develop the numerical solution of the simplified formulation using the computer language of C++,
- provide numerical results that simulate physical and chemical phenomena within the PEM fuel cell.

The general formulation is comprehensive because it includes phenomena in all layers of a PEM fuel cell. Also, the general formulation is consistent, since the same conservation equations are applied to to each phase, solid, gas and liquid, of the PEM fuel cell. Since the equations which govern transport phenomena within each phase are similar, the final set of governing equations for the fuel cell can be derived systematically by applying a volume-averaging procedure to each phase. At the time that this thesis research was undertaken, general governing equations that were valid throughout a PEM fuel cell were not generally available. Instead, individual researchers developed governing equations that were valid in a specific region of the fuel cell. Thus, the development of the general governing equations, which represent the conservation of mass, momentum, species and energy in the gas, solid and liquid phases of a PEM fuel cell, is a unique contribution of this thesis research, and has been published as Baschuk and Li [15].

A simplified subset of the general, governing equations of Baschuk and Li [15] are solved numerically. The simplifications to the general, governing equations include assuming that the cell is

CHAPTER 1. INTRODUCTION

two-dimensional, isothermal and operating at steady-state. Additionally, the polymer electrolyte is considered impervious to the gas phase and it is assumed that the water in the gas phase does not condense to form liquid water. The simplified numerical model represents a unique contribution to fuel cell research because the model uses governing equations for the transport of liquid water and ions in the polymer electrolyte that are novel. Most PEM fuel cell models use a semi-empirical relationship to describe the transport of ions and water in the polymer electrolyte. Instead of the semi-empirical relationship, the mathematical model of this thesis research develops a membrane transport model based on the Generalized Stefan-Maxwell equations and acid-base equilibrium.

Chapter 2 summarizes PEM fuel cell models that currently exist in the published literature. The general governing equations for the mathematical model are presented in Chapter 3 and these general equations are simplified for numerical solution in Chapter 4. Chapter 5 documents the numerical solution of the simplified governing equations. Since the governing equations for water and ion transport in the electrolyte are novel, parameters such as diffusion coefficients must be obtained from experimental data. Chapter 6 determines these parameters and also compares the electrolyte model used in this thesis with the most commonly used electrolyte model in the published literature. The insights to the physical phenomena occurring within a PEM fuel cell that result from numerical simulation using the mathematical model of this thesis are examined in Chapter 7. A summary and suggestions for future work are given in Chapter 8.

Chapter 2

Literature Review

For approximately the past two decades, PEM fuel cells have been investigated as a possible zero-emission power source for transportation applications. As a result, many research studies have been undertaken with the goal of improving PEM fuel cell performance such that it is competitive with an internal combustion engine. Numerical modeling efforts have been a major part of this research, with the models fulfilling two purposes. The first purpose of the modeling efforts is to predict the performance of a PEM fuel cell; this involves predicting the polarization curve. The second purpose is to provide insight on the processes occurring within the PEM fuel cell during operation; this knowledge allows for the optimization of performance.

Several modeling studies exist in the published literature and can be classified as empirical or mathematical models. Empirical models are primarily concerned with predicting PEM fuel cell performance with a single, algebraic equation. Mathematical models apply fundamental conservation equations to the processes occurring within the PEM fuel cell and solve the resulting partial differential equations. The solution of a mathematical model includes the overall cell performance, as well as internal details such as reactant distribution. In this chapter, empirical and mathematical PEM fuel cell models in the published literature are reviewed.

2.1 Empirical Models

In the empirical modeling studies, the cell voltage is assumed to have a functional dependence on one or more variables, and the functional dependence is developed by applying a curve-fitting scheme to experimentally determined, PEM fuel cell polarization curves. The complexity of an empirical modeling study can be measured by the number of independent variables used in the cell voltage function. The simplest empirical modeling studies employ only one independent variable: cell current or current density. The model of Kim *et al.* [16] simulated all regions of the polarization curve with the function:

$$E = E_{\text{rev}} - b \log \left(\frac{J}{J_o} \right) - RJ - m \exp(nJ) \quad (2.1)$$

where E_{rev} is the reversible cell voltage, J is the cell current density, and b , J_o , R , m and n are fitting parameters. Each term in Equation (2.1) can be given physical significance: $b \log \left(\frac{J}{J_o} \right)$ represents the activation overpotential, RJ represents the ohmic overpotential, and $m \exp(nJ)$ represents the concentration overpotential regions of the polarization curve. Therefore, b and J_o are related to the kinetic parameters, particularly the Tafel constants of the oxygen reduction reaction, while R can be taken as the ohmic resistance of the polymer electrolyte membrane layer. The m and n were given physical meaning in the empirical function employed by Squadrito *et al.* [17]:

$$E = E_{\text{rev}} - b \log \left(\frac{J}{J_o} \right) - RJ + \alpha J^k \ln(1 - \beta J) \quad (2.2)$$

The variables α and k are fitting parameters and β is the inverse of the limiting current density, which is the maximum current density achievable.

The shape of the polarization curve depends on many parameters in addition to the current density. Therefore, Amphlett *et al.* [18, 19] developed a generalized steady state electro-chemical

model (GSSEM) of PEM fuel cell performance using the relationship:

$$\begin{aligned}
 E &= E_{\text{rev}} + \eta_{\text{act}} + \eta_{\text{ohmic}} & (2.3) \\
 \eta_{\text{act}} &= \zeta_1 + \zeta_2 T + \zeta_3 T \ln(c^{\text{O}_2}) + \zeta_4 T \ln(I) \\
 \eta_{\text{ohmic}} &= \gamma_1 + \gamma_2 T + \gamma_3 I
 \end{aligned}$$

where η_{act} is the activation overpotential, η_{ohmic} is the ohmic overpotential, T is the cell temperature, c^{O_2} is the concentration of oxygen, I is the cell current, and ζ , γ are empirical constants. Other independent variables have also been added to the GSSEM, such as carbon monoxide concentration [20] and effects due to aging [21].

2.2 Mathematical Models

Empirical models are effective at predicting performance, but provide little insight on the processes occurring within the PEM fuel cell. Both performance predictions and detailed information about the processes occurring within the PEM fuel cell are supplied by mathematical models. The processes occurring within a fuel cell include mass, momentum, species, and energy transport in the gaseous reactants and liquid water of the gas flow channels, electrode backing layers, catalyst layers, and polymer electrolyte membrane layer. These processes can be described, mathematically, by fundamental conservation laws, subject to assumptions. The assumptions include idealizations of the physical structure of each component and the relative importance of each process. Mathematical modeling studies solve the differential equations that are derived from these conservation laws, and the choice of assumptions influences the predictive capabilities of the model and the amount of information that can be gleaned from the modeling study. Additionally, a distinction should be made between micro-scale and macro-scale models. In micro-scale models, transport phenomena are modeled at the molecular level; for example, the interactions of ion, water and polymer molecules in the polymer electrolyte has been modeled by Jinnouchi and Okazaki [22]. However,

this scale of modeling is impractical for entire PEM fuel cells, since the number of molecules that can be modeled using the molecular dynamics (MD) method are limited. Typical polymer electrolyte systems are modeled for approximately 500 water molecules [23]. Thus, the mathematical models reviewed here are macro-scale models. Molecular interactions are represented by quantities such as a diffusion coefficients; thus, numerical solution of the entire fuel cell is possible.

The macro-scale mathematical models can be classified into two groups. In one group, the processes occurring within the MEA are modeled in detail, while the flow in the gas flow channels is either ignored or characterized by a boundary condition. The approach that this group uses can be referred to as the MEA-centered approach.

However, the gas flow channels are a significant component of a PEM fuel cell, and the flow in them is coupled to the processes occurring within the MEA. Therefore, the second group of modeling efforts concentrates on the modeling the flow in the gas flow channels using techniques from Computational Fluid Dynamics (CFD). These modeling efforts are referred to as the channel-centered approach. The MEA-centered approach predated the channel-centered approach and as a result, the channel-centered approach uses many of the equations of the MEA-centered approach as a starting point. A review of both approaches is included in this section.

2.2.1 MEA-Centered Approach

The majority of the modeling efforts using the MEA-centered approach are modifications or combinations of two pioneering models: the models of Bernardi and Verbrugge [24, 25] and Springer *et al.* [26, 27]. Both of these models assumed that the cell operated at steady-state and was isothermal. Additionally, both models were one-dimensional in their analysis of the processes in the gas flow channels and the MEA. Species transport was assumed to be one-dimensional through the MEA, while transport in the gas flow channels was considered to be one-dimensional along the channel with a uniform flow velocity, referred to as plug flow, in the channel.

Specifically, in the model of Bernardi and Verbrugge [24, 25], the flow in the gas flow channels, along the direction of the main flow, was assumed to have no pressure drop; hence, only the

CHAPTER 2. LITERATURE REVIEW

conservation of species was applied to the gas in the gas flow channels. The species transport was through the mechanism of convection only, and flow in the gas flow channels was analyzed in order to obtain the average concentration of reactants within the gas flow channels. This value was used as the boundary condition at the gas flow channel/electrode backing layer interface for the MEA model.

The electrode backing layers were assumed to be isotropic, porous media with both gaseous reactants and liquid water present in the pore regions. However, the gaseous reactants and the liquid water were assumed to travel in separate pore networks; there was no interaction between the two fluid streams. The gas phase flow was assumed to have no pressure drop and species transport was through diffusion only, with the Stefan-Maxwell equations being used to describe the diffusive fluxes. The conservation of mass and momentum were applied to the liquid phase, with the conservation of momentum equation being written as Darcy's law. Electron migration in the electrode backing layers were modeled using Ohm's law.

The polymer electrolyte layer was assumed to consist of a porous network of channels, filled with liquid water and H^+ ions. The liquid water transport was described by the conservation of mass and the conservation of momentum, with the conservation of momentum taking the form of Schlögl's equation. The ion transport was governed by the Nernst-Planck equation; however, Bernardi and Verbrugge [24, 25] assumed that the membrane was fully hydrated. With the fully hydrated membrane assumption, the concentration of H^+ ions was constant and the transport of ions was due to the potential gradient only.

The catalyst layers were assumed to be composed of a porous media with polymer electrolyte in the void regions. While the polymer electrolyte layer was assumed to be impervious to reactant gases, the polymer electrolyte in the void region allowed gas transport through diffusion only, with the diffusional flux being described by Fick's law. Hence, transport of liquid water and gaseous reactants were modeled in a similar manner as in the polymer electrolyte membrane layer. The oxidation of hydrogen in the anode catalyst layer, and the reduction of oxygen in the cathode catalyst layer, were modeled using the Butler-Volmer equation. Thus, equations for the conservation of

CHAPTER 2. LITERATURE REVIEW

species in each layer could be formed for each layer of the MEA, coupled with boundary conditions, and solved.

The model for water and charge transport in the polymer electrolyte membrane in the model of Bernardi and Verbrugge [24, 25] assumed that the water content of the membrane was constant. However, in a PEM fuel cell, a constant water content in the polymer electrolyte is unlikely to be achieved during the production of current. Water is produced at the cathode catalyst layer and electro-osmotic drag transports water from the anode to the cathode catalyst layer. Hence, a water concentration gradient in the membrane occurs, which, through diffusion, allows some water to “back-diffuse” from the cathode to the anode. Also, the protonic conductivity of the membrane is highly dependent on the water content. Thus, the effect of a variable membrane hydration in a PEM fuel cell was modeled by Springer *et al.* [26, 27]. The semi-empirical, governing equation for transport of water in the membrane consisted of two terms: a Fickian, concentration gradient term and another term consisting of the flux of H^+ ions multiplied by an osmotic-drag coefficient. The diffusional velocity of the H^+ ions was assumed to depend on the potential gradient through Ohm’s law, but the electrical conductivity of the membrane was allowed to be variable and a function of membrane hydration. Using experimental data, the water diffusion coefficient, electro-osmotic drag coefficient, and electrical conductivity were found as functions of membrane hydration. The membrane hydration was found to be a function of the relative humidity in the reactant gases.

The gas flow channels of Springer *et al.* [26, 27] were modeled in a similar manner as in Bernardi and Verbrugge [24, 25], as were the electrode backing layers. However, Springer *et al.* [26, 27] simplified the analysis of the catalyst layers, in that the electro-chemical reactions were assumed to occur on the surface of the electrode backing layer/polymer electrolyte membrane layer interface. Thus, the coupling of mass transfer, electron and proton migration, and electro-chemical reactions within the catalyst layers were not included in the model. In the model of Bernardi and Verbrugge [24, 25], the effect of liquid water in restricting reactant access to the catalyst layer was not modeled and the concentration overpotential region of the polarization curve could not be simulated. Springer *et al.* [26, 27] observed that the concentration overpotential region could be simulated if

CHAPTER 2. LITERATURE REVIEW

the porosity of the electrode backing layer was varied as a function of current density, allowing the model of Springer *et al.* [26, 27] to simulate all regions of the polarization curve.

Many other PEM fuel cell models, which used the MEA-centered approach, were based on the approaches of Bernardi and Verbrugge [24, 25] and Springer *et al.* [26, 27]. Weisbrod *et al.* [28] coupled the detailed catalyst layer model of Bernardi and Verbrugge [24, 25] with the variable hydration membrane model of Springer *et al.* [26, 27]. In order to obtain agreement with experimental data, the model of Bernardi and Verbrugge [24, 25] used an oxygen reduction rate constant, the exchange current density, several times larger than the experimental value. Gloaguen and Durand [29] remedied this by considering the catalyst layer to consist of a solid matrix with the void space occupied by reactant gas; the enhanced species diffusion allowed for the use of an exchange current density closer to the experimental value. Eikerling and Kornyshev [30] concentrated their modeling efforts on the cathode catalyst layer and developed analytical solutions corresponding to high and low cathode overpotentials, and either poor electrical conductivity or poor oxygen transport.

Marr and Li [11] used the membrane model of Bernardi and Verbrugge [24, 25], but improved the gas flow channel and catalyst layer formulations. Instead of assuming that the pressure drop was zero, the pressure was allowed to vary in the gas flow channels through the assumption that the flow was equivalent to one-dimensional pipe flow. As well, the average concentrations of reactants at the gas flow channel/electrode backing layer interface were not assumed to be the same as the average concentrations in the bulk flow of the gas flow channel. Rather, through the use of the heat and mass transfer equivalence assumption, the average concentrations at the interface were calculated using a log mean concentration relationship, analogous to the log mean temperature relationship used in heat transfer applications. The catalyst layer model of Bernardi and Verbrugge [24, 25] was also modified by Marr and Li [11], with the void space of the catalyst layer being occupied by both polymer electrolyte and liquid water. Baschuk and Li [14] further improved the electrode backing layer and catalyst layer models by allowing the void space to be occupied by gaseous reactants, liquid water, and polymer electrolyte; this allowed the model, through the variation of a parameter called the degree of water flooding, to simulate the concentration overpotential region

CHAPTER 2. LITERATURE REVIEW

of the polarization curve. Two-phase flow was added to the model of Bernardi and Verbrugge [24, 25] by Pisani *et al.* [31], whereby the flow of liquid water was governed by Darcy's law and the permeability of the electrode backing and catalyst layers was dependent on the liquid water saturation. This alteration allowed for the simulation of the concentration overpotential region of the polarization curve. Chu *et al.* [32] combined the electrode backing layer and catalyst layer models of Bernardi and Verbrugge [24, 25] with the membrane model of Springer *et al.* [26, 27], but allowed the porosity of the electrode backing and catalyst layers to vary with position.

Most modeling efforts concentrated on the cathode side of the PEM fuel cell, since the losses attributed to the oxygen reduction reaction are the largest source of voltage loss in a PEM fuel cell. However, if CO is present in the anode fuel, the voltage loss attributed to the anode side of the PEM fuel cell become significant due to CO poisoning. Wang and Savinell [33] developed a model of the anode catalyst layer using the variable membrane hydration of Springer *et al.* [26, 27] and the gas filled catalyst layer of Gloaguen and Durand [29]. CO poisoning was incorporated by altering the Butler-Volmer equation to take into account the reaction sites occupied by adsorbed CO. The coverage of CO on the electrode was modeled with the empirical relationship of Dhar *et al.* [34]. Springer *et al.* [35] used fundamental, reaction kinetics that included the adsorption, desorption, and electro-oxidation of both CO and H₂ in the anode catalyst layer. The model of Chan *et al.* [36] incorporated the reaction kinetics model of Springer *et al.* [35] into the PEM fuel cell model of Bernardi and Verbrugge [24, 25]. Baschuk and Li [37] simulated the mitigation effect of oxygen bleeding on CO poisoning through incorporating reaction kinetics models for the adsorption, desorption, and electro-oxidation of CO and H₂, the adsorption and desorption of O₂, and the heterogeneous oxidation of CO and H₂ by O₂ into the PEM fuel cell model of Baschuk and Li [14].

The overall PEM fuel cell reaction is exothermic; hence heat is produced by a PEM fuel cell. The transport of the heat produced by the PEM fuel cell reactions out of the cell is of interest, primarily because the water management of a PEM fuel cell is strongly connected to the thermal management. In order to provide details on the heat transfer in a PEM fuel cell, the isothermal

CHAPTER 2. LITERATURE REVIEW

assumption must be discarded and conservation of energy applied to the components of the PEM fuel cell. The model of Bevers *et al.* [38] and Wöhr *et al.* [39] incorporated the transport of mass, momentum, species, and energy in the electrode backing layers, catalyst layers, and polymer electrolyte membrane layer. Although the temperature was allowed to vary within the PEM fuel cell, the temperature of the fluid in the void space and the solid phase of the porous media were assumed to be equal. The flow of both the gaseous reactants and liquid water were analyzed, with the Dusty Gas Model being employed to describe the mass, momentum, and species transport for the gaseous reactants in the electrode backing and catalyst layers. The transport of liquid water in the electrode backing and catalyst layers was assumed proportional to the gradient of the water loading, defined as the ratio of the mass of water to the mass of the solid phase. The flow of the gaseous reactants and liquid water were coupled through the porosity; the presence of liquid water would decrease the pore volume available for gaseous reactants, inhibiting reactant flow. In the catalyst layers, the reaction kinetics were modeled with the Butler-Volmer equation and heat generation due to entropy changes and charge transfer resistance, or reversible and irreversible heat generation, were included. The transport of water and protons in the polymer electrolyte membrane layer was modeled with the Stefan-Maxwell equation.

Rowe and Li [40] also developed a non-isothermal model of a PEM fuel cell, and it was similar to the model of Bevers *et al.* [38] and Wöhr *et al.* [39] in that the fluid and solid temperatures were assumed to be equal. However, the model of Rowe and Li [40] included mass and species transport in the gas flow channels in a similar manner as the model of Bernardi and Verbrugge [24, 25]. Species transport in the electrode backing and catalyst layers was assumed to be through diffusion only, with the diffusional flux being described by the Stefan-Maxwell equations. The transport of liquid water was not analyzed, but the amount of flooding was included as an input parameter in order to simulate the entire polarization curve. The reactants in the electrode backing and catalyst layers were allowed to have a variable amount of humidification; thus the variable humidification membrane model of Springer *et al.* [26, 27] was used for the polymer electrolyte membrane layer.

In the one-dimensional models listed previously, the flow in the gas flow channels and electrode

backing layers were solved separately. Thus, the interaction between the gas flow channels and the electrode backing layers was not modeled, yet this interaction is important, since the water produced in a PEM fuel cell must be removed by the flow in the gas flow channels. As well, reactant depletion along the channels affect the electro-chemical reactions occurring within the catalyst layers. The interaction between the gas flow channels and the MEA were modeled by the MEA-centered approach by Fuller and Newman [9]. The transport in the gas flow channels and MEA were coupled; the one-dimensional MEA model was integrated along the flow direction in the gas flow channel. As a result, variations in parameters along the flow direction of the gas flow channels, such as reactant concentration and temperature, were transmitted to the MEA model; the fuel cell model was quasi-two-dimensional. Similar to Bernardi and Verbrugge [24, 25], the model of Fuller and Newman [9] assumed that there was no pressure drop in the PEM fuel cell. Also, the transport of species in the electrode backing and catalyst layers was by diffusion only, with the Stefan-Maxwell equation being employed to describe the diffusional fluxes. However, Fuller and Newman [9] differed from both Bernardi and Verbrugge [24, 25] and Springer *et al.* [26, 27] in modeling transport in the polymer electrolyte. Water and H^+ transport in the polymer electrolyte membrane layer was modeled using concentrated solution theory; the transport was assumed to be though diffusion only and the polymer electrolyte membrane was considered as a diffusing species, with a diffusional velocity of zero. The conservation of energy was applied by assuming that sections taken through the thickness of the MEA were of uniform temperature. Therefore, the temperature varied only along the flow direction of the gas flow channel.

Nguyen and White [41] also developed a quasi-two-dimensional, PEM fuel cell model. The model was similar to that of Fuller and Newman [9], except that the polymer electrolyte membrane layer was modeled using the variable hydration model of Springer *et al.* [26, 27], and the catalyst layer was considered to be an interface. The pressure drop in the gas flow channels was added to the model by Thirumalai and White [42], through considering the gas flow channels as a pipe network. Yi and Nguyen [43] further refined the energy transport analysis of the model of Nguyen and White [41] by allowing the bipolar plate, MEA, and the gas within the gas flow channels to

have different temperatures. Although most modeling studies assumed that the cell is operating in steady-state, van Bussel *et al.* [44] developed a transient, quasi-two-dimensional model, based on the one-dimensional model of Springer *et al.* [26, 27]. CO poisoning was incorporated into a quasi-two-dimensional model by Springer *et al.* [45].

Another method for coupling the MEA and gas flow channels within the MEA-centered approach is to model the MEA in a multi-dimensional manner and simulate any variations along the channel as a specified boundary condition at the MEA/gas flow channel interface. Singh *et al.* [46] developed a two-dimensional model consisting of the electrode backing layers, catalyst layers and polymer electrolyte membrane layer, using the same approach as the model of Bernardi and Verbrugge [24, 25]. Kazim *et al.* [47] applied the conservation of mass, momentum and species to the cathode electrode backing layer. The conservation of momentum was assumed to take the form of Darcy's law, and the catalyst layer was assumed to be a surface. The cathode electrode backing layer was also the focus of the model of Bradean *et al.* [48]. In addition to the conservation of mass, momentum, and species, the conservation of energy was also applied, with the solid and gas phases assumed to have the same temperature.

Two-phase flow has also been modeled using the differential equation, quasi-two-dimensional approach. He *et al.* [49] used a two-fluid approach to model the cathode electrode backing layer of a PEM fuel cell in two-dimensions. The catalyst layer was considered to be a surface and the effect of the gas flow channels were included as boundary conditions. The conservation of mass, momentum, and species were applied to both the liquid and the gas phases and then solved separately. Darcy's law was used for the conservation of momentum equation in the gas and liquid phases; however, using the definition of the capillary pressure, conservation of momentum for the liquid phase was rewritten so that the liquid phase velocity was proportional to the gas phase velocity and the gradient of saturation. Mass transport between the liquid and gas phases was included through an interfacial source term that was proportional to the difference between the water vapor partial pressure and the liquid water saturation pressure. Natarajan and Nguyen [50] also developed a two-phase, two-dimensional model of the cathode electrode backing layer that also included a

transient term. This two-dimensional model was extended into a quasi-three-dimensional model by Natarajan and Nguyen [51]. As in the quasi-two-dimensional models, the flow in the gas flow channels was analyzed by assuming that it was one-dimensional along the flow direction. This analysis supplied boundary conditions to the two-dimensional analysis, coupling the flow in the gas flow channels and electrode backing layers.

2.2.2 Channel-Centered Approach

Because the MEA-centered approach avoids solving the Navier-Stokes equations, the transport processes in the gas flow channel can not be fully coupled with the processes occurring within the MEA. Thus, the channel-centered approach is used, in which the governing equations for the entire fuel cell are discretized with the finite volume method. Three research groups have pioneered channel-centered approaches which can simulate an entire PEM fuel cell. These research groups are located at the University of Miami, Pennsylvania State University, and the University of South Carolina.

The University of Miami group first started the channel-centered approach with the model of Gurau *et al.* [52]. Gurau *et al.* [52] developed a single-phase, two-dimensional model that included the gas flow channels, electrode backing layers, catalyst layers, and polymer electrolyte membrane layer. The mathematical model was unified in that the equations representing the conservation of mass, momentum, species, and energy in each layer had the same general form, and differed through source terms. With the unified approach, the conservation of momentum in the electrode backing layers resulted in the generalized Darcy's law equation; a source term was added to the Navier-Stokes equations such that it reduced to Darcy's law for small values of permeability. The catalyst layer was assumed to consist of a solid matrix with the void space filled with polymer electrolyte membrane; the transport of liquid water in the polymer electrolyte membrane was modeled by a generalized Schlögl's equation. Thus, the water transport model for the polymer electrolyte membrane was similar to the model of Bernardi and Verbrugge [24, 25]. Current flow in the polymer electrolyte was modeled with Ohm's law, and the electrical conductivity was allowed

CHAPTER 2. LITERATURE REVIEW

to vary with membrane hydration using the conductivity model of Springer *et al.* [26, 27]. The diffusional flux of each species was modeled with Fick's law, and the temperature of the solid and gas phases were assumed to be equal. Zhou and Liu [53] extended the two-dimensional model of Gurau *et al.* [52] into three-dimensions, while You and Liu [54] developed a two-phase, isothermal, two-dimensional model of the cathode gas flow channels, electrode backing layer and catalyst layer.

The research group in the University of South Carolina began their channel-centered approach with a three-dimensional, single phase model [55]. The model started as an isothermal, three-dimensional model that incorporated the gas flow channels and MEA and was implemented by the commercial CFD software FLUENT. The conservation of mass, momentum, and species were applied to the gas flow channels, electrode backing layers, catalyst layers and polymer electrolyte membrane layer. The generalized Darcy's law was used for the conservation of momentum in the electrode backing layers and Fick's law was used to describe the diffusive flux. Water and current transport in the polymer electrolyte membrane layer were modeled with the membrane model of Springer *et al.* [26, 27]. The reaction rate in the catalyst layer, current flow and water transport in the polymer electrolyte membrane layer were not allowed to vary in the direction of thickness in the MEA; the effect of this was that the catalyst and polymer electrolyte membrane layers were effectively modeled as surfaces. The conservation of energy was added in Shimpalee and Dutta [56], and time-dependence added in Shimpalee *et al.* [57, 58]. Liquid water transport was added to the single-phase, three-dimensional model in Shimpalee *et al.* [59]. The liquid water was treated as a diffusing species, with the diffusional flux being proportional to the liquid water concentration gradient. In a manner similar to He *et al.* [49], the interfacial mass transfer rate was proportional to the difference between the water vapor partial pressure and the saturation pressure.

The research group in Pennsylvania State University began their channel-centered approach with a two-phase, two-dimensional model of the cathode gas flow channel and electrode backing layer using the Multiphase Mixture Model (MMM) [60]. The catalyst layer was treated as a surface, and modeled with a boundary condition. The conservation of mass, momentum, and species were applied to both the gas and liquid phases, and then added together to form equations governing

CHAPTER 2. LITERATURE REVIEW

the conservation of mass, momentum, and species in the two-phase mixture. The conservation of momentum in the cathode electrode backing layer was in the form of Darcy's law, and through algebraic manipulations, the flux of liquid water, relative to the mass flux of the two-phase mixture, was found to be a function of the capillary pressure and gravitational body force. The capillary pressure, in turn, was a function of the saturation, or volume fraction of liquid water in the electrode backing void space. Thus, although the conservation equations were solved for mixture values of velocity, pressure, and concentration, the values for each phase could be determined with an algebraic relationship. A single phase, isothermal, two-dimensional, transient model, using a similar formulation as in Gurau *et al.* [52], was presented in Um *et al.* [61], and extended to three dimensions in Um *et al.* [61]. More recently, several analyses with a single phase model that uses the membrane water transport equations of Springer *et al.* [26, 27] have been presented, with sample works being Wang and Wang [62] and Wang and Wang [63]. Unlike the FLUENT model of the University of South Carolina group, the recent models do not assume that the catalyst and polymer electrolyte layers are one-dimensional. Instead, they used the procedure introduced by Kulikovsky [64] to couple the gas phase and membrane water transport.

Kulikovsky [64] coupled a three-dimensional flow channel and electrode backing model with a one-dimensional model of the transport in the catalyst layers and polymer electrolyte. The transport of water in the electrolyte was modeled with the same model as Springer *et al.* [26], while gas transport in the catalyst layer was assumed to be due to Knudsen diffusion only. In the catalyst layer, the conservation of water included the water flux due to a gradient in gas phase water concentration and a gradient in the hydration of the membrane; thus, there were two unknowns but only one equation. However, the membrane hydration and the concentration of water in the gas phase were not independent, but rather related through the hydration versus relative humidity curves of Springer *et al.* [26]. Thus, the gradient of membrane hydration could be transformed to a gradient of gas phase water concentration and the conservation of total water was solved.

Other modeling approaches also assumed that the mass transport in the catalyst layers was due to Knudsen diffusion. Mazumder and Cole [65] developed a non-isothermal, two-phase, three-

dimensional model that treated the transport in the catalyst layer as Knudsen diffusion. The water transport in the electrolyte was highly simplified in that water transport was through electro-osmotic drag only. The amount of water dragged by the current was assumed to be proportional to the volume fraction of liquid water. Lister *et al.* [66] simulated a fuel cell cathode that was open to the atmosphere; hence, the reactants and products depended on natural convection for transport. The electrode backing and catalyst layers were assumed to have a small pore size such that Knudsen diffusion dominated the transport of the species.

An alternative to collapsing the transport of gas phase water and liquid water in the electrolyte to a function of one variable is to solve the gas phase and liquid water transport separately and couple them with an interfacial mass transfer term. This was the approach taken by the two-dimensional model of Siegel *et al.* [67]. Siegel *et al.* [67] assumed that the void space of the catalyst layer was filled with both gas and polymer electrolyte. The conservation of mass, momentum and species was applied to the gas phase, while the conservation of water was considered in the polymer electrolyte. The membrane model of Springer *et al.* [26, 27] was used to describe the water and current transport in the polymer electrolyte. The water in the gas phase and electrolyte were coupled by an interfacial mass transfer term that was analogous to Newton's law of cooling for convective heat transfer.

Other channel-centered approach models share characteristics with the ones previously mentioned. Jang *et al.* [68] used a model similar to Gurau *et al.* [52], but included the effect of liquid water by calculating the liquid saturation and correcting the gas phase diffusivities for the reduced porosity. The models of the University of South Carolina and University of Miami groups have been used by other researchers; Jen *et al.* [69] used the model of Zhou and Liu [53] and Kumar and Reddy [70] used the model of Shimpalee *et al.* [55]. Berning *et al.* [71] developed a three-dimensional, single-phase fuel cell model that included the gas flow channels, electrode backing layers, and polymer electrolyte membrane layer; the catalyst layers were treated as interfaces in a similar manner as Shimpalee *et al.* [55]. The conservation of mass, momentum, species and energy was applied to the PEM fuel cell, and the conservation of energy in the gas and solid phases

were considered separately; thus the temperatures of the gas and solid phases could differ. Heat transfer between the solid and gas phases was modeled with a convective heat transfer coefficient. Ferng *et al.* [72] applied the mixture approach to the conservation of mass, momentum, species, and energy in the cathode gas flow channel and electrode backing layer. The cathode catalyst layer was considered an interface, similar to the model of Wang *et al.* [60]. However, the model assumed homogeneous flow; the gas and liquid phases were assumed to have the same velocity. Also, the conservation of momentum equation used in the electrode backing layers added the Forchheimer drag term to the generalized Darcy's law used by other modeling approaches. Stockie [73] explored the effect of using a hydrophobic versus a hydrophilic capillary pressure function with a model similar to that of Wang *et al.* [60].

2.3 Summary

PEM fuel cell models can be classified as empirical models, mathematical models that use a MEA-centered approach, or mathematical models that use a channel-centered approach. The first PEM fuel cell models were empirical. Although empirical models were effective at reproducing PEM fuel cell performance, they had limited predictive capability.

The MEA-centered approach typically modeled the MEA, but not the gas flow channels. The governing equations were formulated for the specific layers in the MEA and the layers were linked with internal boundary conditions, based on the continuity of total mass and current flows from one layer to the next. However, this approach has significant numerical challenges when applied to a multi-dimensional analysis, because while the total mass or current transfer between layers can be easily calculated, the distribution along a multi-dimensional boundary can not be easily determined. Thus, the MEA-centered approach is limited mainly to a one-dimensional analysis.

While the MEA-centered approach concentrates mainly on the MEA, the channel-centered approach traditionally concentrated on solving the Navier-Stokes equations for the flow in the gas flow channels. Many of the models neglected the MEA and replaced it with boundary conditions,

CHAPTER 2. LITERATURE REVIEW

or concentrated on a half cell, instead of the entire PEM fuel cell.

Therefore, most of the fundamental-based models available in the literature either focused on the MEA exclusively, such as the MEA-centered approach, or the flow channels, such as the channel-centered approach. However, the interactions between the processes occurring within the MEA and gas flow channels are significant and a more comprehensive PEM fuel cell model, that considers both the MEA and gas flow channel, is required. One reason that many channel-centered approaches concentrated on the gas flow channels and neglected the MEA was that governing equations for the fuel cell, which could be applied to all layers, were not available. Thus, this thesis research develops a mathematical model that consists of comprehensive, general governing equations that can be consistently and systematically applied to all layers of the PEM fuel cell; the general formulation was published in Baschuk and Li [15].

The numerical solution presented in this thesis is based on a simplified version of the general governing equations. The simplifying assumptions include the assumption that all water outside of the polymer electrolyte is in the gas phase only, the cell is operating in steady state and isothermally, and that the cell is two-dimensional. These assumptions make the numerical model similar to those from the Pennsylvania State University group; a similar numerical solution method is used in which the the method of Kulikovsky [64] is used to couple the gas phase and membrane water transport. However, it differs from the reviewed models in that neither the membrane model of Springer *et al.* [26, 27] nor Bernardi and Verbrugge [24, 25] are used. Instead, a membrane model based on the general governing equations, similar to the general membrane transport analysis of Scattergood and Lightfoot [74], is employed.

Chapter 3

General Formulation

When this thesis research was undertaken, a set of general governing equations for the conservation of mass, momentum, species and energy that were applicable to all layers of a PEM fuel cell were not readily available. Therefore, part of this thesis research consists of formulating the general governing equations for a PEM fuel cell, and this general formulation has been published in Baschuk and Li [15]. The general governing equations are also presented in this chapter.

The general governing equations are influenced by the physical structure of a PEM fuel cell, which consists of several co-existing phases. Conservation equations govern the transport of mass, momentum, species and energy in each phase. Since the phases co-exist, interfacial interactions between the phases occur. These interactions are incorporated into the governing equations through source terms that are the result of a volume-averaging procedure. The values of the interfacial source terms are unique in each layer.

The physical structure of the PEM fuel cell is presented in this chapter, along with the major assumptions and the volume-averaging procedure. The volume-averaged equations representing the conservation of momentum, conservation of species and mass, and the conservation of energy are each presented.

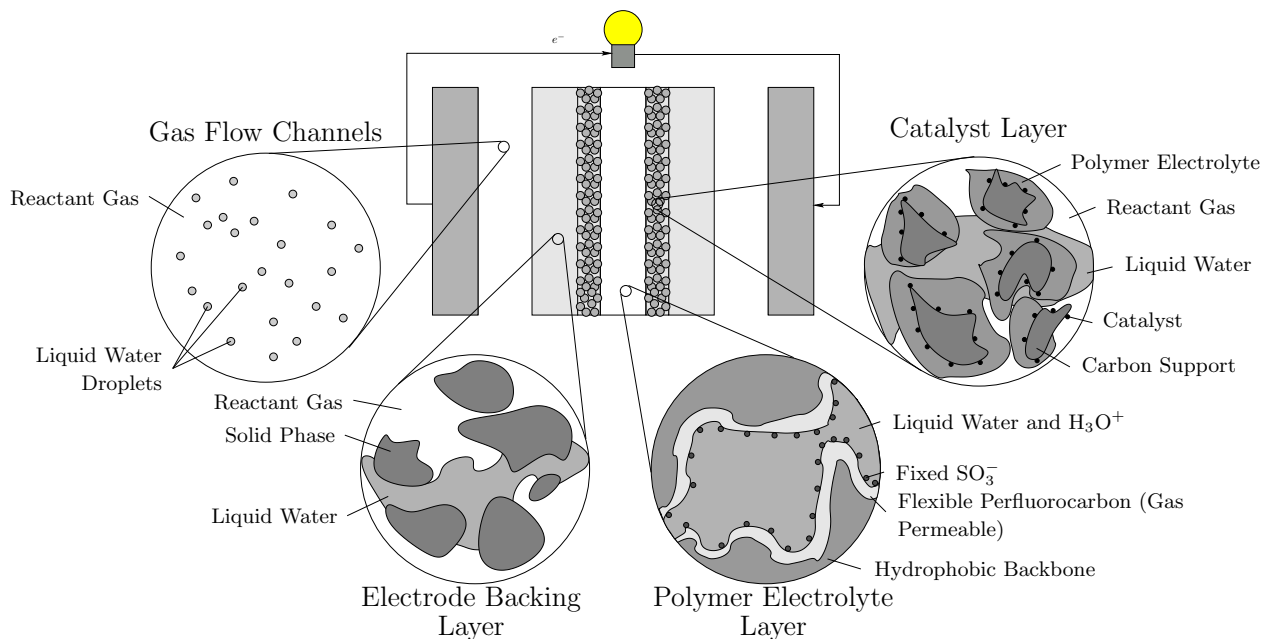


Figure 3.1: The structure of the layers within a PEM fuel cell.

3.1 Physical Structure

A PEM fuel cell can be visualized as several, co-existing phases, which are shown in Figure 3.1. Three phases exist within the fuel cell: solid, liquid and gas. The bipolar plates are composed of only a solid phase consisting of carbon. In the gas flow channels, both a multi-component gas phase and a liquid phase that consists of water are present. The liquid water is shown in Figure 3.1 as being composed of droplets. However, other types of two phase flow are possible, such as stratified, depending on the Reynolds number [75]. The electrode backing layers consist of the gas and liquid phases of the gas flow channels and a solid phase consisting of porous carbon paper or cloth.

The polymer electrolyte layer is composed of Nafion which, according to the ionic cluster model of Gierke and Hsu [76], can also be considered as a combination of solid, liquid and gas phases. In the presence of water, the Nafion membrane is composed of three regions [77]. One region is composed of a liquid phase that contains water and hydronium ions. The liquid water and hydronium ions are contained within clusters that have a diameter of approximately 4 nm [76]. Channels interconnect the clusters, with the channels having a diameter of approximately 1 nm [76]. The surface of the

channels and clusters are lined with immobile sulfonate and sulfonate ions. The second region is the rigid, hydrophobic backbone of the polymer. The third region is located between the clusters and the rigid, hydrophobic backbone of the polymer and can be described as the amorphous part of the perfluorinated backbone. This hydrophobic region is permeable to gases; thus, transport of reactant gas occurs in this region. Although the polymer electrolyte is permeable to gas, the permeability is low and reactant cross-over is small.

In the model presented in this thesis, the positive ion in the polymer electrolyte is assumed to be H_3O^+ , rather than H^+ , as was assumed in the models of Bernardi and Verbrugge [24] and Springer *et al.* [27]. The reason for this assumption is that in the presence of water, a H^+ ion solvates [78] and becomes $\text{H}^+ \cdot [\text{H}_2\text{O}]_n$, where n is the number of water molecules attached to the H^+ ion. From experimental studies, the number of water molecules that accompany ion transport in the electrolyte is 1 [79]. Thus, the experimental evidence suggests that $n = 1$ and the H^+ exists within the electrolyte pores as a hydronium ion: H_3O^+ . Other electrolyte models, such as Thampan *et al.* [78], also assume that the positive ion is hydronium.

The catalyst layers combine the structure of the electrode backing and polymer electrolyte layers. Thus, the catalyst layers are a porous media, with a solid matrix consisting of carbon supported platinum catalyst. The multi-component reactant gases, liquid phase water and polymer electrolyte are contained in the void spaces. Within the polymer electrolyte, the ion-containing liquid phase, reactant gas, and polymer backbone exist. The electro-chemical reactions of hydrogen oxidation and oxygen reduction take place on the catalyst surfaces.

Thus, a PEM fuel cell consists of several phases. The solid phases include the carbon in the bipolar plates, electrode backing and catalyst layers, as well as the polymer matrix of the electrolyte. Pure, liquid water is present in the gas flow channels, electrode backing and catalyst layers, while a liquid mixture containing water and hydronium is contained within the polymer electrolyte of the polymer electrolyte and catalyst layers. The multi-component reactant gases are present throughout the cell, except in the solid portions of the bipolar plates. The governing equations for each phase are derived using volume-averaging, which is examined in the next section.

3.2 Assumptions

The major assumption in the general formulation developed in this section is the length scale that is considered. The model presented in this thesis is a continuum model in which the interactions between the phases are not directly resolved, but rather represented by interfacial source terms that are functions of the mean properties and flow in each phase. Other approaches to the problem of modeling a PEM fuel cell are possible. For example, Bultel *et al.* [80] modeled the catalyst layer at the particle level. Thus, no averaging procedure was necessary, since boundary conditions could be applied between the catalyst particles and the reactants. Jinnouchi and Okazaki [22] modeled the polymer electrolyte at the molecular scale: the motion of individual molecules were resolved. Thus, the thesis research model is macroscopic, compared to other possible approaches. However, these alternate approaches are impractical for modeling practical PEM fuel cells. In order to model a fuel cell, which has dimensions in the order of centimeters or even meters, at the small scales of individual particles or molecules would be impossible using current computational resources. Thus, the macroscopic approach used in this thesis research must be used in order to model entire PEM fuel cells. However, in order to accurately model the processes occurring within the cell, the interfacial source terms should include the effect of the small scale phenomena on the mean values considered in the model.

3.3 Volume-Averaging Method

The PEM fuel cell consists of several co-existing phases. Within each phase, the transport of mass, momentum, species and energy are governed by conservation equations. In order to capture the interactions between the phases, a volume-averaging procedure is applied to the conservation equations for each species. The volume-averaging procedure integrates the conservation equation for each species over a representative volume. The representative volume is illustrated in Figure 3.2. The integration process is represented by

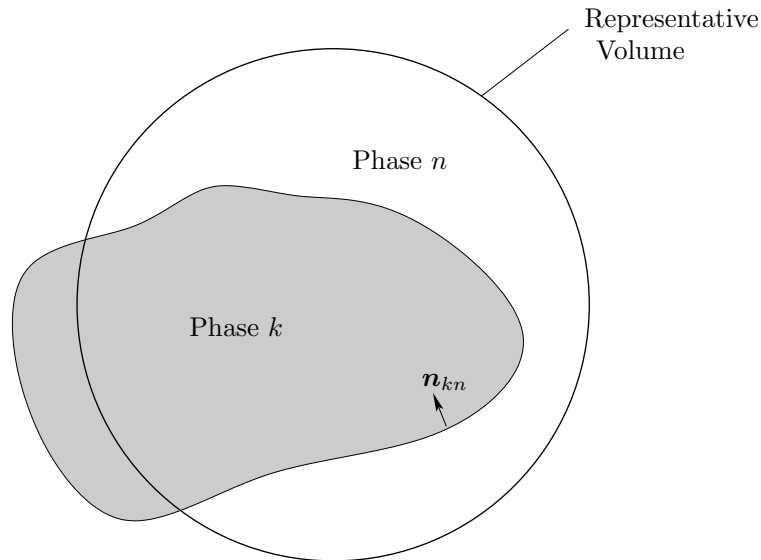


Figure 3.2: Representative volume for volume-averaging the conservation equations.

$$\langle \text{Conservation Equation} \rangle = \frac{1}{V_r} \int_{V_r} (\text{Conservation Equation}) dV, \quad (3.1)$$

where V_r is the representative volume.

In general, three approaches exist for deriving conservation equations [81]:

1. Infinitesimal particle,
2. Infinitesimal control volume,
3. Finite control volume.

The infinitesimal particle approach considers a fluid particle as it moves relative to a fixed coordinate system. Then, the description of the motion of a single fluid particle is transformed into a description of various particles at a fixed point in space. In the infinitesimal control volume approach, a mass, momentum, species, or energy balance is applied to an infinitesimal cubic control volume in space. Finally, the finite control volume approach applies mass, momentum, species or energy balances to a finite control volume and uses various integral relations to obtain the final governing equations. Of the three approaches, the infinitesimal control volume approach is the most physically descriptive, since the various fluxes are accounted for directly in the flux balance on the control

volume. However, this is a disadvantage for deriving the governing equations used in this thesis due to the presence of co-existing phases; it would be easy to omit a physically relevant interfacial force or flux. Thus, the approach taken in this thesis, as represented by Equation (3.1), is the finite control volume approach.

Applying the integration process requires two relationships. The first relationship is the transport theorem [82]:

$$\int_{V_k} \frac{\partial \Psi_k}{\partial t} dV = \frac{\partial}{\partial t} \int_{V_k} \Psi_k dV - \int_{A_{kn}} \Psi_k \mathbf{w}_{kn} \cdot \mathbf{n}_{kn} dS \quad (3.2)$$

where A_{kn} is the surface area and \mathbf{w}_{kn} is the velocity of the interface between phases k and n . The second relationship is the averaging theorem [82]:

$$\begin{aligned} \int_{V_k} \nabla \Psi_k dV &= \nabla \int_{V_k} \Psi_k dV + \int_{A_{kn}} \Psi_k \mathbf{n}_{kn} dS && \text{scalar} \\ \int_{V_k} \nabla \cdot \mathbf{\Psi}_k dV &= \nabla \cdot \int_{V_k} \mathbf{\Psi}_k dV + \int_{A_{kn}} \mathbf{\Psi}_k \cdot \mathbf{n}_{kn} dS && \text{vector/tensor} \end{aligned} \quad (3.3)$$

Using the transport and averaging theorems, the volume-averaged conservation equations can be expressed in terms of volume-averaged quantities, such as density and velocity, and interfacial source terms. For quantities such as density and velocity, the phase-volume, or intrinsic, average is defined as

$$\langle \Psi_k \rangle^* = \frac{1}{V_k} \int_{V_k} \Psi_k dV, \quad (3.4)$$

where V_k is the volume of phase k within the representative volume and Ψ_k is a quantity within phase k , such as density or velocity. The phase-volume average of Equation (3.4) and the total-volume average of Equation (3.1) are related with

$$\frac{\langle \Psi_k \rangle}{\langle \Psi_k \rangle^*} = \frac{V_k}{V_r} = \epsilon_k, \quad (3.5)$$

where ϵ_k is the volume fraction of phase k within the representative volume. One assumption is necessary in order to allow the volume-averaged equations to be a function of volume-averaged quantities. If Ψ_k and Ω_k are two quantities in phase k , then it is assumed that:

$$\langle \Psi_k \Omega_k \rangle^* = \langle \Psi_k \rangle^* \langle \Omega_k \rangle^* \quad (3.6)$$

After volume-averaging, transport properties, such as viscosity and thermal conductivity, differ from their bulk values. In general, they are correlated as functions of the bulk value and porous media structure [83]. For PEM fuel cells, the Bruggemann correction is often used [24]:

$$\Psi_k^{\text{eff}} = (\epsilon_k)^{\frac{1}{2}} \Psi_k \quad (3.7)$$

The volume-averaging procedure is applied to the conservation of momentum, species and mass, and energy for each phase. These volume-averaged conservation equations become the general, governing equations for a PEM fuel cell. The interfacial source terms, which represent the interactions between the phases, differ from layer-to-layer in the fuel cell. The conservation equations for each phase are presented in the next sections, along with recommended interfacial source terms.

3.4 Conservation of Momentum

The conservation of momentum only applies to the gas and liquid phases because the velocity of the solid phase is zero. The conservation of momentum is [84]

$$\frac{\partial}{\partial t} (\rho_k \mathbf{u}_k) + \nabla \cdot (\rho_k \mathbf{u}_k \mathbf{u}_k) + \nabla P_k - \nabla \cdot \boldsymbol{\tau}_k - \rho_k \mathbf{g} - \mathbf{b} = 0, \quad (3.8)$$

where the subscript k denotes the phase. The density and velocity of the phase are denoted by ρ_k and \mathbf{u}_k , respectively. In the conservation of momentum, Equation (3.8), momentum change due to pressure (P_k), viscous stress ($\boldsymbol{\tau}_k$), gravity (\mathbf{g}), and a body force (\mathbf{b}_k) are included. The viscous

stress is expressed as [84]

$$\boldsymbol{\tau}_k = \mu_k \left[\nabla \mathbf{u}_k + (\nabla \mathbf{u}_k)^\dagger \right], \quad (3.9)$$

where \dagger represents the transpose and μ_k is the viscosity of phase k ; it is assumed that each phase is a Newtonian fluid and that the dilation effect on the viscous stress tensor is negligible. The body force, \mathbf{b}_k , only applies to the liquid phase in the polymer electrolyte membrane. Because of the immobile sulfonate ions, the liquid phase has a net positive charge. In the presence of an electric field, a force is exerted on the fluid and the body force is

$$\mathbf{b}_{\ell,e} = c_{\ell,e}^{\text{H}_3\text{O}^+} \mathcal{F} \nabla \Phi_e, \quad (3.10)$$

where $c_{\ell,e}^{\text{H}_3\text{O}^+}$ is the concentration of hydronium ions in the electrolyte, \mathcal{F} is the Faraday constant, and Φ_e is the potential in the polymer electrolyte.

After the volume-averaging procedure, the conservation of momentum becomes

$$\begin{aligned} \frac{\partial}{\partial t} (\epsilon_k \langle \rho_k \rangle^* \langle \mathbf{u}_k \rangle^*) + \nabla \cdot (\epsilon_k \langle \rho_k \rangle^* \langle \mathbf{u}_k \rangle^* \langle \mathbf{u}_k \rangle^*) + \nabla (\epsilon_k \langle P_k \rangle^*) \\ - \langle P_k \rangle^* \nabla (\epsilon_k) - \nabla \cdot (\epsilon_k \langle \boldsymbol{\tau}_k \rangle^*) - \epsilon_k \langle \rho_k \rangle^* \mathbf{g} - \epsilon_k \langle \mathbf{b} \rangle^* = \Gamma_{F,k}, \end{aligned} \quad (3.11)$$

where $\Gamma_{F,k}$ represents the interfacial source term. The volume-averaged forms of the viscous stress tensor ($\langle \boldsymbol{\tau}_k \rangle^*$) and body force ($\langle \mathbf{b}_k \rangle^*$) are

$$\langle \boldsymbol{\tau}_k \rangle^* = \mu_k^{\text{eff}} \left[\nabla \langle \mathbf{u}_k \rangle^* + (\nabla \langle \mathbf{u}_k \rangle^*)^\dagger \right], \quad (3.12)$$

$$\langle \mathbf{b}_{\ell,e} \rangle^* = \left\langle c_{\ell,e}^{\text{H}_3\text{O}^+} \right\rangle^* \mathcal{F} \nabla \langle \Phi_e \rangle^*, \quad (3.13)$$

where the assumption of Equation (3.6) was used to express the stress tensor and body force in terms of phase-averaged quantities.

Mathematically, the interfacial source term in the conservation of momentum is expressed as

$$\begin{aligned} \Gamma_{F,k} = & - \sum_n \frac{1}{V_r} \int_{A_{kn}} \rho_k \mathbf{u}_k (\mathbf{u}_k - \mathbf{u}_{kn}) \cdot \mathbf{n}_{kn} dA \\ & - \sum_n \frac{1}{V_r} \int_{A_{kn}} \tilde{P}_k \mathbf{n}_{kn} dA - \sum_n \frac{1}{V_r} \int_{A_{kn}} \boldsymbol{\tau}_k \cdot \mathbf{n}_{kn} dA, \end{aligned} \quad (3.14)$$

where \sum_n represents the summation over all adjacent n phases, A_{kn} is the interfacial area of phases k and n , and \mathbf{u}_{kn} is the velocity of the interface of k and n within the representative volume. The pressure deviation, \tilde{P}_k , is given by [82]

$$\tilde{P}_k = P_k - \langle P_k \rangle^*. \quad (3.15)$$

In order to solve the volume-averaged conservation of momentum equation, the interfacial source term must be expressed as a function of volume-averaged quantities. The expression for the interfacial source term depends on phase distribution. Thus, the interfacial source term in the gas flow channels, where only the gas and liquid phases are present, is different than the interfacial source term for the other layers where a solid phase is present.

The interfacial source term in the gas flow channel depends on the nature of the flow and the definition of it is beyond the scope of this thesis. In general, there are two possible methods for dealing with two-phase, liquid-gas flow. One method is to combine the gas and liquid conservation of momentum equations, eliminating the interfacial source terms. If homogeneous flow is assumed, then the gas and liquid velocities are equal and the conservation of momentum equation can be solved for the mixture velocity; this approach is referred to as the mixture approach [75] and can be used if one phase is dispersed in the other phase. The second approach is referred to as the two-fluid approach and is more widely applicable. The two conservation of momentum equations are solved separately and either the interfacial source term [85] or an expression for the velocity difference between the two phases [86] is defined.

In the other layers of the PEM fuel cell, the gas and liquid phases are in contact with a solid

phase and the flow is characterized as porous media flow. If the electrode backing layer is assumed to be isotropic, the interfacial source term can be expressed as a generalized Darcy term [87, 88]:

$$\Gamma_{F,k} = -\frac{(\epsilon_k)^2 \mu_k}{K k_{rk}} \mathbf{u}_k, \quad (3.16)$$

where K and permeability and k_{rk} is the relative permeability of phase k in the porous media. The permeability is independent of the fluid, but the relative permeability is a function of the liquid water saturation:

$$s = \frac{\epsilon_\ell}{\epsilon_g + \epsilon_\ell}. \quad (3.17)$$

The capillary pressure is also a function of the saturation, and is defined as the difference between the gas and liquid phase pressures:

$$P_{cgl} = P_g - P_\ell. \quad (3.18)$$

In a cylindrical pore, the difference between the gas and liquid pressure is a function of the surface tension, contact angle, and pore radius [89]:

$$P_{cgl} = \frac{2\sigma \cos \theta_c}{r}, \quad (3.19)$$

where σ is the surface tension between the gas and liquid phases, θ_c is the contact angle, and r is the pore radius. If the pore material is hydrophilic, the contact angle is less than 90° and P_{cgl} is positive; hydrophobic materials have a negative P_{cgl} and a water contact angle greater than 90° , as illustrated in Figure 3.3. The wetting fluid is generally taken to be the fluid with a contact angle of less than 90° . Therefore, for a hydrophilic material, the wetting fluid refers to water, while in a hydrophobic material, the wetting fluid would be air.

A porous media can be considered to be composed of a large distribution of pores with different

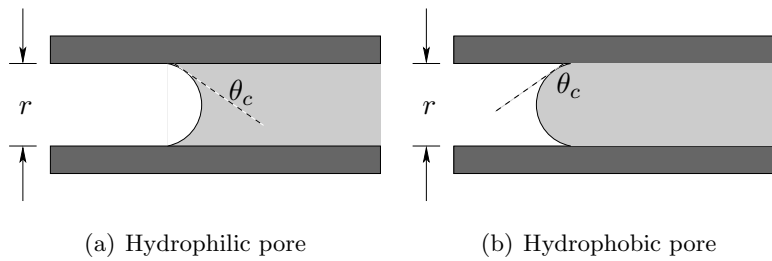
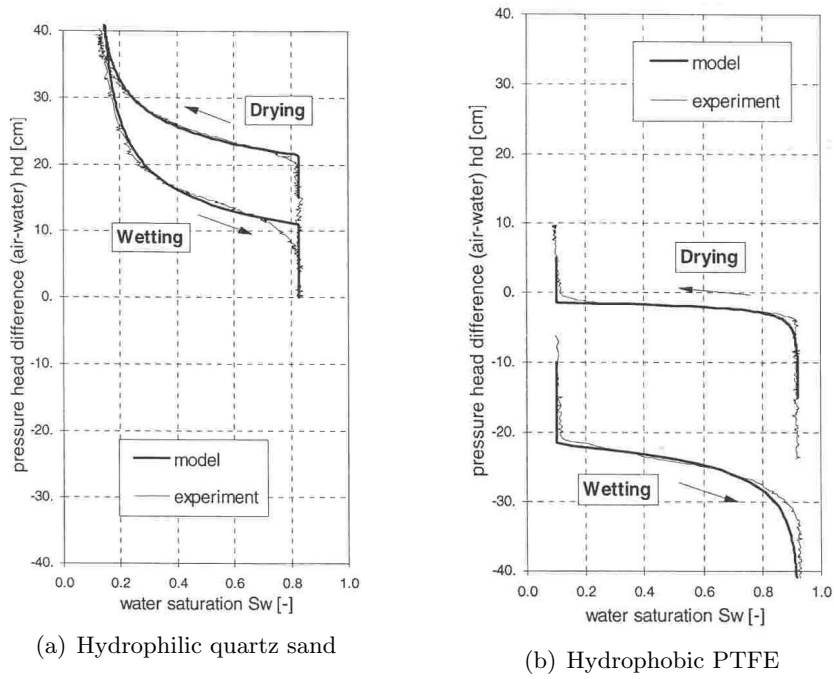


Figure 3.3: Cylindrical pore having (a) hydrophilic and (b) hydrophobic characteristics.

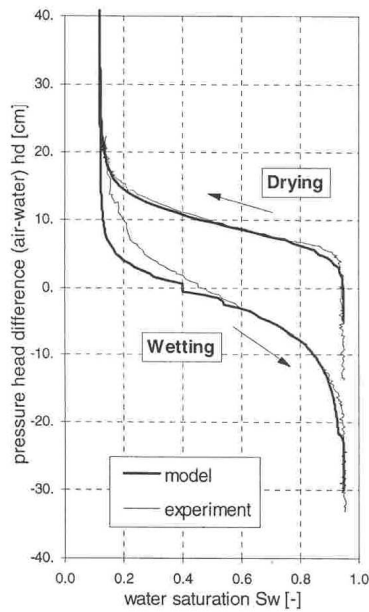
diameters. For a set pressure difference between the wetting and non-wetting fluids, the surface tension effects will result in some pores containing only the wetting fluid, some pores containing only the non-wetting fluid, and some pores containing both fluids, as illustrated in Figure 3.3. Thus, the total volume of the wetting or non-wetting fluid within the porous media and the capillary pressure are related. If the two-phase fluid system consists of water and air, the water content of the porous media is expressed as the saturation, which is defined as the fraction of the void space occupied by liquid. The functional dependence of capillary pressure on liquid water saturation is illustrated in Figure 3.4, for a porous media with hydrophilic, hydrophobic and mixed pore wettability. The figures have been reproduced from Ustohal *et al.* [90], and were produced using a porous media consisting of granular packed quartz sand, for Figure 3.4(a), PTFE, for Figure 3.4(b) and a 1:2 mixture of quartz sand and PTFE for Figure 3.4(c). Except at the extreme values of saturation, the capillary pressure for a hydrophilic material is always positive and always negative for a hydrophobic material. Both positive and negative capillary pressures are possible for a mixed wettability material. All of the capillary pressure curves in Figure 3.4 show hysteresis, with different curves being produced if water is entering or leaving the porous media; thus the capillary pressure depends on both liquid saturation and flow history. The hysteresis is due to the contact angle being different if the water is advancing or receding from the pores [91]. For the mixed material, the designation of a wetting and non-wetting fluid is ambiguous and the water is typically designated as the wetting fluid.

The capillary pressure asymptotically approaches infinity at a finite, minimum value of satu-



(a) Hydrophilic quartz sand

(b) Hydrophobic PTFE



(c) Mixed

Figure 3.4: Capillary pressure dependence on liquid water saturation for (a) hydrophilic quartz sand, (b) hydrophobic PTFE and (c) a 1:2 mixture of hydrophilic quartz sand and hydrophobic PTFE. The curves are from Ustohal *et al.* [90], and the pressure head difference is related to the capillary pressure by $P_{cgl} = (\rho_l)(g)(hd)$.

ration, and approaches negative infinity for a maximum value of water saturation. This can be interpreted as there being a residual saturation of water, $s_{\ell r}$, and a residual saturation of air, s_{gr} , in the porous media. The residual saturation represents the saturation at which the fluid loses the capability to move as a bulk phase in response to a hydraulic gradient, resulting in the transport of the residual fluid being dominated by advective-diffusive transport as a dispersed phase in the fluid with the larger volume fraction [92].

Attempts have been made to correlate capillary pressure curves, with a comprehensive representation being [92]:

$$P_{NW} - P_W = 2Z\sigma \cos(\theta_{cW}) \sqrt{\frac{\epsilon}{K}} \mathcal{L}(s_W^{\text{eff}}), \quad (3.20)$$

where P_{NW} and P_W are the pressures of the non-wetting and wetting fluids, respectively, Z is a correction factor to account for the change in contact angle due to roughness, θ_{cW} is the intrinsic contact angle of the wetting fluid to the solid, and $\mathcal{L}(s_W^{\text{eff}})$ is a function of the effective saturation of the wetting fluid. The effective saturation is defined as:

$$s_W^{\text{eff}} = \frac{s_W - s_{W_r}}{1 - s_{NW_r} - s_{W_r}}, \quad (3.21)$$

where s_{NW_r} and s_{W_r} are the residual saturations of the non-wetting and wetting fluids, respectively. Therefore, if one capillary pressure curve is available, it can be applied to different porous media, using corrections for the porosity, permeability and roughness. However, the function \mathcal{L} is not fully universal, and depends on several other parameters, such as pore structure.

Predictive models for the relative permeability were developed from conceptual models of flow in capillary tubes combined with models of pore-size distribution [93]. The common conceptual models are the Burdine and Mualem functions. In addition to the conceptual models, several porous media modeling studies have successfully used a simple power law relationship for the

relative permeability [83]. The Burdine, Mualem, and power law models are expressed as:

$$k_{rW} = \left(s_W^{\text{eff}}\right)^2 \left[\frac{\int_0^{s_W^{\text{eff}}} \frac{ds_W^{\text{eff}}}{P_c^2}}{\int_0^1 \frac{ds_W^{\text{eff}}}{P_c^2}} \right] \quad k_{rNW} = \left(1 - s_W^{\text{eff}}\right)^2 \left[\frac{\int_{s_W^{\text{eff}}}^1 \frac{ds_W^{\text{eff}}}{P_c^2}}{\int_0^1 \frac{ds_W^{\text{eff}}}{P_c^2}} \right] \quad (3.22)$$

$$k_{rW} = \left(s_W^{\text{eff}}\right)^\eta \left[\frac{\int_0^{s_W^{\text{eff}}} \frac{ds_W^{\text{eff}}}{P_c}}{\int_0^1 \frac{ds_W^{\text{eff}}}{P_c}} \right]^2 \quad k_{rNW} = \left(1 - s_W^{\text{eff}}\right)^\eta \left[\frac{\int_{s_W^{\text{eff}}}^1 \frac{ds_W^{\text{eff}}}{P_c}}{\int_0^1 \frac{ds_W^{\text{eff}}}{P_c}} \right]^2 \quad (3.23)$$

$$k_{rW} = \left(s_W^{\text{eff}}\right)^n \quad k_{rNW} = \left(s_{NW}^{\text{eff}}\right)^n \quad (3.24)$$

where Equation (3.22) is the Burdine function, Equation (3.23) is the Mualem function, and Equation (3.24) is the power law function. The relative permeability of the wetting and non-wetting functions are denoted by k_{rW} and k_{rNW} , respectively.

3.5 Conservation of Mass and Species

No reactions occur within any of the phases in the PEM fuel cell. Thus, for the solid, liquid or gas phases, the conservation of mass and species are [84]

$$\frac{\partial \rho_k}{\partial t} + \nabla \cdot (\rho_k \mathbf{u}_k) = 0, \quad (3.25)$$

$$\frac{\partial}{\partial t} (\rho_k \omega_k^\alpha) + \nabla \cdot (\rho_k \omega_k^\alpha \mathbf{u}_k + \mathcal{J}_k^\alpha) = 0, \quad (3.26)$$

where the mass fraction of species α within phase k is denoted by ω_k^α and \mathcal{J}_k^α represents the mass flux of species α due to molecular diffusion. The conservation of species applies to all phases, while the conservation of mass applies only to the gas and liquid phases. The mass flux due to molecular diffusion is [84]:

$$-c_k^\alpha \nabla \ln a_k^\alpha - \frac{z_\alpha c_k^\alpha \mathcal{F}}{\mathcal{R}T_k} \nabla \Phi_k = \sum_{\beta \neq \alpha} \frac{\hat{M}_k}{\hat{M}_\alpha \hat{M}_\beta \mathcal{D}_{\alpha-\beta,k}} \left(\omega_k^\beta \mathcal{J}_k^\alpha - \omega_k^\alpha \mathcal{J}_k^\beta \right). \quad (3.27)$$

CHAPTER 3. GENERAL FORMULATION

The Generalized Stefan-Maxwell equations are used to describe the diffusive mass flux, with the temperature and pressure effects neglected. The molar concentration is c_k^α and the molecular weights of the phase and species are denoted by \hat{M}_k and \hat{M}_α , respectively. The activity, a_k^α is given by

$$a_k^\alpha = \gamma_k^\alpha x_k^\alpha. \quad (3.28)$$

The activity coefficient is γ_k^α and x_k^α is the mole fraction. The definition of activity given in Equation (3.28) is valid for both charged and uncharged species and for an ideal gas or a dilute solution, the activity coefficient is unity.

After the volume-averaging procedure, the conservation of mass and species become

$$\frac{\partial}{\partial t} (\epsilon_k \langle \rho_k \rangle^*) + \nabla \cdot (\epsilon_k \langle \rho_k \rangle^* \langle \mathbf{u}_k \rangle^*) = \Gamma_{M,k}, \quad (3.29)$$

$$\frac{\partial}{\partial t} (\epsilon_k \langle \rho_k \rangle^* \langle \omega_k^\alpha \rangle^*) + \nabla \cdot (\epsilon_k \langle \rho_k \rangle^* \langle \omega_k^\alpha \rangle^* \langle \mathbf{u}_k \rangle^* + \epsilon_k \langle \mathcal{J}_k^\alpha \rangle^*) = \Gamma_{S,k}^\alpha, \quad (3.30)$$

where $\Gamma_{S,k}^\alpha$ represents gain or loss of species α from adjacent phases:

$$\Gamma_{S,k}^\alpha = - \sum_n \frac{1}{V_r} \int_{A_{kn}} \rho_k \omega_k^\alpha (\mathbf{u}_k - \mathbf{u}_{kn}) \cdot \mathbf{n}_{kn} dA. \quad (3.31)$$

The total mass entering or exiting phase k is denoted by $\Gamma_{M,k}$ and is equal to the sum of the species interfacial source terms:

$$\Gamma_{M,k} = \sum_\alpha \Gamma_{S,k}^\alpha \quad (3.32)$$

Because of the small pore diameters, especially within the polymer electrolyte, molecular interactions between species in the fluid phases and the solid phase can be significant. These interactions can be incorporated within the Generalized Stefan-Maxwell equations by considering the solid phase as a diffusing species with a velocity of zero [74]. Thus, the volume-averaged form of the Generalized

Stefan-Maxwell equations become

$$\begin{aligned}
 - \langle c_k^\alpha \rangle^* \nabla \ln \langle a_k^\alpha \rangle^* - \frac{z_\alpha \langle c_k^\alpha \rangle^* \mathcal{F}}{\mathcal{R} \langle T_k \rangle^*} \nabla \langle \Phi_e \rangle^* = \\
 \sum_{\beta \neq \alpha} \frac{\hat{M}_k}{\hat{M}_\alpha \hat{M}_\beta D_{\alpha-\beta,k}^{\text{eff}}} \left(\langle \omega_k^\beta \rangle^* \langle \mathcal{J}_k^\alpha \rangle^* - \langle \omega_k^\alpha \rangle^* \langle \mathcal{J}_k^\beta \rangle^* \right) + \frac{\langle \mathcal{J}_k^\alpha \rangle^*}{\hat{M}_\alpha D_{\alpha-s,k}^{\text{eff}}}, \quad (3.33)
 \end{aligned}$$

where \mathcal{J}_k^α is the total mass flux of species α and $D_{\alpha-s,k}^{\text{eff}}$ represents the interactions between the solid phase and the species within the fluid phases. Thus, $D_{\alpha-s,k}^{\text{eff}}$ represents transport due to Knudsen diffusion. In regions of the PEM fuel cell where the solid phase does not exist, or does not have an appreciable effect on species mass flux, $D_{\alpha-s,k}^{\text{eff}} \rightarrow \infty$ and Equation (3.33) reduces to the standard Stefan-Maxwell equations: Equation (3.27). For the polymer electrolyte, the pore region is small such that interactions between the fluid and solid polymer are significant [94].

For a PEM fuel cell, the interfacial source terms for the conservation of species stem from either adjacent phases or heterogeneous reactions:

$$\Gamma_{S,k}^\alpha = \sum_{n \neq k} \Gamma_{S,k-n}^\alpha + \Gamma_{S,k-\text{react}}^\alpha, \quad (3.34)$$

where $\Gamma_{S,k-n}^\alpha$ represents the transfer of species α from phase n to phase k and $\Gamma_{S,k-\text{react}}^\alpha$ is the production of species α due to the reactions. The first type of interfacial source term only affects the species water. Water in the gas phase can be condensed into, or evaporated from, the liquid phase. As well, liquid water in the pore region of the polymer electrolyte can leave or enter the gas or liquid phases.

For water being exchanged through the gas/liquid, gas/electrolyte, or liquid/electrolyte boundaries, two methods can be used to determine the value of the interfacial source term. In the first method, local thermodynamic equilibrium can be assumed between the water in the adjacent phases. All of the conservation of species equations for water can be summed together and, with local equilibrium assumed, the water mass fractions in the different phases can be collapsed into a single variable [87]. The other method retains the conservation of species for the co-existing phases

separate and uses a function for the interfacial source terms. For example, the interfacial source term between the gas and liquid phases can be expressed as [49]:

$$\Gamma_{S,g-\ell}^{\text{H}_2\text{O}} = -\Gamma_{S,\ell-g}^{\text{H}_2\text{O}} = A \left(P_{\text{sat}} - \langle x_g^{\text{H}_2\text{O}} \rangle^* \langle P_g \rangle^* \right), \quad (3.35)$$

where P_{sat} is the saturation pressure of water and A is constant.

The mass transfer due to the heterogeneous electro-chemical reactions can be expressed as

$$\Gamma_{S,k-\text{react}}^\alpha = \hat{M}_\alpha A_v \dot{\mathcal{P}}^\alpha, \quad (3.36)$$

where $\dot{\mathcal{P}}^\alpha$ is the molar production or consumption of species α and A_v is the reactive surface area per unit volume. The expression for $\dot{\mathcal{P}}^\alpha$ depends on the reaction kinetics, which are examined in the next section.

3.5.1 Reaction

The reactions in a PEM fuel cell require a catalyst and thus are confined to the catalyst layers. The main reaction in the anode catalyst layer is hydrogen electro-oxidation, while oxygen reduction occurs in the cathode catalyst layer. However, other reactions can occur, such as carbon monoxide adsorption in the anode catalyst layer and heterogeneous oxidation of hydrogen by oxygen due to reactant cross-over through the polymer electrolyte layer. All of these reactions are considered in this general formulation.

The main reactions are electron transfer reactions, and thus are functions of the overpotential, defined as [95]:

$$\eta = \Phi_s - \Phi_e - U', \quad (3.37)$$

where U' is the overpotential at a reference state for the particular reaction. For the electro-

oxidation of hydrogen, U' is taken as zero while for oxygen reduction [62],

$$U' = 1.23 - 0.9 \times 10^{-3} (T - 298), \quad (3.38)$$

where U' is in V and T is in K. The anode and cathode reactions are considered in the next sections, with the anode being examined first.

Anode Kinetics

Hydrogen, carbon monoxide, and oxygen are all present in the anode catalyst layer. Thus, the following reactions are considered:

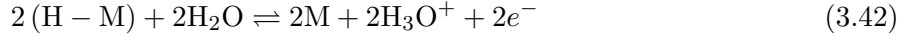
1. Hydrogen adsorption, desorption and electro-oxidation,
2. Carbon monoxide adsorption, desorption and electro-oxidation,
3. Heterogeneous oxidation of carbon monoxide by oxygen,
4. Heterogeneous oxidation of hydrogen by oxygen.

The adsorption and electro-oxidation of hydrogen in an acidic environment has been extensively studied. The mechanism for electro-chemical hydrogen oxidation over platinum is the slow dissociation of adsorbed hydrogen molecules to hydrogen atoms, known as the Tafel reaction, followed by the fast electro-chemical oxidation of the adsorbed hydrogen atoms, known as the Volmer reaction [96]:



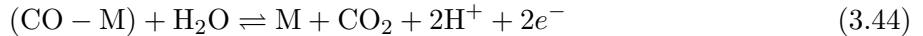
where Reaction (3.39) represents the Tafel reaction, Reaction (3.40) represents the Volmer step and M denotes a reaction site. The electro-oxidation of hydrogen occurs within the potential range of 0 to 0.2 V. Reactions (3.39) and (3.40) represent the standard representation of the Tafel-Volmer

mechanism. However, in the polymer electrolyte membrane, the hydrogen ions exist as hydronium (H_3O^+) ions [78]; thus the hydrogen electro-oxidation reaction can be expressed as:

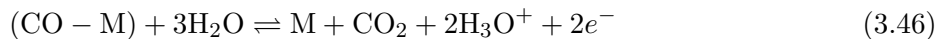


The H^+ ions have been replaced by H_3O^+ ions, and water is now required on the left hand side of the Volmer step. This representation of the electro-oxidation of hydrogen in a PEM fuel cell explicitly shows the need for proper humidification; without water, proton transport would be impossible and the electron transfer step could not proceed.

The electro-chemistry of CO in an acidic environment has also been studied extensively [97]. The adsorption of CO involves linearly bonded CO to platinum while the oxidation of CO occurs from a voltage range of 0.6 to 0.9 V, depending on the voltage sweep rate used in the voltammetry experiment [97]. The rate of oxidation of CO at low coverage is rapid while the rate is poisoned by a high coverage of CO. This dependence on coverage indicates that the electro-chemical oxidation of CO involves adjacent surface sites. Thus, the “reactant pair” mechanism for CO oxidation has been proposed [98]:



This mechanism of CO oxidation is similar to the catalyzed gas phase oxidation of CO by oxygen [97]. As with the hydrogen electro-oxidation reactions, the electro-oxidation of CO can be expressed such that the existence of the H^+ ions as H_3O^+ ions is explicit:

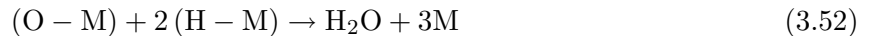
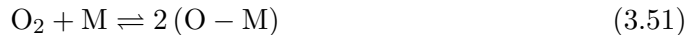


The kinetics of carbon monoxide and hydrogen on platinum indicates the mechanism of CO poisoning of the anode [99]. CO chemisorbs to the platinum sites to the exclusion of hydrogen. This is possible because CO is more strongly bonded to platinum than hydrogen, as indicated by a greater potential required for the electro-oxidation of CO than hydrogen, and a sticking probability of CO on platinum of 15 times higher than that of hydrogen on platinum [99]. Thus, even a relatively small concentration of CO can result in the complete coverage of the platinum surface, to the exclusion of hydrogen. Without access to reaction sites, the electro-chemical oxidation of hydrogen can not proceed.

One method to mitigate the effect of CO poisoning is the introduction of a small amount of oxygen into the anode gas stream. The carbon monoxide and oxygen react; thus freeing reaction sites for the electro-oxidation of hydrogen. The amount of oxygen is usually 2 to 5 percent of the volume flow rate of hydrogen and this process is referred to as O₂ bleeding [13]. It is assumed that the gas phase oxidation of CO and H₂ by oxygen is negligible; thus the oxidation is described by heterogeneous catalysis. The heterogeneous catalysis of CO on platinum proceeds by a Langmuir-Hinshelwood mechanism [100].

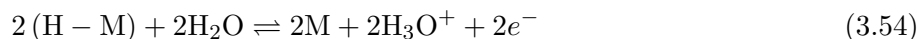


The oxidation of H₂ by O₂ on platinum has many intermediate reactions [101], but it can be approximated by a Langmuir-Hinshelwood mechanism [102].



Note that Reactions (3.49) and (3.52) are assumed to proceed in one direction only.

Therefore, to summarize, the following reactions are assumed to occur within the anode catalyst layer.



The adsorption and desorption kinetics of CO are assumed to follow a Temkin model, which has been verified by the experimental data of Dhar *et al.* [34], while the adsorption and desorption kinetics of hydrogen and oxygen are assumed to follow Langmuir kinetics. Electro-oxidation of carbon monoxide and hydrogen are assumed to follow Volmer/Erdey-Gruz kinetics, with the anodic and cathodic transfer coefficients being equal [95]. As a result, the reaction rates of the anode catalyst reactions, in units of mole/(m² · s), are:

$$\mathcal{R}_{a,ads}^{\text{H}} = k_{ads}^{\text{H}} \left(c_g^{\text{H}_2} (\theta_s^{\text{M}})^2 - b_{ads}^{\text{H}} (\theta_s^{\text{H}})^2 \right) \quad (3.60)$$

$$\mathcal{R}_{a,ox}^{\text{H}} = \frac{J_o^{\text{H}}}{\mathcal{F}} \left\{ \left[\frac{\theta_s^{\text{H}}}{\theta_s^{\text{H}}} \right] \exp\left(\frac{\eta_a}{B_a^{\text{H}}}\right) - \left[\frac{\theta_s^{\text{M}}}{\theta_s^{\text{M}}} \right] \left[\frac{c_{\ell,e}^{\text{H}_3\text{O}^+}}{c_{\ell,e}^{\text{H}_3\text{O}^+}} \right] \exp\left(-\frac{\eta_a}{B_a^{\text{H}}}\right) \right\} \quad (3.61)$$

$$\mathcal{R}_{a,ads}^{\text{CO}} = k_{ads}^{\text{CO}} \left\{ c_g^{\text{CO}} \theta_s^{\text{M}} \exp\left(-\frac{\beta r \theta_s^{\text{CO}}}{\mathcal{R}T}\right) - b_{ads}^{\text{CO}} \theta_s^{\text{CO}} \exp\left(\frac{[1-\beta] r \theta_s^{\text{CO}}}{\mathcal{R}T}\right) \right\} \quad (3.62)$$

$$\begin{aligned} \mathcal{R}_{a,ox}^{\text{CO}} = \frac{J_o^{\text{CO}}}{2\mathcal{F}} \left\{ \left[\frac{\theta_s^{\text{CO}}}{\theta_s^{\text{CO}}} \right] \left[\frac{c_{\ell,e}^{\text{H}_2\text{O}}}{c_{\ell,e}^{\text{H}_2\text{O}}} \right]^2 \exp\left(\frac{\eta_a}{B_a^{\text{CO}}}\right) \right. \\ \left. - \left[\frac{\theta_s^{\text{M}}}{\theta_s^{\text{M}}} \right] \left[\frac{c_g^{\text{CO}_2}}{c_g^{\text{CO}_2}} \right] \left[\frac{c_{\ell,e}^{\text{H}_3\text{O}^+}}{c_{\ell,e}^{\text{H}_3\text{O}^+}} \right]^3 \exp\left(-\frac{\eta_a}{B_a^{\text{CO}}}\right) \right\} \end{aligned} \quad (3.63)$$

$$\mathcal{R}_{a,ads}^O = k_{ads}^O \left\{ c_{\ell,e}^{O_2} (\theta_s^M)^2 - b_{ads}^O (\theta_s^O)^2 \right\} \quad (3.64)$$

$$\mathcal{R}_{a,ox}^{H-O} = k_{ox}^{H-O} \left\{ \theta_s^O (\theta_s^H)^2 - b_{ox}^{H-O} c_{\ell,e}^{H_2O} (\theta_s^M)^3 \right\} \quad (3.65)$$

$$\mathcal{R}_{a,ox}^{CO-O} = k_{ox}^{CO-O} \left\{ \theta_s^O \theta_s^{CO} - b_{ox}^{CO-O} c_{\ell,e}^{CO_2} (\theta_s^M)^2 \right\} \quad (3.66)$$

where k_i^α denotes the forward rate reaction constant, b_i^α denotes the ratio of backward to forward reaction rate constant, and J_o^α is the exchange current density. The fraction of the platinum reaction sites in the solid phase covered by species α is denoted by θ_s^α , with $\theta_s^M = 1 - \theta_s^H - \theta_s^{CO} - \theta_s^O$ representing the fraction of free reaction sites. An overbar over the concentration ($\bar{c}_{\ell,e}^\alpha$) or the coverage ($\bar{\theta}_s^\alpha$) represents the value at equilibrium, or when the PEM fuel cell is producing no current.

In the carbon monoxide adsorption/desorption reaction rate, Equation (3.62), β is a symmetry factor that has a value between zero and one, and r is an interaction parameter that represents the effect of lateral-interaction on the adsorption/desorption process [103]. In general, the Tafel slope, B , is [95]:

$$B_{\text{forward}} = \frac{\mathcal{R}T}{\beta n \mathcal{F}}, \quad (3.67)$$

$$B_{\text{backward}} = \frac{\mathcal{R}T}{(1 - \beta) n \mathcal{F}}, \quad (3.68)$$

where B_{forward} and B_{backward} are the Tafel slopes for the forward and backward reaction directions, respectively. The number of electrons transferred in the reaction is denoted by n and β is a symmetry factor that is between 0 and 1. In Equations (3.61) and (3.63), B_a^α is the Tafel slope for species α ; the Tafel slopes for the forward and backward directions are considered equivalent and are equal to:

$$B_a^H = B_a^{CO} = \frac{2\mathcal{R}T}{\mathcal{F}}. \quad (3.69)$$

CHAPTER 3. GENERAL FORMULATION

The production of reaction intermediates (θ_s^H , θ_s^{CO} , and θ_s^O) are assumed to be in steady state, and therefore equal to zero. This results in the relationships:

$$\dot{\mathcal{P}}_a^{\theta_s^H} = 2\mathcal{R}_{a,ads}^H - \mathcal{R}_{a,ox}^H - 2\mathcal{R}_{a,ox}^{H-O} = 0 \quad (3.70)$$

$$\dot{\mathcal{P}}_a^{\theta_s^{CO}} = \mathcal{R}_{a,ads}^{CO} - \mathcal{R}_{a,ox}^{CO} - \mathcal{R}_{a,ox}^{CO-O} = 0 \quad (3.71)$$

$$\dot{\mathcal{P}}_a^{\theta_s^O} = 2\mathcal{R}_{a,ads}^O - \mathcal{R}_{a,ox}^{H-O} - \mathcal{R}_{a,ox}^{CO-O} = 0 \quad (3.72)$$

Using Equations (3.70) to (3.72), the production of the reactants and products can be expressed in terms of $\mathcal{R}_{a,ox}^H$, $\mathcal{R}_{a,ox}^{CO}$, $\mathcal{R}_{a,ox}^{H-O}$ and $\mathcal{R}_{a,ox}^{CO-O}$:

$$\dot{\mathcal{P}}_a^{H_2} = -\frac{1}{2}\mathcal{R}_{a,ox}^H - \mathcal{R}_{a,ox}^{H-O} \quad (3.73)$$

$$\dot{\mathcal{P}}_a^{CO} = -\mathcal{R}_{a,ox}^{CO} - \mathcal{R}_{a,ox}^{CO-O} \quad (3.74)$$

$$\dot{\mathcal{P}}_a^{O_2} = -\frac{1}{2}\mathcal{R}_{a,ox}^{H-O} - \frac{1}{2}\mathcal{R}_{a,ox}^{CO-O} \quad (3.75)$$

$$\dot{\mathcal{P}}_a^{e^-} = \mathcal{R}_{a,ox}^H + 2\mathcal{R}_{a,ox}^{CO} \quad (3.76)$$

$$\dot{\mathcal{P}}_a^{H_3O^+} = \mathcal{R}_{a,ox}^H + 2\mathcal{R}_{a,ox}^{CO} \quad (3.77)$$

$$\dot{\mathcal{P}}_a^{H_2O} = -\mathcal{R}_{a,ox}^H - 3\mathcal{R}_{a,ox}^{CO} + \mathcal{R}_{a,ox}^{H-O} \quad (3.78)$$

$$\dot{\mathcal{P}}_a^{CO_2} = \mathcal{R}_{a,ox}^{CO} + \mathcal{R}_{a,ox}^{CO-O} \quad (3.79)$$

Cathode Kinetics

The major reaction occurring in the cathode catalyst layer is oxygen reduction:



As in the anode catalyst layer, the hydrogen ions exist as hydronium ions; thus Equation (3.80) can be rewritten as:



The reaction rate of the oxygen reduction reaction in a polymer electrolyte/platinum system has been studied [104] and the production of electrons is governed by Volmer/Erdey-Gruz kinetics:

$$\mathcal{R}_{c,red}^{\text{O}_2} = \frac{J_o^{\text{O}_2}}{4\mathcal{F}} \left\{ \left[\frac{c_{\ell,e}^{\text{H}_2\text{O}}}{c_{\ell,e}^{\text{H}_2\text{O}}} \right]^6 \exp\left(\frac{\eta_c}{B_c^{\text{O}_2}}\right) - \left[\frac{c_g^{\text{O}_2}}{c_g^{\text{O}_2}} \right] \left[\frac{c_{\ell,e}^{\text{H}_3\text{O}^+}}{c_{\ell,e}^{\text{H}_3\text{O}^+}} \right]^4 \exp\left(-\frac{\eta_c}{B_c^{\text{O}_2}}\right) \right\} \quad (3.82)$$

where $J_o^{\text{O}_2}$ is the exchange current density for oxygen reduction and c_k^α is the concentration of species α . The Tafel slope is denoted by $B_c^{\text{O}_2}$ and is given by:

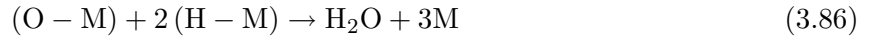
$$B_c^{\text{O}_2} = \frac{\mathcal{R}T}{\mathcal{F}}. \quad (3.83)$$

The definition of Tafel slope in Equation (3.83) does not match the general expression for Tafel slope in Equation (3.67). However, Equation (3.83) results in a Tafel slope of 68 mV/decade at a temperature of 70°C, which agrees with the experimental value of 70 mV/decade from Parthasarathy *et al.* [104]. The discrepancy between the actual and theoretical Tafel slope is because the oxygen reduction reaction is not a single step reaction; the general expression for Tafel slope is valid only for a single step reaction.

Gases can dissolve into the polymer electrolyte and be transported between the anode and cathode; however, compared to the gas phase, the transport of gases in the polymer electrolyte is slow [24]. On the anode side of the fuel cell, the concentration of carbon monoxide is approximately 100 ppm. If the solubility and diffusivity of carbon monoxide in Nafion is assumed to be similar to that of oxygen or hydrogen, then it is unlikely that a significant amount could be transported across the polymer electrolyte membrane layer and react in the cathode catalyst layer. However,

CHAPTER 3. GENERAL FORMULATION

cross-over of hydrogen could be possible and as a result, the heterogeneous oxidation of hydrogen by oxygen is included in the cathode catalyst layer. The chemical reaction and reaction rate are represented in the same manner as in the anode catalyst layer:



$$\mathcal{R}_{c,ads}^{\text{H}} = k_{ads}^{\text{H}} \left\{ c_e^{\text{H}_2} (\theta_s^{\text{M}})^2 - b_{ads}^{\text{H}} (\theta_s^{\text{H}})^2 \right\} \quad (3.87)$$

$$\mathcal{R}_{c,ads}^{\text{O}} = k_{ads}^{\text{O}} \left\{ c_e^{\text{O}_2} (\theta_s^{\text{M}})^2 - b_{ads}^{\text{O}} (\theta_s^{\text{O}})^2 \right\} \quad (3.88)$$

$$\mathcal{R}_{c,ox}^{\text{H-O}} = k_{ox}^{\text{H-O}} \left\{ \theta_s^{\text{O}} (\theta_s^{\text{H}})^2 - b_{ox}^{\text{H-O}} c_e^{\text{H}_2\text{O}} (\theta_s^{\text{M}})^3 \right\} \quad (3.89)$$

As in the anode catalyst layer, the net production of θ_s^{H} and θ_s^{O} are taken to be zero and hence,

$$\dot{\mathcal{P}}_c^{\theta_s^{\text{H}}} = 2\mathcal{R}_{c,ads}^{\text{H}} - 2\mathcal{R}_{c,ox}^{\text{H-O}}, \quad (3.90)$$

$$\dot{\mathcal{P}}_c^{\theta_s^{\text{O}}} = 2\mathcal{R}_{c,ads}^{\text{O}} - \mathcal{R}_{c,ox}^{\text{H-O}}. \quad (3.91)$$

The net production of each species in the cathode catalyst layer can be calculated:

$$\dot{\mathcal{P}}_c^{\text{O}_2} = \mathcal{R}_{c,red}^{\text{O}_2} - \frac{1}{2}\mathcal{R}_{c,ox}^{\text{H-O}}, \quad (3.92)$$

$$\dot{\mathcal{P}}_c^{\text{H}_2} = -\mathcal{R}_{c,ox}^{\text{H-O}}, \quad (3.93)$$

$$\dot{\mathcal{P}}_c^{\text{H}_2\text{O}} = -6\mathcal{R}_{c,red}^{\text{O}_2} + \mathcal{R}_{c,ox}^{\text{H-O}}, \quad (3.94)$$

$$\dot{\mathcal{P}}_c^{\text{H}_3\text{O}^+} = 4\mathcal{R}_{c,red}^{\text{O}_2}, \quad (3.95)$$

$$\dot{\mathcal{P}}_c^{e^-} = 4\mathcal{R}_{c,red}^{\text{O}_2}. \quad (3.96)$$

3.6 Conservation of Energy

The conservation of energy can be written for all phases as [84]

$$\frac{\partial}{\partial t} \left(\sum_{\alpha} \rho_k \omega_k^{\alpha} H_k^{\alpha} \right) + \nabla \cdot \left(\sum_{\alpha} \mathbf{F}_k^{\alpha} H_k^{\alpha} \right) = -\nabla \cdot \mathbf{q}_k. \quad (3.97)$$

Energy transfer due to pressure work and viscous dissipation are both neglected in the conservation of energy, which is expressed as Equation (3.97). The enthalpy of phase k is denoted by H_k , and \mathbf{q}_k represents the transport of energy due to conduction. The total mass flux of species α is

$$\mathbf{F}_k^{\alpha} = \rho_k \omega_k^{\alpha} \mathbf{u}_k + \mathcal{J}_k^{\alpha} \quad (3.98)$$

The conductive heat transfer is a function of temperature:

$$\mathbf{q}_k = -\lambda_k \nabla T_k, \quad (3.99)$$

where λ_k is the thermal conductivity of phase k .

Thus, the independent variables in Equation (3.97) include the temperature and the enthalpy of each phase. For the neutral phases, the enthalpy can be expressed as a function of temperature [84]:

$$dH_k^{\alpha} = C_{p,k}^{\alpha} dT_k \quad (3.100)$$

where $C_{p,k}^{\alpha}$ is the constant pressure specific heat for species α .

For the charged species, the enthalpy is potential dependent. Using the Gibbs equation, the enthalpy of a charged species can be expressed in terms of the electro-chemical energy ($\hat{\mu}_k^{\alpha\pm}$) and the partial molar entropy ($\hat{S}_k^{\alpha\pm}$) [105]:

$$\hat{H}_k^{\alpha\pm} = \hat{\mu}_k^{\alpha\pm} + T_k \hat{S}_k^{\alpha\pm}. \quad (3.101)$$

The electro-chemical energy can be expressed as

$$\nabla \hat{\mu}_k^{\alpha\pm} = \mathcal{R}T_k \nabla \ln a_k^{\alpha\pm} + z_{\alpha\pm} \mathcal{F} \nabla \Phi_k, \quad (3.102)$$

where $z_{\alpha\pm}$ is the charge and $a_k^{\alpha\pm}$ is the activity [106]. Thus, for a charged species, the convective term of Equation (3.97) becomes:

$$\begin{aligned} \nabla \cdot (\mathbf{F}_k^{\alpha\pm} H_k^{\alpha\pm}) &= \nabla \cdot (\mathbf{N}_k^{\alpha\pm} \hat{H}_k^{\alpha\pm}) = \mathbf{N}_k^{\alpha\pm} \cdot \nabla \hat{H}_k^{\alpha\pm} \\ &= \mathbf{N}_k^{\alpha\pm} \cdot \left[\mathcal{R}T_k \nabla \ln a_k^{\alpha\pm} + z_{\alpha\pm} \mathcal{F} \nabla \Phi_k + \nabla (T_k \hat{S}_k^{\alpha\pm}) \right], \end{aligned} \quad (3.103)$$

where $z_{\alpha\pm}$ is the charge of species α and $\mathbf{N}_k^{\alpha\pm}$ is the molar flux of charged species α . For electro-chemical systems, only the potential gradient term is significant [105]. Thus, this term can be manipulated to represent Joule heating.

After the volume-averaging procedure, the conservation equations become

$$\frac{\partial}{\partial t} \left(\sum_{\alpha} \epsilon_k \langle \rho_k \rangle^* \langle \omega_k^{\alpha} \rangle^* \langle H_k^{\alpha} \rangle^* \right) + \nabla \cdot \left(\sum_{\alpha} \epsilon_k \langle \mathbf{F}_k^{\alpha} \rangle^* \langle H_k^{\alpha} \rangle^* \right) = -\nabla \cdot (\epsilon_k \langle \mathbf{q}_k \rangle^*) + \Gamma_{E,k}, \quad (3.104)$$

where $\Gamma_{E,k}$ represents the energy entering phase k from adjacent phases:

$$\Gamma_{E,k} = - \sum_n \frac{1}{V_r} \int_{A_{kn}} \sum_{\alpha} H_k^{\alpha} (\mathbf{F}_k^{\alpha} - \rho_k \mathbf{u}_{kn}) \cdot \mathbf{n}_{kn} dA - \sum_n \frac{1}{V_r} \int_{A_{kn}} \mathbf{q}_k \cdot \mathbf{n}_{kn} dA, \quad (3.105)$$

The volume-averaged form of the heat flux ($\langle q \rangle_k^*$) is

$$\langle q \rangle_k^* = -\lambda_k^{\text{eff}} \nabla \langle T_k \rangle^* \quad (3.106)$$

where the effective thermal conductivity is denoted λ_s^{eff} .

Two solution methods are possible for the volume-averaged conservation equations. For the first method, the energy equations for each phase are solved separately and are coupled through

the interfacial source terms. However, this method has the disadvantage of requiring closed forms for the interfacial source terms. The other method involves assuming that all co-existing phases are at the same temperature. As a result, the energy equations for each phase can be added together and the interfacial source terms are not required. The assumption that all phases are at the same temperature is reasonable because the porous media has a large surface area per unit volume. Thus, the effective heat transfer coefficient between the phases is very high and the interfacial resistance to heat transfer is low. For example, in the catalyst layers, the reactive surface area per unit volume is of the order of 10^5 m^{-1} .

If all of the phases have the same local temperature, the conservation of energy for the fuel cell simplifies to

$$\begin{aligned} \frac{\partial}{\partial t} \left(\sum_k \sum_{\alpha \neq \alpha^\pm} \epsilon_k \langle \rho_k \rangle^* \langle \omega_k^\alpha \rangle^* C_{p,k}^\alpha \langle T \rangle^* \right) + \nabla \cdot \left(\sum_k \sum_{\alpha \neq \alpha^\pm} \epsilon_k \langle \mathbf{F}_k^\alpha \rangle^* C_{p,k}^\alpha \langle T \rangle^* \right) = -\nabla \cdot (\langle \mathbf{q} \rangle^*) \\ + E_J^{\alpha^\pm} + E_W + E_m + E_{\text{react}}, \end{aligned} \quad (3.107)$$

where $E_J^{\alpha^\pm}$ is the energy production due to Joule heating, E_W is the energy from water condensation and evaporation, E_m contains terms resulting from the variable change to temperature from enthalpy, and E_{react} is the energy from the electro-chemical reactions. Only the neutral species are included in the summations of Equation (3.107), with the contribution of the charged species being included in the $E_J^{\alpha^\pm}$ term. The heat transfer due to conduction is defined as

$$\langle \mathbf{q} \rangle^* = -\lambda^{\text{eff}} \nabla T \quad (3.108)$$

where λ^{eff} is the effective thermal conductivity for the solid, gas and liquid phases.

The energy production due to Joule heating is

$$E_J^{\alpha^\pm} = \sum_k \sum_{\alpha = \alpha^\pm} -N_k^{\alpha^\pm} \cdot [+z_{\alpha^\pm} \mathcal{F} \nabla \Phi_k], \quad (3.109)$$

where the non-potential terms are neglected. The transient term for the charged species is also neglected because the timescale of the electrical storage effects is much shorter than thermal timescales of the solid, liquid and gas phases. Thus, the electrical transport can be always assumed to operate in steady state. The energy due to water condensation and evaporation is

$$E_W = - \sum_k \sum_{n \neq k} H_k^{\text{H}_2\text{O}} \Gamma_{S,k-n}^{\text{H}_2\text{O}}, \quad (3.110)$$

where k and n are phases that contain water. Converting from enthalpy to temperature creates the E_m term:

$$E_m = T \sum_k \sum_{\alpha \neq \alpha^\pm} C_{p,k}^\alpha \Gamma_{S,k}^\alpha, \quad (3.111)$$

where E_m is zero if all of the specific heats are equal or if no species production or consumption occurs.

The energy from the reactions is

$$\begin{aligned} E_{\text{react}} &= - \sum_k \sum_\alpha H_k^\alpha \Gamma_{S,k-\text{react}}^\alpha \\ &= A_v q_{\text{react}}, \end{aligned} \quad (3.112)$$

where q_{react} is the heat of reaction:

$$q_{\text{react}} = - \sum_k \sum_\alpha \hat{H}_k^\alpha \dot{\mathcal{P}}^\alpha. \quad (3.113)$$

The conversion of the chemical energy of hydrogen and oxygen into electrical work is exothermic; therefore, heat is generated in the catalyst layers of a PEM fuel cell. For the heterogeneous reactions, the determination of the heat production is straightforward and depends on the reaction rate and the enthalpy change of the reaction. However, the heat produced by the electro-chemical reactions must

be treated differently due to the electron-transfer step. The heat produced by the electro-chemical reactions can be separated into two parts: the reversible and irreversible heat generation. The irreversible heat generation is a function of the reaction rate and the catalyst layer overpotential, while the reversible heat generation term is a function of the reaction rate and the entropy change for the reaction. The entropy change for an electron transfer reaction is not rigorously defined [105]; hence assumptions must be made in order to calculate the reversible heat generation in the catalyst layers. The following sections express q_{react} as a function of the enthalpy of reaction, overpotential, and reversible heat generation in the anode and cathode catalyst layers. As well, the determination of the reversible heat generation is discussed.

3.6.1 Anode Heat of Reaction

Using the information from the reaction kinetics section, the anode heat of reaction is:

$$\begin{aligned} q_{\text{react}}^a &= - \sum_k \sum_{\alpha} \hat{H}_k^{\alpha} \dot{\mathcal{P}}^{\alpha} \\ &= -\mathcal{R}_{a,ox}^H \Delta \hat{H}_{R,ox}^H - \mathcal{R}_{a,ox}^{\text{CO}} \Delta \hat{H}_{R,ox}^{\text{CO}} - \mathcal{R}_{a,ox}^{\text{H-O}} \Delta \hat{H}_{R,ox}^{\text{H}_2\text{-O}} - \mathcal{R}_{a,ox}^{\text{CO-O}} \Delta \hat{H}_{R,ox}^{\text{CO-O}}. \end{aligned} \quad (3.114)$$

The enthalpy of reactions for the hydrogen and carbon monoxide electro-oxidation reactions are denoted by $\Delta \hat{H}_{R,ox}^H$ and $\Delta \hat{H}_{R,ox}^{\text{CO}}$, respectively. The heterogeneous oxidation of hydrogen and carbon monoxide have enthalpy of reactions represented by $\Delta \hat{H}_{R,ox}^{\text{H-O}}$ and $\Delta \hat{H}_{R,ox}^{\text{CO-O}}$, respectively. The enthalpy of reactions are related to the enthalpy of formations of each species through:

$$\Delta \hat{H}_{R,ox}^H = \hat{H}_e^{\text{H}_3\text{O}^+} + \hat{H}_s^{e^-} - \frac{1}{2} \hat{H}_e^{\text{H}_2} - \hat{H}_e^{\text{H}_2\text{O}} \quad (3.115)$$

$$\Delta \hat{H}_{R,ox}^{\text{CO}} = \hat{H}_e^{\text{CO}_2} + 2\hat{H}_e^{\text{H}_3\text{O}^+} + 2\hat{H}_s^{e^-} - \hat{H}_e^{\text{CO}} - 3\hat{H}_e^{\text{H}_2\text{O}} \quad (3.116)$$

$$\Delta \hat{H}_{R,ox}^{\text{H-O}} = \hat{H}_e^{\text{H}_2\text{O}} - \hat{H}_e^{\text{H}_2} - \frac{1}{2} \hat{H}_e^{\text{O}_2} \quad (3.117)$$

$$\Delta \hat{H}_{R,ox}^{\text{CO-O}} = \hat{H}_e^{\text{CO}_2} - \hat{H}_e^{\text{CO}} - \frac{1}{2} \hat{H}_e^{\text{O}_2} \quad (3.118)$$

The enthalpy of reaction for the heterogeneous reactions can be obtained by finding the enthalpy of formations for each of the participating species. However, the enthalpy of formation for the species in the electro-oxidation reactions can not be easily calculated due to the presence of charged species. The enthalpies of the participating species must be expressed in terms of the electro-chemical energy and entropy using the Gibbs function [106]:

$$\hat{\mu} = \hat{H} - T\hat{S} \quad (3.119)$$

Therefore, the enthalpy of reaction for hydrogen electro-oxidation can be expressed as:

$$\Delta\hat{H}_{R,ox}^H = \Delta\hat{\mu}_{R,ox}^H + T\Delta\hat{S}_{R,ox}^H \quad (3.120)$$

where $\Delta\hat{\mu}_{R,ox}^H$ and $\hat{S}_{R,ox}^H$ are:

$$\Delta\hat{\mu}_{R,ox}^{H,ox} = \hat{\mu}_{\ell,e}^{H_3O^+} + \hat{\mu}_s^{e^-} - \frac{1}{2}\hat{\mu}_g^{H_2} - \hat{\mu}_{\ell,e}^{H_2O} \quad (3.121)$$

$$\Delta\hat{S}_{R,ox}^H = \hat{S}_{\ell,e}^{H_3O^+} + \hat{S}_s^{e^-} - \frac{1}{2}\hat{S}_{\ell,e}^{H_2} - \hat{S}_{\ell,e}^{H_2O} \quad (3.122)$$

Similarly, the enthalpy of reaction for the carbon monoxide electro-oxidation reaction can be expressed as:

$$\Delta\hat{H}_{R,ox}^{CO} = \Delta\hat{\mu}_{R,ox}^{CO} + T\Delta\hat{S}_{R,ox}^{CO} \quad (3.123)$$

$$\Delta\hat{\mu}_{R,ox}^{CO} = \hat{\mu}_g^{CO_2} + 2\hat{\mu}_{\ell,e}^{H_3O^+} + 2\hat{\mu}_s^{e^-} - \hat{\mu}_g^{CO} - 3\hat{\mu}_{\ell,e}^{H_2O} \quad (3.124)$$

$$\Delta\hat{S}_{R,ox}^{CO} = \hat{S}_g^{CO_2} + 2\hat{S}_{\ell,e}^{H_3O^+} + 2\hat{S}_s^{e^-} - \hat{S}_g^{CO} - 3\hat{S}_{\ell,e}^{H_2O} \quad (3.125)$$

The change in electro-chemical energy for the reaction contributes to the irreversible heat generation, while the entropy change for the reactions is responsible for the reversible heat generation.

CHAPTER 3. GENERAL FORMULATION

For an electron transfer reaction of the form:

$$\sum_i \nu_i \alpha_i^{z_i} \rightarrow n e^-$$

The surface overpotential is defined as [105]:

$$-\mathcal{F}\eta = \hat{\mu}^{e^-} - \sum_i \frac{\nu_i \hat{\mu}^i}{n} \quad (3.126)$$

As a result, the change in electro-chemical energy for hydrogen and carbon monoxide electro-oxidation becomes:

$$\Delta \hat{\mu}_R^{\text{H},ox} = -\mathcal{F}\eta_a \quad \Delta \hat{\mu}_R^{\text{CO},ox} = -2\mathcal{F}\eta_a$$

Therefore, the heat of reaction can be expressed in terms of overpotential, enthalpy of reaction for the heterogeneous reactions, and the reversible heat generation:

$$q_{\text{react}} = \mathcal{F}\eta_a [\mathcal{R}_{a,ox}^{\text{H}} + 2\mathcal{R}_{a,ox}^{\text{CO}}] + q_{a,rev}^{\text{H}} + q_{a,rev}^{\text{CO}} - \mathcal{R}_{a,ox}^{\text{H-O}} \Delta \hat{H}_{R,ox}^{\text{H-O}} - \mathcal{R}_{a,ox}^{\text{CO-O}} \Delta \hat{H}_{R,ox}^{\text{CO-O}} \quad (3.127)$$

where $q_{a,rev}$ is the reversible heat generation of the electro-oxidation reactions and is given by:

$$q_{a,rev}^{\text{H}} = -T \mathcal{R}_{a,ox}^{\text{H}} \Delta \hat{S}_{R,ox}^{\text{H}} \quad (3.128)$$

$$q_{a,rev}^{\text{CO}} = -T \mathcal{R}_{a,ox}^{\text{CO}} \Delta \hat{S}_{R,ox}^{\text{CO}} \quad (3.129)$$

The determination of the reversible heat generation is examined in Section 3.6.3.

3.6.2 Cathode Heat of Reaction

The heat of reaction in the cathode catalyst layer can be determined in the same manner as in the anode catalyst layer. Thus, the heat of reaction in the cathode catalyst layer is:

$$q_{\text{react}}^c = 4\mathcal{F}\eta_c\mathcal{R}_{c,\text{red}}^{\text{O}_2} + q_{c,\text{rev}}^{\text{O}_2} - \mathcal{R}_{c,\text{ox}}^{\text{H-O}} \Delta\hat{H}_R^{\text{H-O}} \quad (3.130)$$

The enthalpy of reaction for the heterogeneous oxidation of hydrogen is given by Equation (3.117), while the reversible heat generation in the cathode catalyst layer ($q_{c,\text{rev}}$) is expressed as:

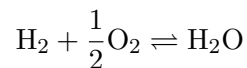
$$q_{c,\text{rev}}^{\text{O}_2} = \mathcal{R}_{c,\text{red}}^{\text{O}_2} \Delta\hat{S}_{R,\text{red}}^{\text{O}_2} \quad (3.131)$$

$$\Delta\hat{S}_{R,\text{red}}^{\text{O}_2} = 6\hat{S}_{\ell,e}^{\text{H}_2\text{O}} - \hat{S}_g^{\text{O}_2} - 4\hat{S}_{\ell,e}^{\text{H}_3\text{O}^+} - 4\hat{S}_g^{e^-} \quad (3.132)$$

3.6.3 Reversible Heat Generation

Determining the reversible heat generation in the anode and cathode catalyst layers requires the entropy of formations for each species participating in the electro-chemical reactions. As with the enthalpy, the entropy for the species in the electrolyte phase are taken to be the values in the gas phase, for species O₂, H₂, CO₂, and CO. The entropy of water is the same in the electrolyte and liquid phases. However, the entropy of formations for ions, such as H₃O⁺ and e⁻, are not well defined [105]; the dependence of $\hat{S}_e^{\text{H}_3\text{O}^+}$ and $\hat{S}_e^{e^-}$ on temperature, or even potential, is not known.

The reactions occurring within the anode and cathode catalyst layers can be added together to form the overall PEM fuel cell reactions. If carbon monoxide is not present in the fuel, then the overall reaction for the cell is:

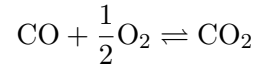


Since the overall reaction does not involve any charged species, the reversible heat generation can

be determined with:

$$q_{rev}^{\text{H}_2;\text{O}_2} = -T\mathcal{R}_{a,ox}^{\text{H}} \left(\hat{S}_e^{\text{H}_2\text{O}} - \hat{S}_e^{\text{H}_2} - \frac{1}{2}\hat{S}_e^{\text{O}_2} \right) \quad (3.133)$$

When carbon monoxide is present in the fuel, there is an additional overall reaction:



and the reversible heat generation can be calculated with:

$$q_{rev}^{\text{CO};\text{O}_2} = -T\mathcal{R}_{a,ox}^{\text{H}} \left(\hat{S}_e^{\text{CO}_2} - \hat{S}_e^{\text{CO}} - \frac{1}{2}\hat{S}_e^{\text{O}_2} \right) \quad (3.134)$$

Therefore, the reversible heat generation in each catalyst layer will be a fraction of the reversible heat generation of the overall reactions:

$$\begin{aligned} q_{a,rev}^{\text{H}} &= \zeta_{\text{H}} q_{rev}^{\text{H}_2;\text{O}_2} \\ q_{a,rev}^{\text{CO}} &= \zeta_{\text{CO}} q_{rev}^{\text{CO};\text{O}_2} \\ q_{c,rev}^{\text{O}_2,ox} &= (1 - \zeta_{\text{H}}) q_{rev}^{\text{H}_2;\text{O}_2} + (1 - \zeta_{\text{CO}}) q_{rev}^{\text{CO};\text{O}_2} \end{aligned}$$

The value of ζ , ($0 \leq \zeta \leq 1$), will depend on the values assumed for $\hat{S}_e^{\text{H}_3\text{O}^+}$ and $\hat{S}_s^{e^-}$. One reasonable assumption is to assume that $\hat{S}_s^{e^-} = 0$. Also, the standard entropy for the hydronium ion is assumed to be given by:

$$\hat{S}_e^{\text{H}_3\text{O}^+} = \hat{S}_e^{\text{H}^+} + \hat{S}_e^{\text{H}_2\text{O}}$$

Since the entropy of an hydrogen ion in an aqueous solution at 25°C is zero [107], the entropy of

the hydronium ion is taken as:

$$\hat{S}_e^{\text{H}_3\text{O}^+} = \hat{S}_e^{\text{H}_2\text{O}}. \quad (3.135)$$

With these assumptions, the reversible heat generation component of the heat of reaction for the anode and cathode catalyst layers can be determined.

3.6.4 Irreversible Heat Generation

Section 3.6.3 described the reversible heat generation of the electro-chemical reactions. The irreversible heat generation would be the terms in Equations (3.127) and (3.130) that are functions of the overpotential:

$$q_{a,irr} = \mathcal{F}\eta_a [\mathcal{R}_{a,ox}^{\text{H}} + 2\mathcal{R}_{a,ox}^{\text{CO}}], \quad (3.136)$$

$$q_{c,irr} = 4\mathcal{F}\eta_c \mathcal{R}_{c,red}^{\text{O}_2}, \quad (3.137)$$

where $q_{a,irr}$ and $q_{c,irr}$ are the irreversible components of the anode and cathode electro-chemical reactions, respectively.

3.7 Summary

The PEM fuel cell is considered to be composed of several, co-existing phases. These phases include a solid phase, which is present as the solid matrix of the polymer electrolyte and the carbon of the bipolar plates, electrode backing layer and catalyst layers. In addition, a multi-component gas phase is present in all regions of the fuel cell except the solid portion of the bipolar plates. Finally, two liquid phases are present. One liquid phase is composed of pure water and can exist in the gas flow channels, electrode backing and catalyst layers. The other liquid phase consists of water and hydronium and it is confined to the pore regions of the polymer electrolyte in the catalyst and polymer electrolyte layers. The governing equations for these phases are the conservation of mass,

momentum, species and energy:

$$\frac{\partial}{\partial t} (\epsilon_k \langle \rho_k \rangle^*) + \nabla \cdot (\epsilon_k \langle \rho_k \rangle^* \langle \mathbf{u}_k \rangle^*) = \Gamma_{M,k}, \quad (3.138)$$

$$\begin{aligned} \frac{\partial}{\partial t} (\epsilon_k \langle \rho_k \rangle^* \langle \mathbf{u}_k \rangle^*) + \nabla \cdot (\epsilon_k \langle \rho_k \rangle^* \langle \mathbf{u}_k \rangle^* \langle \mathbf{u}_k \rangle^*) + \nabla (\epsilon_k \langle P_k \rangle^*) \\ - \langle P_k \rangle^* \nabla (\epsilon_k) - \nabla \cdot (\epsilon_k \langle \boldsymbol{\tau}_k \rangle^*) - \epsilon_k \langle \rho_k \rangle^* \mathbf{g} - \epsilon_k \langle \mathbf{b} \rangle^* = \Gamma_{F,k}, \end{aligned} \quad (3.139)$$

$$\frac{\partial}{\partial t} (\epsilon_k \langle \rho_k \rangle^* \langle \omega_k^\alpha \rangle^*) + \nabla \cdot (\epsilon_k \langle \rho_k \rangle^* \langle \omega_k^\alpha \rangle^* \langle \mathbf{u}_k \rangle^*) + \epsilon_k \langle \mathcal{J}_k^\alpha \rangle^* = \Gamma_{S,k}^\alpha, \quad (3.140)$$

$$\begin{aligned} \frac{\partial}{\partial t} \left(\sum_k \sum_{\alpha \neq \alpha^\pm} \epsilon_k \langle \rho_k \rangle^* \langle \omega_k^\alpha \rangle^* C_{p,k}^\alpha \langle T \rangle^* \right) + \nabla \cdot \left(\sum_k \sum_{\alpha \neq \alpha^\pm} \epsilon_k \langle \mathbf{F}_k^\alpha \rangle^* C_{p,k}^\alpha \langle T \rangle^* \right) = -\nabla \cdot (\langle \mathbf{q} \rangle^*) \\ + E_J^{\alpha^\pm} + E_W + E_m + E_{\text{react}}. \end{aligned} \quad (3.141)$$

The formulated equations apply to each layer and phase in the PEM fuel cell, including the polymer electrolyte membrane. Hence, transport phenomena in the the polymer electrolyte are derived directly from first principles. Since the governing equations are similar for each layer and phase, the formulation presented in this thesis is consistent, comprehensive and systematic.

The interfacial source terms, Γ , and the energy source terms, E , depend on the location within the fuel cell. In the conservation of momentum equation, the interfacial source term, $\Gamma_{F,k}$, depends on the adjacent phases. If a solid phase is present, the momentum interfacial source term becomes the Darcy term.

The interfacial source term in the conservation of species equation has two contributions. One contribution represents the interfacial mass transport of water between the gas and liquid phases. The other contribution is the reactions that occur in the catalyst layers; this contribution is not present in any of the other layers of the PEM fuel cell.

The energy source terms represent Joule heating ($E_J^{\alpha^\pm}$), water condensation and evaporation (E_W), the heat of the catalyst layer reactions (E_{react}), and a miscellaneous term resulting from the

CHAPTER 3. GENERAL FORMULATION

variable change from enthalpy to temperature (E_m). Of these terms, Joule heating will be present in all of the fuel cell layers due to electron migration in the solid phase or hydronium migration in the electrolyte. The presence of water condensation and evaporation requires both the liquid and gas phases to exist, while the heat of reaction only exists in the catalyst layers.

The governing equations derived in this chapter represent a general description of the processes occurring within a PEM fuel cell. However, the inclusion of all these processes may not be necessary in order to successfully model PEM fuel cell performance. As well, the specific form of the interfacial source terms and energy source terms are subject to assumptions. The next chapter applies simplifying assumptions to the general governing equations and further chapters numerically solve the simplified set of governing equations.

Chapter 4

Simplified Formulation for Numerical Implementation

The equations presented in Chapter 3 represent a general formulation for modeling a single PEM fuel cell. However, the full solution of these equations are beyond the scope of this thesis research due to time constraints. Therefore, some simplifying assumptions are applied to the general governing equations in order to reduce the number of equations that require numerical solution. Even though the governing equations are simplified, the reduced equation set still includes the novel transport equations for the polymer electrolyte membrane.

This chapter presents the assumptions, and the resulting governing equations for the simplified formulation. After application of the simplifying assumptions, the only phases that are considered within the fuel cell are the gas phase, the liquid phase in the polymer electrolyte, and the solid phase in the bipolar plates, electrode backing layers and catalyst layers. Although the general, governing equations of Chapter 3 apply to each phase in the PEM fuel cell, the specific details of the governing equations, such as the interfacial source terms, can be unique to each phase. Thus, this governing equations for each phase are presented in this chapter.

4.1 Assumptions

One method of simplifying the governing equation set is to non-dimensionalize the governing equations. The relative size of the resulting non-dimensional groups can then be used to neglect certain terms in the general governing equations. However, for PEM fuel cells, this approach is difficult to implement because the non-dimensionalization process yields many dimensionless groups that can not be easily quantified [108]. Thus, the general governing equations of this thesis are simplified using physical arguments instead. For the model presented in this thesis, five major assumptions are used to simplify the general mathematical model.

1. The cell operates in steady state.
2. Liquid water only exists within the polymer electrolyte; water elsewhere in the PEM fuel cell is assumed to be in the gas phase.
3. The cell is isothermal; hence, the conservation of energy is not required.
4. The polymer electrolyte is impervious to the gas phase.
5. The anode fuel consists of only hydrogen and water.

Of the above mentioned assumptions, all but the second assumption can be easily justified. A PEM fuel cell operating under a constant electrical load and reactant supply would be operating in steady-state. Although the electro-chemical reactions within a fuel cell are exothermic, with sufficient external cooling, PEM fuel cell temperature gradients can range from 0.7 to 0.53 K [109].

Since the reactants typically enter the fuel cell at a relative humidity of 100% and water is produced within the fuel cell, ignoring the presence of condensed, liquid phase water is harder to justify. However, since the density of liquid water is much higher than water in the gas phase, the volume occupied by the liquid water should be small. Therefore, if little water is being produced in the PEM fuel cell, as in low current density operation, then ignoring liquid water can be justified. Further, a PEM fuel cell can be designed such that all water is removed in vapor form [110].

As a result of the five major assumptions, the number of conservation equations governing the transport in each phase are reduced. Transport in the gas phase is described by the conservation of mass, momentum and species. The solid phase is stationary; thus, only the conservation of species, with the species being electrons, is required. The convective flow in the polymer electrolyte is assumed to be zero; thus, the governing equations are the conservation of hydronium ions and water. Finally, if the anode reactants are humidified hydrogen, the detailed anode kinetics outlined in Chapter 3 are not required. With no reactant cross-over through the electrolyte, the cathode reactions are also simplified. These simplified governing equations and the simplified reaction kinetics are examined in this chapter, as well as appropriate boundary conditions.

4.2 Gas Phase

Transport in the gas phase is described by the conservation of mass, momentum, and species:

$$\nabla \cdot (\epsilon_g \langle \rho_g \rangle^* \langle \mathbf{u}_g \rangle^*) = \Gamma_{M,g}, \quad (4.1)$$

$$\nabla \cdot (\epsilon_g \langle \rho_g \rangle^* \langle \mathbf{u}_g \rangle^* \langle \mathbf{u}_g \rangle^*) + \nabla (\epsilon_g \langle P_g \rangle^*) - \langle P_g \rangle^* \nabla (\epsilon_g) - \nabla \cdot (\epsilon_g \langle \boldsymbol{\tau}_g \rangle^*) = \Gamma_{F,g}, \quad (4.2)$$

$$\nabla \cdot (\epsilon_g \langle \rho_g^\alpha \rangle^* \langle \mathbf{u}_g \rangle^* + \epsilon_g \langle \mathcal{J}_g^\alpha \rangle^*) = \Gamma_{S,g}^\alpha. \quad (4.3)$$

The conservation of species is written in terms of partial density:

$$\rho_k^\alpha = \rho_k \omega_k^\alpha. \quad (4.4)$$

In order to obtain closure for Equations (4.1) to (4.3), constitutive equations for $\Gamma_{M,g}$, $\Gamma_{F,g}$, \mathcal{J}_g^α and $\Gamma_{S,g}^\alpha$ are required.

Siegel *et al.* [67] found that the pore size, even in the catalyst layer, can be as large as 10 μm . Thus, it is assumed that the solid phase does not interfere with the diffusion of the gas species. Since the activity of an ideal gas is the mole fraction [106], the gas phase Generalized Stefan-Maxwell

equations become

$$-\langle c_g \rangle^* \nabla \langle x_g^\alpha \rangle^* = \sum_{\beta \neq \alpha} \frac{\hat{M}_g}{\hat{M}_\alpha \hat{M}_\beta D_{\alpha-\beta,g}^{\text{eff}}} \left(\langle \omega_g^\beta \rangle^* \langle \mathcal{J}_g^\alpha \rangle^* - \langle \omega_g^\alpha \rangle^* \langle \mathcal{J}_g^\beta \rangle^* \right). \quad (4.5)$$

For the species in the gas phase, the bulk values of the binary diffusion coefficients can be calculated with the Fuller, Schettler and Giddings method [111]. The Stefan-Maxwell equations can be “inverted” and the diffusional flux of species α expressed as a function of mass fraction [112]:

$$\langle \mathcal{J}_g^\alpha \rangle^* = -\langle \rho_g \rangle^* D_{\alpha-g}^{\text{eff}} \nabla \langle \omega_g^\alpha \rangle^* + \frac{\langle \omega_g^\alpha \rangle^* D_{\alpha-g}^{\text{eff}}}{(1 - \langle x_g^\alpha \rangle^*)} \sum_{\beta \neq \alpha} \left[\frac{\langle \rho_g \rangle^* \hat{M}_g}{\hat{M}_\beta} \nabla \langle \omega_g^\beta \rangle^* + \frac{\hat{M}_g \langle \mathcal{J}_g^\beta \rangle^*}{\hat{M}_\beta \mathcal{D}_{\alpha-\beta,g}^{\text{eff}}} \right] \quad (4.6)$$

where $D_{\alpha-g}^{\text{eff}}$ is the overall, effective diffusion coefficient of species α in phase k and is expressed as:

$$\frac{1 - \langle x_g^\alpha \rangle^*}{D_{\alpha-g}^{\text{eff}}} = \sum_{\beta \neq \alpha} \frac{\langle x_g^\beta \rangle^*}{\mathcal{D}_{\alpha-\beta,g}^{\text{eff}}} \quad (4.7)$$

The mass fraction gradient of Equation (4.6) can be converted to a gradient of partial density through the product rule [113]:

$$\nabla \langle \omega_g^\alpha \rangle^* = \frac{\nabla \langle \rho_g^\alpha \rangle^*}{\langle \rho_g \rangle^*} - \frac{\langle \omega_g^\alpha \rangle^*}{\langle \rho_g \rangle^*} \nabla \langle \rho_g \rangle^*. \quad (4.8)$$

Thus, the diffusional mass flux of species α is

$$\begin{aligned} \langle \mathcal{J}_g^\alpha \rangle^* = & -D_{\alpha-g}^{\text{eff}} \nabla \langle \rho_g^\alpha \rangle^* + \frac{\langle \omega_g^\alpha \rangle^* D_{\alpha-g}^{\text{eff}}}{(1 - \langle x_g^\alpha \rangle^*)} \sum_{\beta \neq \alpha} \left[\frac{\langle \rho_g \rangle^* \hat{M}_g}{\hat{M}_\beta} \nabla \langle \omega_g^\beta \rangle^* + \frac{\hat{M}_g \langle \mathcal{J}_g^\beta \rangle^*}{\hat{M}_\beta \mathcal{D}_{\alpha-\beta,g}^{\text{eff}}} \right] \\ & + \langle \omega_g^\alpha \rangle^* D_{\alpha-g}^{\text{eff}} \nabla \langle \rho_g \rangle^*. \quad (4.9) \end{aligned}$$

The momentum interfacial source term between the gas and solid phase can be modeled with

the Darcy term [114]:

$$\Gamma_{F,g} = -\frac{(\epsilon_g)^2 \mu_g}{K} \langle \mathbf{u}_g \rangle^* \quad (4.10)$$

where K is the absolute permeability of the porous media. If no solid phase exists, then $K = \infty$.

The source term in the conservation of mass equation can be expressed in terms of the source terms for the conservation of species:

$$\Gamma_{M,g} = \sum_{\alpha} \Gamma_{S,g}^{\alpha} \quad (4.11)$$

The source terms in the conservation of species can be split into two groups:

$$\Gamma_{S,g}^{\alpha} = \begin{cases} \hat{M}_{\alpha} A_v \dot{\mathcal{P}}^{\alpha} & \alpha \neq \text{H}_2\text{O} \\ \hat{M}_{\alpha} A_v \dot{\mathcal{P}}^{\alpha} + \Gamma_{S,g-e}^{\text{H}_2\text{O}} & \alpha = \text{H}_2\text{O} \end{cases}, \quad (4.12)$$

where $\dot{\mathcal{P}}^{\alpha}$ is the production of species α , in units of mole/m³ s, due to the electro-chemical reactions, and $\Gamma_{S,g-e}^{\text{H}_2\text{O}}$ represents the mass transfer of water from the electrolyte to the gas phase. An expression for $\dot{\mathcal{P}}^{\alpha}$ can be obtained from the electro-chemical reaction kinetics. There is no general equation for $\Gamma_{S,g-e}^{\alpha}$ available in literature. However, it is not required in the solution method since a local thermodynamic equilibrium is assumed between the water in the gas phase and water in the electrolyte.

4.3 Solid Phase

For the solid phase, there is no convective velocity and only one species exists: electrons. The conservation of species, in terms of molar flux, is

$$\nabla \cdot (\epsilon_s \langle \mathcal{N}_s^{e^-} \rangle^*) = \Gamma_{S,s}^{e^-}, \quad (4.13)$$

where $\mathcal{N}_s^{e^-}$ is the molar flux of electrons. Assuming the solid phase is a good electronic conductor (not a semi-conductor), there are no concentration gradients of electrons in the solid phase; thus, the Generalized Stefan-Maxwell equations reduce to

$$-\frac{z_{e^-} \langle c_s^{e^-} \rangle^* \mathcal{F}}{\mathcal{R} \langle T_s \rangle^*} \nabla \langle \Phi_s \rangle^* = \frac{\langle \mathcal{N}_s^{e^-} \rangle^*}{\hat{M}_{e^-} D_{e^- - s, s}^{\text{eff}}} \quad (4.14)$$

Electron flow is generally expressed in terms of current density through Faraday's law [105]:

$$\mathbf{J}_s = z_{e^-} \mathcal{F} \mathcal{N}_s^{e^-}. \quad (4.15)$$

Using Faraday's law, the conservation of species and Generalized Stefan-Maxwell equations can be expressed in terms of current density:

$$\begin{aligned} \nabla \cdot (\epsilon_s \langle \mathbf{J}_s \rangle^*) &= z_{e^-} \mathcal{F} \Gamma_{S,s}^{e^-}, \\ \mathbf{J}_s &= -\kappa_s^{\text{eff}} \nabla \langle \Phi_s \rangle^*, \\ \nabla \cdot (\epsilon_s \kappa_s^{\text{eff}} \nabla \langle \Phi_s \rangle^*) &= \mathcal{F} \Gamma_{S,s}^{e^-}, \end{aligned} \quad (4.16)$$

where the constant terms of Equation (4.14) are combined to form the electrical conductivity of the solid phase, κ_s^{eff} . For the solid phase in this thesis research, the bulk value of electrical conductivity is 1.67×10^4 S/m. The interfacial source term, $\Gamma_{S,s}^{e^-}$, represents the production of electrons in units of mole/m³ s:

$$\Gamma_{S,s}^{e^-} = A_v \dot{\mathcal{P}}^{e^-}, \quad (4.17)$$

where $\dot{\mathcal{P}}^{e^-}$ can be calculated with the electro-chemical kinetics.

4.4 Liquid Phase in the Electrolyte

The transport of water and ions in the electrolyte is modeled using the general membrane model of Scattergood and Lightfoot [74]. In this membrane model, the convective velocity is assumed to be zero; thus the only equation is the conservation of species:

$$\nabla \cdot (\epsilon_{\ell,e} \langle \mathcal{J}_{\ell,e}^\alpha \rangle^*) = \Gamma_{S,e}^\alpha. \quad (4.18)$$

The subscript ℓ,e is used to denote the liquid phase in the electrolyte pores. The volume fraction of liquid water can be expressed as

$$\epsilon_{\ell,e} = \epsilon_e \epsilon_e^\ell, \quad (4.19)$$

where ϵ_e is the volume fraction of electrolyte and ϵ_e^ℓ is the volume fraction of liquid within the polymer electrolyte.

The transport of water and ions in the membrane is governed by the Generalized Stefan-Maxwell equations, whereby the polymer matrix is considered to be an immobile species:

$$\begin{aligned} - \langle c_{\ell,e} \rangle^* \nabla \langle x_{\ell,e}^\alpha \rangle^* - \frac{z_\alpha \langle c_{\ell,e}^\alpha \rangle^* \mathcal{F}}{\mathcal{R} \langle T_{\ell,e} \rangle^*} \nabla \langle \Phi_e \rangle^* = \\ \sum_{\beta \neq \alpha} \frac{\hat{M}_{\ell,e}}{\hat{M}_\alpha \hat{M}_\beta D_{\alpha-\beta,e}^{\text{eff}}} \left(\langle \omega_{\ell,e}^\beta \rangle^* \langle \mathcal{J}_{\ell,e}^\alpha \rangle^* - \langle \omega_{\ell,e}^\alpha \rangle^* \langle \mathcal{J}_{\ell,e}^\beta \rangle^* \right) + \frac{\langle \mathcal{J}_{\ell,e}^\alpha \rangle^*}{\hat{M}_\alpha D_{\alpha-s,e}^{\text{eff}}}, \end{aligned} \quad (4.20)$$

where the activity of each species is assumed to be equal to the mole fraction. There are two mobile species in the electrolyte: water and hydronium ions. For the mobile ions, the Generalized

Stefan-Maxwell equations are

$$\begin{aligned}
 -\langle c_{\ell,e} \rangle^* \nabla \langle x_{\ell,e}^{\text{H}_2\text{O}} \rangle^* &= \frac{\hat{M}_{\ell,e}}{\hat{M}_{\text{H}_2\text{O}} \hat{M}_{\text{H}_3\text{O}^+} D_{\text{H}_2\text{O}-\text{H}_3\text{O}^+,e}^{\text{eff}}} \times \\
 &\quad \left(\langle \omega_{\ell,e}^{\text{H}_3\text{O}^+} \rangle^* \langle \mathcal{J}_{\ell,e}^{\text{H}_2\text{O}} \rangle^* - \langle \omega_{\ell,e}^{\text{H}_2\text{O}} \rangle^* \langle \mathcal{J}_{\ell,e}^{\text{H}_3\text{O}^+} \rangle^* \right) + \frac{\langle \mathcal{J}_{\ell,e}^{\text{H}_2\text{O}} \rangle^*}{\hat{M}_{\text{H}_2\text{O}} D_{\text{H}_2\text{O}-s,e}^{\text{eff}}}, \quad (4.21)
 \end{aligned}$$

$$\begin{aligned}
 -\langle c_{\ell,e} \rangle^* \nabla \langle x_{\ell,e}^{\text{H}_3\text{O}^+} \rangle^* - \frac{\langle c_{\ell,e}^{\text{H}_3\text{O}^+} \rangle^* \mathcal{F}}{\mathcal{R} \langle T_{\ell,e} \rangle^*} \nabla \langle \Phi_e \rangle^* &= \frac{\hat{M}_{\ell,e}}{\hat{M}_{\text{H}_3\text{O}^+} \hat{M}_{\text{H}_2\text{O}} D_{\text{H}_3\text{O}^+-\text{H}_2\text{O},e}^{\text{eff}}} \times \\
 &\quad \left(\langle \omega_{\ell,e}^{\text{H}_2\text{O}} \rangle^* \langle \mathcal{J}_{\ell,e}^{\text{H}_3\text{O}^+} \rangle^* - \langle \omega_{\ell,e}^{\text{H}_3\text{O}^+} \rangle^* \langle \mathcal{J}_{\ell,e}^{\text{H}_2\text{O}} \rangle^* \right) + \frac{\langle \mathcal{J}_{\ell,e}^{\text{H}_3\text{O}^+} \rangle^*}{\hat{M}_{\text{H}_3\text{O}^+} D_{\text{H}_3\text{O}^+-s,e}^{\text{eff}}}. \quad (4.22)
 \end{aligned}$$

The water and hydronium flux equations can be simplified. The mole fractions of water and ions are not independent:

$$\langle x_{\ell,e}^{\text{H}_3\text{O}^+} \rangle^* = 1 - \langle x_{\ell,e}^{\text{H}_2\text{O}} \rangle^*. \quad (4.23)$$

Additionally, the gradient of mole fraction can be converted to a mass fraction gradient. For two species, the mole fraction gradient becomes [84]:

$$\nabla \langle x_{\ell,e}^{\text{H}_2\text{O}} \rangle^* = \frac{(\hat{M}_{\ell,e})^2}{\hat{M}_{\text{H}_2\text{O}} \hat{M}_{\text{H}_3\text{O}^+}} \nabla \langle \omega_{\ell,e}^{\text{H}_2\text{O}} \rangle^* \quad (4.24)$$

Therefore, the two independent variables are the mass fraction of water and the potential in the electrolyte. The two species equations for the electrolyte pore fluid can be expressed in matrix form:

$$\begin{bmatrix} A_{11} & A_{12} \\ A_{21} & A_{22} \end{bmatrix} \begin{bmatrix} \langle \mathcal{J}_{\ell,e}^{\text{H}_2\text{O}} \rangle^* \\ \langle \mathcal{J}_{\ell,e}^{\text{H}_3\text{O}^+} \rangle^* \end{bmatrix} = \begin{bmatrix} B_{11} \\ B_{21} \end{bmatrix} \nabla \langle \omega_{\ell,e}^{\text{H}_2\text{O}} \rangle^* + \begin{bmatrix} B_{12} \\ B_{22} \end{bmatrix} \nabla \langle \Phi_e \rangle^* \quad (4.25)$$

where the matrix coefficients are defined as

$$A_{11} = \frac{\hat{M}_{\ell,e} \langle \omega_{\ell,e}^{\text{H}_3\text{O}^+} \rangle^*}{\hat{M}_{\text{H}_3\text{O}^+} \hat{M}_{\text{H}_2\text{O}} D_{\text{H}_3\text{O}^+ - \text{H}_2\text{O},e}^{\text{eff}}} + \frac{1}{\hat{M}_{\text{H}_2\text{O}} D_{\text{H}_2\text{O} - s,e}^{\text{eff}}} \quad (4.26)$$

$$A_{12} = -\frac{\hat{M}_{\ell,e} \langle \omega_{\ell,e}^{\text{H}_2\text{O}} \rangle^*}{\hat{M}_{\text{H}_3\text{O}^+} \hat{M}_{\text{H}_2\text{O}} D_{\text{H}_3\text{O}^+ - \text{H}_2\text{O},e}^{\text{eff}}} \quad (4.27)$$

$$A_{21} = -\frac{\hat{M}_{\ell,e} \langle \omega_{\ell,e}^{\text{H}_3\text{O}^+} \rangle^*}{\hat{M}_{\text{H}_3\text{O}^+} \hat{M}_{\text{H}_2\text{O}} D_{\text{H}_3\text{O}^+ - \text{H}_2\text{O},e}^{\text{eff}}} \quad (4.28)$$

$$A_{22} = \frac{\hat{M}_{\ell,e} \langle \omega_{\ell,e}^{\text{H}_2\text{O}} \rangle^*}{\hat{M}_{\text{H}_3\text{O}^+} \hat{M}_{\text{H}_2\text{O}} D_{\text{H}_3\text{O}^+ - \text{H}_2\text{O},e}^{\text{eff}}} + \frac{1}{\hat{M}_{\text{H}_3\text{O}^+} D_{\text{H}_3\text{O}^+ - s,e}^{\text{eff}}} \quad (4.29)$$

$$B_{11} = -\frac{\langle c_{\ell,e} \rangle^* (\hat{M}_{\ell,e})^2}{\hat{M}_{\text{H}_2\text{O}} \hat{M}_{\text{H}_3\text{O}^+}} \quad (4.30)$$

$$B_{21} = \frac{\langle c_{\ell,e} \rangle^* (\hat{M}_{\ell,e})^2}{\hat{M}_{\text{H}_2\text{O}} \hat{M}_{\text{H}_3\text{O}^+}} \quad (4.31)$$

$$B_{12} = 0 \quad (4.32)$$

$$B_{22} = -\frac{\langle c_{\ell,e}^{\text{H}_3\text{O}^+} \rangle^* \mathcal{F}}{\mathcal{R}T_{\ell,e}} \quad (4.33)$$

Equations (4.25) to (4.33) can be inverted to yield

$$\langle \mathcal{J}_{\ell,e}^{\text{H}_2\text{O}} \rangle^* = \mathcal{D}_{\text{H}_2\text{O}}^{\text{H}_2\text{O}} \nabla \langle \omega_{\ell,e}^{\text{H}_2\text{O}} \rangle^* + \mathcal{D}_{\text{H}_3\text{O}^+}^{\text{H}_2\text{O}} \nabla \langle \Phi_e \rangle^* \quad (4.34)$$

$$\langle \mathcal{J}_{\ell,e}^{\text{H}_3\text{O}^+} \rangle^* = \mathcal{D}_{\text{H}_2\text{O}}^{\text{H}_3\text{O}^+} \nabla \langle \omega_{\ell,e}^{\text{H}_2\text{O}} \rangle^* + \mathcal{D}_{\text{H}_3\text{O}^+}^{\text{H}_3\text{O}^+} \nabla \langle \Phi_e \rangle^* \quad (4.35)$$

where \mathcal{D}_α^β is the effective diffusion coefficient of species α for the flux of species β . Finally, equations (4.34) and (4.35) can be expressed in terms of partial density gradients:

$$\langle \mathcal{J}_{\ell,e}^{\text{H}_2\text{O}} \rangle^* = \frac{\mathcal{D}_{\text{H}_2\text{O}}^{\text{H}_2\text{O}}}{\langle \rho_{\ell,e} \rangle^*} \nabla \langle \rho_{\ell,e}^{\text{H}_2\text{O}} \rangle^* + \mathcal{D}_{\text{H}_3\text{O}^+}^{\text{H}_2\text{O}} \nabla \langle \Phi_e \rangle^* - \frac{\langle \omega_{\ell,e}^{\text{H}_2\text{O}} \rangle^* \mathcal{D}_{\text{H}_2\text{O}}^{\text{H}_2\text{O}}}{\langle \rho_{\ell,e} \rangle^*} \nabla \langle \rho_{\ell,e} \rangle^* \quad (4.36)$$

$$\langle \mathcal{J}_{\ell,e}^{\text{H}_3\text{O}^+} \rangle^* = \frac{\mathcal{D}_{\text{H}_2\text{O}}^{\text{H}_3\text{O}^+}}{\langle \rho_{\ell,e} \rangle^*} \nabla \langle \rho_{\ell,e}^{\text{H}_2\text{O}} \rangle^* + \mathcal{D}_{\text{H}_3\text{O}^+}^{\text{H}_3\text{O}^+} \nabla \langle \Phi_e \rangle^* - \frac{\langle \omega_{\ell,e}^{\text{H}_2\text{O}} \rangle^* \mathcal{D}_{\text{H}_2\text{O}}^{\text{H}_3\text{O}^+}}{\langle \rho_{\ell,e} \rangle^*} \nabla \langle \rho_{\ell,e} \rangle^* \quad (4.37)$$

The source terms for the liquid species in the electrolyte are similar to the gas phase source terms:

$$\Gamma_{S,e}^\alpha = \begin{cases} \hat{M}_\alpha A_v \dot{\mathcal{P}}^\alpha & \alpha \neq \text{H}_2\text{O} \\ \hat{M}_\alpha A_v \dot{\mathcal{P}}^\alpha + \Gamma_{S,e-g}^{\text{H}_2\text{O}} & \alpha = \text{H}_2\text{O} \end{cases}, \quad (4.38)$$

where $\Gamma_{S,e-g}^{\text{H}_2\text{O}} = -\Gamma_{S,g-e}^{\text{H}_2\text{O}}$ and $\dot{\mathcal{P}}^\alpha$ is calculated from the electro-chemical reaction kinetics.

If the polymer electrolyte and the gas phase co-exist, such as in the catalyst layers, the concentration of water in the gas phase and the pores of the polymer electrolyte are not independent. The polymer electrolyte will absorb or desorb water from the gas phase until an equilibrium is reached. The water content of the membrane can be expressed with the hydration:

$$\mathcal{L} = \frac{\text{moles of liquid water}}{\text{moles of SO}_3\text{H}}. \quad (4.39)$$

As the electrolyte absorbs more water, the value of \mathcal{L} increases. The volume fraction of liquid within the electrolyte is related to the membrane hydration with

$$\epsilon_e^\ell = \frac{\mathcal{L}}{\frac{\hat{V}_M}{\hat{V}_{\text{H}_2\text{O}}} + \mathcal{L}}, \quad (4.40)$$

where \hat{V}_M is the molar volume of the polymer matrix and $\hat{V}_{\text{H}_2\text{O}}$ is the molar volume of liquid water. The molar volumes of the polymer matrix and water are $537 \text{ cm}^3/\text{mol}$ and $18 \text{ cm}^3/\text{mol}$, respectively.

The water content of the air is expressed in terms of ‘‘activity’’ [27]:

$$\tilde{a} = \frac{x_g^{\text{H}_2\text{O}} P_g}{P_{\text{sat}}^{\text{H}_2\text{O}}}, \quad (4.41)$$

where $P_{\text{sat}}^{\text{H}_2\text{O}}$ is the saturation pressure of water. Note that the definition of activity in Equation (4.41) is not equivalent to the activity in the Generalized Stefan-Maxwell equations. The activity defined by Equation (4.41) is equivalent to the relative humidity.

Since the water in the gas and membrane are in equilibrium, the hydration of the membrane can be expressed as a function of the water activity. The first function relating water activity and membrane hydration was developed by Springer *et al.* [26]. Since then, several other similar studies have been undertaken for a wider range of temperatures and relative humidities than the ones examined by Springer *et al.* [26]. One of the most comprehensive curve fits of the hydration/water activity function has been done by Futerko and Hsing [115], using a Flory-Huggins model. The Flory-Huggins model predicts the activity of a solvent in a polymer-solvent mixture and is based upon the thermodynamics of mixtures [116]. The model consists of a series of equations:

$$\tilde{a} = (1 - \epsilon_e^s) \exp \left[\left(1 - \frac{1}{r} \right) \epsilon_e^s + \chi (\epsilon_e^s)^2 \right] \quad (4.42)$$

$$\epsilon_e^s = \frac{r + \mathcal{L}_c}{r + \mathcal{L}} \quad (4.43)$$

$$\xi = \frac{\mathcal{L}_c}{(1 - \mathcal{L}_c) \tilde{a}}, \quad (4.44)$$

where the volume fraction of the solid polymer matrix in the membrane is denoted as ϵ_e^s . The symbol r is the ratio of molar volumes between the solid polymer and liquid water:

$$r = \frac{\hat{V}_s}{\hat{V}_{\text{H}_2\text{O}}}. \quad (4.45)$$

The parameters χ and ξ are dimensionless functions of temperature:

$$\chi = 1.936 - \frac{2.18 \text{ kJ/mole}}{\mathcal{R}T} \quad (4.46)$$

$$\xi = 0.0256 \exp \left(\frac{22.4 \text{ kJ/mole}}{\mathcal{R}T} \right) \quad (4.47)$$

The relationship between the activity of water in the gas and the hydration of the polymer electrolyte is illustrated in Figure 4.1

If the membrane water content is known, the concentration of water and hydronium in the pore fluid, as well as the volume fraction of liquid in the polymer electrolyte can be calculated. The

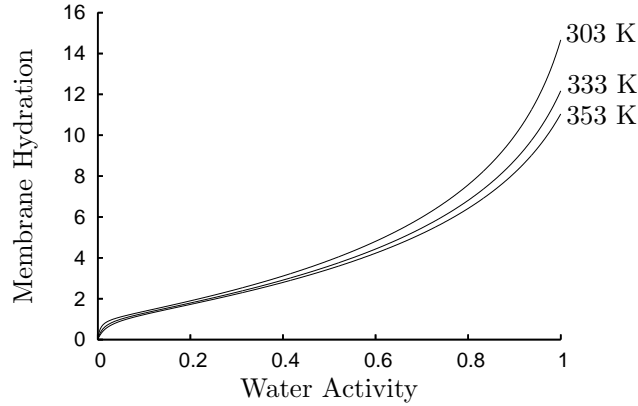


Figure 4.1: The hydration of the polymer electrolyte membrane as a function of the activity of water in the gas phase for various temperatures.

concentrations of H_3O^+ and liquid water are related through the acid-base equilibrium reaction occurring within the electrolyte pores [78]:



The concentrations of each component are related with

$$\mathbb{K}_e = \frac{c_e^{\text{H}_3\text{O}^+} c_e^{\text{SO}_3^-}}{c_e^{\text{H}_2\text{O}} c_e^{\text{SO}_3\text{H}}} \quad (4.49)$$

where the acid-base equilibrium constant is a function of temperature:

$$\mathbb{K}_e = \mathbb{K}_e^o \exp \left[-\frac{\Delta H^o}{\mathcal{R}} \left(\frac{1}{T} - \frac{1}{298} \right) \right] \quad (4.50)$$

The value of \mathbb{K}_e^o is 6.2, $\Delta H^o = -52.3 \text{ kJ/mole}$ [78], and T is in K.

The concentrations of hydronium and the sulfonate ions are related through electro-neutrality:

$$c_e^{\text{H}_3\text{O}^+} = c_e^{\text{SO}_3^-} . \quad (4.51)$$

Using the definition of membrane hydration, the reference values of water and sulfonate concentra-

tion can be related with

$$\mathcal{L} = \frac{c_{e,\text{ref}}^{\text{SO}_3\text{H}}}{c_{e,\text{ref}}^{\text{H}_2\text{O}}}, \quad (4.52)$$

where the reference concentration values are the concentrations before the acid-base equilibrium. Using a mass balance, the reference concentrations can be related to the concentrations after the acid-base equilibrium reaction:

$$c_{e,\text{ref}}^{\text{H}_2\text{O}} = c_e^{\text{H}_2\text{O}} + c_e^{\text{H}_3\text{O}^+} \quad (4.53)$$

$$c_{e,\text{ref}}^{\text{SO}_3\text{H}} = c_e^{\text{SO}_3\text{H}} + c_e^{\text{SO}_3^-} \quad (4.54)$$

If the membrane hydration is known, then Equations (4.49) to (4.54) can be solved for the concentrations of water, hydronium, sulfonate and sulfonate ions. The mole fractions in Equation (4.20) are the mole fractions of the mobile species only. They are related in the concentrations in Equations (4.49) to (4.54) through

$$x_{\ell,e}^{\text{H}_2\text{O}} = \frac{c_e^{\text{H}_2\text{O}}}{c_e^{\text{H}_2\text{O}} + c_e^{\text{H}_3\text{O}^+}}, \quad (4.55)$$

$$x_{\ell,e}^{\text{H}_3\text{O}^+} = \frac{c_e^{\text{H}_3\text{O}^+}}{c_e^{\text{H}_2\text{O}} + c_e^{\text{H}_3\text{O}^+}}. \quad (4.56)$$

The degree of dissociation of the acid membrane is defined as

$$\begin{aligned} \mathcal{A} &= \frac{c_e^{\text{H}_3\text{O}^+}}{c_{e,\text{ref}}^{\text{SO}_3\text{H}}}, \quad (4.57) \\ &= \frac{(\mathcal{L} + 1) - \sqrt{(\mathcal{L} + 1)^2 - 4\mathcal{L} \left(1 - \frac{1}{\mathbb{K}_e}\right)}}{2 \left(1 - \frac{1}{\mathbb{K}_e}\right)}. \end{aligned}$$

Using the definition of the degree of dissociation, the mole fractions of water and hydronium in the

electrolyte pores become a function of membrane hydration and temperature:

$$x_{\ell,e}^{\text{H}_2\text{O}} = 1 - \frac{\mathcal{A}}{\mathcal{L}}, \quad (4.58)$$

$$x_{\ell,e}^{\text{H}_3\text{O}^+} = \frac{\mathcal{A}}{\mathcal{L}}, \quad (4.59)$$

where \mathcal{A} is a function of hydration and the acid-base equilibrium constant, which is a function of temperature.

If the polymer electrolyte is in contact with liquid water, the membrane hydration is significantly greater than if it is in contact with fully humidified air. For example, at a temperature of 80°C, the hydration of membrane is approximately 10 when in equilibrium with water vapor, but is approximately 20 when immersed in liquid water [117]. Since liquid water is not considered in the model, this phenomenon is not included.

4.5 Reaction

Two electro-chemical reactions are considered in the simplified formulation of this thesis. In the anode catalyst layer, hydrogen electro-oxidation occurs, while oxygen reduction is modeled in the cathode catalyst layer. Both of these reactions are electron-transfer reactions.

The cathode reactions are the same as in Chapter 3, except that only the electro-chemical reaction is included; the reaction kinetics are repeated here. Since the positive charge is assumed to be a H_3O^+ ion, the overall reaction in the cathode catalyst layer is



The rate of reaction is governed by Volmer/Erdey-Gruz kinetics [95]:

$$\mathcal{R}_{c,\text{red}}^{\text{O}_2} = \frac{J_o^{\text{O}_2}}{4\mathcal{F}} \left\{ \left[\frac{c_{\ell,e}^{\text{H}_2\text{O}}}{c_{\ell,e}^{\text{H}_2\text{O}}} \right]^6 \exp\left(\frac{\eta_c}{B_c^{\text{O}_2}}\right) - \left[\frac{c_{g,e}^{\text{O}_2}}{c_{g,e}^{\text{O}_2}} \right] \left[\frac{c_{\ell,e}^{\text{H}_3\text{O}^+}}{c_{\ell,e}^{\text{H}_3\text{O}^+}} \right]^4 \exp\left(-\frac{\eta_c}{B_c^{\text{O}_2}}\right) \right\}, \quad (4.61)$$

Table 4.1: The exchange current density for oxygen reduction at the reference conditions corresponding to a fully hydrated electrolyte and oxygen partial pressure of 1 atm [104].

Temperature (K)	$\log \left(\frac{J_o^{O_2}}{A/cm^2} \right)$
303	-9.7714
313	-9.1347
323	-8.822
333	-8.6026
343	-8.2566
353	-7.7284

where $J_o^{O_2}$ is the exchange current density for oxygen reduction at the reference concentrations. The exchange current density is a function of temperature and the values are listed in Table 4.1 [104]. An overbar denotes the reference concentrations. The reference concentrations for the gas phase species are the concentrations of the pure species at a reference pressure of 1 atm and the cell temperature. For the species in the liquid phase, the reference concentrations correspond to the concentrations when the membrane is fully hydrated. The Tafel slope is denoted by $B_c^{O_2}$ and is given by Parthasarathy *et al.* [104]:

$$B_c^{O_2} = \frac{\mathcal{R}T}{\mathcal{F}}. \quad (4.62)$$

The reaction rate is a function of the concentration and has an exponential dependence on the potential. This is analogous to combustion, whereby the reaction rate is a function of the concentration and also has an exponential relationship to temperature [118]. Thus, for isothermal electro-chemical systems, the potential has the same affect on reaction rate as the temperature does in gas phase systems.

If the fuel is contaminated with carbon monoxide, then the anode reaction should be modeled as a multi-step reaction [119]. However, since the fuel is assumed to be pure hydrogen, the overpotential will be small and the electro-oxidation of hydrogen can be modeled as a single step

reaction:



As with the cathode reaction, the anode reaction can be modeled with Volmer/Erdey-Gruz kinetics [95]:

$$\mathcal{R}_{a,ox}^{\text{H}_2} = \frac{J_o^{\text{H}_2}}{2\mathcal{F}} \left\{ \left[\frac{c_g^{\text{H}_2}}{c_g^{\text{H}_2}} \right] \left[\frac{c_{l,e}^{\text{H}_2\text{O}}}{c_{l,e}^{\text{H}_2\text{O}}} \right]^2 \exp\left(\frac{\eta_a}{B_a^{\text{H}_2}}\right) - \left[\frac{c_{l,e}^{\text{H}_3\text{O}^+}}{c_{l,e}^{\text{H}_3\text{O}^+}} \right]^2 \exp\left(-\frac{\eta_a}{B_a^{\text{H}_2}}\right) \right\}, \quad (4.64)$$

where η_a is the anode overpotential, and $B_a^{\text{H}_2}$ is the Tafel slope of the hydrogen oxidation reaction:

$$B_a^{\text{H}_2} = \frac{2\mathcal{R}T}{\mathcal{F}}. \quad (4.65)$$

The exchange current density for hydrogen oxidation, $J_o^{\text{H}_2}$, is considered to be constant and equal to 0.055 A/cm² [33].

The production and consumption of species in the catalyst layers are related to the reaction rate. In the cathode catalyst layer, the production of species is given by

$$\dot{\mathcal{P}}^{\text{O}_2} = \mathcal{R}_{c,red} \quad (4.66)$$

$$\dot{\mathcal{P}}^{\text{H}_2\text{O}} = -6\mathcal{R}_{c,red} \quad (4.67)$$

$$\dot{\mathcal{P}}^{\text{H}_2\text{O}} = 4\mathcal{R}_{c,red} \quad (4.68)$$

$$\dot{\mathcal{P}}^{e^-} = 4\mathcal{R}_{c,red} \quad (4.69)$$

where A_v is the reactive surface area per unit volume. In the anode catalyst layer, the rate of species production is

$$\dot{\mathcal{P}}^{\text{H}_2} = -\mathcal{R}_{a,ox} \quad (4.70)$$

$$\dot{\mathcal{P}}^{\text{H}_2\text{O}} = -2\mathcal{R}_{a,ox} \quad (4.71)$$

$$\dot{\mathcal{P}}^{\text{H}_3\text{O}^+} = 2\mathcal{R}_{a,ox} \quad (4.72)$$

$$\dot{\mathcal{P}}^{e^-} = 2\mathcal{R}_{a,ox} \quad (4.73)$$

For all species not included in Equations (4.66) to (4.73), the rate of production is zero.

4.6 Boundary Conditions and Computational Domain

The boundary conditions for the PEM fuel cell model are chosen with regard to an experimental investigation into PEM fuel cell performance. The performance of a PEM fuel cell can be characterized by a voltage versus current plot. When testing a PEM fuel cell, several operating conditions can be varied, such as

- the inlet concentration, temperature, and flow rate of the reactants;
- the cell temperature;
- the electrical load; and
- either the inlet or outlet pressure.

The cell temperature is controlled by heating or cooling the external surfaces of the PEM fuel cell. The electrical load on the PEM fuel cell is specified by setting the voltage of the PEM fuel cell or the current drawn from the cell. The inlet and outlet pressures are related through the pressure drop in the gas flow channels; hence, specifying both pressures as input conditions is redundant. If the PEM fuel cell is not pressurized, then the gas flow channels exhaust to the atmosphere; thus the outlet pressure is specified. During pressurized operation, the inlet pressure is generally specified and regulated with a back-pressure control valve that is located at the outlet of the gas flow channels.

Therefore, one set of input parameters are the operating conditions, and these become the boundary conditions for the PEM fuel cell model. The boundary conditions and computational

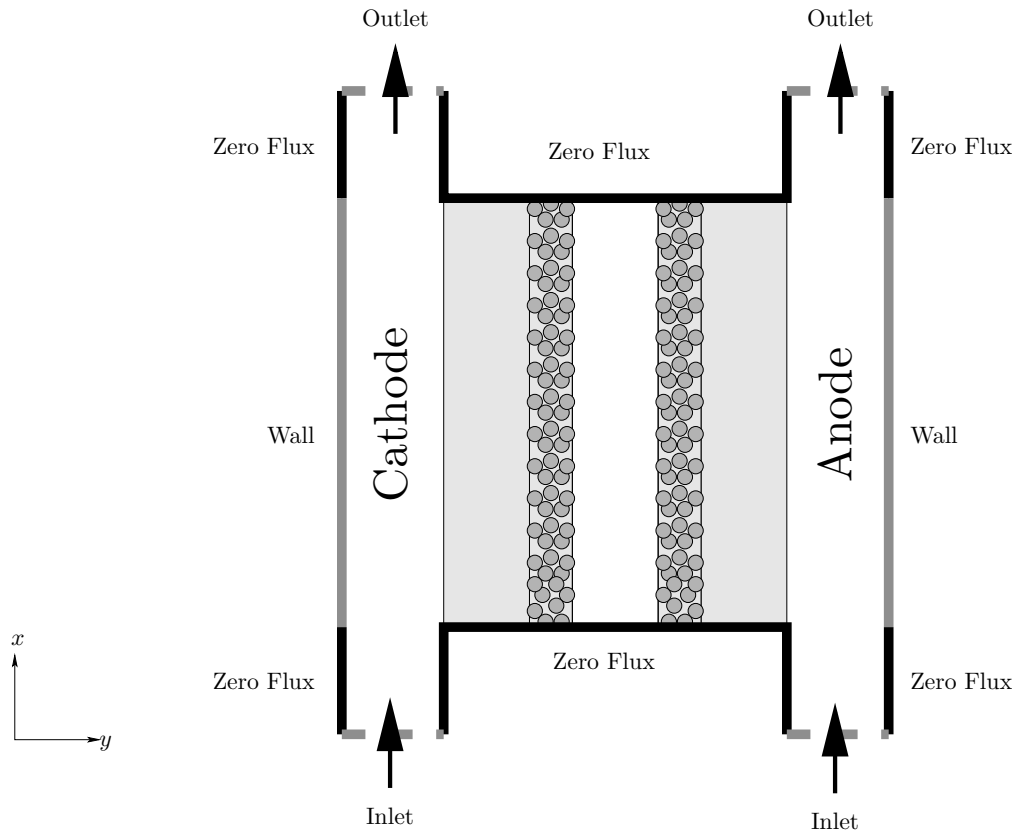


Figure 4.2: The boundary conditions and computational domain of the PEM fuel cell model.

domain, for the simplified formulation, are illustrated in Figure 4.2. The computational domain is two-dimensional and includes the gas flow channels, electrode backing, catalyst and polymer electrolyte layers. In addition, the computational domain extends from the inlets and outlets of the fuel cell; this is to minimize the effect of the boundary conditions of the processes occurring within the PEM fuel cell.

Four types of boundary conditions are present on the exterior of the PEM fuel cell in Figure 4.2: the Zero Flux, Wall, Inlet, and Outlet boundary conditions. The gas phase velocity and species flux or composition, the species flux in the electrolyte pore fluid, and the potential or current density in the solid phase must be specified at the boundaries. A value for the cell temperature must also be specified, although not as a boundary condition because the temperature is assumed to be constant within the fuel cell. The Zero Flux boundary condition specifies that all velocities and species flux

are zero:

$$\left\{ \begin{array}{l} \mathbf{u}_k = 0 \\ \mathcal{J}_k^\alpha \cdot \hat{\mathbf{i}} = 0 \\ \mathbf{J}_s \cdot \hat{\mathbf{i}} = 0 \end{array} \right\} \quad \text{Zero Flux}$$

At the wall boundary condition, the velocity and species flux, except for electrons, are zero. The potential of the solid phase is set at the wall boundary condition.

$$\left\{ \begin{array}{l} \mathbf{u}_k = 0 \\ \mathcal{J}_k^\alpha \cdot \hat{\mathbf{i}} = 0 \\ \Phi_s = \text{Specified} \end{array} \right\} \quad \text{Wall}$$

By setting the solid potential, the cell voltage is being specified:

$$E_{\text{cell}} = \Phi_s|_{\text{cathode}} - \Phi_s|_{\text{anode}}$$

Typically, the anode potential is set to zero and the cathode potential is set to the specified cell voltage. The inlet boundary conditions specify the velocity of the gas flow and the gas composition. Additionally, the electronic current density is set to zero.

$$\left\{ \begin{array}{l} \mathbf{u}_k = \text{Specified} \\ \omega_g^\alpha = \text{Specified} \\ \mathbf{J}_s \cdot \hat{\mathbf{i}} = 0 \end{array} \right\} \quad \text{Inlet}$$

At the outlet boundary condition, the flow is assumed to be fully developed. Thus, the gas mass flux and composition does not vary in the x direction. As well, the gas pressure is specified. As with the inlet boundary condition, the electronic current density is set to zero at the outlet boundary

condition.

$$\left\{ \begin{array}{l} \frac{\partial \rho_g \mathbf{u}_g}{\partial x} = 0 \\ \frac{\partial \omega_g^\alpha}{\partial x} = 0 \\ P_g = \text{Specified} \\ \mathbf{J}_s \cdot \hat{\mathbf{i}} = 0 \end{array} \right\} \quad \text{Outlet}$$

The cell voltage is an input parameter; hence, the total cell current is an output parameter in the PEM fuel cell model of this thesis.

$$I = \int_{A_{\text{bp}}} \mathbf{J}_s \cdot \hat{\mathbf{j}} dA, \quad (4.74)$$

where A_{bp} is the surface area of the bipolar plate and \mathbf{J}_s is the current density, which changes over the active cell surface.

4.7 Summary

The governing equation set consists of the conservation of mass, momentum, and species for the gas phase, and the conservation of species for the liquid electrolyte and solid phases. For the gas phase, the equations are

$$\nabla \cdot (\epsilon_g \langle \rho_g \rangle^* \langle \mathbf{u}_g \rangle^*) = \Gamma_{M,g}, \quad (4.75)$$

$$\nabla \cdot (\epsilon_g \langle \rho_g \rangle^* \langle \mathbf{u}_g \rangle^* \langle \mathbf{u}_g \rangle^*) + \nabla (\epsilon_g \langle P_g \rangle^*) - \langle P_g \rangle^* \nabla (\epsilon_g) - \nabla \cdot (\epsilon_g \langle \boldsymbol{\tau}_g \rangle^*) = \Gamma_{F,g}, \quad (4.76)$$

$$\nabla \cdot (\epsilon_g \langle \rho_g^\alpha \rangle^* \langle \mathbf{u}_g \rangle^* + \epsilon_g \langle \mathcal{J}_g^\alpha \rangle^*) = \Gamma_{S,g}^\alpha. \quad (4.77)$$

The conservation of species can be written for α corresponding to hydrogen, oxygen, water and nitrogen. Thus, the variables for the gas phase are the x and y components of velocity, the pressure, and the partial density of hydrogen, oxygen, nitrogen, and water. The solid phase conservation of

species is

$$\nabla \cdot \left(\epsilon_s \kappa_s^{\text{eff}} \nabla \langle \Phi_s \rangle^* \right) = \mathcal{F} \Gamma_{S,s}^{e-}, \quad (4.78)$$

where the only unknown is the solid potential. For the liquid phase in the electrolyte pores, the conservation of species is

$$\nabla \cdot \left(\epsilon_{\ell,e} \langle \mathcal{J}_{\ell,e}^\alpha \rangle^* \right) = \Gamma_{S,e}^\alpha, \quad (4.79)$$

where α is water and hydronium ions. The diffusional mass flux is a function of water partial density and electrolyte potential; thus, these are the unknowns.

Therefore, the set of governing equations contains a total of 10 equations. The number of primary variables, that are to be solved for, is also 10 and includes the x and y components of gas phase velocity; gas phase pressure; partial density of hydrogen, oxygen, water and nitrogen in the gas phase; potential in the solid phase; partial density of water in the liquid phase; and electrolyte potential. However, the governing equations are not continuous in the computational domain. The equations for the gas and solid phases do not exist in the polymer electrolyte layer. The polymer electrolyte and catalyst layers are the domain for the conservation of species in the liquid of the electrolyte pores.

The interfacial source terms are also discontinuous. The momentum source term, $\Gamma_{F,g}$, is zero in the gas flow channels and equal to Equation (4.10) elsewhere. The interfacial source terms in the conservation of species equations, $\Gamma_{S,g}^\alpha$ and $\Gamma_{S,e}^\alpha$, are only non-zero in the catalyst layers. All but one of the interfacial source terms can be expressed as a function of the primary variables, with the exception being $\Gamma_{S,g-e}^{\text{H}_2\text{O}}$ which represents the water transport between the gas and liquid phases. However, through the use of the relationship between membrane activity and hydration of Equation (4.42), coupled with the electrolyte acid-base relationship of Equation (4.49), the partial densities of water in the gas and liquid phases can be linked together. Thus, $\Gamma_{S,g-e}^{\text{H}_2\text{O}}$ is not required

CHAPTER 4. SIMPLIFIED FORMULATION FOR NUMERICAL IMPLEMENTATION

for the numerical solution. The details of the numerical solution are presented in the next chapter.

Chapter 5

Numerical Implementation

This chapter describes the numerical procedure used to solve the governing equations presented in the previous chapter. For the two-dimensional domain, the equation set contains the

1. x -direction conservation of momentum for the gas phase,
2. y -direction conservation of momentum for the gas phase,
3. Conservation of total mass for the gas phase,
4. Conservation of species for the gas phase,
5. Conservation of species for the liquid phase, and
6. Conservation of species for the solid phase.

Within the equation set, the independent variables are

1. x -direction gas velocity (u_g),
2. y -direction gas velocity (v_g),
3. Gas pressure (P_g),
4. Partial density of the species in the gas phase (ρ_g^α),

CHAPTER 5. NUMERICAL IMPLEMENTATION

5. Potential in the electrolyte (Φ_e), and
6. Potential in the solid phase (Φ_s).

Note that the partial density of liquid water in the electrolyte is not included in the list of independent variables: the partial densities of the water in the gas phase and in the pores of the electrolyte can be combined into one variable using the method of Kulikovsky [64]. This method is presented in detail in Section 5.6, which develops the numerical solution for the partial density of water in the gas phase.

The general numerical solution method employed to solve the governing equations is the finite volume method [120]. The fuel cell is divided into control volumes. A staggered mesh is used, whereby the velocities are defined at the faces of the control volumes and all other variables are defined at the center of the control volumes. The conservation equations are then applied to the discrete volumes, resulting in a series of algebraic equations that, when coupled with the boundary conditions, can be solved for the independent variables.

The discretized conservation equations can not be directly solved for the independent variables. Instead, an iterative, multi-level solution procedure is used. In the innermost level of iteration, each conservation equation is solved for one of the independent variables. The x - and y -direction conservation of momentum for the gas phase equations are solved for u_g and v_g , respectively. The conservation of total mass for the gas phase is solved for the pressure. For the non-water gas species, the partial densities are determined with the conservation of species equations in the gas phase. Since water exists both in the gas phase and in a liquid phase within the electrolyte pores, the equations for the conservation of water in the gas phase and electrolyte pore regions are combined into one equation that represents the total conservation of water in the PEM fuel cell. The conservation of hydronium ions in the electrolyte is solved to yield the potential in the electrolyte, while the conservation of electrons in the solid phase is used to determine the solid potential.

For the next level of iterations, the governing equations are gathered into two groups. The first group consists of the conservation of momentum and mass equations, while the second group contains all of the equations derived from the conservation of species. Keeping the partial densities and potentials constant, the momentum and mass equations are solved for the velocities and pressure sequentially using the SIMPLE algorithm [120]. Similarly, the velocities and pressure are kept constant while the conservation of species equations are solved sequentially until the partial densities and potentials are determined. The solutions of the momentum/mass and the species equation groups are alternated until all of the independent variables have converged. Then, the properties such as total density, viscosity, and diffusivity are updated and the solution procedure is repeated.

The details of this numerical solution procedure are outlined in this chapter. First, the finite volume grid is illustrated, and the general discretization procedure for the conservation equations is presented. The specific procedure for the discretization of each conservation equation is discussed and the overall numerical procedure is outlined. In this section, it is assumed that all variables are volume-averaged; hence, the volume-averaging operators, $\langle \rangle$ and $\langle \rangle^*$, are omitted.

5.1 Finite Volume Grid

The governing equations are discretized using the Finite Volume Method [120]. One continuous grid is used to mesh the entire two-dimensional domain, as illustrated in Figure 5.1. Although the grid is continuous, it can be broken into 11 distinct regions. Seven of these regions correspond to the separate components of the PEM fuel cell, which are the anode and cathode gas flow channels, electrode backing layers, catalyst layers, and the polymer electrolyte layer. In addition to the regions of the PEM fuel cell, the entrance and exit of the gas flow channels are extended in the x direction; these are the plus and minus anode or cathode extensions. These extensions are added to the grid in order to minimize the effect of the boundary conditions of the solution.

A staggered grid arrangement is used. The vector quantities, which are the velocities, are

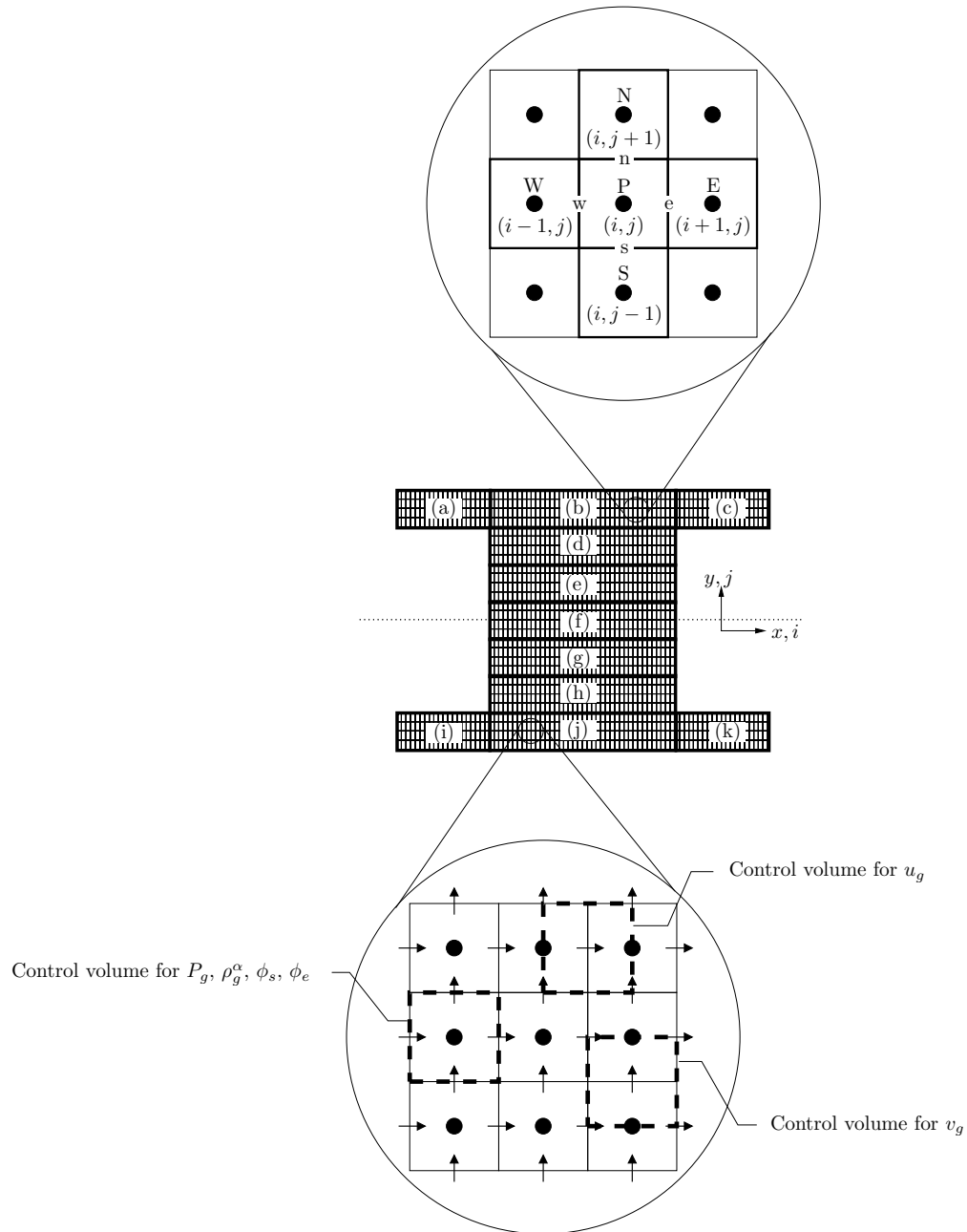


Figure 5.1: The sample grid used for the PEM fuel cell model. The grid is continuous and consists of 11 distinct regions: (a) anode minus extension, (b) anode gas flow channel, (c) anode plus extension, (d) anode electrode backing layer, (e) anode catalyst layer, (f) polymer electrolyte layer, (g) cathode catalyst layer, (h) cathode electrode backing layer, (i) cathode minus extension, (j) cathode gas flow channel, and (k) cathode plus extension. Note that the figure is not to scale, with the y direction being exaggerated in the figure.

located at the faces, while the scalar variables, which are all other variables, are located at the control volume centers. The computational molecule for a scalar control volume is also illustrated in Figure 5.1. The value of a control volume at the coordinates (i, j) , P , depends on its north (N), south (S), east (E) and west (W) neighbors. The north, south, east, and west faces of the control volume are denoted as n,s,e and w, respectively. A similar labeling convention is used for the u and v velocities.

The grid illustrated in Figure 5.1 is uniform, with each control volume having the same dimensions. For most of the simulations, however, the grid will be non-uniform. A constant expansion or contraction factor can be used such that

$$\frac{\Delta x_{i+1}}{\Delta x_i} = \beta, \quad (5.1)$$

where β is a constant. In addition, the grid spacing in each region can be independently specified.

5.2 General Discretization Methods

The Finite Volume Method involves applying a conservation equation to a discrete control volume, resulting in a balance of the inflow and outflow in the control volume. Figure 5.2 illustrates the two types of flux that are encountered in the control volume balance: convective and diffusive fluxes. The convective and diffusive fluxes are denoted by F_c and F_d , respectively. The distance from the control volume center, P , to the east control volume, E , is Δ_E , while the distance from the control volume center to the east face is Δ_e .

For a scalar quantity, ψ , the fluxes are

$$F_c|_e = u|_e \psi|_e, \quad (5.2)$$

$$F_d|_e = -\Gamma|_e \left(\frac{\psi|_E - \psi|_P}{\Delta_E} \right), \quad (5.3)$$

where $u|_e$ is velocity on the face between control volumes P and E , $\Gamma|_e$ is the diffusion coefficient

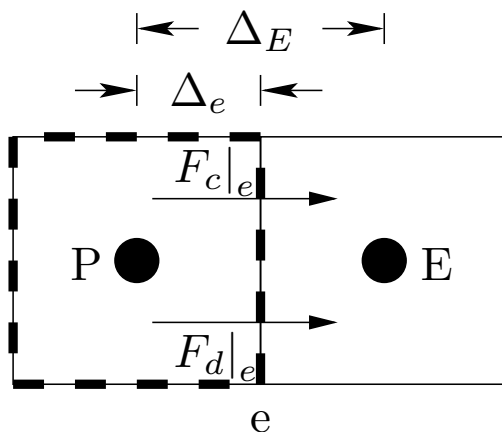


Figure 5.2: The two types of fluxes encountered in the Finite Volume Method: F_c is the convective flux, while F_d is the diffusive flux.

at the face, and Δ_E is the distance between P and W . The velocity is defined at the face, but the value of ψ is only known at the control volume centers. Typically, Γ_e is a function of ψ ; therefore it can also only be calculated at the control volume centers. Therefore, the face values must be approximated by the control volume center values. For the value of the variable, ψ , two approximations are used:

$$\psi|_e^{UDS} = \begin{cases} \psi|_P & u|_e > 0 \\ \psi|_W & u|_e < 0 \end{cases}, \quad (5.4)$$

$$\psi|_e^{CDS} = \frac{\Delta_e}{\Delta_E} \psi|_E + \left(1 - \frac{\Delta_e}{\Delta_E}\right) \psi|_P, \quad (5.5)$$

where $\psi|_e^{UDS}$ is the upwind difference scheme and $\psi|_e^{CDS}$ is the central difference scheme. The PEM fuel cell model presented in this thesis can use either the UDS or CDS approximation. In order to enhance convergence, the CDS approximation can be deferred, or lagged. This is referred as the linear deferred correction and is expressed as

$$\psi|_e^{LDC} = \psi|_e^{UDS} + \left(\psi|_e^{CDS} - \psi|_e^{UDS}\right)^{\text{old}}, \quad (5.6)$$

where the superscript, “old”, denotes a value from the previous iteration. Thus, at convergence,

the LDC approximation is equivalent to the CDS approximation.

The values of all variables except velocity are defined at the control volume centers. Therefore, properties that depend on the gas composition or pressure are also defined at the control volume centers. Thus, interpolation is frequently required. Generally, interpolation is required between two points for the scalar control volumes, and four points for the velocity control volumes. This is illustrated in Figure 5.3. Figure 5.3(a) shows that the interpolation to the face of a scalar control volume relies on the two adjacent control volume centers. However, the interpolation to the face of a velocity control volume, illustrated in Figure 5.3(b) for a u control volume, requires the values at four control volume centers. Thus, the interpolation occurs in two stages, with the first stage being an x direction interpolation, followed by a y direction interpolation.

For both the scalar and velocity control volumes, linear or geometric interpolation is used:

$$\psi_{\text{face}} = \frac{\Delta_- \psi_+ + \Delta_+ \psi_-}{\Delta_- + \Delta_+} \quad \text{Linear} \quad (5.7)$$

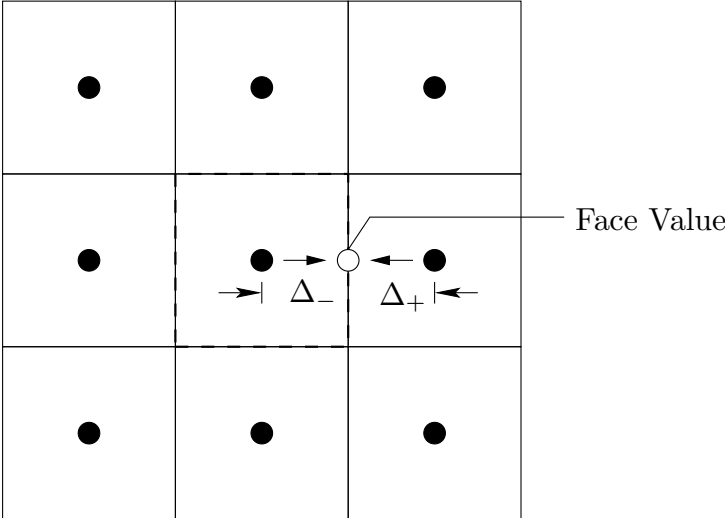
$$\psi_{\text{face}} = \frac{(\Delta_+ + \Delta_-) \psi_+ \psi_-}{\Delta_+ \psi_- + \Delta_- \psi_+} \quad \text{Geometric} \quad (5.8)$$

where Δ is the distance from the node to the face and the subscripts $+$ and $-$ denote the node in the positive or negative direction from the face.

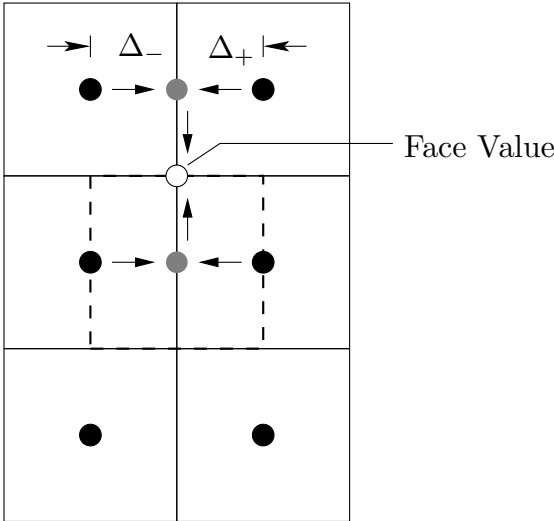
5.3 Conservation of Momentum

The balance of forces on u and v control volumes are illustrated in Figure 5.4. The forces arise from shear stresses (F_τ) and pressure (F_P). Additionally, momentum sources, denoted by S_u and S_v , are present and are the result of the Darcy term. In this section, the equation for the conservation of momentum in a u control volume is assembled; the corresponding equation for the v control volume can be derived in a similar manner.

Applying the conservation of momentum force balance to a u control volume results in



(a) Scalar control volume.



(b) Velocity control volume.

Figure 5.3: The interpolation of scalar quantities to the face of the (a) scalar and (b) velocity control volumes.

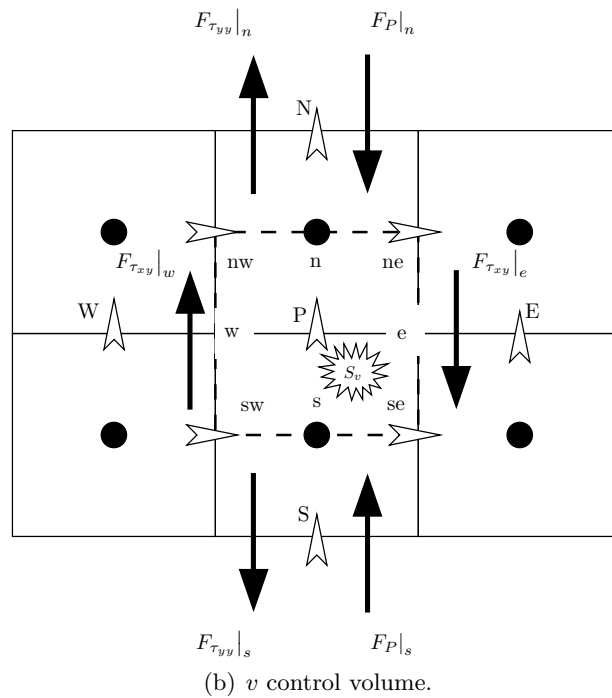
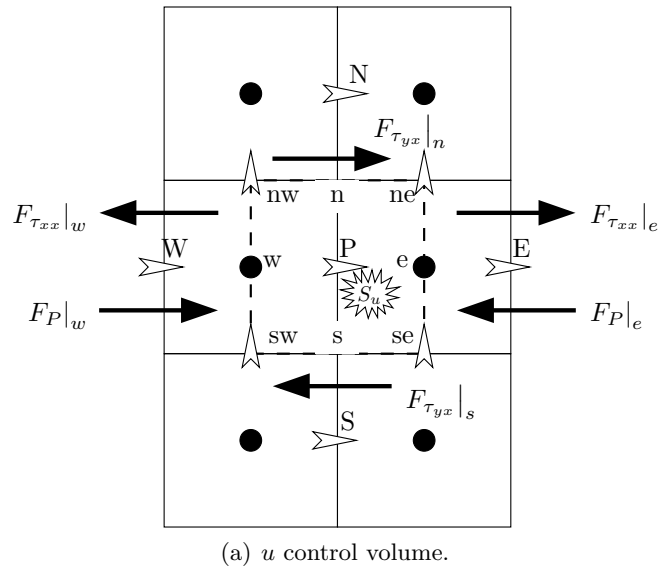


Figure 5.4: The balance of momentum forces on (a) u and (b) v control volumes.

$$\begin{aligned} \epsilon_g m_x'' u_g A_x|_e - \epsilon_g m_x'' u_g A_x|_w + \epsilon_g m_y'' u_g A_y|_n - \epsilon_g m_y'' u_g A_y|_s = F_{\tau_{xx}}|_e - F_{\tau_{xx}}|_w + F_{\tau_{yx}}|_n - F_{\tau_{yx}}|_s \\ - F_P|_e + F_P|_w + S_u|_P, \end{aligned} \quad (5.9)$$

where m_x'' and m_y'' are the mass fluxes through the x and y faces, $F_{\tau_{xx}}$ is the force due to the shear stress on the x face in the x direction, $F_{\tau_{yx}}$ is the force due to the shear stress on the y face in the x direction, F_P is the force due to pressure, and S_u is the momentum source term. The x and y face areas are denoted by A_x and A_y , respectively.

Many of the terms in Equation (5.9) are non-linear; thus, an iterative solution is required. The mass fluxes at the control volume faces are a function of the velocities:

$$m_x''|_w = \frac{1}{2} (\rho_g|_P u_g|_P + \rho_g|_W u_g|_W), \quad (5.10)$$

$$m_x''|_e = \frac{1}{2} (\rho_g|_P u_g|_P + \rho_g|_E u_g|_E), \quad (5.11)$$

$$m_y''|_n = \frac{1}{2} (\rho_g|_{nw} v_g|_{nw} + \rho_g|_{ne} v_g|_{ne}), \quad (5.12)$$

$$m_y''|_s = \frac{1}{2} (\rho_g|_{sw} v_g|_{sw} + \rho_g|_{se} v_g|_{se}), \quad (5.13)$$

where the corner values of v_g , with subscripts of sw , se , nw and ne , correspond to the centers of the v control volumes. If a linear deferred correction is used, the convection term in the east face becomes

$$m_x'' u_g A_x|_e = A_E^c|_e u_g|_E + A_P^c|_e u_g|_P + B^c|_e, \quad (5.14)$$

$$A_E^c|_e = \min(\epsilon_g|_e m_x''|_e A_x, 0),$$

$$A_P^c|_e = \max(\epsilon_g|_e m_x''|_e A_x, 0),$$

$$B^c|_e = \left[\epsilon_g|_e m_x''|_e A_x \left(u_g|_e^{CDS} - u_g|_e^{UDS} \right) \right],$$

where the A and B coefficients are calculated using velocity and property values based on the previous iteration. The expressions of $\min(a, b)$ and $\max(a, b)$ denote the maximum or minimum

values of a and b , respectively. Hence, for positive mass flux, $A_E^e|_e$ is zero. Similar terms can be written for the other faces.

The force due to the yx shear stress can be expressed as

$$F_{\tau_{yx}} = \tau_{yx}A_y = \epsilon_g\mu A_y \left(\frac{\partial u_g}{\partial y} + \frac{\partial v_g}{\partial x} \right). \quad (5.15)$$

For the north face, Equation (5.15) can be approximated with

$$\begin{aligned} F_{\tau_{yx}}|_n &= A^{\tau_{xy}}|_n (u_g|_N - u_g|_P) + B^{\tau_{xy}}|_n, \\ A^{\tau_{xy}}|_n &= \frac{\epsilon_g|_n \mu|_n A_y}{\Delta_N}, \\ B^{\tau_{xy}}|_n &= \left[\epsilon_g|_n \mu|_n A_y \left(\frac{v_g|_{ne} - v_g|_{nw}}{\Delta_e + \Delta_w} \right) \right], \end{aligned} \quad (5.16)$$

where Δ_N is the distance from the u control volumes P and N , and Δ_e and Δ_w are the distances to the east and west faces, respectively. The face value of viscosity is approximated with a geometric average.

Similarly, the force due to the shear stress on the x face can be written as

$$F_{\tau_{xx}} = \tau_{xx}A_x = \epsilon_g\mu A_x \left(\frac{\partial u_g}{\partial x} + \frac{\partial u_g}{\partial x} \right). \quad (5.17)$$

For the east face of the control volume, the discretization of Equation (5.17) results in

$$\begin{aligned} F_{\tau_{xx}}|_e &= A^{\tau_{xx}}|_e (u_g|_E - u_g|_P) + B^{\tau_{xx}}|_e, \\ A^{\tau_{xx}}|_e &= \frac{\epsilon_g|_e \mu|_e A_x}{\Delta_E}, \\ B^{\tau_{xx}}|_e &= \left[\epsilon_g|_e \mu|_e A_x \left(\frac{u_g|_E - u_g|_P}{\Delta_E} \right) \right], \end{aligned} \quad (5.18)$$

where Δ_E is the distance between the P and E velocities.

The forces due to pressure arise from the pressure gradient term in the conservation of momen-

tum:

$$F_P|_w - F_P|_e = \int_{V_{cv}} -\epsilon_g \nabla P dV, \quad (5.19)$$

where $\int_{V_{cv}}$ represents the integral over the volume of the u control volume and ϵ_g is the volume fraction of the gas phase. The volume fraction of gas is equal to one in the gas flow channels, zero in the polymer electrolyte layer, and between zero and one in the other layers of the PEM fuel cell. In order to represent the volume integral as a surface integral, all terms should be under the gradient. Therefore, Equation (5.19) is approximated with

$$\begin{aligned} F_P|_w - F_P|_e &= -\epsilon_g|_P \int_{V_{cv}} \nabla P dV, \\ &= \epsilon_g|_P P|_w A_x - \epsilon_g|_P P|_e A_x, \end{aligned} \quad (5.20)$$

where $\epsilon_g|_P$ is calculated using a linear interpolation between the scalar nodes.

The source term is due to the Darcy term, and is approximated by

$$S_u|_P = -\frac{\mu|_P (\epsilon_g|_P)^2}{K|_P} u_g|_P, \quad (5.21)$$

where $K|_P$ is approximated with a linear interpolation.

After all the terms are gathered, an equation for u_g at each control volume can be formed:

$$A_P^u u_g|_P + A_N^u u_g|_N + A_S^u u_g|_S + A_E^u u_g|_E + A_W^u u_g|_W = B_P^u. \quad (5.22)$$

The A and B coefficients are

$$A_E^u = \min(\epsilon_g|_e m_x''|_e A_x, 0) - \frac{\epsilon_g|_e \mu|_e A_x}{\Delta_E} \quad (5.23)$$

$$A_W^u = -\max(\epsilon_g|_w m_x''|_w A_x, 0) - \frac{\epsilon_g|_w \mu|_w A_x}{\Delta_W} \quad (5.24)$$

$$A_N^u = \min \left(\epsilon_g|_n m_y''|_n A_y, 0 \right) - \frac{\epsilon_g|_n \mu|_n A_y}{\Delta_N} \quad (5.25)$$

$$A_S^u = -\max \left(\epsilon_g|_s m_y''|_s A_y, 0 \right) - \frac{\epsilon_g|_s \mu|_s A_y}{\Delta_S} \quad (5.26)$$

$$\begin{aligned} A_P^u &= \max \left(\epsilon_g|_e m_x''|_e A_x, 0 \right) - \min \left(\epsilon_g|_w m_x''|_w A_x, 0 \right) + \max \left(\epsilon_g|_n m_y''|_n A_y, 0 \right) \\ &\quad - \min \left(\epsilon_g|_s m_y''|_s A_y, 0 \right) + \frac{\epsilon_g|_n \mu|_n A_y}{\Delta_N} + \frac{\epsilon_g|_s \mu|_s A_y}{\Delta_S} + \frac{\epsilon_g|_e \mu|_e A_x}{\Delta_E} + \frac{\epsilon_g|_w \mu|_w A_x}{\Delta_W} \\ &\quad + \frac{\mu|_P (\epsilon_g|_P)^2}{K|_P} \end{aligned} \quad (5.27)$$

$$\begin{aligned} B_P^u &= - \left[\epsilon_g|_e m_x''|_e A_x \left(u_g|_e^{CDS} - u_g|_e^{UDS} \right) \right] + \left[\epsilon_g|_w m_x''|_w A_x \left(u_g|_w^{CDS} - u_g|_w^{UDS} \right) \right] \\ &\quad - \left[\epsilon_g|_n m_y''|_n A_y \left(u_g|_n^{CDS} - u_g|_n^{UDS} \right) \right] + \left[\epsilon_g|_s m_y''|_s A_y \left(u_g|_s^{CDS} - u_g|_s^{UDS} \right) \right] \\ &\quad + \left[\epsilon_g|_n \mu|_n A_y \left(\frac{v_g|_{ne} - v_g|_{nw}}{\Delta_e + \Delta_w} \right) \right] - \left[\epsilon_g|_s \mu|_s A_y \left(\frac{v_g|_{se} - v_g|_{sw}}{\Delta_e + \Delta_w} \right) \right] \\ &\quad + \left[\epsilon_g|_e \mu|_e A_x \left(\frac{u_g|_E - u_g|_P}{\Delta_E} \right) \right] - \left[\epsilon_g|_w \mu|_w A_x \left(\frac{u_g|_P - u_g|_W}{\Delta_W} \right) \right] \\ &\quad + \epsilon_g|_P P|_w A_x - \epsilon_g|_P P|_e A_x \end{aligned} \quad (5.28)$$

The equation for v_g is derived in a similar manner as Equation (5.22) and the result is

$$A_P^v v_g|_P + A_N^v v_g|_N + A_S^v v_g|_S + A_E^v v_g|_E + A_W^v v_g|_W = B_P^v. \quad (5.29)$$

The A and B coefficients are

$$A_E^v = \min \left(\epsilon_g|_e m_x''|_e A_x, 0 \right) - \frac{\mu|_e A_x}{\Delta_E} \quad (5.30)$$

$$A_W^v = -\max \left(\epsilon_g|_w m_x''|_w A_x, 0 \right) - \frac{\mu|_w A_x}{\Delta_W} \quad (5.31)$$

$$A_N^v = \min \left(\epsilon_g|_n m_y''|_n A_y, 0 \right) - \frac{\mu|_n A_y}{\Delta_N} \quad (5.32)$$

$$A_S^v = -\max \left(\epsilon_g|_s m_y''|_s A_y, 0 \right) - \frac{\mu|_s A_y}{\Delta_S} \quad (5.33)$$

$$\begin{aligned}
 A_P^v &= \max(\epsilon_g|_e m_x''|_e A_x, 0) - \min(\epsilon_g|_w m_x''|_w A_x, 0) + \max(\epsilon_g|_n m_y''|_n A_y, 0) \\
 &\quad - \min(\epsilon_g|_s m_y''|_s A_y, 0) + \frac{\epsilon_g|_n \mu|_n A_y}{\Delta_N} + \frac{\epsilon_g|_s \mu|_s A_y}{\Delta_S} + \frac{\epsilon_g|_e \mu|_e A_x}{\Delta_E} + \frac{\epsilon_g|_w \mu|_w A_x}{\Delta_W} \\
 &\quad + \frac{\mu|_P (\epsilon_g|_P)^2}{K|_P}
 \end{aligned} \tag{5.34}$$

$$\begin{aligned}
 B_P^v &= - \left[\epsilon_g|_e m_x''|_e A_x (v_g|_e^{CDS} - v_g|_e^{UDS}) \right] + \left[\epsilon_g|_w m_x''|_w A_x (v_g|_w^{CDS} - v_g|_w^{UDS}) \right] \\
 &\quad - \left[\epsilon_g|_n m_y''|_n A_y (v_g|_n^{CDS} - v_g|_n^{UDS}) \right] + \left[\epsilon_g|_s m_y''|_s A_y (v_g|_s^{CDS} - v_g|_s^{UDS}) \right] \\
 &\quad + \left[\epsilon_g|_e \mu|_e A_x \left(\frac{u_g|_{ne} - u_g|_{se}}{\Delta_n + \Delta_s} \right) \right] - \left[\epsilon_g|_w \mu|_w A_x \left(\frac{u_g|_{nw} - u_g|_{sw}}{\Delta_n + \Delta_s} \right) \right] \\
 &\quad + \left[\epsilon_g|_n \mu|_n A_y \left(\frac{v_g|_N - v_g|_P}{\Delta_N} \right) \right] - \left[\epsilon_g|_s \mu|_s A_y \left(\frac{v_g|_P - v_g|_S}{\Delta_S} \right) \right] \\
 &\quad + \epsilon_g|_P P|_s A_y - \epsilon_g|_P P|_n A_y
 \end{aligned} \tag{5.35}$$

where all distances and locations are relative to the v control volume in Figure 5.4(b).

In order to improve convergence, relaxation is applied to Equation (5.22) [120]:

$$\hat{A}_P^u u_g|_P + A_N^u u_g|_N + A_S^u u_g|_S + A_E^u u_g|_E + A_W^u u_g|_W = \hat{B}_P^u, \tag{5.36}$$

where \hat{A}_P^u and \hat{B}_P^u are calculated with

$$\hat{A}_P^u = \frac{A_P^u}{\alpha_u}, \tag{5.37}$$

$$\hat{B}_P^u = B_P^u + (1 - \alpha_u) \hat{A}_P^u u_g|_P^{\text{old}}. \tag{5.38}$$

The value of the relaxation factor, α_u , is 0.8. A similar manipulation is applied to the equation for v_g .

5.4 Conservation of Species in the Gas Phase: Excluding Water

The mass balance on a control volume for a gas species, excluding water, is

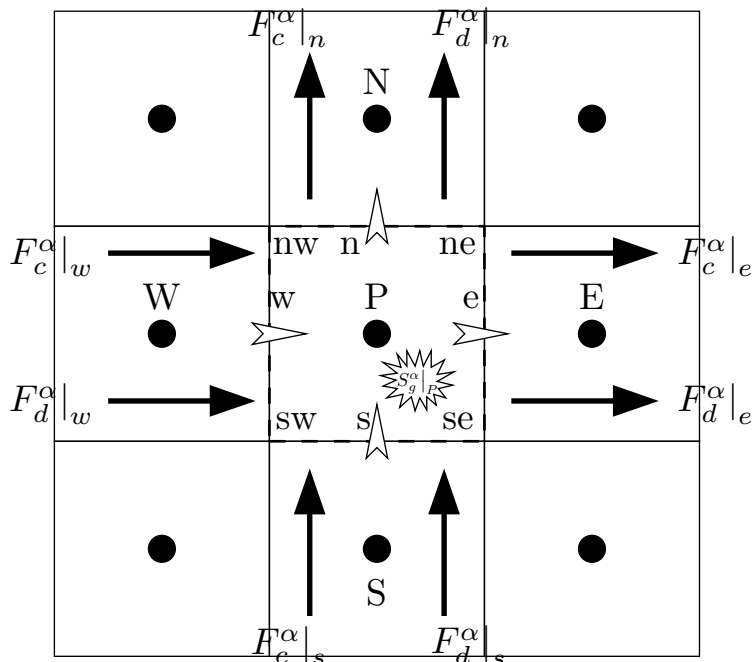


Figure 5.5: The conservation of species for the gas phase.

$$F_c^\alpha|_w - F_c^\alpha|_e + F_c^\alpha|_s - F_c^\alpha|_n + F_d^\alpha|_w - F_d^\alpha|_e + F_d^\alpha|_s - F_d^\alpha|_n + S_g^\alpha|_P = 0, \quad (5.39)$$

where F_c^α is the mass flow of species α due to convection, F_d^α is the mass flow of species α due to diffusion, and S_g^α is the production or consumption of species α . The balance of Equation (5.39) is illustrated in Figure 5.5.

For the east face, the convective mass flow can be expressed as

$$\begin{aligned} F_c^\alpha|_e &= A_E^c|_e \rho_g^\alpha|_E + A_P^c|_e \rho_g^\alpha|_P + B^c|_e, \\ A_E^c|_e &= \epsilon_g|_e \min(u_g|_e A_x, 0), \\ A_P^c|_e &= \epsilon_g|_e \max(u_g|_e A_x, 0), \\ B^c|_e &= \left[\epsilon_g|_e u_g|_e A_x \left(\rho_g^\alpha|_e^{CDS} - \rho_g^\alpha|_e^{UDS} \right) \right]^{\text{old}}, \end{aligned} \quad (5.40)$$

where the linear deferred correction is used as an illustration. Similar expressions can be written for the convective flow through the other faces. The partial density is used as the variable, and

not the mass fraction. This is because during iteration, the sum of the partial densities may not add to the total density, and thus the sum of the mass fractions may not be one. This can cause oscillation or divergence during iterations, which is avoided by using partial density.

In general, the diffusional mass flow is

$$F_d^\alpha = \mathcal{J}_g^\alpha A, \quad (5.41)$$

where A is the face area. The \mathcal{J}_g^α are defined by the inverted Stefan-Maxwell equations, Equation (4.9). For the east face, the diffusional flux is

$$\begin{aligned} F_d^\alpha|_e &= A_d^\alpha|_e \left(\rho_g^\alpha|_E - \rho_g^\alpha|_P \right) + B_d^\alpha|_e \\ A_d^\alpha|_e &= -\frac{\epsilon_g|_e D_{\alpha-g}^{\text{eff}}|_e A_x}{\Delta_E} \\ B_d^\alpha|_e &= \frac{\epsilon_g|_e \omega_g^\alpha|_e D_{\alpha-g}^{\text{eff}}|_e}{\left(1 - x_g^\alpha|_e\right)} \sum_{\beta \neq \alpha} \left[\frac{\rho_g|_e \hat{M}_g}{\hat{M}_\beta} \nabla \omega_g^\beta|_e + \frac{\hat{M}_g \mathcal{J}_g^\beta|_e}{\hat{M}_\beta \mathcal{D}_{\alpha-\beta,g}^{\text{eff}}|_e} \right] A_x - \epsilon_g|_e \omega_g^\alpha|_e D_{\alpha-g}^{\text{eff}}|_e \nabla \rho_g|_e A_x \end{aligned} \quad (5.42)$$

where all terms in the $A_d^\alpha|_e$ and $B_d^\alpha|_e$ are lagged. The face values of the mass and mole fractions are approximated by a linear interpolation. The face value of the diffusion coefficient is calculated with the face values of the mole fractions and Equation (4.7). The diffusion fluxes are also a function of the face values of mole and mass fraction, through Equation (4.6)

The source term in Equation (5.39) is due to the electro-chemical reactions in the catalyst layers. The reaction rates can be non-linear; hence, linearization is used and the source term is expressed as

$$\begin{aligned} S_g^\alpha|_P &= A_S^\alpha|_P \rho_g^\alpha|_P + B_S^\alpha|_P \\ A_S^\alpha|_P &= V_{CV} \hat{M}_\alpha A_v \frac{\partial \dot{\mathcal{P}}^\alpha}{\partial \rho_\alpha} \\ B_S^\alpha|_P &= V_{CV} \hat{M}_\alpha A_v \left[\dot{\mathcal{P}}^\alpha - \frac{\partial \dot{\mathcal{P}}^\alpha}{\partial \rho_\alpha} \rho_{\alpha|P}^{\text{old}} \right] \end{aligned} \quad (5.43)$$

where V_{CV} is the volume of the P control volume. The reaction rates in the cathode and anode are functions of the concentration; however, using the chain rule, they can be converted to functions of partial density:

$$\frac{\partial \dot{\mathcal{P}}^\alpha}{\partial \rho_\alpha} = \hat{M}_\alpha \frac{\partial \dot{\mathcal{P}}^\alpha}{\partial c_\alpha}. \quad (5.44)$$

After assembling Equation (5.39), the following equation for each control volume can be written:

$$A_P^{\rho_g^\alpha} \rho_g^\alpha|_P + A_N^{\rho_g^\alpha} \rho_g^\alpha|_N + A_S^{\rho_g^\alpha} \rho_g^\alpha|_S + A_E^{\rho_g^\alpha} \rho_g^\alpha|_E + A_W^{\rho_g^\alpha} \rho_g^\alpha|_W = B_P^{\rho_g^\alpha}, \quad (5.45)$$

where the A and B coefficients are defined by

$$A_E^{\rho_g^\alpha} = -\epsilon_g|_e \min(u_g|_e A_x, 0) + \frac{\epsilon_g|_e D_{\alpha-g}^{\text{eff}}|_e A_x}{\Delta_E} \quad (5.46)$$

$$A_W^{\rho_g^\alpha} = \epsilon_g|_w \max(u_g|_w A_x, 0) + \frac{\epsilon_g|_w D_{\alpha-g}^{\text{eff}}|_w A_x}{\Delta_W} \quad (5.47)$$

$$A_N^{\rho_g^\alpha} = -\epsilon_g|_n \min(v_g|_n A_y, 0) + \frac{\epsilon_g|_n D_{\alpha-g}^{\text{eff}}|_n A_y}{\Delta_N} \quad (5.48)$$

$$A_S^{\rho_g^\alpha} = \epsilon_g|_s \max(u_g|_s A_x, 0) + \frac{\epsilon_g|_s D_{\alpha-g}^{\text{eff}}|_s A_y}{\Delta_S} \quad (5.49)$$

$$\begin{aligned} A_P^{\rho_g^\alpha} = & -\epsilon_g|_e \max(u_g|_e A_x, 0) + \epsilon_g|_w \min(u_g|_w A_x, 0) - \epsilon_g|_n \max(v_g|_n A_y, 0) \\ & + \epsilon_g|_s \min(u_g|_s A_x, 0) - \frac{\epsilon_g|_e D_{\alpha-g}^{\text{eff}}|_e A_x}{\Delta_E} - \frac{\epsilon_g|_w D_{\alpha-g}^{\text{eff}}|_w A_x}{\Delta_W} - \frac{\epsilon_g|_n D_{\alpha-g}^{\text{eff}}|_n A_y}{\Delta_N} \\ & - \frac{\epsilon_g|_s D_{\alpha-g}^{\text{eff}}|_s A_y}{\Delta_S} - V_{CV} \hat{M}_\alpha A_v \frac{\partial \dot{\mathcal{P}}^\alpha}{\partial \rho_\alpha} \end{aligned} \quad (5.50)$$

$$\begin{aligned}
 B_P^{\rho_g^\alpha} = & \left[\epsilon_g|_e u_g|_e A_x \left(\rho_g^\alpha|_e^{CDS} - \rho_g^\alpha|_e^{UDS} \right) \right]^{\text{old}} - \left[\epsilon_g|_w u_g|_w A_x \left(\rho_g^\alpha|_w^{CDS} - \rho_g^\alpha|_w^{UDS} \right) \right]^{\text{old}} \quad (5.51) \\
 & + \left[\epsilon_g|_n v_g|_n A_x \left(\rho_g^\alpha|_n^{CDS} - \rho_g^\alpha|_n^{UDS} \right) \right]^{\text{old}} - \left[\epsilon_g|_s v_g|_s A_x \left(\rho_g^\alpha|_s^{CDS} - \rho_g^\alpha|_s^{UDS} \right) \right]^{\text{old}} \\
 & + \frac{\epsilon_g|_e \omega_g^\alpha|_e D_{\alpha-g}^{\text{eff}}|_e}{\left(1 - x_g^\alpha|_e\right)} \sum_{\beta \neq \alpha} \left[\frac{\rho_g|_e \hat{M}_g}{\hat{M}_\beta} \nabla \omega_g^\beta|_e + \frac{\hat{M}_g \mathcal{J}_g^\beta|_e}{\hat{M}_\beta \mathcal{D}_{\alpha-\beta,g}^{\text{eff}}|_e} \right] A_x - \epsilon_g|_e \omega_g^\alpha|_e D_{\alpha-g}^{\text{eff}}|_e \nabla \rho_g|_e A_x \\
 & - \frac{\epsilon_g|_w \omega_g^\alpha|_w D_{\alpha-g}^{\text{eff}}|_w}{\left(1 - x_g^\alpha|_w\right)} \sum_{\beta \neq \alpha} \left[\frac{\rho_g|_w \hat{M}_g}{\hat{M}_\beta} \nabla \omega_g^\beta|_w + \frac{\hat{M}_g \mathcal{J}_g^\beta|_w}{\hat{M}_\beta \mathcal{D}_{\alpha-\beta,g}^{\text{eff}}|_w} \right] A_x + \epsilon_g|_w \omega_g^\alpha|_w D_{\alpha-g}^{\text{eff}}|_w \nabla \rho_g|_w A_x \\
 & + \frac{\epsilon_g|_n \omega_g^\alpha|_n D_{\alpha-g}^{\text{eff}}|_n}{\left(1 - x_g^\alpha|_n\right)} \sum_{\beta \neq \alpha} \left[\frac{\rho_g|_n \hat{M}_g}{\hat{M}_\beta} \nabla \omega_g^\beta|_n + \frac{\hat{M}_g \mathcal{J}_g^\beta|_n}{\hat{M}_\beta \mathcal{D}_{\alpha-\beta,g}^{\text{eff}}|_n} \right] A_y - \epsilon_g|_n \omega_g^\alpha|_n D_{\alpha-g}^{\text{eff}}|_n \nabla \rho_g|_n A_y \\
 & - \frac{\epsilon_g|_s \omega_g^\alpha|_s D_{\alpha-g}^{\text{eff}}|_s}{\left(1 - x_g^\alpha|_s\right)} \sum_{\beta \neq \alpha} \left[\frac{\rho_g|_s \hat{M}_g}{\hat{M}_\beta} \nabla \omega_g^\beta|_s + \frac{\hat{M}_g \mathcal{J}_g^\beta|_s}{\hat{M}_\beta \mathcal{D}_{\alpha-\beta,g}^{\text{eff}}|_s} \right] A_y + \epsilon_g|_s \omega_g^\alpha|_s D_{\alpha-g}^{\text{eff}}|_s \nabla \rho_g|_s A_y \\
 & - V_{CV} \hat{M}_\alpha A_v \left[\dot{\mathcal{P}}^\alpha - \frac{\partial \dot{\mathcal{P}}^\alpha}{\partial \rho_\alpha} \rho_\alpha|_P^{\text{old}} \right]
 \end{aligned}$$

5.5 Conservation of Species in the Electrolyte Pores: Hydronium

The species balance for the electrolyte species is similar to the gas species, except that there is no convective flux:

$$F_d^\alpha|_w - F_d^\alpha|_e + F_d^\alpha|_s - F_d^\alpha|_n + S_{\ell,e}^\alpha|_P = 0. \quad (5.52)$$

The balance of Equation (5.52) is illustrated in Figure 5.6.

For the hydronium ions, the mass flow rate at the east face is

$$\begin{aligned}
 F_d^{\text{H}_3\text{O}^+}|_e &= A_d^{\text{H}_3\text{O}^+}|_e \left(\rho_g^{\text{H}_3\text{O}^+}|_E - \rho_g^{\text{H}_3\text{O}^+}|_P \right) + B_d^{\text{H}_3\text{O}^+}|_e \quad (5.53) \\
 A_d^{\text{H}_3\text{O}^+}|_e &= \frac{\epsilon_{\ell,e}|_e \mathcal{D}_{\text{H}_3\text{O}^+}^{\text{H}_3\text{O}^+}|_e A_x}{\Delta_E} \\
 B_d^{\text{H}_3\text{O}^+}|_e &= \frac{\epsilon_{\ell,e}|_e \mathcal{D}_{\text{H}_2\text{O}}^{\text{H}_3\text{O}^+}|_e}{\rho_{\ell,e}|_e} \nabla \rho_{\ell,e}^{\text{H}_2\text{O}}|_e A_x - \frac{\epsilon_{\ell,e}|_e \mathcal{D}_{\text{H}_2\text{O}}^{\text{H}_3\text{O}^+}|_e}{\rho_{\ell,e}|_e} \nabla \rho_{\ell,e}|_e A_x
 \end{aligned}$$

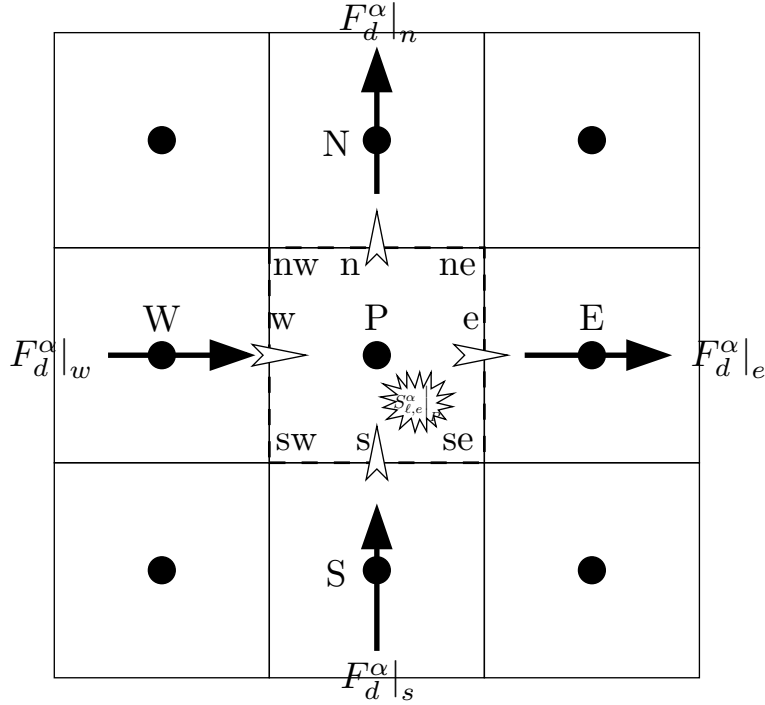


Figure 5.6: The conservation of species for the liquid in the electrolyte pores.

The source term representing the rate of production of hydronium due to the electro-chemical reactions in the catalyst layers is

$$\begin{aligned}
 S_{\ell,e}^{\text{H}_3\text{O}^+} \Big|_P &= A_S^{\text{H}_3\text{O}^+} \Big|_P \rho_g^{\text{H}_3\text{O}^+} \Big|_P + B_S^{\text{H}_3\text{O}^+} \Big|_P \\
 A_S^{\text{H}_3\text{O}^+} \Big|_P &= V_{CV} \hat{M}_{\text{H}_3\text{O}^+} A_v \frac{\partial \dot{\mathcal{P}}^{\text{H}_3\text{O}^+}}{\partial \Phi_e} \\
 B_S^{\text{H}_3\text{O}^+} \Big|_P &= V_{CV} \hat{M}_{\text{H}_3\text{O}^+} A_v \left[\dot{\mathcal{P}}^{\text{H}_3\text{O}^+} - \frac{\partial \dot{\mathcal{P}}^{\text{H}_3\text{O}^+}}{\partial \Phi_e} \Phi_e \Big|_P^{\text{old}} \right]
 \end{aligned} \tag{5.54}$$

After assembling Equation (5.52), the following equation for each control volume can be written:

$$A_P^{\Phi_e} \Phi_e \Big|_P + A_N^{\Phi_e} \Phi_e \Big|_N + A_S^{\Phi_e} \Phi_e \Big|_S + A_E^{\Phi_e} \Phi_e \Big|_E + A_W^{\Phi_e} \Phi_e \Big|_W = B_P^{\Phi_e}. \tag{5.55}$$

The A and B coefficients are defined by

$$A_E^{\Phi_e} = -\frac{\epsilon_{\ell,e}|_e \mathcal{D}_{\text{H}_3\text{O}^+}^{\text{H}_3\text{O}^+}|_e A_x}{\Delta_E} \quad (5.56)$$

$$A_W^{\Phi_e} = -\frac{\epsilon_{\ell,e}|_w \mathcal{D}_{\text{H}_3\text{O}^+}^{\text{H}_3\text{O}^+}|_w A_x}{\Delta_W} \quad (5.57)$$

$$A_N^{\Phi_e} = -\frac{\epsilon_{\ell,e}|_n \mathcal{D}_{\text{H}_3\text{O}^+}^{\text{H}_3\text{O}^+}|_n A_y}{\Delta_N} \quad (5.58)$$

$$A_S^{\Phi_e} = -\frac{\epsilon_{\ell,e}|_s \mathcal{D}_{\text{H}_3\text{O}^+}^{\text{H}_3\text{O}^+}|_s A_y}{\Delta_S} \quad (5.59)$$

$$A_P^{\Phi_e} = +\frac{\epsilon_{\ell,e}|_e \mathcal{D}_{\text{H}_3\text{O}^+}^{\text{H}_3\text{O}^+}|_e A_x}{\Delta_E} + \frac{\epsilon_{\ell,e}|_w \mathcal{D}_{\text{H}_3\text{O}^+}^{\text{H}_3\text{O}^+}|_w A_x}{\Delta_W} + \frac{\epsilon_{\ell,e}|_n \mathcal{D}_{\text{H}_3\text{O}^+}^{\text{H}_3\text{O}^+}|_n A_y}{\Delta_N} \quad (5.60)$$

$$\begin{aligned} & + \frac{\epsilon_{\ell,e}|_s \mathcal{D}_{\text{H}_3\text{O}^+}^{\text{H}_3\text{O}^+}|_s A_y}{\Delta_S} + V_{CV} A_v \hat{M}_{\text{H}_3\text{O}^+} \frac{\partial \dot{\mathcal{P}}^{\text{H}_3\text{O}^+}}{\partial \Phi_e} \\ B_P^{\Phi_e} = & \frac{\epsilon_{\ell,e}|_e \mathcal{D}_{\text{H}_2\text{O}}^{\text{H}_3\text{O}^+}|_e \nabla \rho_{\ell,e}^{\text{H}_2\text{O}}|_e A_x - \frac{\epsilon_{\ell,e}|_e \mathcal{D}_{\text{H}_2\text{O}}^{\text{H}_3\text{O}^+}|_e \nabla \rho_{\ell,e}|_e A_x}{\rho_{\ell,e}|_e} \\ & - \frac{\epsilon_{\ell,e}|_w \mathcal{D}_{\text{H}_2\text{O}}^{\text{H}_3\text{O}^+}|_w \nabla \rho_{\ell,e}^{\text{H}_2\text{O}}|_w A_x - \frac{\epsilon_{\ell,e}|_w \mathcal{D}_{\text{H}_2\text{O}}^{\text{H}_3\text{O}^+}|_w \nabla \rho_{\ell,e}|_w A_x}{\rho_{\ell,e}|_w} \\ & + \frac{\epsilon_{\ell,e}|_n \mathcal{D}_{\text{H}_2\text{O}}^{\text{H}_3\text{O}^+}|_n \nabla \rho_{\ell,e}^{\text{H}_2\text{O}}|_n A_y - \frac{\epsilon_{\ell,e}|_n \mathcal{D}_{\text{H}_2\text{O}}^{\text{H}_3\text{O}^+}|_n \nabla \rho_{\ell,e}|_n A_y}{\rho_{\ell,e}|_n} \\ & + \frac{\epsilon_{\ell,e}|_s \mathcal{D}_{\text{H}_2\text{O}}^{\text{H}_3\text{O}^+}|_s \nabla \rho_{\ell,e}^{\text{H}_2\text{O}}|_s A_y - \frac{\epsilon_{\ell,e}|_s \mathcal{D}_{\text{H}_2\text{O}}^{\text{H}_3\text{O}^+}|_s \nabla \rho_{\ell,e}|_s A_y}{\rho_{\ell,e}|_s} \\ & - V_{CV} \hat{M}_{\text{H}_3\text{O}^+} A_v \left[\dot{\mathcal{P}}^{\text{H}_3\text{O}^+} - \frac{\partial \dot{\mathcal{P}}^{\text{H}_3\text{O}^+}}{\partial \Phi_e} \Phi_e|_P^{\text{old}} \right] \end{aligned} \quad (5.61)$$

5.6 Conservation of Species: Water

Water is present in both the gas and electrolyte. Therefore, the conservation of water in the gas and liquid phases are combined to form the conservation of total water:

$$F_T^{\text{H}_2\text{O}}|_w - F_T^{\text{H}_2\text{O}}|_e + F_T^{\text{H}_2\text{O}}|_s - F_T^{\text{H}_2\text{O}}|_n + S^{\text{H}_2\text{O}}|_P = 0 \quad (5.62)$$

CHAPTER 5. NUMERICAL IMPLEMENTATION

where $F_T^{\text{H}_2\text{O}}$ is the total mass flow of water through a face. It includes the contribution of the gas and electrolyte flows:

$$F_T^{\text{H}_2\text{O}} = F_c^{\text{H}_2\text{O}(\text{g})} + F_d^{\text{H}_2\text{O}(\text{g})} + F_d^{\text{H}_2\text{O}(\ell)} \quad (5.63)$$

In order to solve Equation (5.62), $F_T^{\text{H}_2\text{O}}$ must be in terms of one variable. The water in the electrolyte and gas are assumed to be in equilibrium; hence, it is possible to construct a function such that

$$\rho_{\ell,e}^{\text{H}_2\text{O}} = f(\rho_g^{\text{H}_2\text{O}}) \quad (5.64)$$

Equation (5.64) can be constructed by noting the concentrations of water in the gas and electrolyte can be related to the membrane activity, or relative humidity. The membrane activity is related to the partial density in the gas phase with

$$\tilde{a} = \frac{\rho_g^{\text{H}_2\text{O}}}{\rho_{g,\text{sat}}^{\text{H}_2\text{O}}(T)}, \quad (5.65)$$

where $\rho_{g,\text{sat}}^{\text{H}_2\text{O}}(T)$ is the saturation density of water vapor at the temperature, T .

The partial density of water in the electrolyte is also related to the membrane activity, although it can not be expressed in an explicit formula such as Equation (5.65). Using Equation (4.42), the membrane activity can be used to determine the membrane hydration. The membrane hydration, in conjunction with the acid-base equilibrium relationships of Equations (4.49) to (4.56), yields the concentrations of water and hydronium. From the molar concentrations, the partial density can then be determined. The relationship between the activity and the partial density of water in the electrolyte does not have an analytical form, but can be calculated numerically for a constant temperature. The relationship between the activity and partial density of water for the electrolyte is illustrated in Figure 5.7. In order to reduce computational time, the curves of Figure 5.7 are approximated with a Chebyshev function [121]. This approximation also has the advantage of

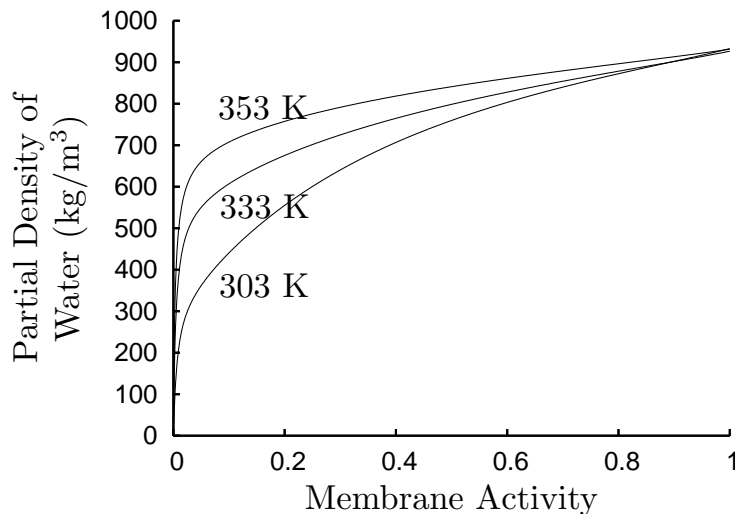


Figure 5.7: The partial density of water in the electrolyte as a function of membrane activity for the temperatures of 303 K, 333 K, and 353 K.

allowing for the calculation of the derivatives.

With the relationships previously discussed, the partial density of water in the gas phase and the partial density of water in the electrolyte can be used interchangeably through the use of membrane activity:

$$\rho_g^{\text{H}_2\text{O}} \longleftrightarrow \tilde{a} \longleftrightarrow \rho_{\ell,e}^{\text{H}_2\text{O}}.$$

Thus, the partial density of water in the electrolyte can be expressed as a function of the partial density of water in the gas phase, as in Equation (5.64). Examining Equation (5.63), both $F_c^{\text{H}_2\text{O}(\text{g})}$ and $F_d^{\text{H}_2\text{O}(\text{g})}$ are functions of $\rho_g^{\text{H}_2\text{O}}$; however, $F_d^{\text{H}_2\text{O}(\ell)}$ is a function of $\rho_{\ell,e}^{\text{H}_2\text{O}}$ and must therefore be converted into a function of $\rho_g^{\text{H}_2\text{O}}$. This can be done with Equation (4.36) and the chain rule [113]:

$$\mathcal{J}_{\ell,e}^{\text{H}_2\text{O}} = \frac{\mathcal{D}_{\text{H}_2\text{O}}^{\text{H}_2\text{O}}}{\rho_{\ell,e}} \left(\frac{\partial \rho_{\ell,e}^{\text{H}_2\text{O}}}{\partial \rho_g^{\text{H}_2\text{O}}} \right) \nabla \rho_g^{\text{H}_2\text{O}} + \mathcal{D}_{\text{H}_3\text{O}^+}^{\text{H}_2\text{O}} \nabla \Phi_e - \frac{\omega_{\ell,e}^{\text{H}_2\text{O}} \mathcal{D}_{\text{H}_2\text{O}}^{\text{H}_2\text{O}}}{\rho_{\ell,e}} \nabla \rho_{\ell,e}, \quad (5.66)$$

where the derivative of water partial density in the electrolyte with respect to the partial density

of water in the gas phase is

$$\frac{\partial \rho_{\ell,e}^{\text{H}_2\text{O}}}{\partial \rho_g^{\text{H}_2\text{O}}} = \frac{\partial \rho_{\ell,e}^{\text{H}_2\text{O}}}{\partial \tilde{a}} \frac{\partial \tilde{a}}{\partial \rho_g^{\text{H}_2\text{O}}}, \quad (5.67)$$

$$\frac{\partial \rho_{\ell,e}^{\text{H}_2\text{O}}}{\partial \tilde{a}} = \text{Slope of Figure 5.7}, \quad (5.68)$$

$$\frac{\partial \tilde{a}}{\partial \rho_g^{\text{H}_2\text{O}}} = \frac{1}{\rho_{g,\text{sat}}(T)}. \quad (5.69)$$

Thus, all terms in Equation (5.63) are functions of $\rho_g^{\text{H}_2\text{O}}$. The gas phase mass flows, $F_c^{\text{H}_2\text{O}(\text{g})}$ and $F_d^{\text{H}_2\text{O}(\text{g})}$, can be expressed with Equations (5.40) and (5.42), respectively. The flow of water in the electrolyte is expressed as

$$F_d^{\text{H}_2\text{O}(\ell)} \Big|_e = A_d^{\text{H}_2\text{O}} \Big|_e \left(\rho_g^{\text{H}_2\text{O}} \Big|_E - \rho_g^{\text{H}_2\text{O}} \Big|_P \right) + B_d^{\text{H}_2\text{O}} \Big|_e, \quad (5.70)$$

$$A_d^{\text{H}_2\text{O}(\ell)} \Big|_e = \frac{\epsilon_{\ell,e} \Big|_e \mathcal{D}_{\text{H}_2\text{O}}^{\text{H}_2\text{O}} \Big|_e \left(\frac{\partial \rho_{\ell,e}^{\text{H}_2\text{O}}}{\partial \rho_g^{\text{H}_2\text{O}}} \right) \Big|_e A_x}{\rho_{\ell,e} \Big|_e \Delta E},$$

$$B_d^{\text{H}_2\text{O}(\ell)} \Big|_e = \epsilon_{\ell,e} \Big|_e \mathcal{D}_{\text{H}_3\text{O}^+}^{\text{H}_2\text{O}} \Big|_e \nabla \Phi_e \Big|_e A_x - \frac{\epsilon_{\ell,e} \Big|_e \mathcal{D}_{\text{H}_2\text{O}}^{\text{H}_2\text{O}} \Big|_e \omega_{\ell,e}^{\text{H}_2\text{O}} \Big|_e}{\rho_{\ell,e} \Big|_e} \nabla \rho_{\ell,e} \Big|_e A_x.$$

The source term is similar to the species in the gas phase, with

$$S^{\text{H}_2\text{O}} \Big|_P = A_S^{\text{H}_2\text{O}} \Big|_P \rho_g^{\text{H}_2\text{O}} \Big|_P + B_S^{\text{H}_2\text{O}} \Big|_P \quad (5.71)$$

$$A_S^{\text{H}_2\text{O}} \Big|_P = V_{CV} \hat{M}_{\text{H}_2\text{O}} A_v \frac{\partial \dot{\mathcal{P}}^{\text{H}_2\text{O}}}{\partial \rho_{\ell,e}^{\text{H}_2\text{O}}} \frac{\partial \rho_g^{\text{H}_2\text{O}}}{\partial \rho_{\ell,e}^{\text{H}_2\text{O}}}$$

$$B_S^{\text{H}_2\text{O}} \Big|_P = V_{CV} \hat{M}_{\text{H}_2\text{O}} A_v \left[\dot{\mathcal{P}}^{\text{H}_2\text{O}} - \frac{\partial \dot{\mathcal{P}}^{\text{H}_2\text{O}}}{\partial \rho_{\text{H}_2\text{O}}} \frac{\partial \rho_g^{\text{H}_2\text{O}}}{\partial \rho_{\ell,e}^{\text{H}_2\text{O}}} \rho_g^{\text{H}_2\text{O}} \Big|_P^{\text{old}} \right]$$

where the derivative of the partial density of water in the gas phase with respect to the partial density of water in the electrolyte can be determined with Equation (5.67). After assembling Equation (5.62), the water balance for each control volume can be written as

$$A_P^{\rho_g^{\text{H}_2\text{O}}} \rho_g^{\text{H}_2\text{O}}|_P + A_N^{\rho_g^{\text{H}_2\text{O}}} \rho_g^{\text{H}_2\text{O}}|_N + A_S^{\rho_g^{\text{H}_2\text{O}}} \rho_g^{\text{H}_2\text{O}}|_S + A_E^{\rho_g^{\text{H}_2\text{O}}} \rho_g^{\text{H}_2\text{O}}|_E + A_W^{\rho_g^{\text{H}_2\text{O}}} \rho_g^{\text{H}_2\text{O}}|_W = B_P^{\rho_g^{\text{H}_2\text{O}}}. \quad (5.72)$$

The A and B coefficients are

$$A_E^{\rho_g^{\text{H}_2\text{O}}} = -\epsilon_g|_e \min(u_g|_e A_x, 0) + \frac{\epsilon_g|_e D_{\text{H}_2\text{O}-g}^{\text{eff}}|_e A_x}{\Delta_E} - \frac{\epsilon_{\ell,e}|_e \mathcal{D}_{\text{H}_2\text{O}}^{\text{H}_2\text{O}}|_e \left(\frac{\partial \rho_{\ell,e}^{\text{H}_2\text{O}}}{\partial \rho_g^{\text{H}_2\text{O}}} \right)|_e A_x}{\rho_{\ell,e}|_e \Delta_E} \quad (5.73)$$

$$A_W^{\rho_g^{\text{H}_2\text{O}}} = \epsilon_g|_w \max(u_g|_w A_x, 0) + \frac{\epsilon_g|_w D_{\text{H}_2\text{O}-g}^{\text{eff}}|_w A_x}{\Delta_W} - \frac{\epsilon_{\ell,e}|_w \mathcal{D}_{\text{H}_2\text{O}}^{\text{H}_2\text{O}}|_w \left(\frac{\partial \rho_{\ell,e}^{\text{H}_2\text{O}}}{\partial \rho_g^{\text{H}_2\text{O}}} \right)|_w A_x}{\rho_{\ell,e}|_w \Delta_W} \quad (5.74)$$

$$A_N^{\rho_g^{\text{H}_2\text{O}}} = -\epsilon_g|_n \min(v_g|_n A_y, 0) + \frac{\epsilon_g|_n D_{\text{H}_2\text{O}-g}^{\text{eff}}|_n A_y}{\Delta_N} - \frac{\epsilon_{\ell,e}|_n \mathcal{D}_{\text{H}_2\text{O}}^{\text{H}_2\text{O}}|_n \left(\frac{\partial \rho_{\ell,e}^{\text{H}_2\text{O}}}{\partial \rho_g^{\text{H}_2\text{O}}} \right)|_n A_x}{\rho_{\ell,e}|_n \Delta_N} \quad (5.75)$$

$$A_S^{\rho_g^{\text{H}_2\text{O}}} = \epsilon_g|_s \max(u_g|_s A_x, 0) + \frac{\epsilon_g|_s D_{\text{H}_2\text{O}-g}^{\text{eff}}|_s A_y}{\Delta_S} - \frac{\epsilon_{\ell,e}|_s \mathcal{D}_{\text{H}_2\text{O}}^{\text{H}_2\text{O}}|_s \left(\frac{\partial \rho_{\ell,e}^{\text{H}_2\text{O}}}{\partial \rho_g^{\text{H}_2\text{O}}} \right)|_s A_x}{\rho_{\ell,e}|_s \Delta_S} \quad (5.76)$$

$$\begin{aligned} A_P^{\rho_g^{\text{H}_2\text{O}}} &= -\epsilon_g|_e \max(u_g|_e A_x, 0) + \epsilon_g|_w \min(u_g|_w A_x, 0) - \epsilon_g|_n \max(v_g|_n A_y, 0) \quad (5.77) \\ &+ \epsilon_g|_s \min(u_g|_s A_x, 0) - \frac{\epsilon_g|_e D_{\text{H}_2\text{O}-g}^{\text{eff}}|_e A_x}{\Delta_E} - \frac{\epsilon_g|_w D_{\text{H}_2\text{O}-g}^{\text{eff}}|_w A_x}{\Delta_W} \\ &- \frac{\epsilon_g|_n D_{\text{H}_2\text{O}-g}^{\text{eff}}|_n A_y}{\Delta_N} - \frac{\epsilon_g|_s D_{\text{H}_2\text{O}-g}^{\text{eff}}|_s A_y}{\Delta_S} + \frac{\epsilon_{\ell,e}|_e \mathcal{D}_{\text{H}_2\text{O}}^{\text{H}_2\text{O}}|_e \left(\frac{\partial \rho_{\ell,e}^{\text{H}_2\text{O}}}{\partial \rho_g^{\text{H}_2\text{O}}} \right)|_e A_x}{\rho_{\ell,e}|_e \Delta_E} \\ &+ \frac{\epsilon_{\ell,e}|_w \mathcal{D}_{\text{H}_2\text{O}}^{\text{H}_2\text{O}}|_w \left(\frac{\partial \rho_{\ell,e}^{\text{H}_2\text{O}}}{\partial \rho_g^{\text{H}_2\text{O}}} \right)|_w A_x}{\rho_{\ell,e}|_w \Delta_W} + \frac{\epsilon_{\ell,e}|_n \mathcal{D}_{\text{H}_2\text{O}}^{\text{H}_2\text{O}}|_n \left(\frac{\partial \rho_{\ell,e}^{\text{H}_2\text{O}}}{\partial \rho_g^{\text{H}_2\text{O}}} \right)|_n A_y}{\rho_{\ell,e}|_n \Delta_N} \\ &+ \frac{\epsilon_{\ell,e}|_s \mathcal{D}_{\text{H}_2\text{O}}^{\text{H}_2\text{O}}|_s \left(\frac{\partial \rho_{\ell,e}^{\text{H}_2\text{O}}}{\partial \rho_g^{\text{H}_2\text{O}}} \right)|_s A_y}{\rho_{\ell,e}|_s \Delta_S} - V_{CV} \hat{M}_{\text{H}_2\text{O}} A_v \frac{\partial \dot{\mathcal{F}}_{\text{H}_2\text{O}}}{\partial \rho_{\text{H}_2\text{O}}} \end{aligned}$$

$$\begin{aligned}
 B_P^{\rho_g^{\text{H}_2\text{O}}} &= \left[\epsilon_g|_e u_g|_e A_x \left(\rho_g^{\text{H}_2\text{O}}|_e^{\text{CDS}} - \rho_g^{\text{H}_2\text{O}}|_e^{\text{UDS}} \right) \right]^{\text{old}} \\
 &\quad - \left[\epsilon_g|_w u_g|_w A_x \left(\rho_g^{\text{H}_2\text{O}}|_w^{\text{CDS}} - \rho_g^{\text{H}_2\text{O}}|_w^{\text{UDS}} \right) \right]^{\text{old}} \\
 &\quad + \left[\epsilon_g|_n v_g|_n A_x \left(\rho_g^{\text{H}_2\text{O}}|_n^{\text{CDS}} - \rho_g^{\text{H}_2\text{O}}|_n^{\text{UDS}} \right) \right]^{\text{old}} \\
 &\quad - \left[\epsilon_g|_s v_g|_s A_x \left(\rho_g^{\text{H}_2\text{O}}|_s^{\text{CDS}} - \rho_g^{\text{H}_2\text{O}}|_s^{\text{UDS}} \right) \right]^{\text{old}} \\
 &\quad + \frac{\epsilon_g|_e \omega_g^{\text{H}_2\text{O}}|_e D_{\text{H}_2\text{O}-g}^{\text{eff}}|_e}{\left(1 - x_g^{\text{H}_2\text{O}}|_e \right)} \sum_{\beta \neq \text{H}_2\text{O}} \left[\frac{\rho_g|_e \hat{M}_g \nabla \omega_g^\beta|_e}{\hat{M}_\beta} + \frac{\hat{M}_g \mathcal{J}_g^\beta|_e}{\hat{M}_\beta \mathcal{D}_{\text{H}_2\text{O}-\beta,g}^{\text{eff}}|_e} \right] A_x \\
 &\quad - \epsilon_g|_e \omega_g^{\text{H}_2\text{O}}|_e D_{\text{H}_2\text{O}-g}^{\text{eff}}|_e \nabla \rho_g|_e A_x \\
 &\quad - \frac{\epsilon_g|_w \omega_g^{\text{H}_2\text{O}}|_w D_{\text{H}_2\text{O}-g}^{\text{eff}}|_w}{\left(1 - x_g^{\text{H}_2\text{O}}|_w \right)} \sum_{\beta \neq \text{H}_2\text{O}} \left[\frac{\rho_g|_w \hat{M}_g \nabla \omega_g^\beta|_w}{\hat{M}_\beta} + \frac{\hat{M}_g \mathcal{J}_g^\beta|_w}{\hat{M}_\beta \mathcal{D}_{\text{H}_2\text{O}-\beta,g}^{\text{eff}}|_w} \right] A_x \\
 &\quad + \epsilon_g|_w \omega_g^{\text{H}_2\text{O}}|_w D_{\text{H}_2\text{O}-g}^{\text{eff}}|_w \nabla \rho_g|_w A_x \\
 &\quad + \frac{\epsilon_g|_n \omega_g^{\text{H}_2\text{O}}|_n D_{\text{H}_2\text{O}-g}^{\text{eff}}|_n}{\left(1 - x_g^{\text{H}_2\text{O}}|_n \right)} \sum_{\beta \neq \text{H}_2\text{O}} \left[\frac{\rho_g|_n \hat{M}_g \nabla \omega_g^\beta|_n}{\hat{M}_\beta} + \frac{\hat{M}_g \mathcal{J}_g^\beta|_n}{\hat{M}_\beta \mathcal{D}_{\text{H}_2\text{O}-\beta,g}^{\text{eff}}|_n} \right] A_y \\
 &\quad - \epsilon_g|_n \omega_g^{\text{H}_2\text{O}}|_n D_{\text{H}_2\text{O}-g}^{\text{eff}}|_n \nabla \rho_g|_n A_y \\
 &\quad - \frac{\epsilon_g|_s \omega_g^{\text{H}_2\text{O}}|_s D_{\text{H}_2\text{O}-g}^{\text{eff}}|_s}{\left(1 - x_g^{\text{H}_2\text{O}}|_s \right)} \sum_{\beta \neq \text{H}_2\text{O}} \left[\frac{\rho_g|_s \hat{M}_g \nabla \omega_g^\beta|_s}{\hat{M}_\beta} + \frac{\hat{M}_g \mathcal{J}_g^\beta|_s}{\hat{M}_\beta \mathcal{D}_{\text{H}_2\text{O}-\beta,g}^{\text{eff}}|_s} \right] A_y \\
 &\quad + \epsilon_g|_s \omega_g^{\text{H}_2\text{O}}|_s D_{\text{H}_2\text{O}-g}^{\text{eff}}|_s \nabla \rho_g|_s A_y + \epsilon_{\ell,e}|_e \mathcal{D}_{\text{H}_3\text{O}^+}^{\text{H}_2\text{O}}|_e \nabla \Phi_e|_e A_x \\
 &\quad - \frac{\epsilon_{\ell,e}|_e \mathcal{D}_{\text{H}_2\text{O}}^{\text{H}_2\text{O}}|_e \omega_{\ell,e}^{\text{H}_2\text{O}}|_e}{\rho_{\ell,e}|_e} \nabla \rho_{\ell,e}|_e A_x - \epsilon_{\ell,e}|_w \mathcal{D}_{\text{H}_3\text{O}^+}^{\text{H}_2\text{O}}|_w \nabla \Phi_e|_w A_x \\
 &\quad + \frac{\epsilon_{\ell,e}|_w \mathcal{D}_{\text{H}_2\text{O}}^{\text{H}_2\text{O}}|_w \omega_{\ell,e}^{\text{H}_2\text{O}}|_w}{\rho_{\ell,e}|_w} \nabla \rho_{\ell,e}|_w A_x + \epsilon_{\ell,e}|_n \mathcal{D}_{\text{H}_3\text{O}^+}^{\text{H}_2\text{O}}|_n \nabla \Phi_e|_n A_y \\
 &\quad - \frac{\epsilon_{\ell,e}|_n \mathcal{D}_{\text{H}_2\text{O}}^{\text{H}_2\text{O}}|_n \omega_{\ell,e}^{\text{H}_2\text{O}}|_n}{\rho_{\ell,e}|_n} \nabla \rho_{\ell,e}|_n A_y - \epsilon_{\ell,e}|_s \mathcal{D}_{\text{H}_3\text{O}^+}^{\text{H}_2\text{O}}|_s \nabla \Phi_e|_s A_y \\
 &\quad + \frac{\epsilon_{\ell,e}|_s \mathcal{D}_{\text{H}_2\text{O}}^{\text{H}_2\text{O}}|_s \omega_{\ell,e}^{\text{H}_2\text{O}}|_s}{\rho_{\ell,e}|_s} \nabla \rho_{\ell,e}|_s A_y - V_{CV} \hat{M}_{\text{H}_2\text{O}} A_v \left[\dot{\rho}_{\text{H}_2\text{O}} - \frac{\partial \dot{\rho}_{\text{H}_2\text{O}}}{\partial \rho_{\text{H}_2\text{O}}} \rho_{\text{H}_2\text{O}}|_P^{\text{old}} \right]
 \end{aligned} \tag{5.78}$$

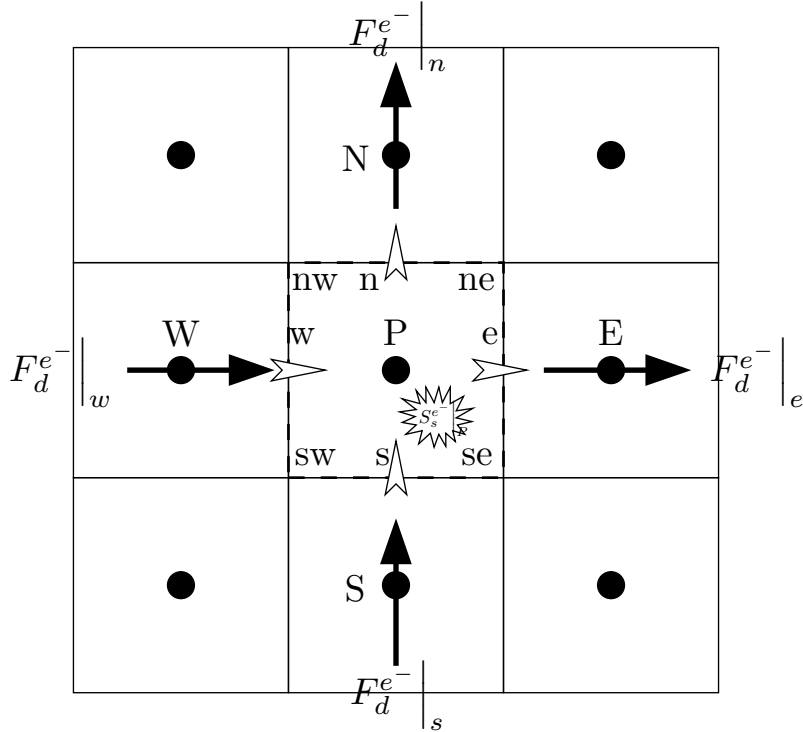


Figure 5.8: The conservation of species for the solid phase.

5.7 Conservation of Species: Solid

The conservation of electrons in the solid phase results in

$$F_d^{e-}|_w - F_d^{e-}|_e + F_d^{e-}|_s - F_d^{e-}|_n + S_s^{e-}|_P = 0, \quad (5.79)$$

where the balance of Equation (5.79) is illustrated in Figure 5.8. The flow of current, F_d^{e-} , can be expressed as a function of potential with Equation (4.16). For the east face, $F_d^{e-}|_e$ is

$$F_d^{e-}|_e = A_d^{e-}|_e \left(\Phi_s^{e-}|_E - \Phi_s^{e-}|_P \right), \quad (5.80)$$

$$A_d^{e-}|_e = -\frac{\epsilon_s|_e \kappa_s^{\text{eff}}|_e A_x}{\Delta E},$$

where the face values of volume fraction and electrical conductivity are evaluated using a linear interpolation. The reaction source term is

$$\begin{aligned} S_s^{e-} \Big|_P &= A_S^{e-} \Big|_P \Phi_s \Big|_P + B_S^{e-} \Big|_P, \\ A_S^{e-} \Big|_P &= -V_{CV} A_v \mathcal{F} \frac{\partial \dot{\mathcal{J}}^{e-}}{\partial \Phi_s}, \\ B_S^{e-} \Big|_P &= -V_{CV} A_v \mathcal{F} \left[\dot{\mathcal{J}}^{e-} - \frac{\partial \dot{\mathcal{J}}^{e-}}{\partial \Phi_s} \Phi_s \Big|_P^{\text{old}} \right], \end{aligned} \quad (5.81)$$

where $(-\mathcal{F})$ is multiplied to the source term because the balance is in terms of current density. After assembling Equation (5.79), each control volume can be written as

$$A_P^{\Phi_s} \Phi_s \Big|_P + A_N^{\Phi_s} \Phi_s \Big|_N + A_S^{\Phi_s} \Phi_s \Big|_S + A_E^{\Phi_s} \Phi_s \Big|_E + A_W^{\Phi_s} \Phi_s \Big|_W = B_P^{\Phi_s}. \quad (5.82)$$

The A and B coefficients are

$$A_E^{\Phi_s} = \frac{\epsilon_s \Big|_e \kappa_s^{\text{eff}} \Big|_e A_x}{\Delta_E} \quad (5.83)$$

$$A_W^{\Phi_s} = \frac{\epsilon_s \Big|_w \kappa_s^{\text{eff}} \Big|_w A_x}{\Delta_W} \quad (5.84)$$

$$A_N^{\Phi_s} = \frac{\epsilon_s \Big|_n \kappa_s^{\text{eff}} \Big|_n A_y}{\Delta_N} \quad (5.85)$$

$$A_S^{\Phi_s} = \frac{\epsilon_s \Big|_s \kappa_s^{\text{eff}} \Big|_s A_y}{\Delta_S} \quad (5.86)$$

$$A_P^{\Phi_s} = -\frac{\epsilon_s \Big|_e \kappa_s^{\text{eff}} \Big|_e A_x}{\Delta_E} - \frac{\epsilon_s \Big|_w \kappa_s^{\text{eff}} \Big|_w A_x}{\Delta_W} - \frac{\epsilon_s \Big|_n \kappa_s^{\text{eff}} \Big|_n A_y}{\Delta_N} - \frac{\epsilon_s \Big|_s \kappa_s^{\text{eff}} \Big|_s A_y}{\Delta_S} \quad (5.87)$$

$$- V_{CV} A_v \mathcal{F} \frac{\partial \dot{\mathcal{J}}^{e-}}{\partial \Phi_s} \quad (5.88)$$

$$B_P^{\Phi_s} = V_{CV} A_v \mathcal{F} \left[\dot{\mathcal{J}}^{e-} - \frac{\partial \dot{\mathcal{J}}^{e-}}{\partial \Phi_s} \Phi_s \Big|_P^{\text{old}} \right] \quad (5.89)$$

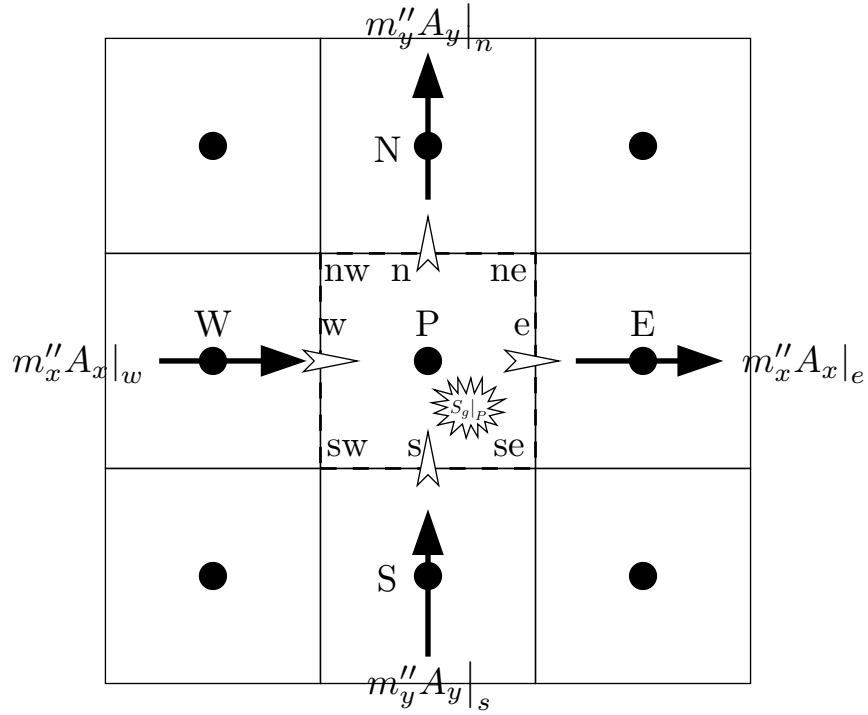


Figure 5.9: The conservation of mass for the gas phase.

5.8 Conservation of Mass

The pressure is solved using the conservation of mass equation and the SIMPLE method [120]. For a single control volume, the conservation of mass can be expressed as

$$\epsilon_g m''_x A_x|_w - \epsilon_g m''_x A_x|_e + \epsilon_g m''_y A_y|_s - \epsilon_g m''_y A_y|_n + S_g|_P = 0, \quad (5.90)$$

where $S_g|_P$ represents the total mass entering the gas phase. The balance of Equation (5.90) is illustrated in Figure 5.9.

Equation (5.90) is not solved for pressure, but rather for the pressure correction. The mass flux through the east face is approximated with

$$\begin{aligned} m''_x &= \rho_g|_{\text{face}} u_g, \\ m''_x &= \rho_g|_{\text{face}} u'_g + \rho_g|_{\text{face}} u_g^{\text{old}}, \end{aligned} \quad (5.91)$$

where ρ_g is evaluated at the face using a linear interpolation and u'_g is the velocity correction. Since the velocity is defined at the face, no interpolation is required. The velocity correction is expressed in terms of the pressure correction with

$$u'_g = -\frac{\epsilon_g|_{face} A_x}{A_P^u} \left(P'_g|_e - P'_g|_w \right), \quad (5.92)$$

where e and w are relative to the u control volume, and A_P^u is the A_p coefficient from Equation (5.22). Therefore, for the east face, the mass flow into the control volume is

$$\begin{aligned} \epsilon_g m''_x A_x|_e &= A|_e \left(P'_g|_E - P'_g|_P \right) + B|_e, \\ A|_e &= -\frac{(\epsilon_g|_e A_x)^2}{A_P^u|_e}, \\ B|_e &= \epsilon_g|_e \rho_g|_e u_g^*|_e A_x, \end{aligned} \quad (5.93)$$

where u_g^* is the velocity obtained by solving the conservation of momentum equation.

The source term in Equation (5.90), $S_g|_P$, includes mass production due to the electro-chemical reactions and any mass transfer through the gas/electrolyte interface:

$$S_g|_P = S_{g,react}|_P + S_{g,g/e}|_P, \quad (5.94)$$

where $S_{g,react}$ is the mass transfer due to reaction and $S_{g,g/e}$ is the mass transfer through the gas/electrolyte interface. The mass production due to reaction can be calculated with Equation (5.43):

$$S_{g,react}|_P = \sum_{\alpha \neq \text{H}_2\text{O}} \hat{M}_\alpha A_v \dot{\mathcal{P}}^\alpha|_P V_{CV}|_P, \quad (5.95)$$

where α is the gas species and the summation does not include water. The mass transfer through

the gas/electrolyte interface is represented by the electrolyte terms in Equation (5.62):

$$S_{g,g-e}|_P = F_d^{\text{H}_2\text{O}}|_w - F_d^{\text{H}_2\text{O}}|_e + F_d^{\text{H}_2\text{O}}|_s - F_d^{\text{H}_2\text{O}}|_s + \hat{M}_{\text{H}_2\text{O}} A_v \dot{\mathcal{P}}^{\text{H}_2\text{O}}|_P. \quad (5.96)$$

Each term in Equation (5.96) is a function of the partial density of water in the gas phase. Thus, both $S_{g,\text{react}}$ and $S_{g,g-e}^{\text{H}_2\text{O}}$ are not functions of pressure or pressure correction.

For a single control volume, the pressure correction equation becomes

$$A_P^P P'_g|_P + A_N^P P'_g|_N + A_S^P P'_g|_S + A_E^P P'_g|_E + A_W^P P'_g|_W = B_P^P. \quad (5.97)$$

The A and B coefficients are

$$A_E^P = \frac{(\epsilon_g|_e A_x)^2}{A_P^u|_e} \quad (5.98)$$

$$A_W^P = \frac{(\epsilon_g|_w A_x)^2}{A_P^u|_w} \quad (5.99)$$

$$A_N^P = \frac{(\epsilon_g|_n A_y)^2}{A_P^v|_n} \quad (5.100)$$

$$A_S^P = \frac{(\epsilon_g|_s A_y)^2}{A_P^v|_s} \quad (5.101)$$

$$A_P^P = -\frac{(\epsilon_g|_e A_x)^2}{A_P^u|_e} - \frac{(\epsilon_g|_w A_x)^2}{A_P^u|_w} - \frac{(\epsilon_g|_n A_y)^2}{A_P^v|_n} - \frac{(\epsilon_g|_s A_y)^2}{A_P^v|_s} \quad (5.102)$$

$$B_P^P = \epsilon_g|_e \rho_g|_e u_g^*|_e A_x - \epsilon_g|_w \rho_g|_w u_g^*|_w A_x + \epsilon_g|_n \rho_g|_n v_g^*|_n A_y - \epsilon_g|_s \rho_g|_s v_g^*|_s A_y \\ - \sum_{\alpha \neq \text{H}_2\text{O}} \hat{M}_\alpha A_v \dot{\mathcal{P}}^\alpha|_P V_{CV}|_P - S_{g,g-e}|_P \quad (5.103)$$

After the solution has been obtained, relaxation is used:

$$P'_g = \alpha_P P_g'^*, \quad (5.104)$$

where $P_g'^*$ is the value of P'_g after solution of Equation (5.104) and $\alpha_P = 0.2$ is the relaxation

factor. With the pressure correction, the velocity correction is determined with Equation (5.92) and applied to the velocity solutions from the conservation of momentum equations.

5.9 Boundary Conditions

The boundary conditions can be classified into three groups: velocity boundary conditions, pressure boundary conditions, and scalar boundary conditions. The velocity boundary conditions affect the u and v velocities, the pressure boundary conditions affect the pressure, while the scalar boundary conditions are applied to the gas phase partial densities and potentials. Within each of the groups, two general boundary conditions exist: external and internal. The external boundary conditions are specified in Section 4.6. The internal boundary conditions arise if a phase becomes discontinuous; hence, internal boundary conditions are necessary where the gas or electrolyte phase are discontinuous, such as at the electrode backing layer/catalyst layer and catalyst layer/polymer electrolyte layer interfaces. The method of dealing with these boundary conditions are examined in this section.

5.9.1 Velocity Boundary Conditions

Two types of external boundary conditions are used for the velocities and these boundary conditions are illustrated in Figure 5.10. Figure 5.10(a) shows a specified velocity boundary condition on the west side of the domain, while Figure 5.10(b) shows a fully developed boundary conditions in the east side of the domain. The governing equation for the control volume is

$$A_P^u u_g|_P + A_N^u u_g|_N + A_S^u u_g|_S + A_E^u u_g|_E + A_W^u u_g|_W = B_P^u. \quad (5.105)$$

For the specified velocity boundary condition of Figure 5.10(a), the W velocity of Equation (5.105) is specified and the equation can be rewritten as

$$A_P^u u_g|_P + A_N^u u_g|_N + A_S^u u_g|_S + A_E^u u_g|_E = \hat{B}_P^u, \quad (5.106)$$

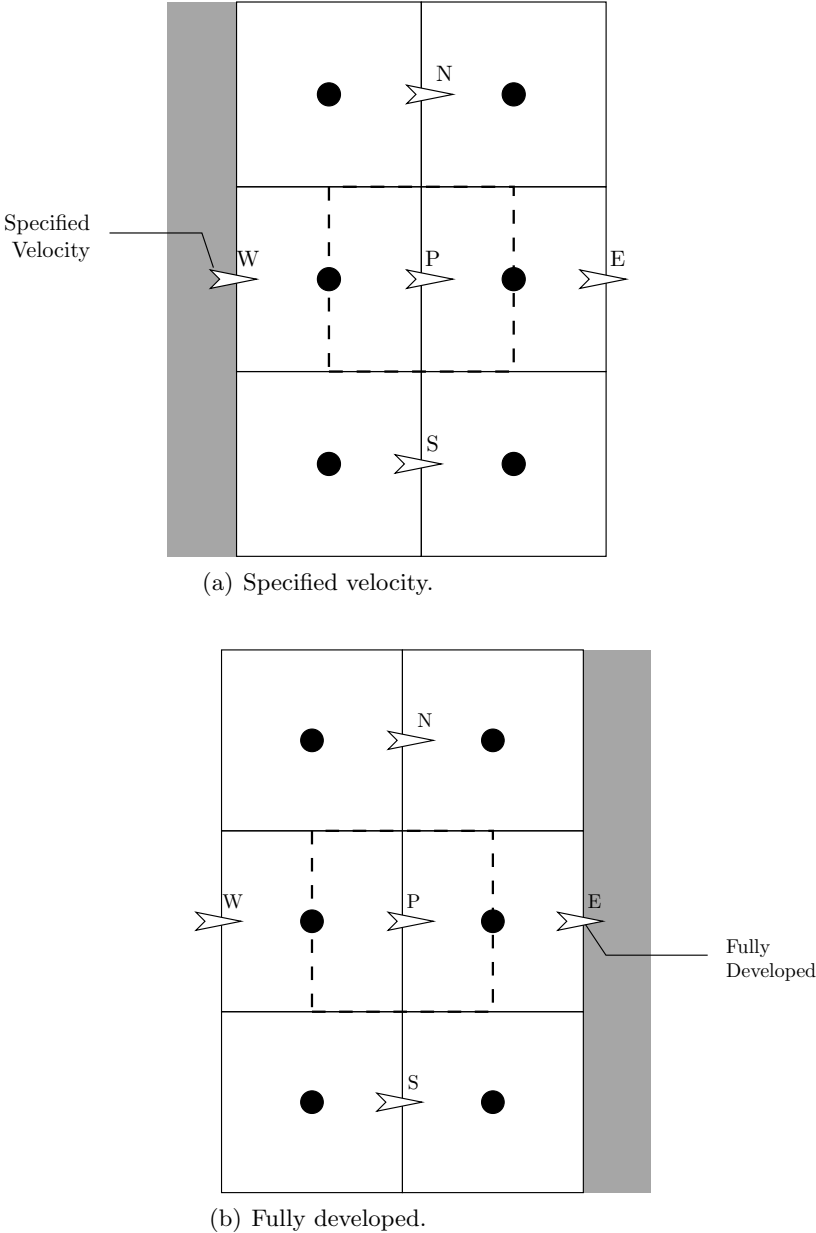


Figure 5.10: The external boundary conditions for the velocity: (a) specified velocity and (b) fully developed.

where \hat{B}_P^u is

$$\hat{B}_P^u = B_P^u - A_W^u u_g|_W. \quad (5.107)$$

The value of $u_g|_W$ is specified by the boundary conditions.

The fully developed boundary condition is approximated with

$$\begin{aligned} \frac{\partial \rho_g u_g}{\partial x} &= 0, \\ \frac{\rho_g|_E u_g|_E - \rho_g|_P u_g|_P}{\Delta_E} &= 0, \\ u_g|_E &= \left(\frac{\rho_g|_P}{\rho_g|_E} \right) u_g|_P. \end{aligned} \quad (5.108)$$

Using Equation (5.108) in Equation (5.105) yields

$$\hat{A}_P^u u_g|_P + A_N^u u_g|_N + A_S^u u_g|_S + A_W^u u_g|_W = B_P^u, \quad (5.109)$$

where

$$\hat{A}_P^u = A_P^u + A_W^u \left(\frac{\rho_g|_P}{\rho_g|_E} \right). \quad (5.110)$$

Figure 5.11 illustrates the situation in which an internal boundary condition is required for the velocity. In Figure 5.11, the E velocity is on a face which divides the domain in which the gas phase exists from the domain in which the volume fraction of the gas phase is zero. This situation is handled by setting the E velocity equal to zero. Thus, the balance on the P control volume becomes

$$A_P^u u_g|_P + A_N^u u_g|_N + A_S^u u_g|_S + A_W^u u_g|_W = B_P^u. \quad (5.111)$$

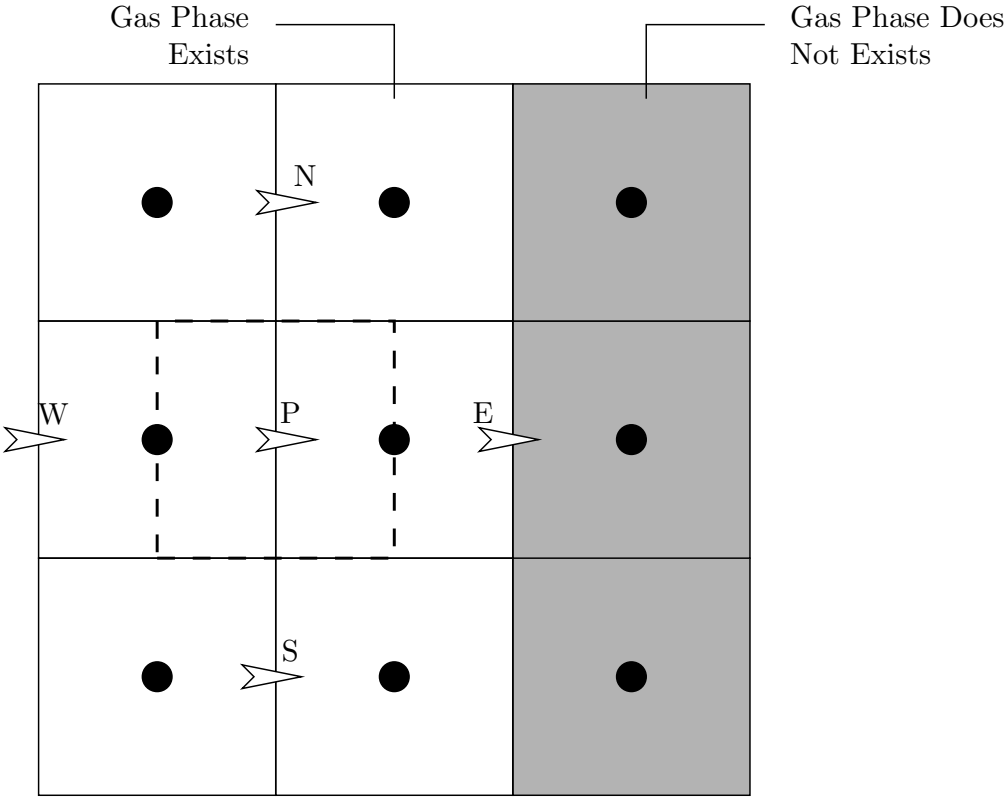


Figure 5.11: Internal boundary condition for the velocity.

5.9.2 Pressure Boundary Conditions

The external boundary conditions relevant to the pressure correction equation are illustrated in Figure 5.12. Figure 5.12(a) shows the specified velocity boundary condition, while Figure 5.12(b) is the specified pressure boundary condition. The specified velocity boundary condition is applied to the initial conservation of mass equation, Equation (5.90):

$$\underbrace{\epsilon_g m''_x A_x|_w}_{\text{specified}} - \epsilon_g m''_x A_x|_e + \epsilon_g m''_y A_y|_s - \epsilon_g m''_y A_y|_n + S_g|_P = 0. \quad (5.112)$$

Since the velocity at the west face is known in Figure 5.12(a), the mass flux is also known and does not need to be expressed in terms of pressure correction. The other mass fluxes at the east, south and north faces can be decomposed into pressure correction values with the procedure outlined in Section 5.8.

If the pressure at the boundary is specified, as illustrated in Figure 5.12(b), then the pressure in the adjacent control volume is set to the specified value:

$$P|_P = \text{Specified}. \quad (5.113)$$

The pressure correction equation for the adjacent control volume is then

$$A_P^P P'_g|_P = 0. \quad (5.114)$$

As with the velocity, internal boundary conditions for the pressure arise if the gas phase is discontinuous, as illustrated in Figure 5.13. The internal boundary conditions are approached in the same manner as the specified velocity external boundary conditions. For the case illustrated in Figure 5.13, the mass balance becomes

$$\epsilon_g m''_x A_x|_w - \underbrace{\epsilon_g m''_x A_x|_e}_0 + \epsilon_g m''_y A_y|_s - \epsilon_g m''_y A_y|_n + S_g|_P = 0, \quad (5.115)$$

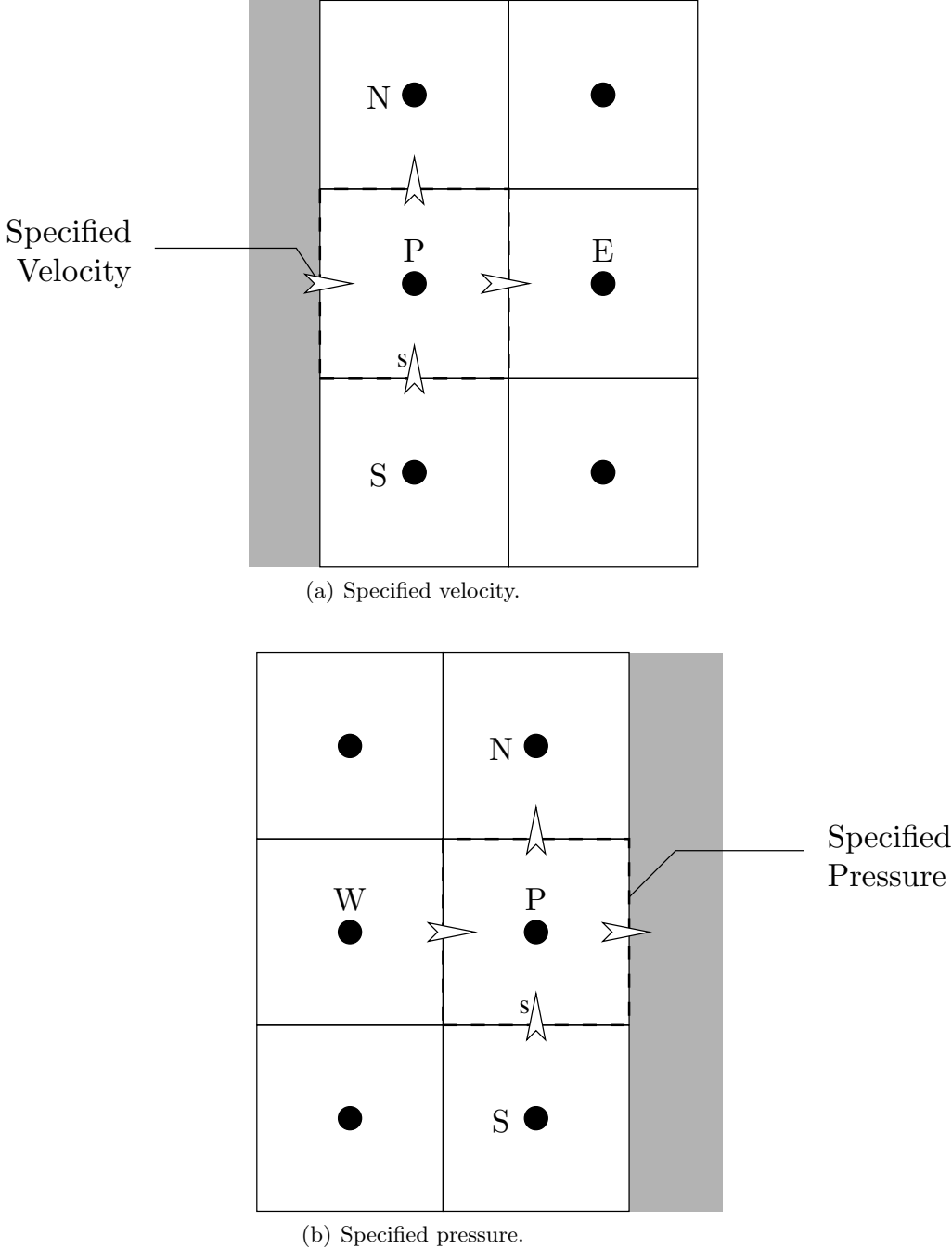


Figure 5.12: The external boundary conditions for the pressure: (a) specified velocity and (b) specified pressure.

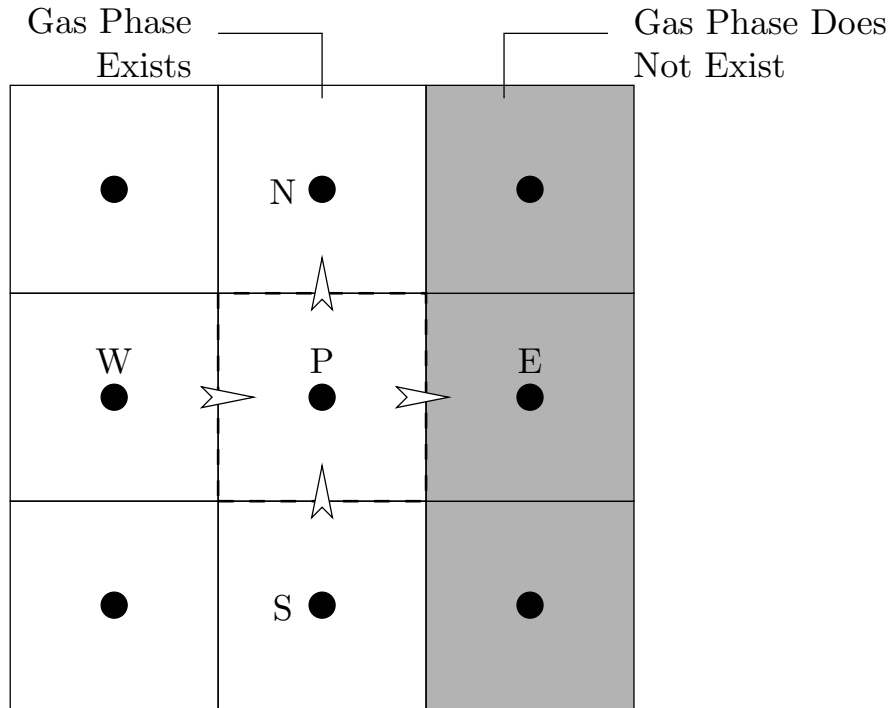


Figure 5.13: Internal boundary condition for the pressure.

where the mass flux through the east face is zero. The other mass fluxes at the west, south and north faces can be decomposed into pressure correction values with the procedure outlined in Section 5.8.

5.9.3 Scalar Boundary Conditions

The conservation of a scalar quantity in a control volume at a boundary is illustrated in Figure 5.14. The mass balance of Figure 5.14 is

$$F_{BC} - F_c|_e + F_c|_s - F_c|_n - F_d|_e + F_d|_s - F_d|_n + S|_P = 0, \quad (5.116)$$

where F_{BC} is the mass entering the control volume from the boundary. In general, the boundary mass flow is expressed as

$$F_{BC} = A_{BC} \psi|_P + B_{BC}, \quad (5.117)$$

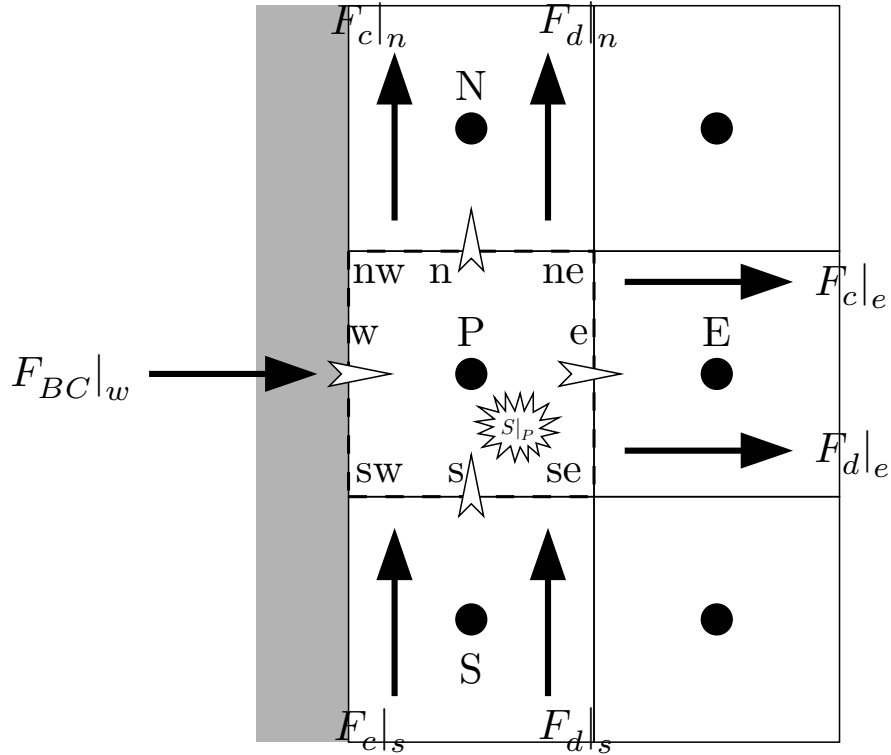


Figure 5.14: The conservation of a scalar quantity near the boundary.

where ψ represents the potential or partial density.

Three types of boundary conditions can be expressed with Equation (5.117): specified flux, specified value and fully developed. For the specified flux boundary condition, $A_{BC} = 0$ and

$$F_{BC} = B_{BC}, \quad (5.118)$$

$$B_{BC} = F''_{\text{specified}} A_x,$$

where $F''_{\text{specified}}$ is the specified mass flux of gas phase species, current density, or mass flux of hydronium. For the model presented in this thesis, the value of the specified flux is always zero.

The total mass flux or current density in the x direction of a scalar quantity can be expressed as

$$F'' = u\psi - \Gamma \frac{\partial \psi}{\partial x} + B_d, \quad (5.119)$$

where u is the convective velocity, Γ is the diffusion coefficient or conductivity, and B_d represents all lagged terms from the diffusive flux. If the value of ψ is specified at the boundary as ψ_f , then the flux becomes

$$F''_{BC} = u_f \psi_f - \left(\frac{\Gamma}{\Delta_w} \right) (\psi|_P - \psi_f) + B_d, \quad (5.120)$$

where the subscript f denotes a face value. Thus, for the specified value boundary condition is

$$\begin{aligned} F_{BC} &= A_{BC} \psi|_P + B_{BC}, \\ A_{BC} &= -\frac{\Gamma A_x}{\Delta_w}, \\ B_{BC} &= \left(\frac{\Gamma A_x}{\Delta_w} \right) \psi_f + u_f \psi_f A_x + B_d A_x. \end{aligned} \quad (5.121)$$

The final type of external boundary condition for the scalar quantities is the fully developed boundary condition. This boundary condition is only applied to the partial densities of the species in the gas phase at the outlet. When the flow is fully developed, the diffusive flux is zero, resulting in

$$\begin{aligned} F_{BC} &= A_{BC} \psi|_P, \\ A_{BC} &= u_g|_P. \end{aligned} \quad (5.122)$$

The mass balance for a control volume adjacent to a phase discontinuity is illustrated in Figure 5.15. The flux at the phase boundary is zero; hence, a mass balance results in

$$F_c|_w + F_c|_s - F_c|_n + F_d|_w + F_d|_s - F_d|_n + S|_P = 0. \quad (5.123)$$

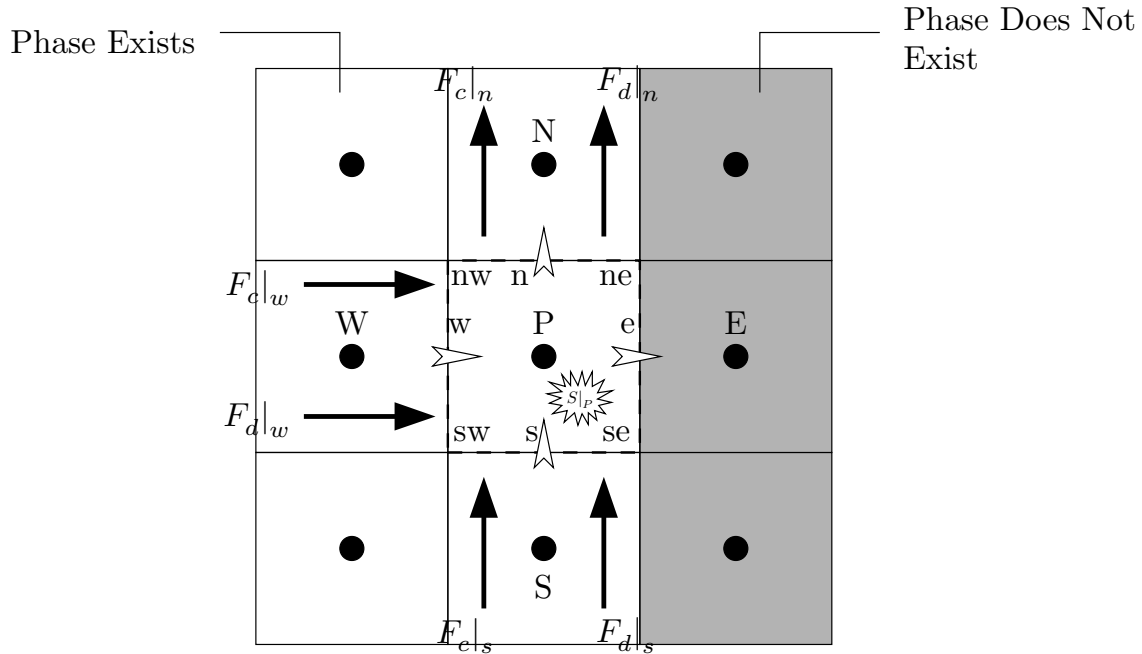


Figure 5.15: The conservation of a scalar quantity near the a phase discontinuity.

5.10 Numerical Procedure

The equations of the previous sections, representing the conservation of mass, momentum and species for a single control volume, have the general form of

$$A_P \psi|_P + A_N \psi|_N + A_S \psi|_S + A_E \psi|_E + A_W \psi|_W = B_P, \quad (5.124)$$

where the A and B can be functions of velocity, pressure, gas and liquid composition, and grid spacing. These equations are solved using a multigrid solver with a Gauss-Seidel smoother [120]. However, since the equations are coupled, an iterative solution procedure is required; this procedure is outlined here.

The overall solution procedure is illustrated in Figure 5.16. The overall solution is composed of an outer loop that contains three procedures. The first procedure, “Calculate Constants”, calculates numerical values for all the quantities that are functions of total pressure and the gas and electrolyte compositions. The second procedure, “Solve Species”, solves for the partial gas densities, solid and

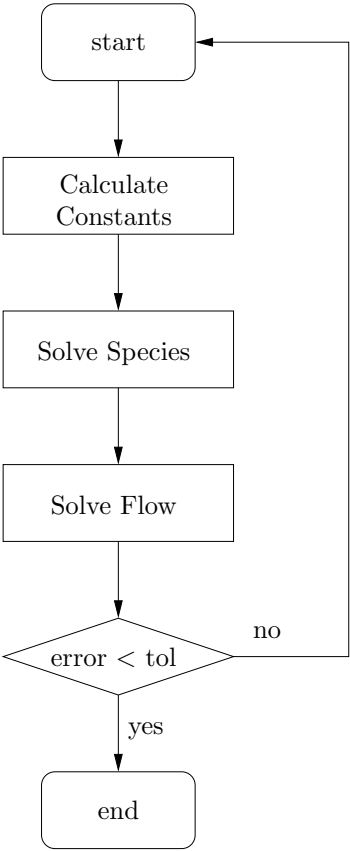


Figure 5.16: The overall solution procedure.

electrolyte potentials. The final procedure, “Solve Flow”, determines the velocity and pressure. The outer loop continues if the error is greater than the convergence criteria, tol . The error is taken as the maximum initial RMS residual of the equations for the partial gas density, solid or electrolyte potentials, velocity, or pressure:

$$\text{error} = \sqrt{\sum [B_P - (A_P \psi|_P + A_N \psi|_N + A_S \psi|_S + A_E \psi|_E + A_W \psi|_W)]^2}, \quad (5.125)$$

where the summation is over all the control volumes.

The three procedures in the outer loop are composed of several steps. The steps that make up the “Calculate Constants” procedure is illustrated in Figure 5.17. The first step in the procedure is to calculate the mass fraction at each control volume using the partial density:

$$\omega_g^\alpha = \frac{\rho_g^\alpha}{\sum_\beta \rho_g^\beta}, \quad (5.126)$$

where the summation is over all the gas species. Using these mass fractions, the total pressure and the temperature, the properties of the gas phase, such as total density, viscosity, and mass diffusivity are determined. Additionally, the Stefan-Maxwell fluxes are calculated at all interior faces. In order to calculate the properties in the liquid of the electrolyte, such as density, mass diffusivity and volume fraction, the membrane hydration must be known. The membrane hydration can be determined from the activity, and the activity is determined from the partial density of water in the gas with Equation (5.65). However, the activity is limited to a range of values:

$$0.1 \leq \tilde{a} \leq 1.0. \quad (5.127)$$

The upper limit is due to the fact that the hydration is not defined for activities greater than 1.0; at activities greater than 1.0 the membrane is in contact with liquid water, resulting in phenomena that are not included in the current model. The lower limit is applied in order to ensure convergence. For activities of less than 0.1, the electrical conductivity of the membrane becomes so small that

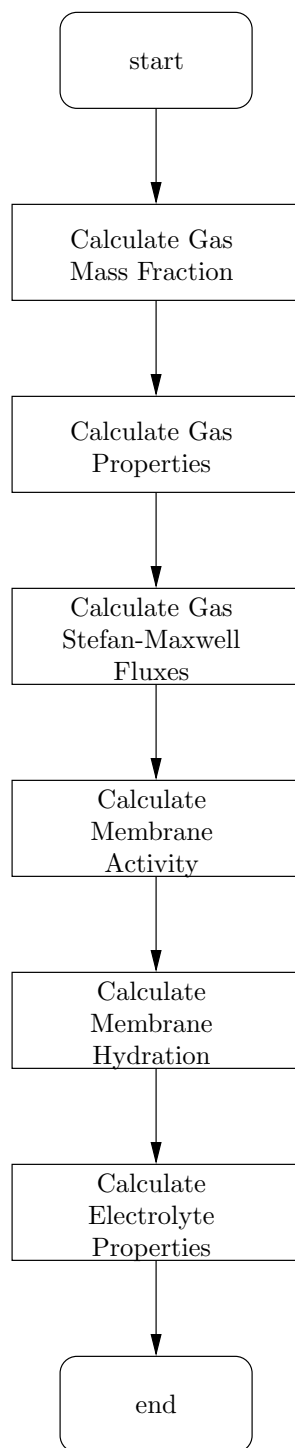


Figure 5.17: The flowchart for the “Calculate Constants” procedure.

the electrolyte becomes an insulator. The low value of conductivity can lead to an A_P value in Equation (5.124) that is zero, which will cause the Gauss-Seidel solver to fail. In addition to the membrane properties, the derivative of the partial density of liquid water with respect to the membrane activity is also calculated here.

The procedure for determining the partial densities and potentials contains two levels of iterations, as illustrated in Figure 5.18. The inner loop solves for the partial density of the gases and the potentials. Although the properties are kept constant in this procedure, the non-linear reactions require an iterative solution procedure. The inner loop solves the gas partial densities and potentials sequentially. However, the rate of reactions are multi-variable functions of partial density and potential; hence, the need for an outer level of iteration.

The procedure for determining the velocities and pressure is illustrated in Figure 5.19. Figure 5.19 shows the basic SIMPLE algorithm [120]. The momentum equations are solved for the x - and y -direction velocities. These velocities are then used in the conservation of mass equation to create the pressure correction equation. The pressure correction is then relaxed, and the x - and y velocities are corrected. The procedure continues until the initial residuals are below the convergence criteria, tol .

5.11 Summary

The simplified formulation was solved numerically using the finite volume method and a staggered mesh. Since the equations were non-linear, a multi-level, iterative solution technique was used. In the lowest level of iteration, each conservation equation was solved for one variable. The conservation of momentum in the x - and y -directions were solved for the x - and y -components of velocity. The pressure in the gas phase was determined from the conservation of mass. The conservation of hydrogen, oxygen and nitrogen were solved to obtain the partial densities of hydrogen, oxygen and nitrogen, respectively. The potential in the electrolyte was obtained with the conservation of hydronium ions, while the conservation of electrons in the solid phase was used to determine the solid

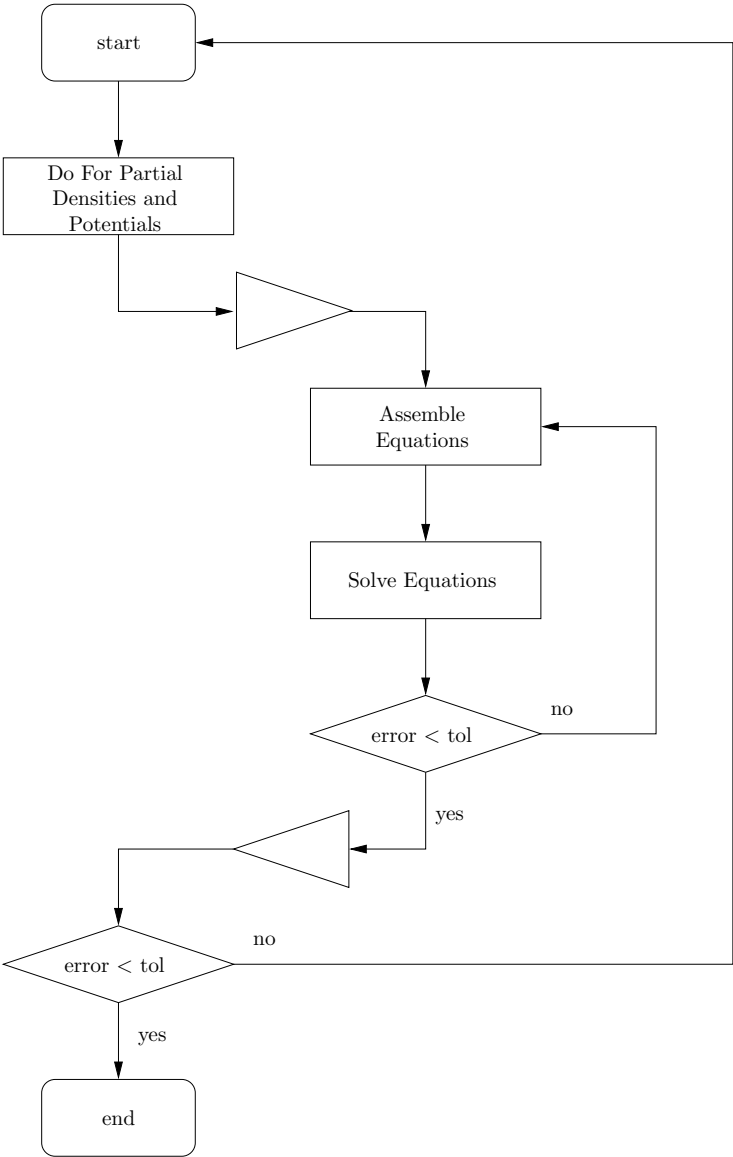


Figure 5.18: The flowchart for the “Calculate Species” procedure.

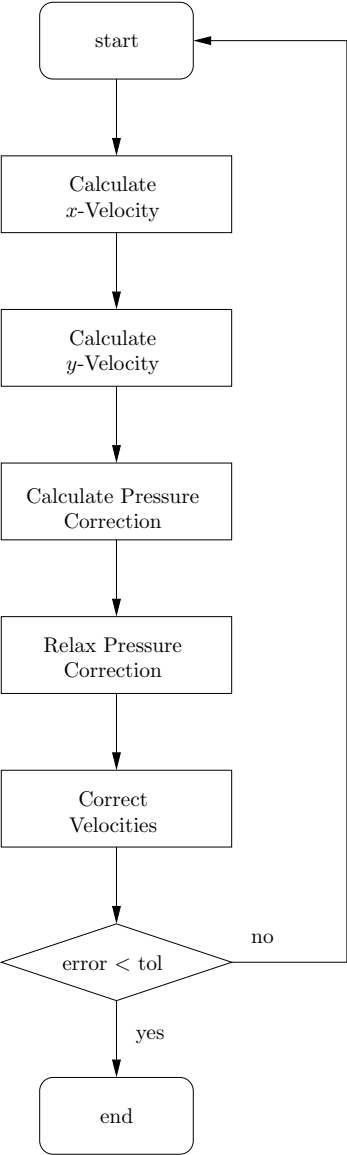


Figure 5.19: The flowchart for the “Calculate Flow” procedure.

phase potential. The equations representing the conservation of water in the gas and liquid-filled pores of the electrolyte were combined and solved for a single variable. Using acid-base equilibrium and empirical membrane hydration curves, the partial density of water in the electrolyte was expressed as a function of partial water density in the gas phase. Hence, the conservation of total water could be solved for the partial density of water in the gas phase.

Because the velocities, pressure, partial densities, and potentials were coupled, two additional levels of iterations were employed. The second level of iterations involved gathering the governing equations into two groups. In one group, the velocities and pressure in the gas phase were calculated by iterating the equations for the conservation of momentum and mass with the SIMPLE algorithm. The second group of iterations alternated between solving for the partial gas densities and potentials until they converged. The final level of iterations alternated between the two groups, until a final converged solution for the velocities, pressure, partial densities and potentials was obtained.

Chapter 6

Parameter Determination for the Electrolyte Model

The transport of water and charge in the polymer electrolyte is modeled using the Generalized Stefan-Maxwell equations of Scattergood and Lightfoot [74]. This is a novel approach, since the majority of mathematical PEM fuel cell studies employ the model developed by Springer *et al.* [26, 27]. As a result, the diffusion coefficients required for the Generalized Stefan-Maxwell approach are not available for a Nafion membrane and they must be determined from published, experimental data.

There are three constants that need to be determined in the electrolyte model. These are the binary diffusion coefficient of hydronium and water ($D_{\text{H}_3\text{O}^+-\text{H}_2\text{O},\ell,e}$), and the diffusion coefficients for hydronium and water in the membrane, $D_{\text{H}_3\text{O}^+-s,\ell,e}$ and $D_{\text{H}_2\text{O}-s,\ell,e}$. Of these three, the binary diffusion coefficient between hydronium and water is known for aqueous systems and can be expressed as [105]

$$D_{\text{H}_3\text{O}^+-\text{H}_2\text{O},\ell,e} = \frac{\lambda_1^0 \mathcal{R}T}{\mathcal{F}^2}, \quad (6.1)$$

where λ_1^0 is 349.8 S cm². Therefore, there are only two unknown coefficients that need to be

determined.

In the published literature on Nafion membranes for PEM fuel cell use, there are three measured quantities. The first is the diffusion coefficient of water, under conditions of a water concentration gradient and no current. The second measurement is the ionic conductivity of the membrane. This is measured for membranes with no water gradient. The third measured property is the electro-osmotic drag coefficient, defined as

$$n_d = \frac{\text{Molar flux of water}}{\text{Molar flux of ions}}. \quad (6.2)$$

The electro-osmotic drag coefficient is determined for membranes with a constant hydration; hence, the membrane is under the same conditions as when the conductivity is measured.

Therefore, in order to find the diffusion coefficients, the equations for hydronium and water transport in the membrane must be simplified to the above two membrane conditions. This chapter determines the value of the diffusion coefficient between water and the polymer matrix, $D_{\text{H}_2\text{O}-s,\ell,e}$, and the diffusion coefficient between hydronium and the polymer matrix, $D_{\text{H}_3\text{O}^+-s,\ell,e}$. The diffusion coefficient between water and the polymer matrix can be determined from experimental water diffusion data, while the diffusion coefficient between hydronium and the polymer matrix is determined from experimental conductivity data. The experimental, electro-osmotic drag data can be used to validate the electrolyte model; using the values of $D_{\text{H}_2\text{O}-s,\ell,e}$ and $D_{\text{H}_3\text{O}^+-s,\ell,e}$ determined from water diffusion and conductivity data, the electro-osmotic drag calculated from the model should match the experimental data. Finally, the differences between the electrolyte model of this thesis and the commonly used model of Springer *et al.* [26, 27] are highlighted.

6.1 Water Diffusion Coefficient

During experiments for determining the diffusion coefficient of water in the electrolyte membrane, the current flow is zero. Therefore, the governing equations for the electrolyte reduce to

$$\mathcal{N}_{\ell,e}^{\text{H}_2\text{O}} = - \left(\frac{x_{\ell,e}^{\text{H}_3\text{O}^+}}{c_{\ell,e} D_{\text{H}_3\text{O}^+ - \text{H}_2\text{O},\ell,e}^{\text{eff}}} + \frac{1}{D_{\text{H}_2\text{O}-s,\ell,e}^{\text{eff}}} \right)^{-1} \nabla x_{\ell,e}^{\text{H}_2\text{O}}, \quad (6.3)$$

where the volume-averaging operator, $\langle \rangle^*$, has been omitted for the concentration and mole fractions. In Equation (6.3), the only unknown is $D_{\text{H}_2\text{O}-s}$.

The water diffusion models in the published literature use a Fickian diffusion equation with the hydration gradient as the driving force for water diffusion [122]:

$$\langle \mathcal{N}_{\ell,e}^{\text{H}_2\text{O}} \rangle = - \frac{\rho_M}{\hat{M}_M} D_{w,F} \nabla \mathcal{L}, \quad (6.4)$$

where the density of the polymer matrix, ρ_M , is 2 g/cm³ and the molecular weight of the polymer matrix, \hat{M}_M , is 1100 g/mole. The operator, $\langle \rangle$, represents the volume average, not intrinsic average, and thus represents the molar flow rate of water divided by the total cross-sectional area of the electrolyte: both polymer matrix and liquid pore. In Equation (6.3), $\mathcal{N}_{\ell,e}^{\text{H}_2\text{O}}$ represents the molar flow rate of water divided by the cross-sectional area of the liquid filled pores only.

Several diffusion coefficients, $D_{w,F}$, have been proposed in the published literature, and Motupally *et al.* [122] found that the best fit with experimental data occurs with

$$D_{w,F} = \begin{cases} 3.1 \times 10^{-3} \mathcal{L} [\exp(0.28\mathcal{L}) - 1] \exp\left(-\frac{2436}{T}\right) & 0 < \mathcal{L} \leq 3 \\ 4.17 \times 10^{-4} \mathcal{L} [161 \exp(-\mathcal{L}) + 1] \exp\left(-\frac{2436}{T}\right) & 3 \leq \mathcal{L} < 17 \end{cases}, \quad (6.5)$$

where $D_{w,F}$ is in units of cm²/s and T is in units of K.

For the same hydration gradient, the molar flux predicted by Equations (6.3) and (6.4) must be equivalent. Comparing Equations (6.3) and (6.4), a relationship between $D_{\text{H}_2\text{O}-s}$ and $D_{w,F}$ can

be written as

$$\epsilon_{\ell,e} \left(\frac{x_{\ell,e}^{\text{H}_3\text{O}^+}}{c_{\ell,e} D_{\text{H}_3\text{O}^+-\text{H}_2\text{O},\ell,e}^{\text{eff}}} + \frac{1}{D_{\text{H}_2\text{O}-s,\ell,e}^{\text{eff}}} \right)^{-1} \frac{\partial x_{\ell,e}^{\text{H}_2\text{O}}}{\partial \mathcal{L}} = \frac{\rho_M}{\hat{M}_M} D_{w,F}. \quad (6.6)$$

With further simplification, an explicit function for $D_{\text{H}_2\text{O}-s,\ell,e}$ can be obtained:

$$D_{\text{H}_2\text{O}-s,\ell,e} = \frac{1}{\sqrt{\epsilon_{\ell,e}}} \left[\frac{\epsilon_{\ell,e} \hat{M}_M}{\rho_M D_{w,F}} \left(\frac{\partial x_{\ell,e}^{\text{H}_2\text{O}}}{\partial \mathcal{L}} \right) - \frac{1 - x_{\ell,e}^{\text{H}_2\text{O}}}{c_{\ell,e} D_{\text{H}_3\text{O}^+-\text{H}_2\text{O},\ell,e}^{\text{eff}}} \right]^{-1}. \quad (6.7)$$

The values on the right-hand-side in Equation (6.7) are functions of membrane hydration. The volume fraction of water in the electrolyte is given by Equation (4.40) and the mole fraction of water can be determined as a function of hydration and temperature with Equation (4.58). The derivative of mole fraction with respect to hydration is

$$\frac{\partial x_{\ell,e}^{\text{H}_2\text{O}}}{\partial \mathcal{L}} = \frac{\mathcal{A}}{\mathcal{L}^2} - \frac{1}{\mathcal{L}} \frac{\partial \mathcal{A}}{\partial \mathcal{L}}, \quad (6.8)$$

where the derivative of the degree of dissociation with respect to hydration is

$$\frac{\partial \mathcal{A}}{\partial \mathcal{L}} = \frac{1 - \frac{(\mathcal{L}+1)-2\left(1-\frac{1}{\mathbb{K}_e}\right)}{\sqrt{(\mathcal{L}+1)^2-4\mathcal{L}\left(1-\frac{1}{\mathbb{K}_e}\right)}}}{2\left(1-\frac{1}{\mathbb{K}_e}\right)}. \quad (6.9)$$

The relationship between the diffusion coefficient of water in the membrane as a function of hydration for temperatures of 303, 333, and 353 K are illustrated in Figure 6.1. The diffusion coefficient increases with increasing temperature, but the relationship between the diffusion coefficient and membrane hydration is complex. Starting at a membrane hydration of zero, the diffusion coefficient increases to a maximum value at a hydration value of 3. Further increases in hydration reduce the diffusion coefficient until a hydration of approximately 6 is reached. An increase in hydration from 6 to full hydration results in an increase in the diffusion coefficient. Thus, the diffusion coefficient has an absolute or local maximum at a hydration value of 3.

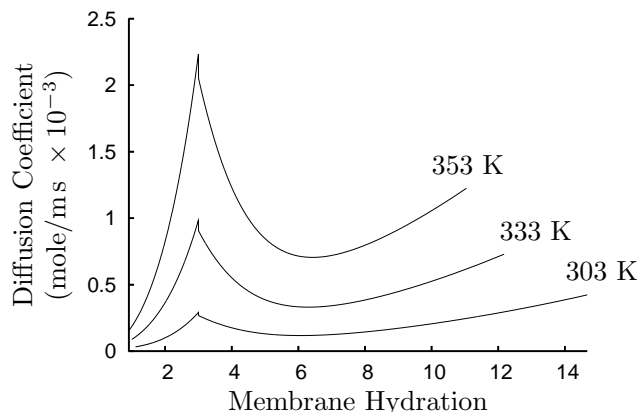


Figure 6.1: The diffusion coefficient of water in the membrane as a function of hydration for temperatures of 303, 333, and 353 K.

However, this maximum may not be a physical phenomena, but rather a function of the data fitting technique used by Motupally *et al.* [122]. In the reference, the experimental expression for $D_{w,F}$, Equation (6.5), was determined with

$$D_{w,F} = D_{w,I} \left[\frac{\partial \ln(\tilde{a})}{\partial \ln(\mathcal{L})} \right], \quad (6.10)$$

where $D_{w,I}$ was curve-fitted to the experimental data of Zawodzinski *et al.* [123]:

$$D_{w,I} = 6.31 \times 10^{-7} (\mathcal{L} - 0.0209\mathcal{L}^2 - 0.501). \quad (6.11)$$

The units of $D_{w,I}$ is cm^2/s . The derivative term in Equation (6.10) is referred to as the Darken factor, and is expressed as

$$\frac{\partial \ln(\tilde{a})}{\partial \ln(\mathcal{L})} = \frac{\mathcal{L}}{\tilde{a} \frac{\partial \mathcal{L}}{\partial \tilde{a}}}. \quad (6.12)$$

Thus, in order to calculate $D_{w,F}$, the functional relationship between hydration and activity is required. Motupally *et al.* [122] used the curve fit of Springer *et al.* [26]:

$$\mathcal{L} = 0.043 + 17.81\tilde{a} - 39.85\tilde{a}^2 + 36.0\tilde{a}^3. \quad (6.13)$$

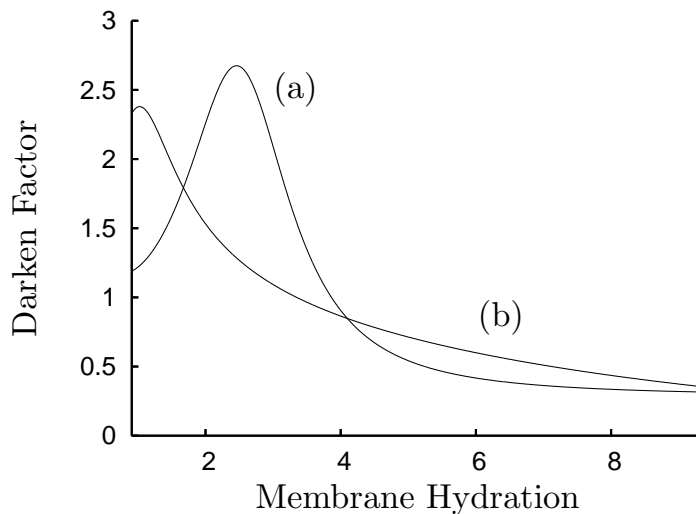


Figure 6.2: The Darken factor based on the electrolyte hydration function of (a) Springer *et al.* [26] and (b) Futerko and Hsing [115]

The maximum of Figure 6.1 is due to the Darken factor. Figure 6.2 compares the Darken factor based on the hydration function of Equation (6.13) with the Darken factor derived by using the relationship of Futerko and Hsing [115], expressed as Equation (4.42). The temperature used to create Figure 6.2 was 353 K. The Darken factor used by Motupally *et al.* [122] exhibits a maximum value, while the Darken factor derived with the hydration function of Futerko and Hsing [115] shows a constant decrease as a function of membrane hydration. If the Darken factor derived from the function of Futerko and Hsing [115] is used, the diffusion coefficient of water in the membrane does not show the same sharp increase in value shown in Figure 6.1, as illustrated in Figure 6.3. The diffusion coefficient of water in the electrolyte based on the Darken factor of Futerko and Hsing [115] has a significantly different functional dependency on membrane hydration than the one determined from Motupally *et al.* [122]. Thus, the choice of hydration function and subsequent Darken factor greatly affects the water diffusion coefficient. Since the function used by Motupally *et al.* [122] agreed well with experimental data, the water diffusion coefficient illustrated in Figure 6.1 is used for the model presented in this thesis. However, further study should be done on the effect of the Darken factor on the diffusion of water in the electrolyte.

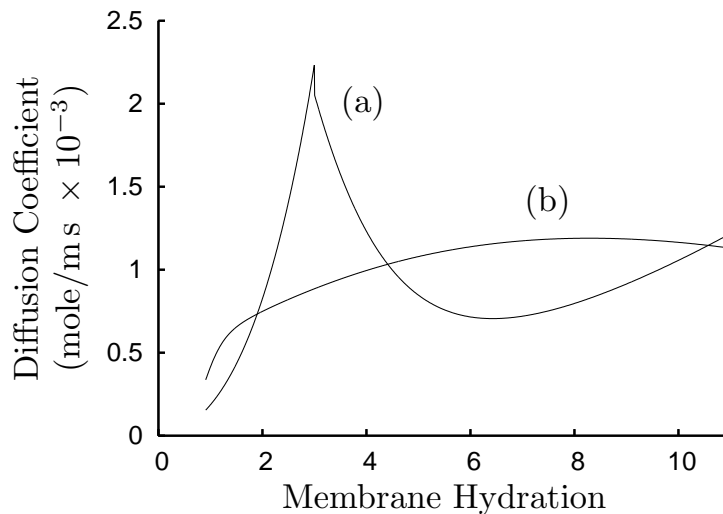


Figure 6.3: The diffusion coefficient of water in the membrane as a function of hydration determined with (a) the Darken factor originally used by Motupally *et al.* [122] and (b) the Darken factor calculated with the hydration function of Futerko and Hsing [115]. The temperature is 353 K.

6.2 Hydronium Diffusion Coefficient

Several experimental studies for determining the conductivity of Nafion exist in the published literature. However, one of the most comprehensive was the study of Sone *et al.* [124], where the conductivity of the membrane was determined for temperatures ranging from 293 to 353 K and membrane activities from 0 to 1. The conductivity was defined as

$$\kappa(\tilde{a}) = -\frac{J}{\nabla\Phi_e}, \quad (6.14)$$

where the electrical conductivity was a function of the membrane activity. The conductivity data was fitted with a third order polynomial:

$$\kappa = a + b(\text{RH}) + c(\text{RH})^2 + d(\text{RH})^3, \quad (6.15)$$

where RH is the relative humidity. Sone *et al.* [124] determined the conductivity for various temperature and membrane heat treatments. In this thesis, the conductivity data for the N-form of Nafion was used because the N-form was heat treated at 80°C; PEM fuel cells typically operate

Table 6.1: The polynomial constants for the experimental conductivity data of Sone *et al.* [124].

Temperature (K)	a ($10^{-1} S/m$)	b ($10^{-2} S/m$)	c ($10^{-4} S/m$)	d ($10^{-6} S/m$)
293	-19.8	16.6	-34.5	28.4
303	-8.01	6.72	-11.6	11.8
318	-1.75	1.45	0.0161	3.45
333	-3.41	2.73	-2.67	5.72
343	-1.56	1.21	1.01	3.95

at a temperature of approximately 353 K. The polynomial constants of Equation (6.15) for the N-form Nafion are reproduced in Table 6.1. Sone *et al.* [124] correlated the electrical conductivity to the relative humidity of the gas phase in equilibrium with the electrolyte. However, the electrical conductivity should be a function of a property within the electrolyte, such as membrane hydration. The relative humidity can be converted to membrane hydration with Equation (4.42).

In order to match this experimental data with the membrane model of this thesis research, the governing equations for the membrane must be simplified in order to correspond to the experimental conditions. No water concentration gradient exists within the membrane; thus, the water and hydronium equations simplify to

$$0 = \frac{1}{c_{\ell,e} D_{\text{H}_2\text{O}-\text{H}_3\text{O}^+, \ell,e}^{\text{eff}}} \left(x_{\ell,e}^{\text{H}_3\text{O}^+} \mathcal{N}_{\ell,e}^{\text{H}_2\text{O}} - x_{\ell,e}^{\text{H}_2\text{O}} \mathcal{N}_{\ell,e}^{\text{H}_3\text{O}^+} \right) + \frac{\mathcal{N}_{\ell,e}^{\text{H}_2\text{O}}}{D_{\text{H}_2\text{O}-s, \ell,e}^{\text{eff}}}, \quad (6.16)$$

$$-\frac{x_{\ell,e}^{\text{H}_3\text{O}^+} \mathcal{F}}{\mathcal{R}T} \nabla \Phi_e = \frac{1}{c_{\ell,e} D_{\text{H}_2\text{O}-\text{H}_3\text{O}^+, \ell,e}^{\text{eff}}} \left(x_{\ell,e}^{\text{H}_2\text{O}} \mathcal{N}_{\ell,e}^{\text{H}_3\text{O}^+} - x_{\ell,e}^{\text{H}_3\text{O}^+} \mathcal{N}_{\ell,e}^{\text{H}_2\text{O}} \right) + \frac{\mathcal{N}_{\ell,e}^{\text{H}_3\text{O}^+}}{D_{\text{H}_3\text{O}^+-s, \ell,e}^{\text{eff}}}. \quad (6.17)$$

The only unknown constant in the above equations is the diffusion coefficient between hydronium and the membrane, $D_{\text{H}_3\text{O}^+-s, \ell,e}^{\text{eff}}$. Using the relationship between current density and molar flux of hydronium,

$$\mathbf{J}_e = \epsilon_{\ell,e} \mathcal{N}_{\ell,e}^{\text{H}_3\text{O}^+} \mathcal{F}, \quad (6.18)$$

an expression for the conductivity from Equations (6.16) and (6.17) can be obtained:

$$\kappa = \frac{\frac{\epsilon_{\ell,e} x_{\ell,e}^{\text{H}_3\text{O}^+} \mathcal{F}^2}{\mathcal{R}T}}{\frac{x_{\ell,e}^{\text{H}_2\text{O}}}{c_{\ell,e} D_{\text{H}_2\text{O}-\text{H}_3\text{O}^+, \ell,e}^{\text{eff}}} - \frac{\frac{x_{\text{H}_3\text{O}^+}^{\text{H}_2\text{O}} x_{\ell,e}^{\text{H}_2\text{O}}}{\left(c_{\ell,e} D_{\text{H}_2\text{O}-\text{H}_3\text{O}^+, \ell,e}^{\text{eff}}\right)^2}}{\frac{x_{\text{H}_3\text{O}^+}}{c_{\ell,e} D_{\text{H}_2\text{O}-\text{H}_3\text{O}^+, \ell,e}^{\text{eff}}} + \frac{1}{D_{\text{H}_2\text{O}-s, \ell,e}^{\text{eff}}}}} + \frac{1}{D_{\text{H}_3\text{O}^+-s, \ell,e}^{\text{eff}}}}. \quad (6.19)$$

The conductivity of Equation (6.19) can be set equal to the conductivity of Sone *et al.* [124] for the range of temperatures and water activity and the value of $D_{\text{H}_3\text{O}^+-s, \ell,e}$ can be determined.

Equation (6.19) can be solved for $D_{\text{H}_3\text{O}^+-s, \ell,e}$:

$$D_{\text{H}_3\text{O}^+-s, \ell,e} = \frac{1}{\sqrt{\epsilon_{\ell,e}}} \left[\frac{\epsilon_{\ell,e} x_{\ell,e}^{\text{H}_3\text{O}^+} \mathcal{F}^2}{\kappa \mathcal{R}T} + \frac{x_{\ell,e}^{\text{H}_2\text{O}}}{c_{\ell,e} D_{\text{H}_2\text{O}-\text{H}_3\text{O}^+, \ell,e}^{\text{eff}}} \left(\frac{\frac{x_{\text{H}_3\text{O}^+}^{\text{H}_2\text{O}}}{c_{\ell,e} D_{\text{H}_2\text{O}-\text{H}_3\text{O}^+, \ell,e}^{\text{eff}}} - 1}{\frac{x_{\text{H}_3\text{O}^+}}{c_{\ell,e} D_{\text{H}_2\text{O}-\text{H}_3\text{O}^+, \ell,e}^{\text{eff}}} + \frac{1}{D_{\text{H}_2\text{O}-s, \ell,e}^{\text{eff}}}} \right) \right]^{-1}, \quad (6.20)$$

where the electrical conductivity, κ , is given by the polynomial relationships of Equation (6.15) and Table 6.1. Figure 6.4 shows the value of $D_{\text{H}_3\text{O}^+-s}$ as a function of membrane hydration for temperatures of 303, 333, and 353 K. As the temperature increases, the diffusion coefficient between hydronium and the polymer matrix also increases.

6.3 Electro-osmotic Drag

With values for all of the diffusivities in the membrane model accounted for, the membrane model can be further validated through the experimentally determined electro-osmotic drag. The electro-

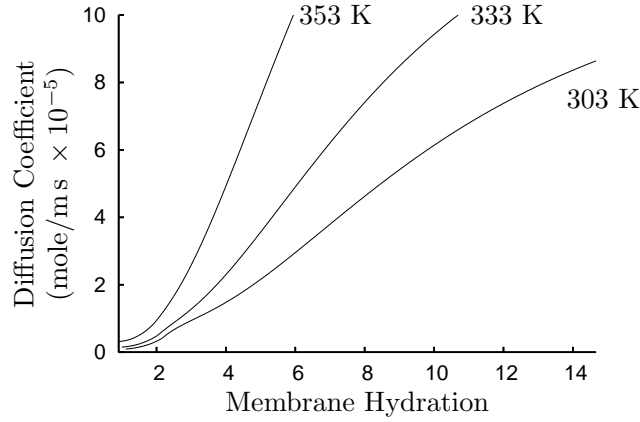


Figure 6.4: The diffusion coefficient for hydronium ions in the membrane as a function of membrane hydration for temperatures of 303, 333, and 353 K.

osmotic drag coefficient for the current membrane model can be expressed as

$$\begin{aligned}
 n_d &= \frac{\mathcal{N}_{l,e}^{\text{H}_2\text{O}} + \mathcal{N}_{l,e}^{\text{H}_3\text{O}^+}}{\mathcal{N}_{l,e}^{\text{H}_3\text{O}^+}} \\
 &= \frac{x_{l,e}^{\text{H}_2\text{O}}}{c_{l,e} D_{\text{H}_3\text{O}^+ - \text{H}_2\text{O}, l, e}^{\text{eff}}} \left(\frac{x_{l,e}^{\text{H}_3\text{O}^+}}{c_{l,e} D_{\text{H}_3\text{O}^+ - \text{H}_2\text{O}, l, e}^{\text{eff}}} + \frac{1}{D_{\text{H}_2\text{O} - s, l, e}^{\text{eff}}} \right)^{-1} + 1.
 \end{aligned} \tag{6.21}$$

Using the diffusion coefficient values that were calculated in the previous sections, the electro-osmotic drag coefficient can be calculated as a function of membrane hydration. Figure 6.5 shows the calculated electro-osmotic drag coefficient as a function of membrane hydration for temperatures of 303, 333, and 353 K. The electro-osmotic drag coefficient ranges from a low value of 1 to a high value of 1.16. This agrees well with the experimental values obtained by Zawodzinski *et al.* [79], which found that the electro-osmotic drag was constant with a value of 1 for the entire range of membrane hydrations when exposed to water vapor. If the value of the binary diffusion coefficient between water and hydronium, $D_{\text{H}_3\text{O}^+ - \text{H}_2\text{O}}$, is increased by one order of magnitude, an almost exact match between the experimental results of Zawodzinski *et al.* [79] and the current membrane model can be obtained. However, in this thesis research, this is not done because some uncertainty exists on the exact value of electro-osmotic drag; the values in Figure 6.5 may be within the experimental error.

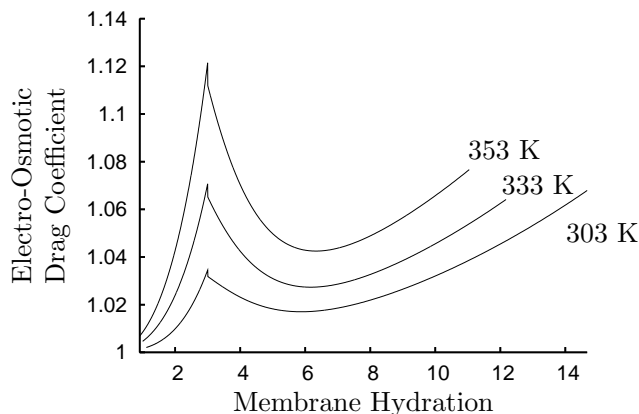


Figure 6.5: Electro-osmotic drag coefficient as a function of membrane hydration for temperature of 303, 333, and 353 K.

In this thesis research, the positive ion in the polymer electrolyte was assumed to be hydronium (H_3O^+), but most other modeling studies assume that the charged species is a free hydrogen ion (H^+). The reason that H_3O^+ , and not H^+ , was chosen as the positive ion is that for acid-base reactions, standard chemical textbooks, such as Mahan and Myers [125], use hydronium for the positive ion. The assumption that the charged ion is hydronium is further justified through the comparison of the membrane model to the electro-osmotic drag data. Using a free hydrogen ion in the electrolyte would result in an electro-osmotic drag coefficient that is much less than one; hence, from the experimental electro-osmotic drag data, it can be concluded that the positive ions are hydronium ions.

6.4 Comparison with Springer Model

Currently, most numerical studies of PEM fuel cells use the electrolyte model of Springer *et al.* [26] to describe the transport of current and water in the polymer electrolyte. The mathematical model of this thesis research used a novel electrolyte transport model; this section compares the electrolyte transport model that is used in this thesis research (the “Thesis” model) to the commonly used model of Springer *et al.* [26] (the “Springer” model).

Within the electrolyte, the Springer model states that current and water transport are governed

by

$$\mathbf{J}_e = -\kappa_e \nabla \Phi_e, \quad (6.22)$$

$$\langle \mathcal{N}_{\ell,e}^{\text{H}_2\text{O}} \rangle = -D_{\text{H}_2\text{O}-e} \nabla \lambda + \frac{n_d}{\mathcal{F}} \mathbf{J}_e. \quad (6.23)$$

where the transport properties of electrical conductivity (κ), diffusion coefficient ($D_{\text{H}_2\text{O}-e}$), and electro-osmotic drag coefficient (n_d) are functions of the membrane hydration. The original values of the electrical conductivity, diffusion coefficient, and electro-osmotic drag coefficient which were presented in Springer *et al.* [26, 27] are generally not used by the recent mathematical models in the published literature. Instead, models, such as Kulikovskiy [64], use the same governing equations as Springer *et al.* [26], but use values of electrical conductivity, diffusion coefficient, and electro-osmotic drag coefficient from other experimental studies, such as Sone *et al.* [124], Zawodzinski *et al.* [123], and Zawodzinski *et al.* [79].

In order to compare the Thesis and Springer models, the transport properties of both models should be derived using the same experimental data. Thus, the electrical conductivity in Equation (6.22) is represented by the experimental data of Sone *et al.* [124] and Equation (6.15). The diffusion coefficient for in Equation (6.23) is given by

$$D_{\text{H}_2\text{O}-e} = \frac{\rho_M D_{w,F}}{\hat{M}_M}, \quad (6.24)$$

where $D_{w,F}$ is defined by Equation (6.5). The electro-osmotic drag coefficient, n_d , is set to the value of one in order to correspond with the experimental data of Zawodzinski *et al.* [79].

For the Thesis model, the mass fluxes of water and hydronium are defined by Equations (4.34) and (4.35). These equations can be converted to relationships similar to the Springer model:

$$\mathbf{J}_e = \frac{\epsilon_{\ell,e} \hat{\mathcal{D}}_{\text{H}_2\text{O}}^{\text{H}_3\text{O}^+}}{\mathcal{F}} \nabla x_{\ell,e}^{\text{H}_2\text{O}} + \frac{\epsilon_{\ell,e} \hat{\mathcal{D}}_{\text{H}_3\text{O}^+}^{\text{H}_3\text{O}^+}}{\mathcal{F}} \nabla \Phi_e, \quad (6.25)$$

$$\langle \mathcal{N}_{\ell,e}^{\text{H}_2\text{O}} \rangle = \epsilon_{\ell,e} \hat{\mathcal{D}}_{\text{H}_2\text{O}}^{\text{H}_2\text{O}} \nabla x_{\ell,e}^{\text{H}_2\text{O}} + \epsilon_{\ell,e} \hat{\mathcal{D}}_{\text{H}_3\text{O}^+}^{\text{H}_2\text{O}} \nabla \Phi_e, \quad (6.26)$$

Table 6.2: The values of \hat{D}_α^β for a fully hydrated membrane at a temperature of 353 K.

α	β	\hat{D}_α^β
H ₂ O	H ₂ O	-6.27×10^{-4} mole/m · s
H ₃ O ⁺	H ₂ O	-9.67×10^{-5} mole/m · V · s
H ₂ O	H ₃ O ⁺	1.68×10^{-5} mole/m · s
H ₃ O ⁺	H ₃ O ⁺	-2.19×10^{-4} mole/m · V · s

where the \hat{D}_α^β terms are related to the \mathcal{D}_α^β of Equations (4.34) and (4.35) with

$$\hat{D}_{\text{H}_2\text{O}}^{\text{H}_3\text{O}^+} = \frac{\hat{M}_{\text{H}_2\text{O}}}{\left(\hat{M}_{\ell,e}\right)^2} \mathcal{D}_{\text{H}_2\text{O}}^{\text{H}_3\text{O}^+}, \quad (6.27)$$

$$\hat{D}_{\text{H}_3\text{O}^+}^{\text{H}_3\text{O}^+} = \frac{\mathcal{D}_{\text{H}_3\text{O}^+}^{\text{H}_3\text{O}^+}}{\hat{M}_{\text{H}_3\text{O}^+}}, \quad (6.28)$$

$$\hat{D}_{\text{H}_2\text{O}}^{\text{H}_2\text{O}} = \frac{\hat{M}_{\text{H}_3\text{O}^+}}{\left(\hat{M}_{\ell,e}\right)^2} \mathcal{D}_{\text{H}_2\text{O}}^{\text{H}_2\text{O}}, \quad (6.29)$$

$$\hat{D}_{\text{H}_3\text{O}^+}^{\text{H}_2\text{O}} = \frac{\mathcal{D}_{\text{H}_3\text{O}^+}^{\text{H}_2\text{O}}}{\hat{M}_{\text{H}_2\text{O}}}. \quad (6.30)$$

The \hat{D}_α^β can be either negative or positive. Using the diffusion coefficients that were determined in this chapter, the values of \hat{D}_α^β can be calculated as functions of membrane hydration and temperature. For a fully hydrated electrolyte at a temperature of 353 K, the values of \hat{D}_α^β are tabulated in Table 6.2. All but one of the \hat{D}_α^β terms are negative, with the single positive coefficient being $\mathcal{D}_{\text{H}_3\text{O}^+}^{\text{H}_2\text{O}}$.

The Thesis model reduces to the Springer model if the current density does not depend on the water gradient: $\hat{D}_{\text{H}_2\text{O}}^{\text{H}_3\text{O}^+} = 0$. Thus, while the Springer model incorporates electro-osmotic flow, which is characterized by fluid flow induced with a potential gradient, it does not include the complimentary effect of the streaming potential, in which a potential gradient is induced by fluid flow [105]. The effect of this assumption can be illustrated by simulating the one-dimensional membrane shown in Figure 6.6. The electrolyte layer of Figure 6.6 has no-flux boundary conditions in the x direction, and specified potential and hydration in the y direction. The anode potential and hydration are denoted by $\Phi_e|_a$ and $\mathcal{L}|_a$, respectively, while the cathode potential and hydration

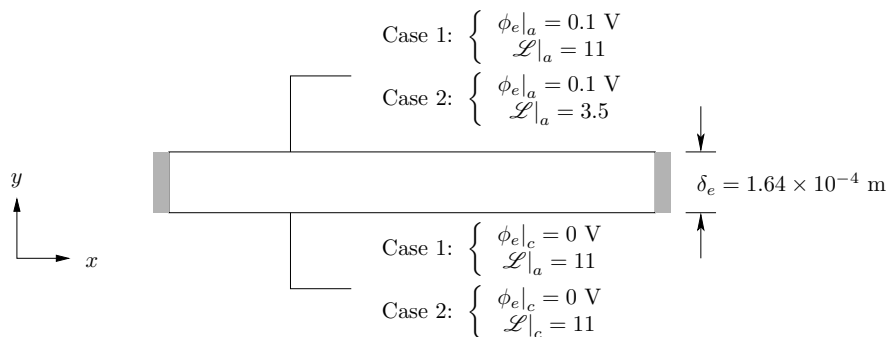


Figure 6.6: One-dimensional membrane simulation for comparing the Thesis and Springer models.

are denoted by $\Phi_e|_c$ and $\mathcal{L}|_c$.

The Thesis and Springer models are applied to the problem of Figure 6.6 with two different sets of boundary conditions. For both sets of boundary conditions, or cases, the temperature is 353 K. In the first set of boundary conditions, the membrane hydration is set to 11 at both the anode and cathode boundaries; a membrane hydration of 11 corresponds to a relative humidity of 100%. Thus, no water concentration gradient exists across the membrane for case 1, but a potential gradient does exist, with the anode potential being set to 0.1 V and the cathode potential grounded at a value of 0 V. Case 2 has both a concentration and potential gradient. The potential boundary conditions are the same between cases 1 and 2. At the cathode side of the electrolyte, the membrane hydration is set to 11, but at the anode side of the electrolyte, the membrane hydration is set to 3.5, which corresponds to the hydration if the membrane is in equilibrium with a gas with 50% humidity. Since water is produced in the cathode and water is consumed in the anode, case 2 approximates the conditions occurring within a PEM fuel cell.

For both cases, the current density and total water molar flux are compared in Table 6.3. For the Springer model, the total molar flux of water is given by Equation (6.23), but for the Thesis model, the total molar flux of water must include the water contained in the hydronium ion:

$$\mathcal{N}_{\ell,e}^{\text{H}_2\text{O}}|_{\text{total}} = \langle \mathcal{N}_{\ell,e}^{\text{H}_2\text{O}} \rangle + \frac{\mathbf{J}_e}{\mathcal{F}}. \quad (6.31)$$

For case 1, the Thesis and Springer models yield similar values for current density and total water

Table 6.3: Comparison between the Thesis and Springer electrolyte models.

Case	Thesis Model		Springer Model		Difference	
	Current	Total	Current	Total	Current	Total
	Density (A/m ²)	Water Flux (mole/m ² · s)	Density (A/m ²)	Water Flux (mole/m ² · s)	Density (%)	Water Flux (%)
1	-3.48×10^3	-4.07×10^{-2}	-3.49×10^3	-3.62×10^{-2}	0.3	12
2	-1.51×10^3	1.82×10^{-2}	-1.04×10^2	-9.34×10^{-3}	31	151

flux. If the difference between the Thesis and Springer model outputs are quantified as

$$\text{Difference} = \left| \frac{\text{Thesis Value} - \text{Springer Value}}{\text{Thesis Value}} \right| \times 100\%, \quad (6.32)$$

then the difference for the current densities is less than 0.3% and 12% for the total water flux. The current densities between the Thesis and Springer models match well because they are both based on the same experimental data. Since there is no concentration gradient within the electrolyte in case 1, the equations for the flux of charged species for the Thesis and Springer models become equal. However, the predicted total water flux is larger for the Thesis model than for the Springer model because the Springer model uses an electro-osmotic drag coefficient of 1, while the electro-osmotic drag coefficient for the Thesis model ranges from 1 to 1.12, as shown in Figure 6.5.

While case 1 shows minor discrepancies between the Thesis and Springer models, case 2 shows a large difference between both the predicted current densities and total water flux. The current density predicted from the Thesis model is significantly larger than the prediction from the Springer model; the difference is approximately 31%. This difference in current density comes from two sources. The first source is the influence of the mole fraction gradient term in Equation (6.25). The mole fraction gradient term is

$$\frac{\epsilon_{\ell,e} \hat{D}_{\text{H}_2\text{O}}^{\text{H}_3\text{O}^+}}{\mathcal{F}} \nabla x_{\ell,e}^{\text{H}_2\text{O}} = \frac{(\text{positive})(\text{positive})}{\mathcal{F}} (\text{negative}) = \text{negative};$$

thus, the mole fraction gradient is beneficial for the current density and the current density from the Thesis model is greater than that of the Springer model.

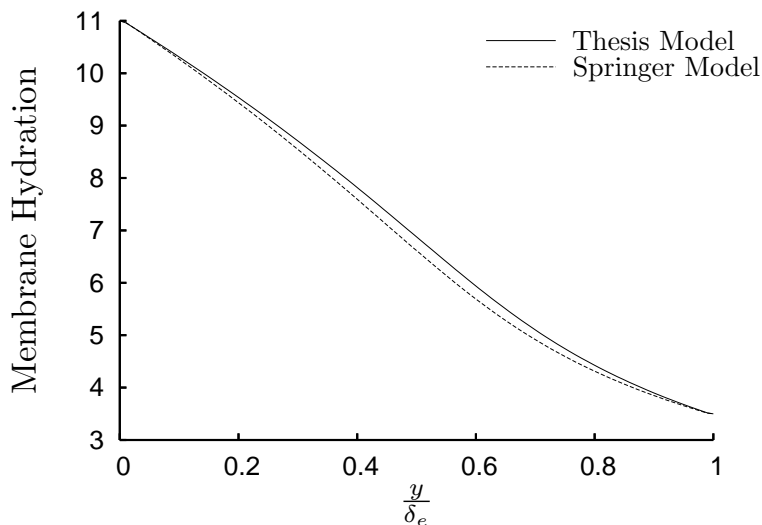


Figure 6.7: The membrane hydration predicted by the Thesis and Springer models for case 2.

The second factor influencing the larger predicted current density in the Thesis model is the difference in water flux between the two models. For the boundary conditions described in Section 6.1, in which the current density is zero but a water concentration gradient exists, both the Thesis and Springer models would predict the same total water flux. This is due to both models being based on the same experimentally derived diffusion coefficient, Equation (6.5). However, in the presence of a potential gradient, the water flux predictions from both models diverge. In the Thesis model, the direction of the water flux is from the cathode to the anode, while the Springer model predicts that the water flux is from the anode to the cathode. Therefore, the Thesis model predicts that the water concentration gradient has a greater influence on water motion than the Springer model if a potential gradient is present.

The different water flux values between the two models affect the predicted current density through the value of membrane hydration. The predicted membrane hydrations from both models are illustrated in Figure 6.7. Throughout the membrane, the Thesis model predicts a larger membrane hydration than the Springer model. Since the resistance to charge transport decreases with increasing hydration, the predicted current density is larger for the Thesis model than the Springer model.

Therefore, there are similarities and differences between the electrolyte transport model used in this thesis and the commonly used model of Springer *et al.* [26]. The Springer model can be derived from the Thesis model if the effect of concentration gradient on current transport is neglected. If the current density is zero, both models will predict the same amount of water transport from a water concentration gradient. Also, if no water concentration gradient exists within the electrolyte, both models predict the same current density if a potential gradient is applied across the membrane. As well, the predicted total water flux under these boundary conditions is similar. However, the predictions of the two models are significantly different for boundary conditions that include both water concentration and potential gradients. The Thesis model predicts a larger current density than the Springer model and the water flux due to the concentration gradient is predicted to be larger by the Thesis model than the Springer model. This discrepancy is significant because under fuel cell operation, both potential and concentration gradients exist within the polymer electrolyte layer. Thus, the use of the Springer model, with the assumption that concentration gradients are insignificant for current transport, may not be justified for modeling the polymer electrolyte in a PEM fuel cell.

6.5 Summary

The thesis research used a transport model for water and ions in the polymer electrolyte that was based upon the Generalized Stefan-Maxwell equations. As a result, values for the diffusion coefficients were not available from the published literature and had to be determined from published, experimental data for membrane water diffusion and conductivity. Using these diffusion coefficients, the electrolyte model was further validated by comparing the model output with published data for the phenomena of electro-osmotic drag. Good agreement was obtained between the model and the experimental, electro-osmotic drag data.

The electrolyte model used in this thesis research was compared with the semi-empirical model that was commonly used in published, PEM fuel cell modeling studies. The electrolyte model in

this thesis reduced to the semi-empirical model if charge transport due to concentration gradients was neglected. By ignoring charge transport via concentration gradients, the semi-empirical model under-estimated the current density, when compared to the transport model used in this thesis.

Chapter 7

Results and Discussion

A mathematical PEM fuel cell model can illustrate the physical phenomena occurring within a PEM fuel cell. This is significant because direct measurement of quantities such as velocity or concentration within all layers of a PEM fuel cell is impossible, due to the thinness of the layers. Therefore, this chapter highlights some of the processes that the current PEM fuel cell model illustrates.

In order to examine the processes occurring within a PEM fuel cell, values for the boundary conditions and design parameters are required. These values are obtained from a previously published experimental investigation of PEM fuel cell performance [126]. For the boundary conditions and design parameters chosen from the experimental investigation, the number of control volumes required for the mesh and the convergence criteria are determined. Then, the gas phase velocity, species mass fluxes, and reactant concentrations are examined, as well as the mass flux, current, and potential distribution within the polymer electrolyte. First, however, the numerical method is validated against another CFD computer code.

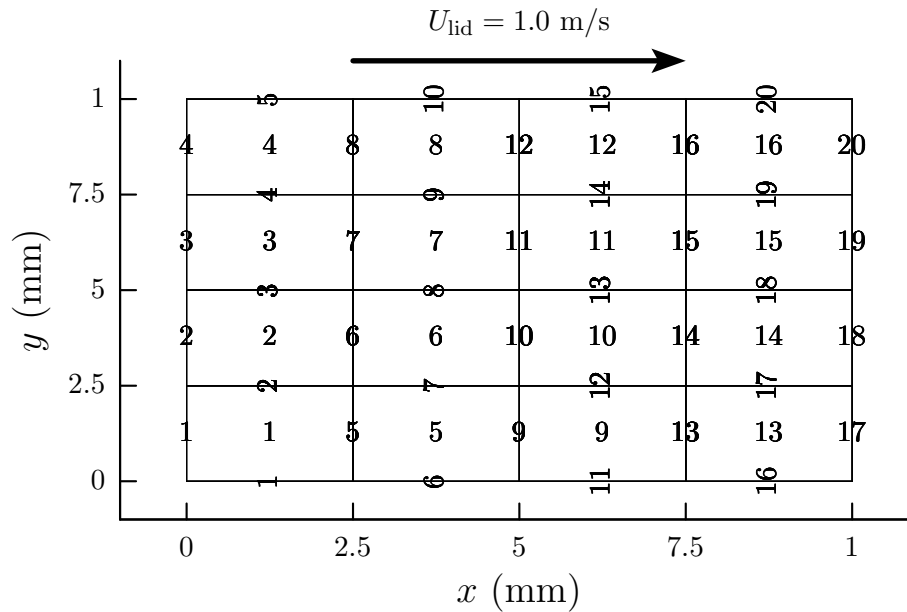


Figure 7.1: Test case for validating the numerical procedure.

7.1 Validation

The numerical procedure outlined in the previous chapter was implemented using the computer language of C++. During implementation, the possibility exists that errors could be introduced into the subroutines, which would affect the values of velocity, pressure, partial density and potential. Therefore, the mathematical model developed for this thesis research was compared with a CFD code that was available from Ferziger and Perić [120]. Ferziger and Perić [120] used a similar grid structure and solution method as the current model, and thus the results generated by the two computer programs should be identical for the same test case. The test case chosen was lid-driven cavity flow, since the code of Ferziger and Perić [120] was designed to illustrate such a flow problem. This test case is illustrated in Figure 7.1. The cavity configuration was square, with each side being 1 mm, and the mesh was 4×4 control volumes. The velocity of the lid was 1 m/s and the fluid has a constant density and viscosity of 1 kg/m^3 and $1 \times 10^{-5} \text{ Pa}\cdot\text{s}$. The u velocities of the thesis research and the program of Ferziger and Perić [120] were compared and are tabulated in Table 7.1. As can be seen in the table, the x direction velocities match perfectly; similar results occur if the y direction velocity and pressure are compared. Therefore, from these results, it can be concluded

Face Number	Thesis Code (m/s)	Ferziger and Perić [120] (m/s)
5	-3.98×10^{-2}	-3.98×10^{-2}
6	-6.05×10^{-2}	-6.05×10^{-2}
7	-4.18×10^{-2}	-4.18×10^{-2}
8	1.42×10^{-1}	1.42×10^{-1}
9	-6.91×10^{-2}	-6.91×10^{-2}
10	-9.46×10^{-2}	-9.46×10^{-2}
11	-5.47×10^{-2}	-5.47×10^{-2}
12	2.18×10^{-1}	2.18×10^{-1}
13	-5.95×10^{-2}	-5.95×10^{-2}
14	-7.53×10^{-2}	-7.53×10^{-2}
15	-3.37×10^{-2}	-3.37×10^{-2}
16	1.68×10^{-1}	1.68×10^{-1}

Table 7.1: The comparison between the thesis research code and that of Ferziger and Perić [120] for lid driven cavity flow: x direction velocity.

that the numerical procedure is free from errors.

7.2 Model Input Parameters

Comparing the model with experimental data is challenging because the current model does not include liquid water transport in the electrode backing layers and gas flow channels. Therefore, the model must be compared against data that is not undergoing liquid water flooding. One way to avoid data influenced by liquid water flooding is to use experimental data that is gathered under high stoichiometry or flow rate conditions. The high flow rate allows for the removal of liquid water from the cells by the flow in the gas flow channels. The stoichiometry is defined as

$$St = \frac{\mathcal{N}_g^\alpha|_{\text{in}}}{\mathcal{N}_g^\alpha|_{\text{react}}}, \quad (7.1)$$

where $\mathcal{N}_g^\alpha|_{\text{in}}$ is inlet molar flow rate of reactant α and $\mathcal{N}_g^\alpha|_{\text{react}}$ is the rate of species α consumption. From Faraday's law, the anode and cathode rates of consumption are related to the cell current density

$$\mathcal{N}_g^{\text{H}_2}|_{\text{react}}^{\text{anode}} = \frac{JA_{\text{cell}}}{2\mathcal{F}}, \quad (7.2)$$

Table 7.2: The operating conditions for the high stoichiometry data from Mughal [127].

Parameter	Value
Outlet Pressure	1 atm
Cell Temperature	343 K
Anode Reactants	Hydrogen with 100% Humidity
Cathode Reactants	Air with 100% Humidity
Anode Stoichiometry	3
Cathode Stoichiometry	5
Cell Voltage	0.8 V
Cell Current Density	220 A/m ²

$$\mathcal{N}_g^{\text{O}_2} \Big|_{\text{react}}^{\text{cathode}} = \frac{JA_{\text{cell}}}{4\mathcal{F}}. \quad (7.3)$$

As the cell stoichiometry is increased, the cell current density increases but eventually plateaus such that further increases in stoichiometry no longer affect the current density.

Another operating condition that would minimize water flooding is the operation at high cell voltages and low current densities. Since the amount of water produced in the fuel cell is proportional to the current density, a low current density would produce a smaller amount of liquid water. Therefore, the model is compared against experimental data that has been gathered under the operating conditions of high stoichiometry and low current density.

Such an experimental study has been undertaken in Mughal [127] and Mughal and Li [126], which produced several polarization curves at different operating conditions using a single 50 cm² fuel cell. The operating conditions chosen for the comparison to the mathematical model are shown in Table 7.2. During the experiments, the cell exhausted to atmospheric pressure and operated at a temperature of 343 K. Fully humidified hydrogen was supplied at a stoichiometry of 3 to the anode, while the cathode of the cell was supplied with fully humidified air at a stoichiometry of 5. At these operating conditions, the cell potential was 0.8 V and the current density was 220 A/m². The operating conditions listed in Table 7.2 translate into boundary conditions that are illustrated in Figure 7.2

In addition to the boundary conditions, the mathematical model also requires the design pa-

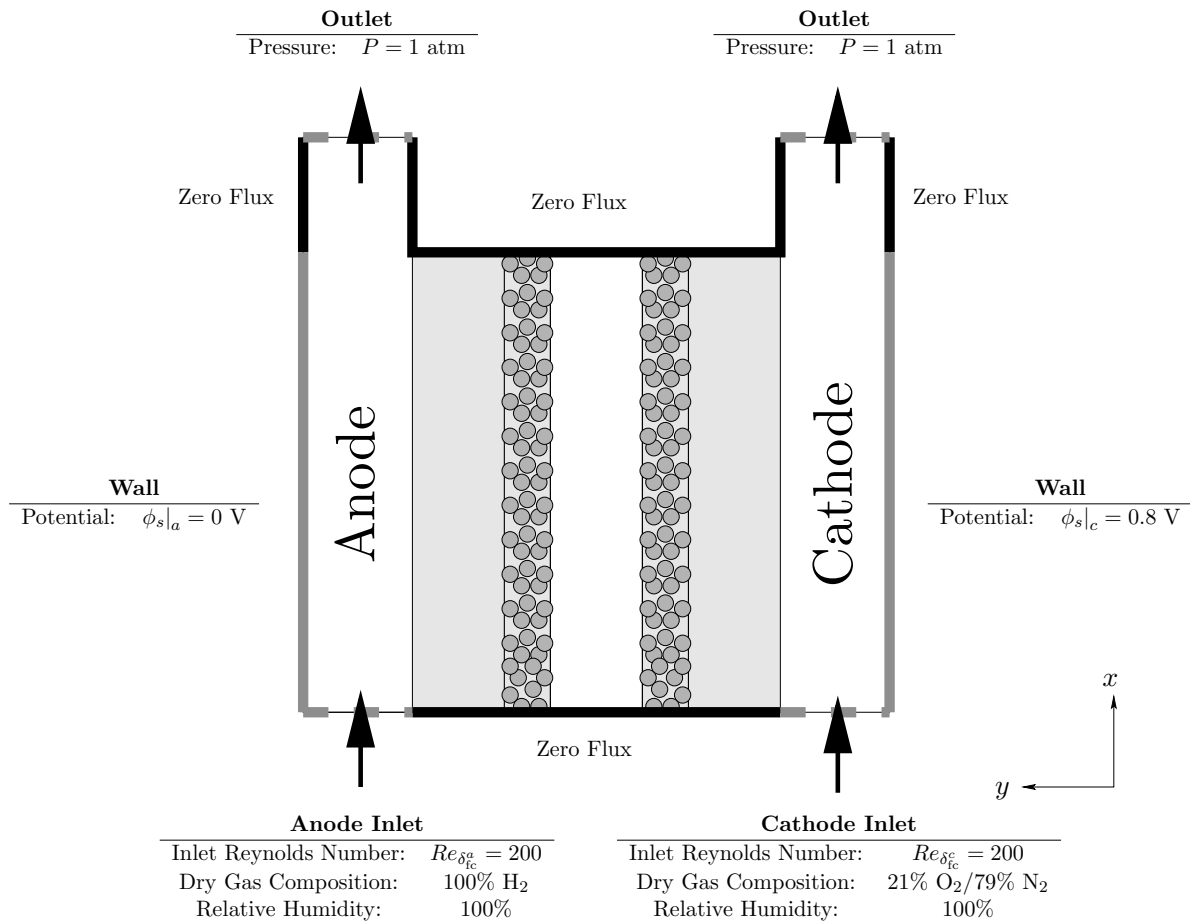


Figure 7.2: The boundary conditions used for comparing the mathematical model with experimental data.

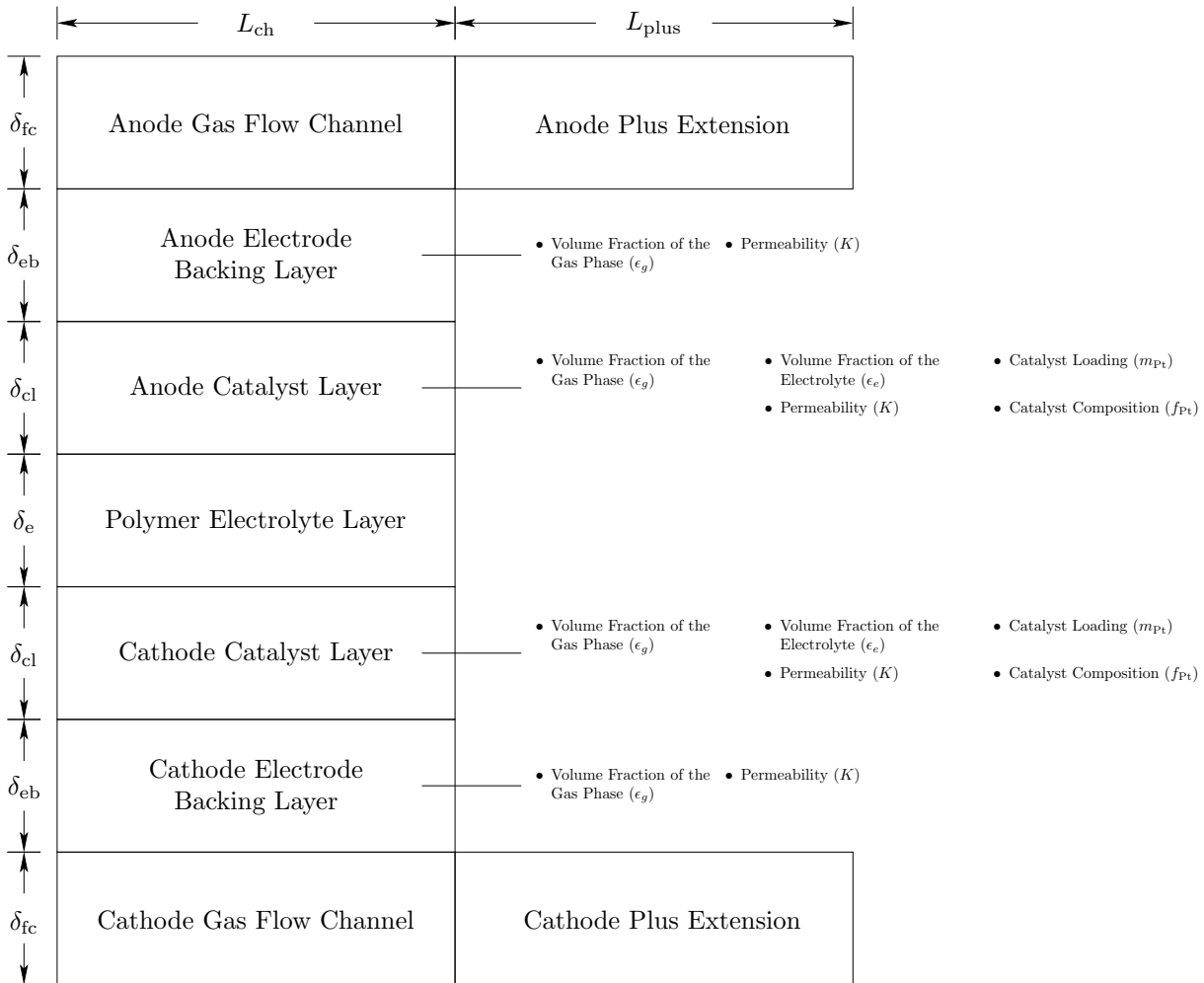


Figure 7.3: The design parameters required for the PEM fuel cell model.

rameters of the experimental cell. The parameters required for the simulation are illustrated in Figure 7.3. Since each layer has a distinct structure, the design parameters can be grouped according to the relevant layer. The anode and cathode layers are identical; hence, the same design parameters apply to the gas flow channels, electrode backing and catalyst layers on the anode and cathode sides. For the gas flow channels, the thickness of the flow channel is required for the mathematical model. The thickness, volume fraction of the gas phase, and the permeability are the design parameters associated with the electrode backing layer. The catalyst layers have several design parameters associated with them. As with the other layers, the thickness is required. The catalyst layer contains a three phase mixture of solid, gas and electrolyte; thus, the volume

Table 7.3: Catalyst surface area per unit mass of catalyst (A_s) as a function of mass ratio of platinum to carbon support (f_{Pt}) [128]

f_{Pt}	A_s (m ² /g)
0.1	140
0.2	112
0.3	88
0.4	72
0.6	32
0.8	11
1	28

fractions of gas and electrolyte are needed for the simulation, as well as the permeability. The platinum loading of the catalyst is also a key parameter, as well as the catalyst composition, which is the mass fraction of platinum in the platinum/carbon support mixture. The platinum loading and the catalyst composition are used to calculate the reactive surface area per unit volume in the catalyst layer:

$$A_v = \frac{A_s m_{Pt}}{\delta_{cl}}, \quad (7.4)$$

where A_s is the catalyst surface area per unit mass of catalyst and is related to the mass ratio of platinum to carbon support according to Table 7.3 [128]. The electrolyte layer has only one independent design parameters: the thickness.

The design parameters used for the comparison to the experimental data are listed in Table 7.4. The thickness of the gas flow channel was measured from the experimental cell to be 1 mm, while the thickness of the electrode backing layer was specified as 2.03×10^{-4} m by the cell manufacturer. The volume fraction of the gas and the permeability were not specified, and had to be estimated from an earlier study [129]. Only two of the design parameters in the catalyst layer were specified by the manufacturer: the catalyst loading of 1 mg/cm² and the mass ratio of platinum in the solid catalyst of 0.2. These two parameters can be used to relate the porosity and thickness:

$$\epsilon_{cl} = 1 - \left(\frac{1}{\rho_{Pt}} + \frac{1 - f_{Pt}}{f_{Pt} \rho_C} \right) \frac{m_{Pt}}{\delta_{cl}}, \quad (7.5)$$

Table 7.4: The design parameters used for comparing the mathematical model with experimental data.

Layer	Parameter	Value
Gas Flow Channel	δ_{fc}	1×10^{-3} m
Electrode Backing Layer	δ_{eb}	2.03×10^{-4} m
	ϵ_g	0.5
	K	1.76×10^{-11} m ²
	δ_{cl}	2.55×10^{-5} m
Catalyst Layer	ϵ_g	0.1
	ϵ_e	0.1
	K	1.76×10^{-11} m ²
	m_{Pt}	1 mg/cm ²
	f_{Pt}	0.2
	δ_{cl}	1.64×10^{-4} m
Polymer Electrolyte Layer	δ_{cl}	1.64×10^{-4} m
Channel Length	L_{ch}	1×10^{-3} m
Anode and Cathode Plus Extensions	L_{plus}	1×10^{-2} m

where ϵ_{cl} is the void fraction of the catalyst layer, ρ_{Pt} is the density of platinum and ρ_C is the density of carbon. Therefore, the void fraction was arbitrarily set to 0.2, which allowed the thickness to be calculated as 2.55×10^{-5} m. The void space was assumed to consist of an equal volume of electrolyte and gas. The polymer electrolyte used was Nafion 115; thus, the thickness of the layer was taken from Baschuk and Li [12].

The length of the fuel cell gas flow channels in the experimental cell was 7.5 cm. However, this length could not be used in the mathematical model because it was too long; convergence of the numerical procedure would be too time consuming. Since the data was gathered under high stoichiometry conditions, the reactant concentrations would not vary significantly along the channel. Thus, a small channel length could be reasonably used to simulate the experimental data. Therefore, a channel length (L_{ch}) of 1 mm was used for the simulations, with outlet channel extensions of 1 cm (L_{plus}).

7.3 Grid Independent Solution

Before the mathematical model can be compared to the experimental data, the number of grid points required for a grid independent solution must be determined. The mesh used for the comparison between the mathematical model and experimental data is illustrated in Figure 7.4. The number of control volumes is specified for each layer of the PEM fuel cell and the grid spacing within each layer is uniform. The number of control volumes in the x direction for the anode and cathode gas flow channels is denoted by N_{ch}^x , while the number of control volume used for the anode and cathode plus extensions is denoted by N_{plus}^x . For the anode and cathode electrode backing layers, the number of control volumes in the y direction are $N_{\text{eb,a}}^y$ and $N_{\text{eb,c}}^y$, respectively. Similarly, $N_{\text{cl,a}}^y$ and $N_{\text{cl,c}}^y$ denote the number of control volumes in the y direction for the anode and cathode catalyst layers. The number of y direction control volumes for the polymer electrolyte layer is represented by N_{e}^y . Although the number of control volumes in the y direction can be different for the anode and cathode sides of the PEM fuel cell, in practice the same values are used for both sides:

$$N_{\text{fc}}^y = N_{\text{fc,a}}^y = N_{\text{fc,c}}^y, \quad (7.6)$$

$$N_{\text{eb}}^y = N_{\text{eb,a}}^y = N_{\text{eb,c}}^y, \quad (7.7)$$

$$N_{\text{cl}}^y = N_{\text{cl,a}}^y = N_{\text{cl,c}}^y. \quad (7.8)$$

Therefore, the total number of control volumes used for the simulation, N_{total} , is

$$N_{\text{total}} = N_{\text{ch}}^x [2 (N_{\text{fc}}^y + N_{\text{eb}}^y + N_{\text{cl}}^y) + N_{\text{e}}^y] + 2N_{\text{fc}}^y N_{\text{plus}}^x. \quad (7.9)$$

Determining the number of grid points required for an accurate solution was done using two steps. For the first step, only the cathode gas flow channel was simulated, and the length of the channel was set at $L_{\text{ch}} = 5$ cm, while the thickness remained the same as in Table 7.4. The aspect ratio of the control volumes was taken as one; hence, $\Delta = \Delta x = \Delta y$. Hence, if the number of

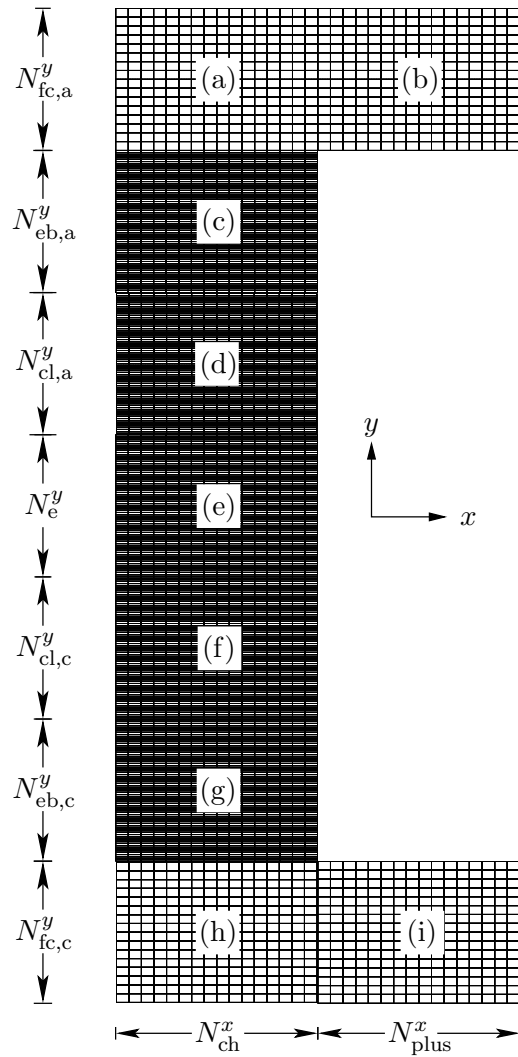


Figure 7.4: The mesh used for the comparison between the mathematical model and experimental data. The regions are the (a) anode gas flow channel, (b) anode plus extension, (c) anode electrode backing layer, (d) anode catalyst layer, (e) polymer electrolyte layer, (f) cathode catalyst layer, (g) cathode electrode backing layer, (h) cathode gas flow channel, (i) cathode plus extension. Note that the figure is not drawn to scale.

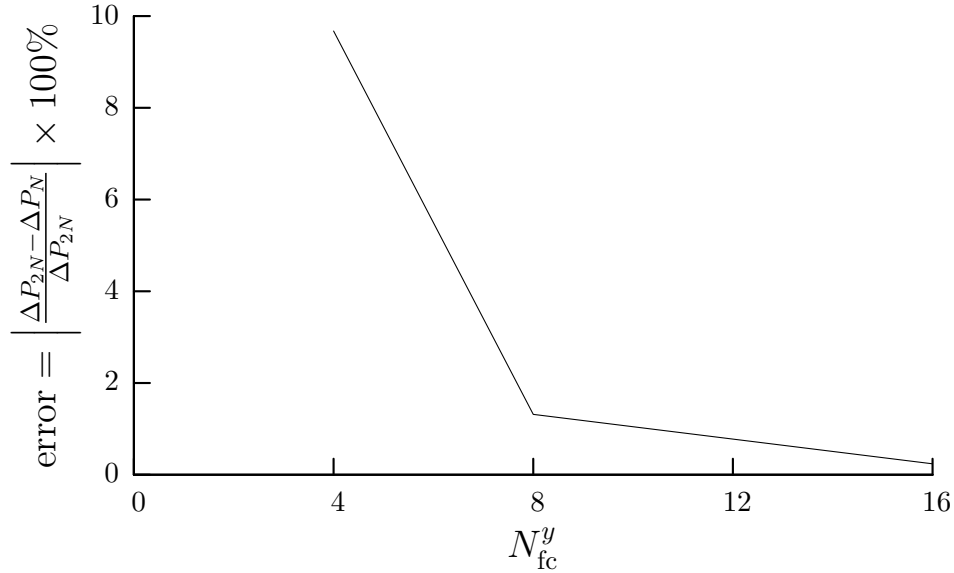


Figure 7.5: The effect of the number of control volumes on the error in the pressure drop.

control volumes in the y direction was specified, the number of control volumes in the x direction became

$$N_{ch}^x = \frac{L_{ch}}{\delta_{fc}} N_{fc}^y. \quad (7.10)$$

In order to determine the number of control volumes required for the grid-independent solution, the pressure drop along the channel was calculated for various values of N_{fc}^y for an inlet Reynolds number of 200. Figure 7.5 shows the pressure drop error for N_{fc}^y of 4, 8, and 16. The number of control volumes in the y direction was determined from Equation (7.10). The error was calculated as

$$\text{error} = \left| \frac{\Delta P_{2N} - \Delta P_N}{\Delta P_{2N}} \right| \times 100\%, \quad (7.11)$$

where ΔP_N is the pressure drop along the length of the channel for $N_{fc}^y = N$ and ΔP_{2N} is the pressure drop associated with $N_{fc}^y = 2N$. The error is approximately 0.2% for a N_{fc}^y of 16; hence, a grid spacing of 0.0626 mm ensures a grid independent solution for the channel.

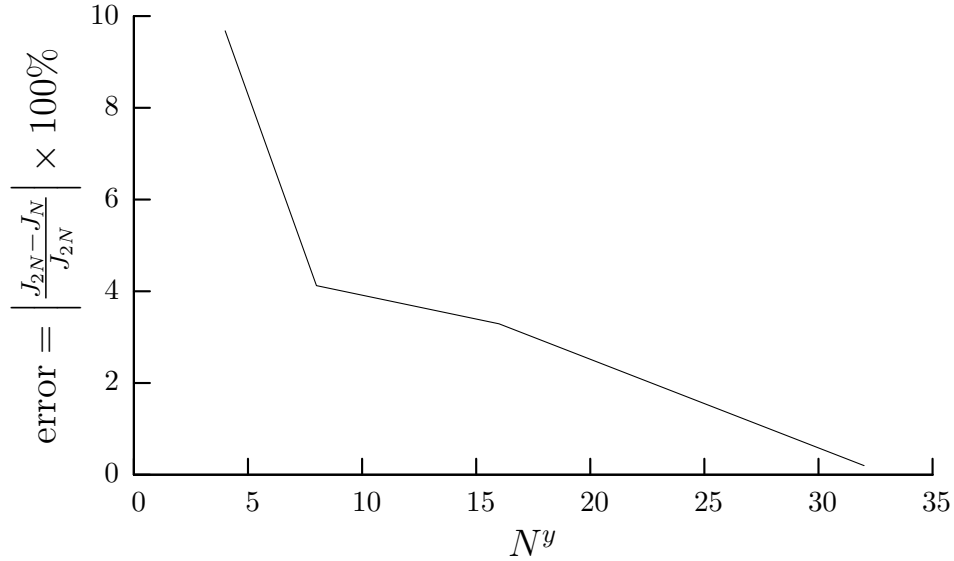


Figure 7.6: The effect of the number of control volumes on the error in the current density.

In the second step of finding the number of control volumes required for a grid independent solution, the number of y direction control volumes for the electrode backing, catalyst, and electrolyte layers was determined. The entire PEM fuel cell was simulated with the boundary conditions listed in Figure 7.2. For the design parameters listed in Table 7.4, the same number of control volumes in the y direction were used for the electrode backing, catalyst and electrolyte layers:

$$N_{\text{eb}}^y = N_{\text{cl}}^y = N_{\text{e}}^y = N^y. \quad (7.12)$$

Figure 7.6 illustrates the effect of increasing the number of control volumes, N^y , on the current density in the solid phase. The error in the current density is defined as

$$\text{error} = \left| \frac{J_{2N} - J_N}{J_{2N}} \right| \times 100\%, \quad (7.13)$$

where J_N is the current density for cell for $N^y = N$ and J_{2N} is the current density corresponding to $N^y = 2N$. From Figure 7.6, the grid independent solution occurs when $N > 32$.

Thus, the number of control volumes required for a grid independent solution was obtained

Table 7.5: The number of control volumes required for a grid independent solution.

Number of y direction control volumes	$N_{fc,a}^y = N_{fc,c}^y = 16$ $N_{eb,a}^y = N_{eb,c}^y = N_{cl,a}^y = N_{cl,c}^y = N_{e,c}^y = 32$
Number of x direction control volumes	$N_{ch}^x = 16$ $N_{plus}^x = 160$

using two steps. The first step determined the grid spacing required in the gas flow channels, while the second step found the number of control volumes needed in the electrode backing, catalyst and polymer electrolyte layers. For the PEM fuel cell with the design parameters listed in Table 7.4, the number of control volumes required are listed in Table 7.5. The total number of control volumes used for the simulations is 8192.

7.4 Convergence Criteria

The iterative solution procedure ends when the residuals are below the convergence criteria (tol) and the choice of tol was influenced by the error in the gas phase density. The conservation of species in the gas phase are solved for the partial density. However, the total gas density, which is used in the conservation of mass and momentum equations, is calculated using the ideal gas law:

$$\rho_g = \frac{P}{RT}, \quad (7.14)$$

where the gas constant, R , is a function of the gas composition through the mass fractions. The mass fractions are determined from the partial densities:

$$\omega_g^\alpha = \frac{\rho_g^\alpha}{\sum_\beta \rho_g^\beta}. \quad (7.15)$$

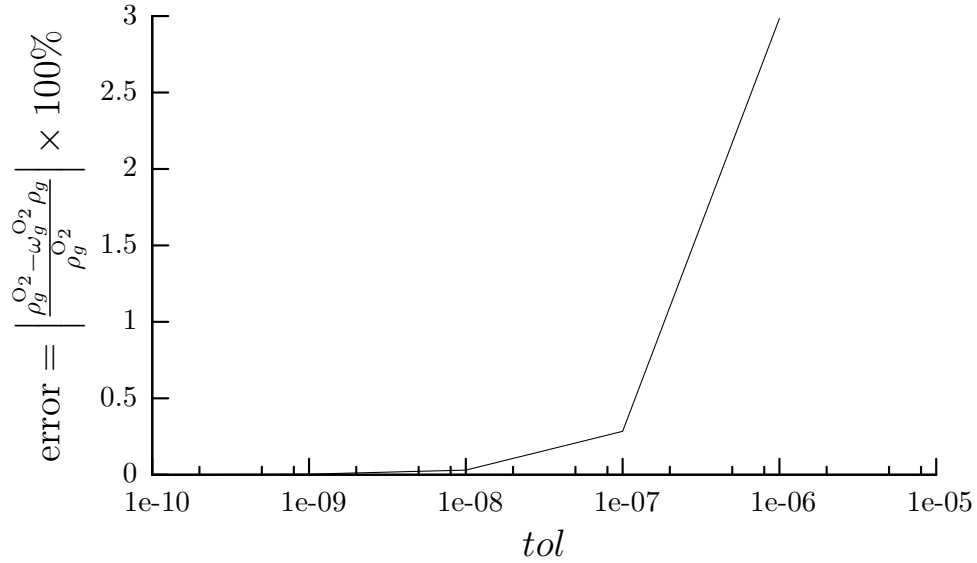


Figure 7.7: The effect of convergence criteria on the error in the partial density of oxygen.

If the conservation of mass, momentum, and species are solved exactly, then the partial density of a gas species would be

$$\rho_g^\alpha = \omega_g^\alpha \rho_g \quad (7.16)$$

However, since tol is not equal to zero, an error exists, which can be defined as

$$\text{error} = \left| \frac{\rho_g^\alpha - \omega_g^\alpha \rho_g}{\rho_g^\alpha} \right| \times 100\% \quad (7.17)$$

By decreasing the convergence criteria, the error of Equation (7.17) can be decreased. Figure 7.7 illustrates the effect of the convergence criteria, tol , on the partial density error for oxygen in the cathode. The error decreases rapidly with lower tol , with a tol of 1×10^{-8} resulting in a density error of less than 0.1%. Therefore, the convergence criteria was chosen to be 1×10^{-8} .

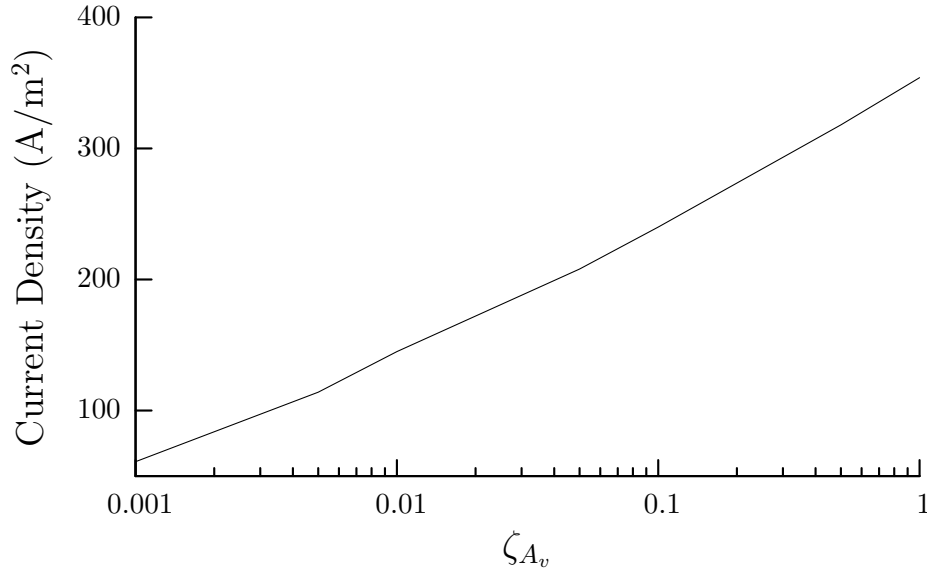


Figure 7.8: Current density as a function of ζ_{A_v} .

7.5 Comparison to Experimental Data

Using the boundary conditions shown in Figure 7.2, the design parameters listed in Table 7.4, the number of control volumes tabulated in Table 7.5, and the convergence criteria of 1×10^{-8} , the mathematical model was compared to the experimental data of Table 7.2. The current density predicted by the mathematical model was compared to the experimental current density of 220 A/m^2 . However, the resulting current density exceeded that of the experimental data. One possible explanation for this discrepancy is that the reactive surface area of the real PEM fuel cell is lower than the result of Equation (7.4). Therefore, the reactive surface area was reduced by multiplying by a factor, ζ_{A_v} :

$$\tilde{A}_v = \zeta_{A_v} A_v, \quad (7.18)$$

where A_v is the reactive surface area per unit volume calculated by Equation (7.4). The current density at a cell voltage of 0.8 V as a function of ζ_{A_v} is illustrated in Figure 7.8. Examining the figure, the current density is a logarithmic function ζ_{A_v} . In order to obtain a current density of

220 A/m², the value of ζ_{A_v} should be 6.5×10^{-2} . If this value is used in a simulation, then the output current density of the model is 217 A/m²; thus, the model matches the experimental data. Adjusting the reactive surface area per unit volume to match the experimental data can be justified. Equation (7.4) determines the reactive surface area per unit volume for the void space. However, it does not take into account the effect of the three phase boundary. In order for a reaction to occur, both the gas, electrolyte and solid phase must be in contact. Therefore, a large reduction in reactive surface area from the ideal case is reasonable.

7.6 Transport Phenomena Within the PEM Fuel Cell

A mathematical PEM fuel cell model allows for the study of the processes occurring within the fuel cell. For the boundary conditions and design parameters of Section 7.5, the processes occurring within the gas, solid, and liquid phase within the electrolyte are examined in this section. The bulk motion of the gas phase is examined in Section 7.6.1. Within the gas phase, the transport of hydrogen, in the anode, and oxygen, in the cathode is explored in Sections 7.6.2 and 7.6.3. Section 7.6.4 presents the transport of liquid water in both the gas phase and liquid phase of the polymer electrolyte pores. Charge transport, both due to electrons in the solid phase and hydronium ions in the electrolyte, are examined in Sections 7.6.5 and 7.6.6, respectively. The distribution of reaction rate in the catalyst layers is explored in Section 7.6.7. Finally, the effect of channel length on the water content and performance of a fuel cell is shown in Figure 7.6.8

7.6.1 Bulk Gas Phase Transport

The bulk flow of the gas phase can be illustrated through the use of the stream function:

$$\frac{\partial \psi}{\partial x} = u_g \qquad \frac{\partial \psi}{\partial y} = -v_g \qquad (7.19)$$

where ψ is the stream function and a contour plot of ψ results in the streamlines of the flow [130]. The streamlines of the numerical simulation are illustrated in Figure 7.9. In the anode side of the

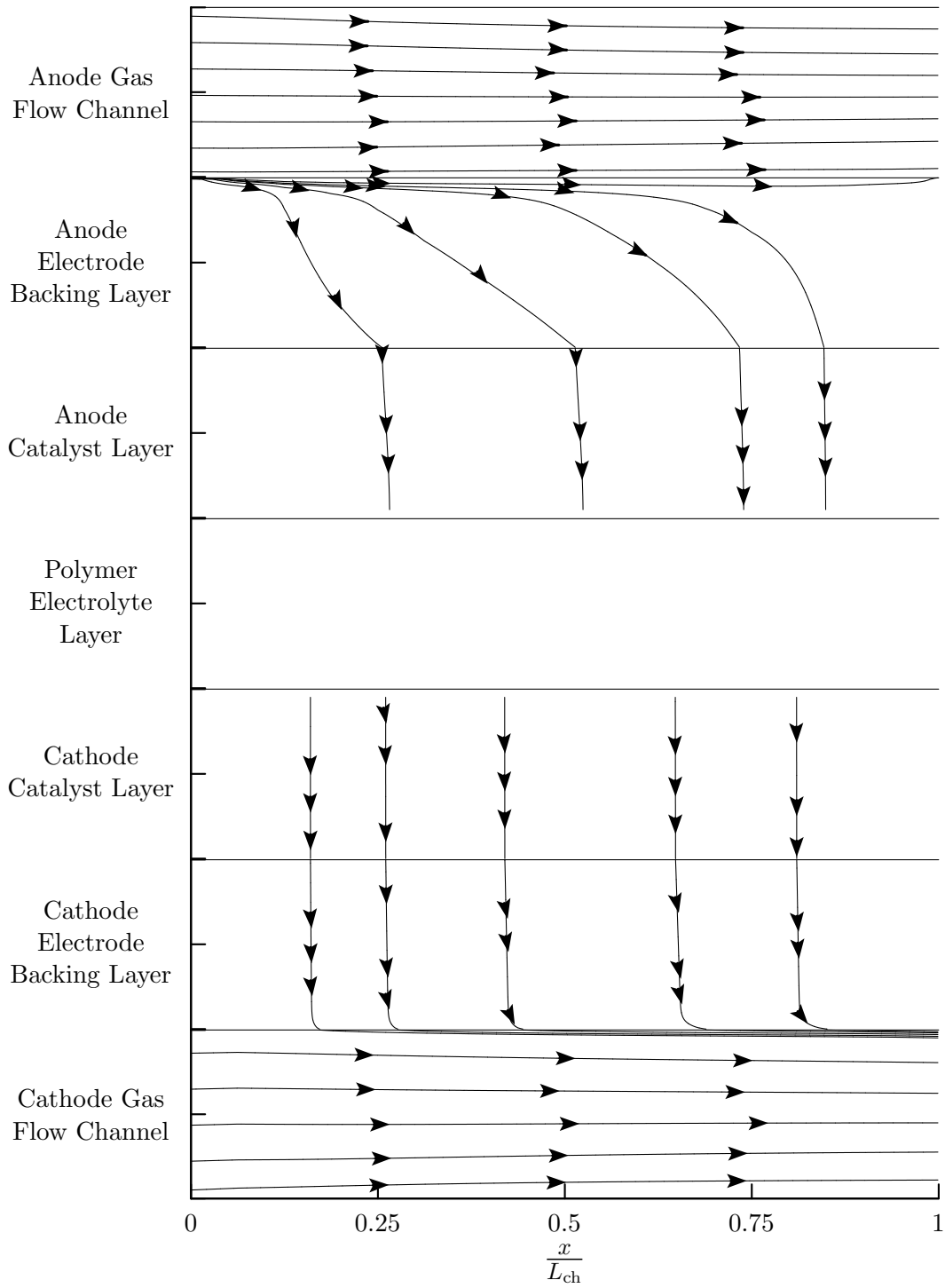
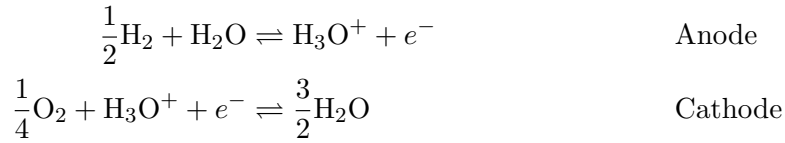


Figure 7.9: The gas phase streamlines in the PEM fuel cell

cell, the streamlines show that the gas phase is transported from the gas flow channels, through the anode electrode backing layer, and into the anode catalyst layer. The gas phase does not exist in the polymer electrolyte layer; hence, no streamlines are present. In the cathode side of the cell, the gas phase travels through the cathode catalyst and electrode backing layers before entering the cathode gas flow channel. Thus, the streamlines show that a net mass transfer occurs between the anode and cathode sides of the PEM fuel cell. The loss of mass in the anode and gain in the cathode can be explained by examining the electro-chemical reactions:



where the anode and cathode reactions are expressed on a per mole of hydronium basis. If only hydronium is transferred through the polymer electrolyte layer, the mass produced per mole of hydronium is

$$\Delta M_{\text{anode}} = -\frac{1}{2}\hat{M}_{\text{H}_2} - \hat{M}_{\text{H}_2\text{O}} = -1.903 \times 10^{-2} \text{ kg/mole}, \quad (7.20)$$

$$\Delta M_{\text{cathode}} = \frac{3}{2}\hat{M}_{\text{H}_2\text{O}} - \frac{1}{4}\hat{M}_{\text{O}_2} = 1.903 \times 10^{-2} \text{ kg/mole}, \quad (7.21)$$

where ΔM_{anode} and $\Delta M_{\text{cathode}}$ are the mass production per mole of hydronium in the anode and cathode catalyst layers, respectively. Thus, the transfer of the hydronium ion across the polymer electrolyte layer results in loss of mass in the anode and a gain of mass in the cathode catalyst layers.

The magnitude of the velocity in each layer of the PEM fuel cell is illustrated in Figure 7.10. Figure 7.10 shows the magnitude of the phase-averaged velocity, which is defined as

$$\text{Velocity Magnitude} = \sqrt{(\langle u_g \rangle^*)^2 + (\langle v_g \rangle^*)^2}, \quad (7.22)$$

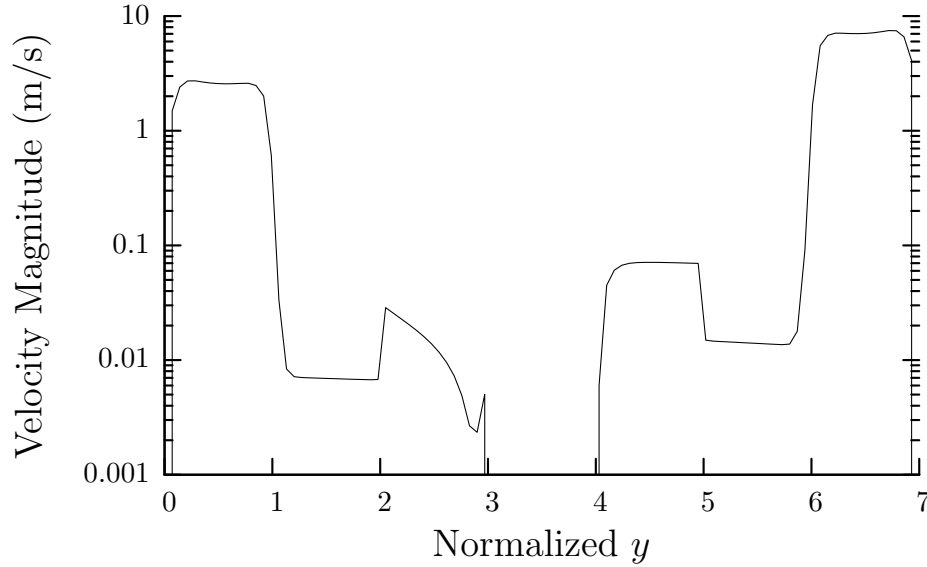


Figure 7.10: The magnitude of the phase-averaged, bulk gas phase velocity the PEM fuel cell at $x/L_{\text{ch}} = 0.5$. The y direction has been normalized such that the cathode gas flow channel corresponds to $(0 \leq y \leq 1)$, the cathode electrode backing layer corresponds to $(1 \leq y \leq 2)$, the cathode catalyst layer corresponds to $(2 \leq y \leq 3)$, the polymer electrolyte layer corresponds to $(3 \leq y \leq 4)$, the anode catalyst layer corresponds to $(4 \leq y \leq 5)$, the anode electrode backing layer corresponds to $(5 \leq y \leq 6)$, and the anode gas flow channel corresponds to $(6 \leq y \leq 7)$.

where u_g and v_g are the x - and y -direction gas phase velocities, respectively. The velocity in the electrode backing layers is approximately two orders of magnitude smaller than in the gas flow channels. The porous media has a higher resistance to flow; hence, the velocity is smaller in the porous media than in the gas flow channels. An increase in velocity occurs at the interface between the electrode backing and catalyst layers. This increase in velocity is due to a change in porosity between the two layers; from Table 7.4, the volume fraction of the gas phase in the electrode backing layer is 0.5, while the catalyst layer has a smaller gas phase volume fraction of 0.1; Thus, if the density of the gas phase is constant across the interface between the two layers, the velocities are related with

$$\frac{\text{Velocity Magnitude in Catalyst Layer}}{\text{Velocity Magnitude in Electrode Backing Layer}} = \frac{\epsilon_g|_{\text{electrode backing layer}}}{\epsilon_g|_{\text{catalyst layer}}}. \quad (7.23)$$

Using the values in Table 7.4, the magnitude of the velocity in the catalyst layer should be approx-

imately five times that in the electrode backing layer. This is in agreement with the results shown in Figure 7.10. Also in Figure 7.10, the velocity magnitude in the cathode catalyst layer exhibits a local minimum near the catalyst layer/polymer electrolyte interface. This is due to the directional change of the mass flux of water, which is examined in more detail in Section 7.6.4.

7.6.2 Hydrogen Transport

For the gas phase species, the total mass flux is the result of both convection and diffusion:

$$\begin{aligned}\mathbf{F}_g^\alpha &= \epsilon_g \rho_g^\alpha \mathbf{u} + \epsilon_g \mathcal{J}_g^\alpha, \\ &= \mathbf{F}_{c,g}^\alpha + \mathbf{F}_{d,g}^\alpha,\end{aligned}\tag{7.24}$$

where $\mathbf{F}_{c,g}^\alpha$ and $\mathbf{F}_{d,g}^\alpha$ are the species mass flux due to convection and diffusion, respectively. The stream function for the total mass flux can be defined as

$$\frac{\partial \psi}{\partial x} = F_x^\alpha \qquad \frac{\partial \psi}{\partial y} = -F_y^\alpha\tag{7.25}$$

For hydrogen, the streamlines for total mass flux are illustrated in Figure 7.11. The streamlines of total hydrogen mass flux show that hydrogen is transported from the anode gas flow channels to the anode catalyst layers. If the diffusional flux of hydrogen was negligible, then the hydrogen mass flux streamlines of Figure 7.11 would be identical to the streamlines of the bulk flow, which are illustrated in Figure 7.9. However, the streamline patterns differ between the bulk flow and total hydrogen mass flux, resulting in the conclusion that diffusional transport is significant in the anode electrode backing and catalyst layers.

The streamlines for the diffusional flux of hydrogen are shown in Figure 7.12. In the anode electrode backing and catalyst layers, the diffusional flux is in the opposite direction than both the total hydrogen mass flux and the convective velocity. Since the reaction requires hydrogen to be supplied to the anode catalyst layer, diffusion acts to hinder the electro-chemical reactions. The

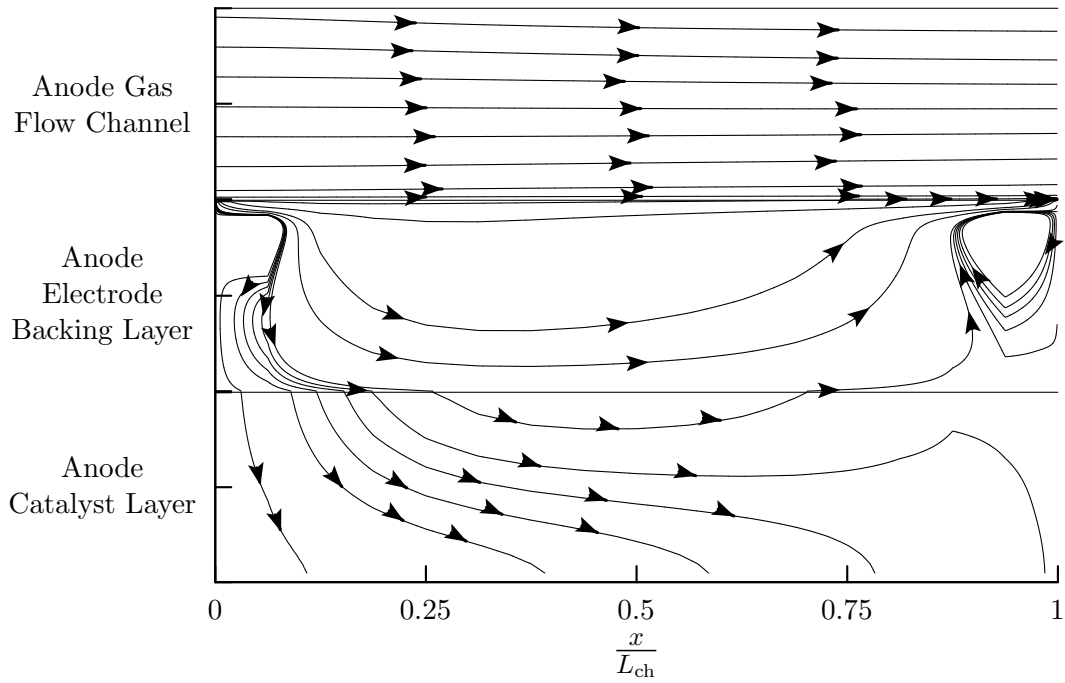


Figure 7.11: The streamlines for the total mass flux of hydrogen in the PEM fuel cell

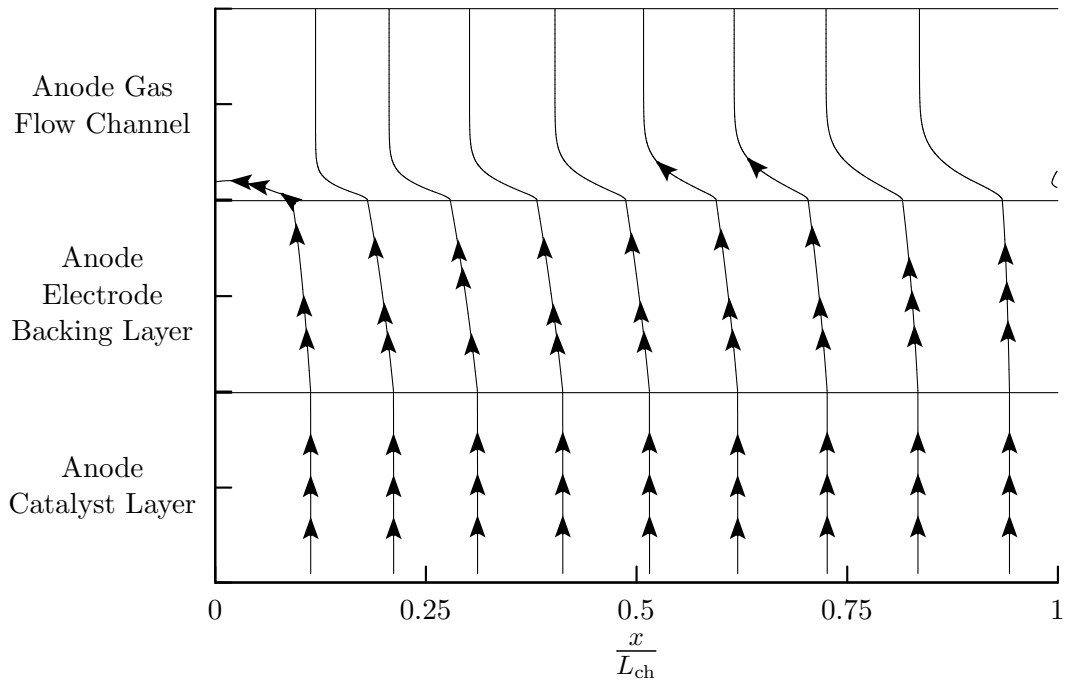


Figure 7.12: The streamlines for the diffusional mass flux of hydrogen in the PEM fuel cell

diffusional flux is proportional to the mass or mole gradient:

$$\mathcal{J}_g^\alpha \propto -\nabla\omega_g^\alpha \propto -\nabla x_g^\alpha$$

Therefore, since the direction of the diffusional flux is from the anode catalyst layer to the anode electrode backing layer, the mole and mass fractions of hydrogen must be higher in the anode catalyst layer than the electrode backing layer. The increase in mass fraction of hydrogen from the gas flow channels to the anode catalyst layer is illustrated in Figure 7.13. Figure 7.13(a) shows the two-dimensional mass fraction distribution, while Figure 7.13(b) shows the mass fraction distribution for a constant x/L_{ch} of 0.5. Both figures show a significant decrease of hydrogen mass fraction from the anode catalyst layer to the anode gas flow channel. The mass fraction is larger in the catalyst and electrode backing layers, while in the gas flow channel, the mass fraction is nearly constant, only increasing near the electrode backing layer/gas flow channel interface. The concentration of hydrogen also increases, as illustrated in Figure 7.14. Figure 7.14(a) shows the two-dimensional distribution, while Figure 7.14(b) shows the concentration distribution for a constant x/L_{ch} of 0.5.

Thus, although hydrogen is consumed, the mass fraction increases. The increase in mass fraction is due to the nature of the electro-chemical reactions, and can be explained by considering the test problem illustrated in Figure 7.15. A tube of length L is illustrated in Figure 7.15. At the inlet of the tube, hydrogen and water are supplied, while at the outlet of the tube, hydrogen and water are removed in a molar ratio of 1:2: for every one mole of hydrogen removed, two moles of water are also removed. This rate of removal is equivalent to the reaction stoichiometry of the anode catalyst layer. The bulk velocity in the tube is

$$\begin{aligned} \rho_g u_g &= F_g^{\text{H}_2} \Big|_{x=L} + F_g^{\text{H}_2\text{O}} \Big|_{x=L} \\ &= r \left(\hat{M}_{\text{H}_2} + 2\hat{M}_{\text{H}_2\text{O}} \right), \end{aligned} \quad (7.26)$$

where r is the molar flux of hydrogen at $x = L$. The conservation of hydrogen in the tube results

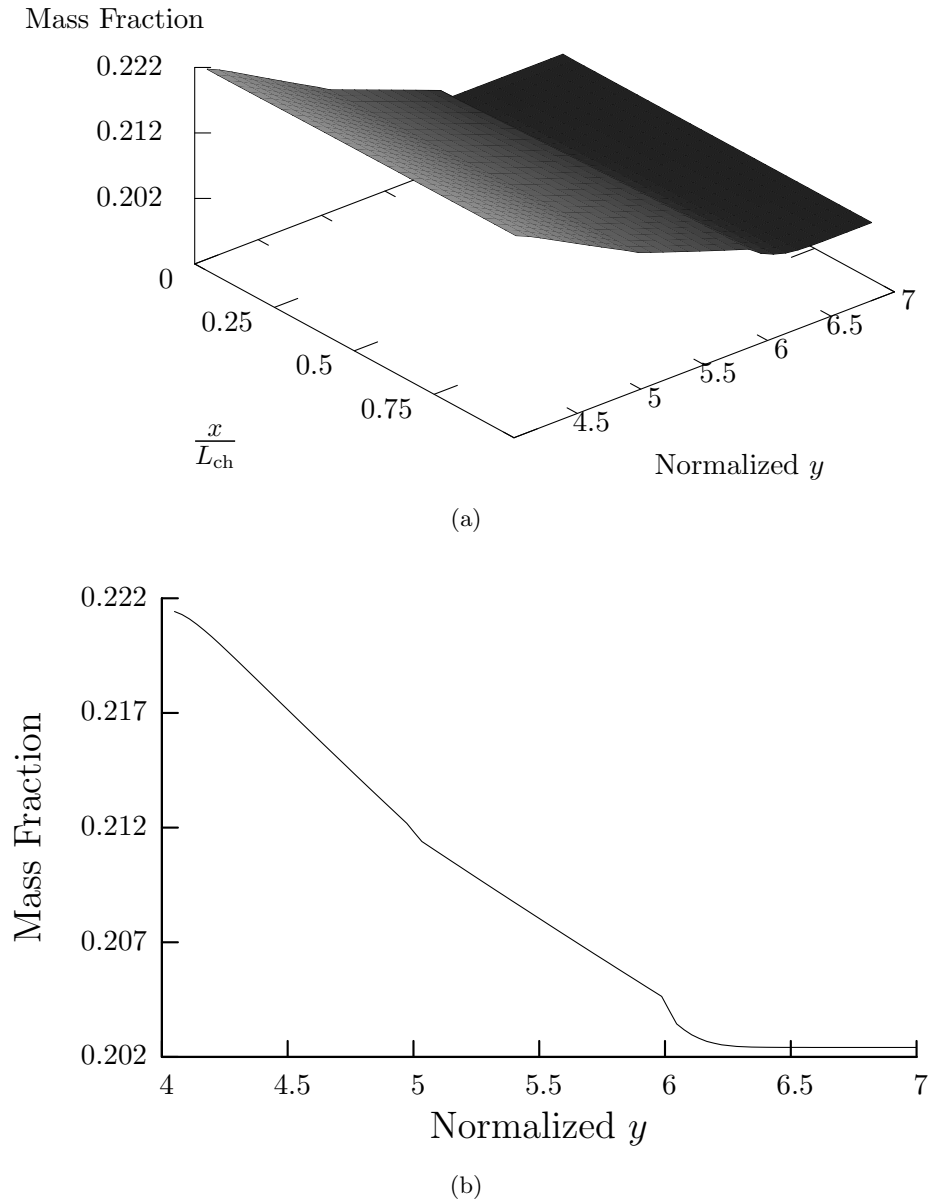


Figure 7.13: The mass fraction of hydrogen in the anode gas flow channel, electrode backing layer and catalyst layer. The y direction has been normalized such that the anode catalyst layer corresponds to ($4 \leq y \leq 5$), the anode electrode backing layer corresponds to ($5 \leq y \leq 6$) and the anode gas flow channel corresponds to ($6 \leq y \leq 7$). The (a) two-dimensional distribution and the (b) one-dimensional distribution at $x/L_{ch} = 0.5$ are shown.

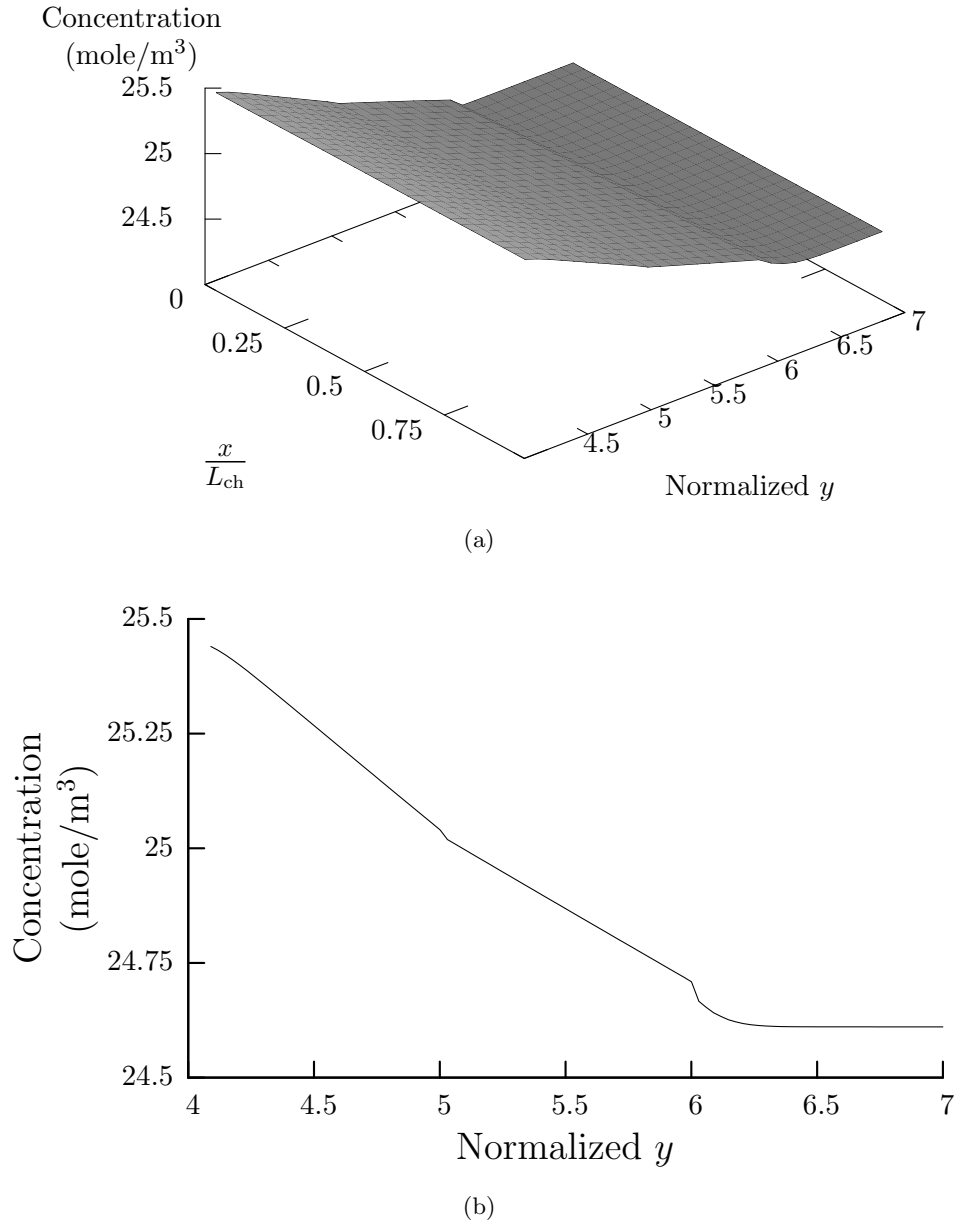


Figure 7.14: The concentration of hydrogen in the anode gas flow channel, electrode backing layer and catalyst layer. The y direction has been normalized such that the anode catalyst layer corresponds to ($4 \leq y \leq 5$), the anode electrode backing layer corresponds to ($5 \leq y \leq 6$) and the anode gas flow channel corresponds to ($6 \leq y \leq 7$). The (a) two-dimensional distribution and the (b) one-dimensional distribution at $x/L_{ch} = 0.5$ are shown.

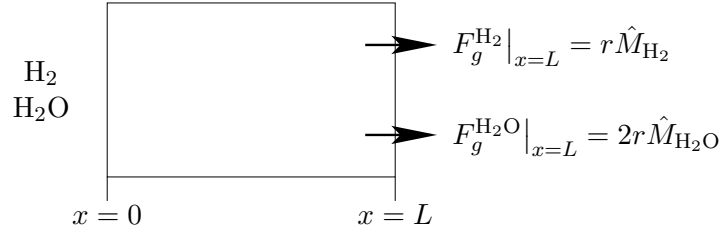


Figure 7.15: Test problem for explaining the hydrogen mass fraction gradient in the anode catalyst layer.

in

$$\frac{\partial}{\partial x} (\rho_g u_g \omega_g^{\text{H}_2} + \mathcal{J}_g^{\text{H}_2}) = 0. \quad (7.27)$$

Integration of Equation (7.27) yields

$$\rho_g u_g \omega_g^{\text{H}_2} + \mathcal{J}_g^{\text{H}_2} = r \hat{M}_{\text{H}_2}. \quad (7.28)$$

Since the gas mixture in Figure 7.15 is binary, the diffusive flux can be expressed as Fick's law. Additionally, since the convective velocity is defined by Equation (7.26), the mass gradient of hydrogen is

$$\frac{\partial \omega_g^{\text{H}_2}}{\partial x} = \frac{r}{\rho_g \mathcal{D}_{\text{H}_2-\text{H}_2\text{O},g}} \left[\omega_g^{\text{H}_2} (\hat{M}_{\text{H}_2} + 2\hat{M}_{\text{H}_2\text{O}}) - \hat{M}_{\text{H}_2} \right]. \quad (7.29)$$

Therefore, the gradient of hydrogen mass fraction will be positive if

$$\begin{aligned} \omega_g^{\text{H}_2} &> \frac{\hat{M}_{\text{H}_2}}{\hat{M}_{\text{H}_2} + 2\hat{M}_{\text{H}_2\text{O}}}, \\ &> 0.053. \end{aligned} \quad (7.30)$$

Since the mass fraction of hydrogen in the anode side is greater than 0.2, hydrogen oxidation results in an increase in mass fraction for hydrogen.

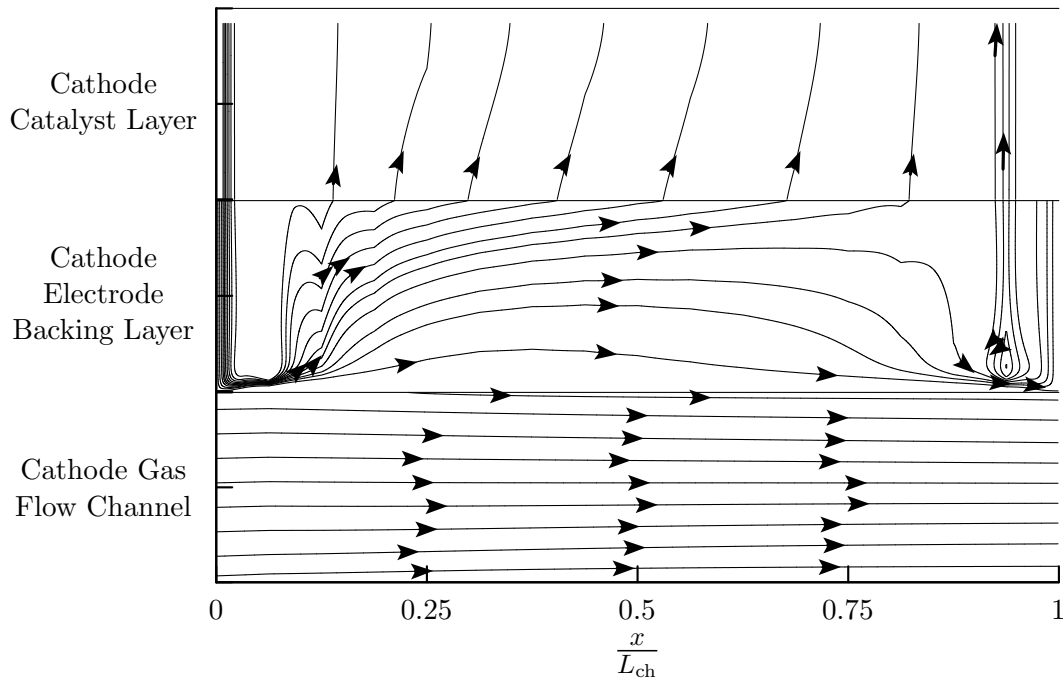
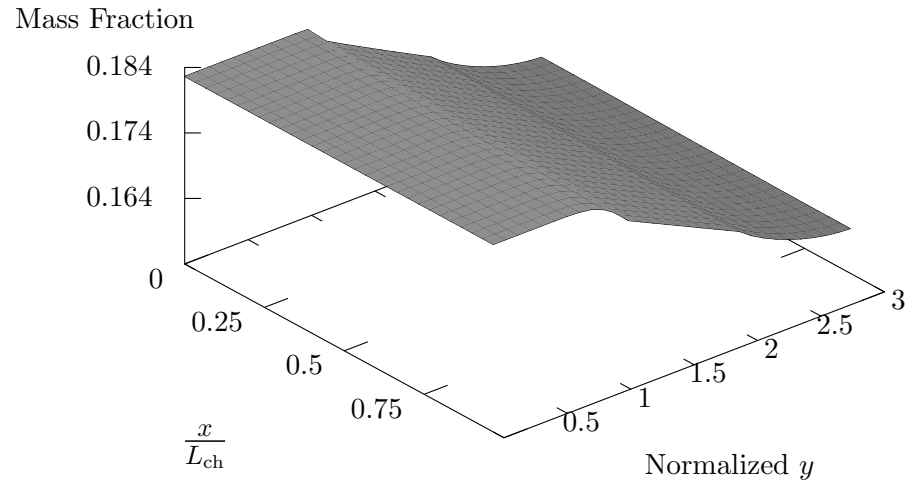


Figure 7.16: The streamlines for the total mass flux of oxygen in the PEM fuel cell

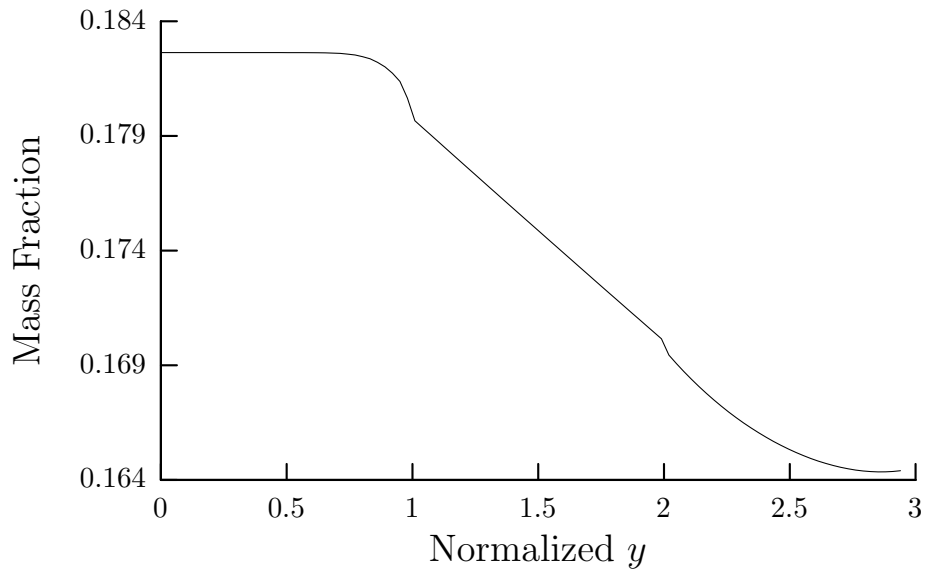
7.6.3 Oxygen Transport

Although oxygen is consumed, water is produced in the cathode catalyst layer. Thus, the bulk gas flow exits the cathode catalyst layer to the cathode electrode backing layer and gas flow channel, as shown in Figure 7.9. However, oxygen must travel from the gas flow channel to the cathode catalyst layer, as illustrated by the streamlines for the total mass flux of oxygen which are shown in Figure 7.16. The direction of oxygen transport in Figure 7.16 is opposite to that of the bulk flow. Therefore, the transport of oxygen from the gas flow channel to the reaction sites in the cathode catalyst layer is due to diffusion.

The diffusional flux of oxygen is driven by mass or mole fraction gradients and Figure 7.17 illustrates the mass fraction of oxygen in the cathode gas flow channel, electrode backing and catalyst layers. Figure 7.17(a) shows the two-dimensional mass fraction distribution, while Figure 7.17(b) shows the mass fraction distribution for a constant x/L_{ch} of 0.5. Both figures show a significant decrease of oxygen mass fraction from the cathode gas flow channel to the cathode electrode back-



(a)



(b)

Figure 7.17: The mass fraction of oxygen in the anode gas flow channel, electrode backing layer and catalyst layer. The y direction has been normalized such that the cathode gas flow channel corresponds to ($0 \leq y \leq 1$), the cathode electrode backing layer corresponds to ($1 \leq y \leq 2$) and the cathode catalyst layer corresponds to ($2 \leq y \leq 3$). The (a) two-dimensional distribution and the (b) one-dimensional distribution at $x/L_{ch} = 0.5$ are shown.

ing layer. The magnitude of the mass fraction gradient is larger in the electrode backing and catalyst layers, while the gradient in the gas flow channel is zero except near the gas flow channel/electrode backing layer interface. Also, the oxygen mass fraction gradient becomes zero at the cathode catalyst layer/polymer electrolyte layer interface because the electrolyte is impervious to the gas phase. The distribution of oxygen molar concentration follows that of the mass fraction and is illustrated in Figure 7.18. The two- and one-dimensional concentration distributions are shown in Figure 7.18(a) and Figure 7.18(b), respectively. The decrease in oxygen concentration has a negative effect on fuel cell performance, since the rate of electro-chemical reaction is proportional to oxygen concentration.

7.6.4 Water Transport

Water exists both in the gas phase and the pores of the polymer electrolyte. Thus, unlike hydrogen and oxygen, water transport is continuous throughout the PEM fuel cell. The total water flux is defined as

$$\mathbf{F}_T^{\text{H}_2\text{O}} = \mathbf{F}_g^{\text{H}_2\text{O}} + \mathbf{F}_{\ell,e}^{\text{H}_2\text{O}} \quad (7.31)$$

where $\mathbf{F}_g^{\text{H}_2\text{O}}$ and $\mathbf{F}_{\ell,e}^{\text{H}_2\text{O}}$ are the total mass fluxes of water in the gas and polymer electrolyte, respectively. In the gas flow channels and electrode backing layers, the electrolyte phase is not present and $\mathbf{F}_{\ell,e}^{\text{H}_2\text{O}}$ is zero, while the mass flux in the gas phase is zero for the polymer electrolyte layer. Water is transported in both the gas and electrolyte within the catalyst layers.

The streamlines for the total water flux are illustrated in Figure 7.19. Due to the electro-chemical reactions, water is consumed in the anode catalyst layer and produced in the cathode catalyst layer. Water is drawn into the anode catalyst layer from the anode gas flow channel and extracted from the cathode catalyst layer to the cathode gas flow channel. Thus, Figure 7.19 shows that the direction of water flux in the electrode backing layers and gas flow channels is from the anode to the cathode. However, the direction of water flux in the polymer electrolyte layer is from

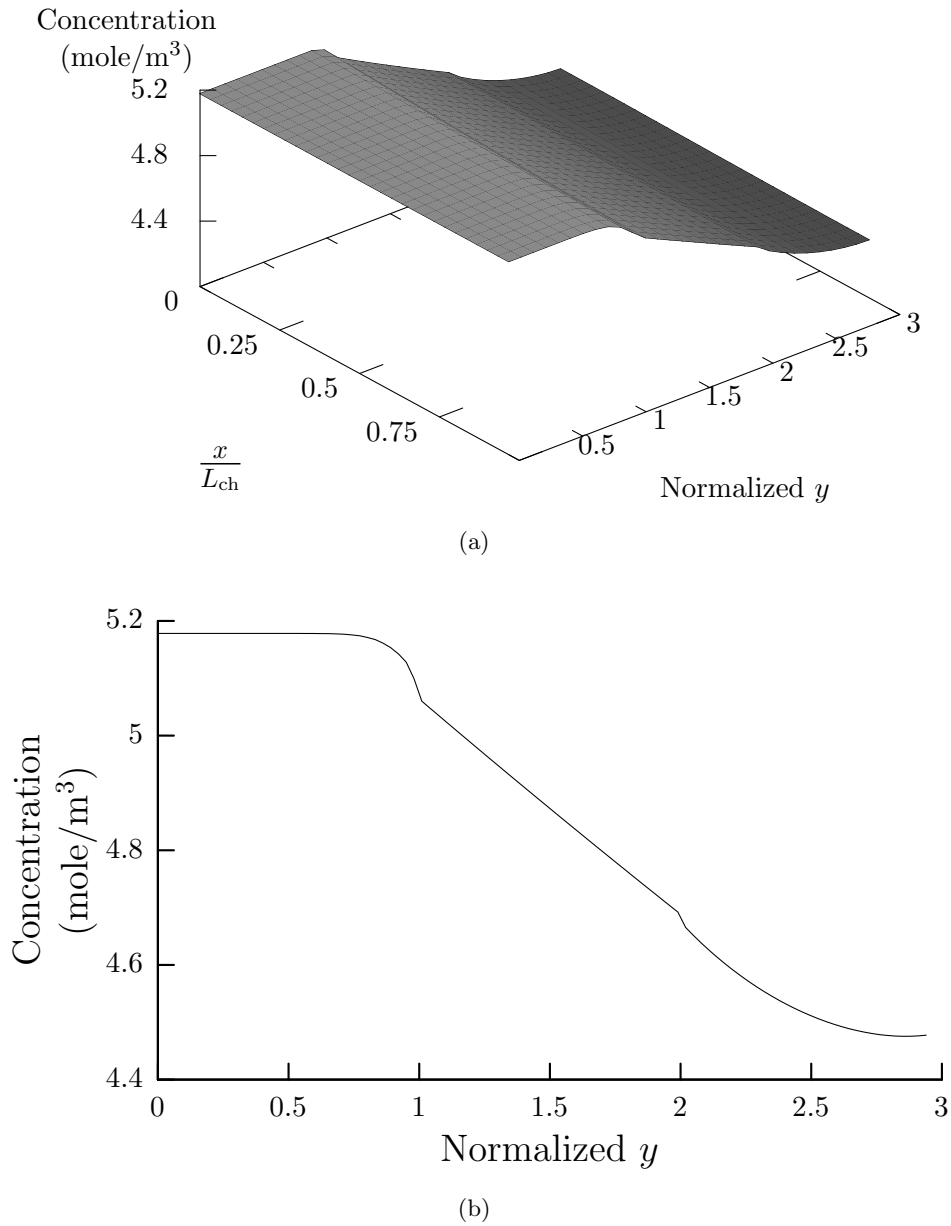


Figure 7.18: The concentration of oxygen in the anode gas flow channel, electrode backing layer and catalyst layer. The y direction has been normalized such that the cathode gas flow channel corresponds to ($0 \leq y \leq 1$), the cathode electrode backing layer corresponds to ($1 \leq y \leq 2$) and the cathode catalyst layer corresponds to ($2 \leq y \leq 3$). The (a) two-dimensional distribution and the (b) one-dimensional distribution at $x/L_{ch} = 0.5$ are shown.

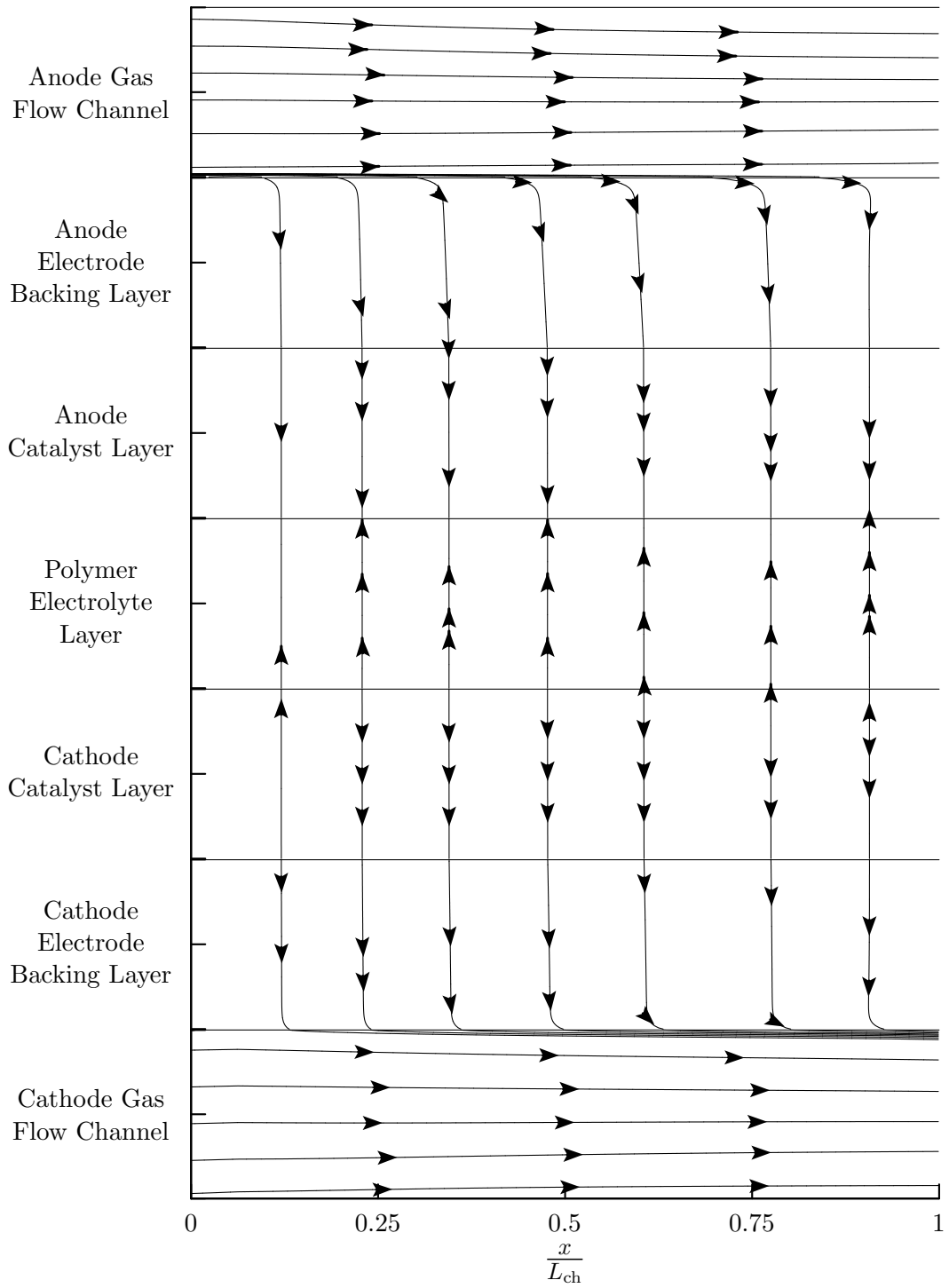


Figure 7.19: The streamlines of total water mass flux in the PEM fuel cell.

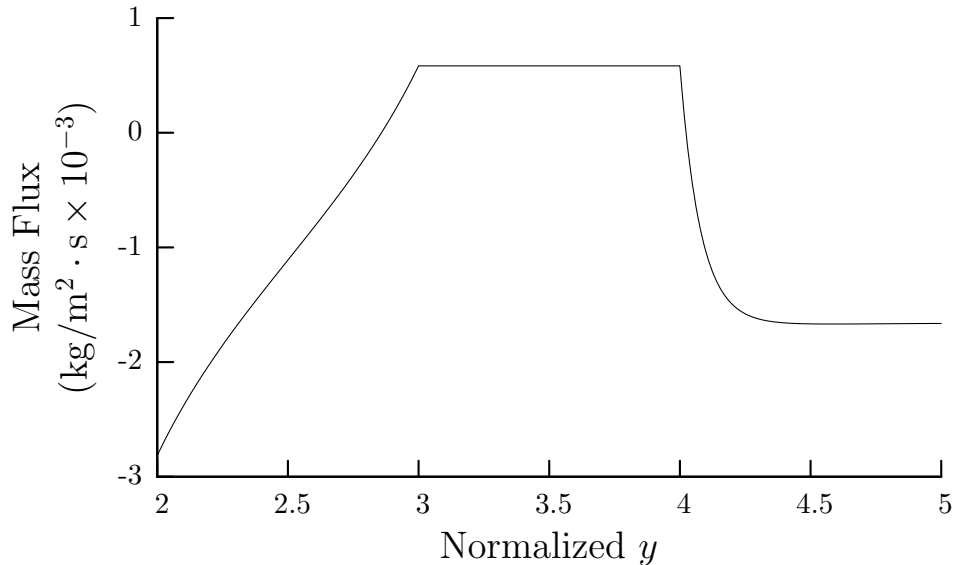


Figure 7.20: The y direction water mass flux in the catalyst layers and polymer electrolyte layer at $x/L_{\text{ch}} = 0.5$. The y direction has been normalized such that the cathode catalyst layer corresponds to ($2 \leq y \leq 3$), the polymer electrolyte layer corresponds to ($3 \leq y \leq 4$), and the anode catalyst layer corresponds to ($4 \leq y \leq 5$).

the cathode to the anode, which is opposite to that in the electrode backing layers and gas flow channels. In the catalyst layers, the water flux is in both directions.

The change in direction of the water mass flux in the catalyst layers and polymer electrolyte is further illustrated in Figure 7.20. Figure 7.20 shows the y -direction total mass flux of water in the cathode catalyst layer, polymer electrolyte layer, and anode catalyst layer. A negative mass flux corresponds to water traveling to the cathode side of the fuel cell, with a positive mass flux indicating that the direction of water transport is from the cathode to the anode. In most of the PEM fuel cell, the y -direction water flux is negative, meaning that the flow direction is from the anode to the cathode. However, in the polymer electrolyte layer and in the catalyst layers near the catalyst layer/polymer electrolyte interfaces, the water mass flux changes direction and becomes positive. This change in direction is responsible for the local minimum of velocity magnitude in the cathode catalyst layer that is illustrated in Figure 7.10.

Water is produced in the cathode catalyst layer and consumed in the anode catalyst layer. If the polymer electrolyte was impermeable to water, the direction of water flux would always be from

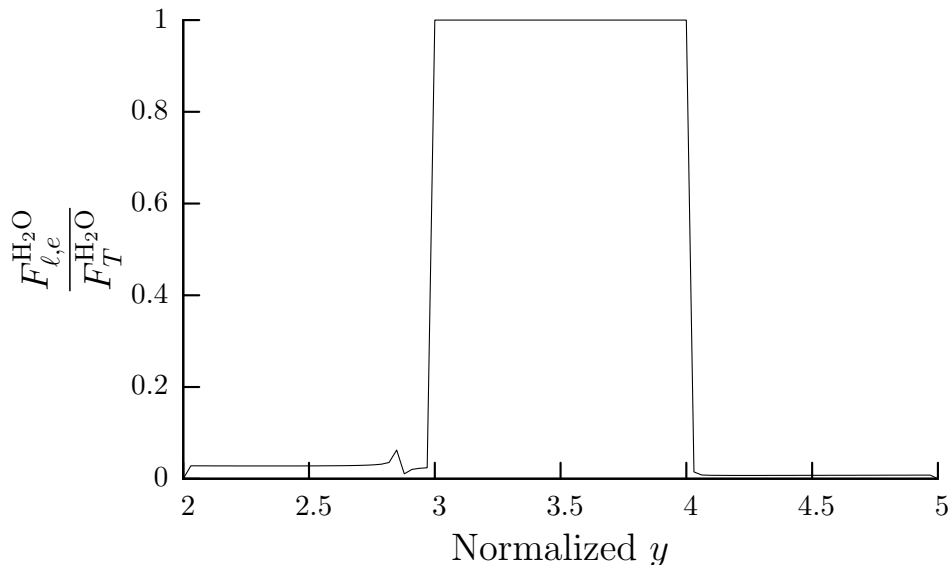


Figure 7.21: The fraction of y direction water mass flux that is transported in the electrolyte at $x/L_{\text{ch}} = 0.5$. The y direction has been normalized such that the cathode catalyst layer corresponds to $(2 \leq y \leq 3)$, the polymer electrolyte layer corresponds to $(3 \leq y \leq 4)$, and the anode catalyst layer corresponds to $(4 \leq y \leq 5)$.

anode to cathode. The water required for the anode reaction would be extracted from the anode gas flow channel, while the water produced by the cathode catalyst layer would be removed by entering the cathode gas flow channel. Instead, since the electrolyte is permeable to water, some of the water required by the anode reaction can be supplied by the cathode reaction. However, the resistance to water transport in the electrolyte is much larger than in the gas phase, as illustrated in Figure 7.21. Figure 7.21 shows the fraction of total water mass flux that is transported in the electrolyte for the catalyst layers and polymer electrolyte layer. The catalyst layers are composed of both gas and electrolyte, but in most of the catalyst layers, water transport is almost entirely in the gas phase; this indicates that the resistance to mass transport is lower in the gas phase than in the electrolyte.

The higher resistance to mass transport in the electrolyte results in the situation that is illustrated in Figure 7.22. The void space of the catalyst layers consists of the gas phase and polymer electrolyte. Water can be transported through each phase, but the resistance to water transport is higher in the polymer electrolyte than in the gas phase. As a result, most of the water pro-

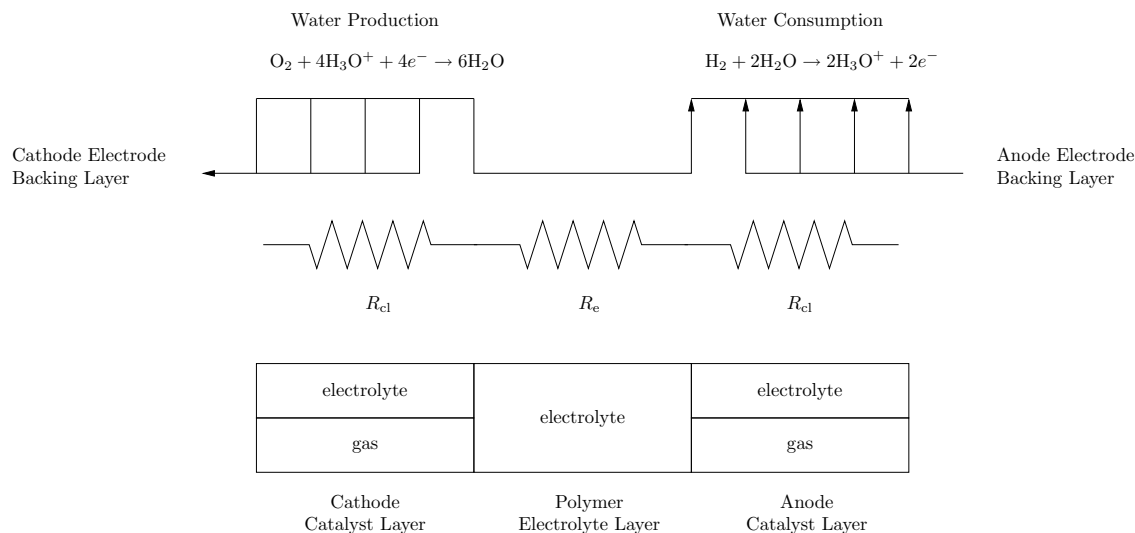


Figure 7.22: Diagram of water transport in the MEA of a PEM fuel cell.

duced on the cathode side of the fuel cell exits through the cathode electrode backing layer and gas flow channels. Similarly, most of the water required for the anode reaction is extracted from the anode gas flow channels and electrode backing layer. However, near the electrolyte/catalyst layer interfaces, the resistance to mass transport becomes small enough that water is transported from the cathode catalyst layer to the anode catalyst layer. From Figure 7.20, the amount of water entering the anode catalyst layer from the anode electrode backing layer is approximately $1.5 \times 10^{-3} \text{ kg/m}^2 \text{ s}$, while the amount transferred from the cathode to the anode catalyst layer is approximately $5.0 \times 10^{-4} \text{ kg/m}^2 \text{ s}$. Therefore, approximately 25% of the water consumed by the anode catalyst layer reaction comes from the cathode catalyst layer. Ideally, the water produced in the cathode catalyst layer should provide 100% of the water needed by the anode catalyst layer since this would eliminate the need to have fully hydrated reactants. However, in practice, the reactants must be fully humidified in order to sufficiently hydrate the membrane and this is confirmed by the simulation.

The water transport across the polymer electrolyte layer is driven by a water concentration gradient. The amount of water contained in the gas phase and electrolyte can be characterized by the membrane activity as defined by Equation (4.41). In the gas phase, the membrane activity is

the relative humidity, while the water content of the electrolyte is proportional to the membrane activity. The membrane activity in the PEM fuel cell is illustrated in Figure 7.23. The two-dimensional distribution of membrane activity is shown in Figure 7.23(a), while Figure 7.23(b) illustrates the one-dimensional membrane activity distribution at an x/L_{ch} of 0.5. In the y direction of the PEM fuel cell, the membrane activity is constant throughout most of the cathode gas flow channel, but starts increasing near the cathode gas flow channel/electrode backing layer. The membrane activity increases in the cathode electrode backing layer and in the cathode catalyst layer, reaching a maximum value near the cathode catalyst layer/polymer electrolyte layer interface. The membrane activity then decreases throughout the polymer electrolyte layer and reaches a minimum in the anode catalyst layer near the polymer electrolyte layer/anode catalyst layer interface. The anode electrode backing layer has an increasing membrane activity, with the slope decreasing to zero in the anode gas flow channel at a location near the anode electrode backing layer/gas flow channel interface.

The membrane activity is greater than one in the cathode electrode backing and catalyst layers, and this corresponds to a relative humidity in the gas phase of greater than 100%. Thus, liquid water formation would occur within the cathode side of the PEM fuel cell, leading to the phenomenon of liquid water flooding. Water flooding is characterized by liquid water filling the void spaces of the catalyst and electrode backing layers, inhibiting the flow of oxygen to the reaction sites in the cathode catalyst layer, and decreasing the cell current density. However, liquid water formation is not included in the model presented in this thesis. In the anode side of the cell, the membrane activity is less than one in the gas flow channel, electrode backing and catalyst layers. A membrane activity of less than one is not desirable because the ability of the electrolyte to transport ions is lower at lower membrane activities; the decrease in electrolyte conductivity due to low water content is referred to as membrane dehydration. Thus, Figure 7.23 illustrates that both water flooding and membrane dehydration can occur simultaneously.

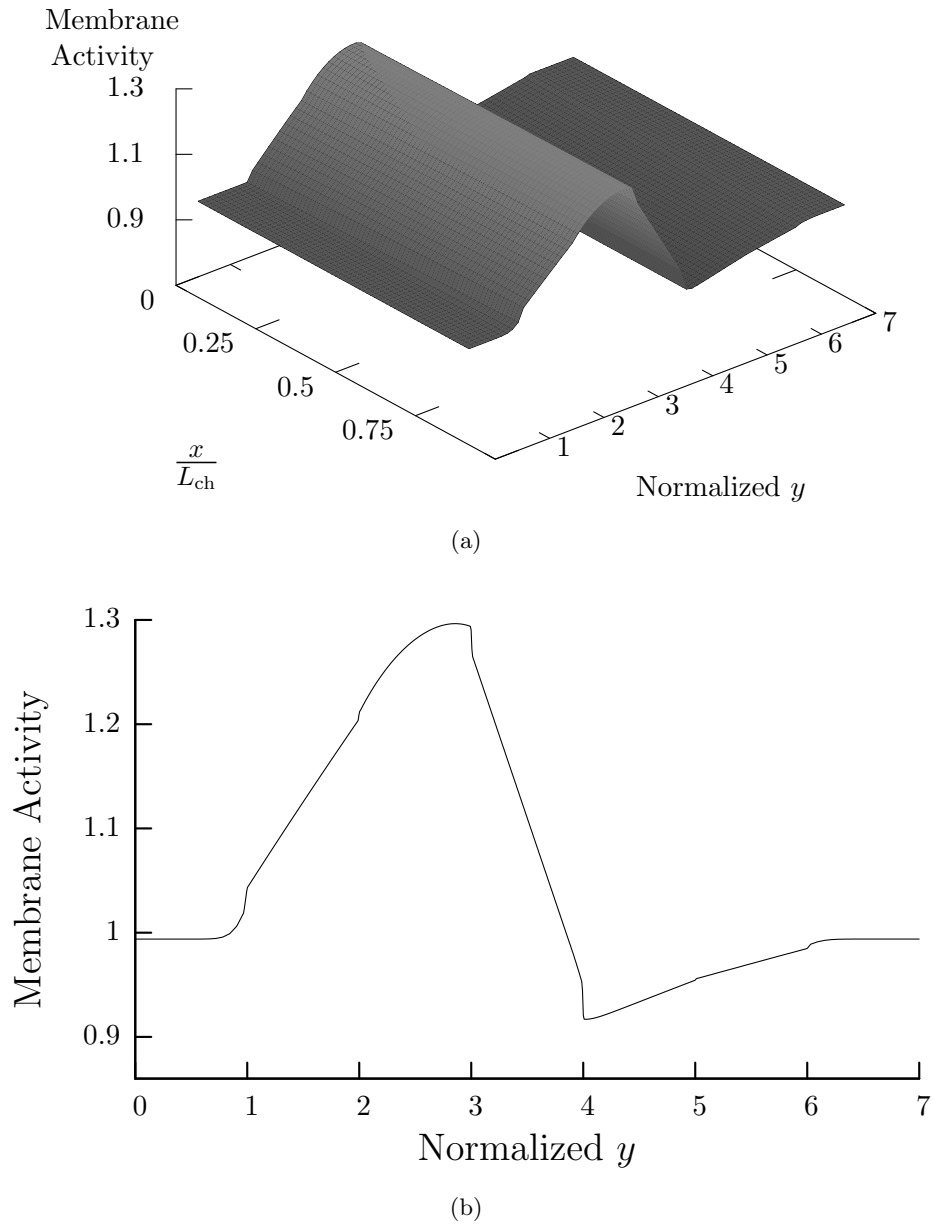


Figure 7.23: The membrane activity in the PEM fuel cell. The y direction has been normalized such that the cathode gas flow channel corresponds to ($0 \leq y \leq 1$), the cathode electrode backing layer corresponds to ($1 \leq y \leq 2$), the cathode catalyst layer corresponds to ($2 \leq y \leq 3$), the polymer electrolyte layer corresponds to ($3 \leq y \leq 4$), the anode catalyst layer corresponds to ($4 \leq y \leq 5$), the anode electrode backing layer corresponds to ($5 \leq y \leq 6$), and the anode gas flow channel corresponds to ($6 \leq y \leq 7$). The (a) two-dimensional distribution and the (b) one-dimensional distribution at $x/L_{ch} = 0.5$ are shown.

7.6.5 Electron Transport

Electrons are produced in the anode catalyst layer, consumed in the cathode catalyst layer, and transported in the solid phase. The x -component of the electronic current density is less than 1% of the y -component value; thus, the electronic current density distribution is effectively one-dimensional. Figure 7.24 shows the y -component of the electronic current density within the PEM fuel cell. The two-dimensional distribution is shown in Figure 7.24(a), while Figure 7.24 shows the y -component of electronic current density at a x/L_{ch} value of 0.5. The polymer electrolyte layer is electronically insulative; thus, the electronic current density is zero. In the other regions of the fuel cell, the direction of the electronic current density is from the anode to the cathode. The electronic current density is constant, with a value of -220 A/m^2 , in the gas flow channels and electrode backing layers. In the catalyst layers, the magnitude of the electronic current density is reduced, from the value 220 A/m^2 at the electrode backing/catalyst layer interfaces, to the value of zero at the catalyst layer/polymer electrolyte interfaces. The slope of the current density is steeper in the anode catalyst layer than in the cathode catalyst layer due to the faster reaction kinetics of the hydrogen oxidation reaction compared to the oxygen reduction reaction. With slower reaction kinetics, the oxygen reduction reaction requires a larger surface area and thus a thicker reaction zone than the reaction occurring within the anode catalyst layer.

The solid potential distribution is illustrated in Figure 7.25. The two-dimensional distribution is shown in Figure 7.25(a), while the one-dimensional distribution of solid phase potential is illustrated in Figure 7.25(b). Because of the high conductivity of the solid phase and the low current density, the potential in the solid phase appears constant in Figure 7.25. The potential in the solid phase is 0.8 V in the cathode side of the fuel cell and 0 V in the anode side.

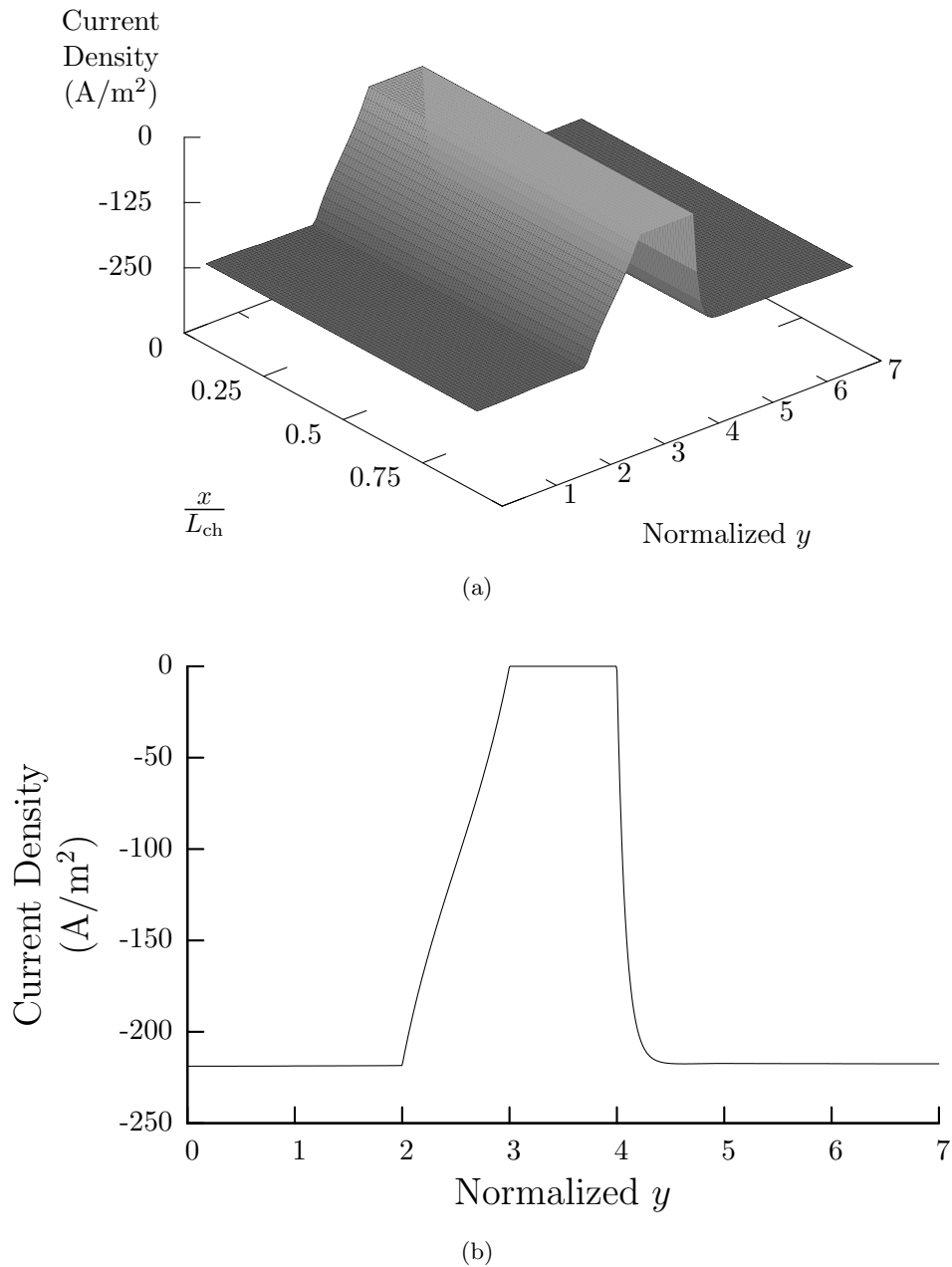


Figure 7.24: The y -component of electronic current density in the PEM fuel cell. The y direction has been normalized such that the cathode gas flow channel corresponds to ($0 \leq y \leq 1$), the cathode electrode backing layer corresponds to ($1 \leq y \leq 2$), the cathode catalyst layer corresponds to ($2 \leq y \leq 3$), the polymer electrolyte layer corresponds to ($3 \leq y \leq 4$), the anode catalyst layer corresponds to ($4 \leq y \leq 5$), the anode electrode backing layer corresponds to ($5 \leq y \leq 6$), and the anode gas flow channel corresponds to ($6 \leq y \leq 7$). The (a) two-dimensional distribution and the (b) one-dimensional distribution at $x/L_{ch} = 0.5$ are shown.

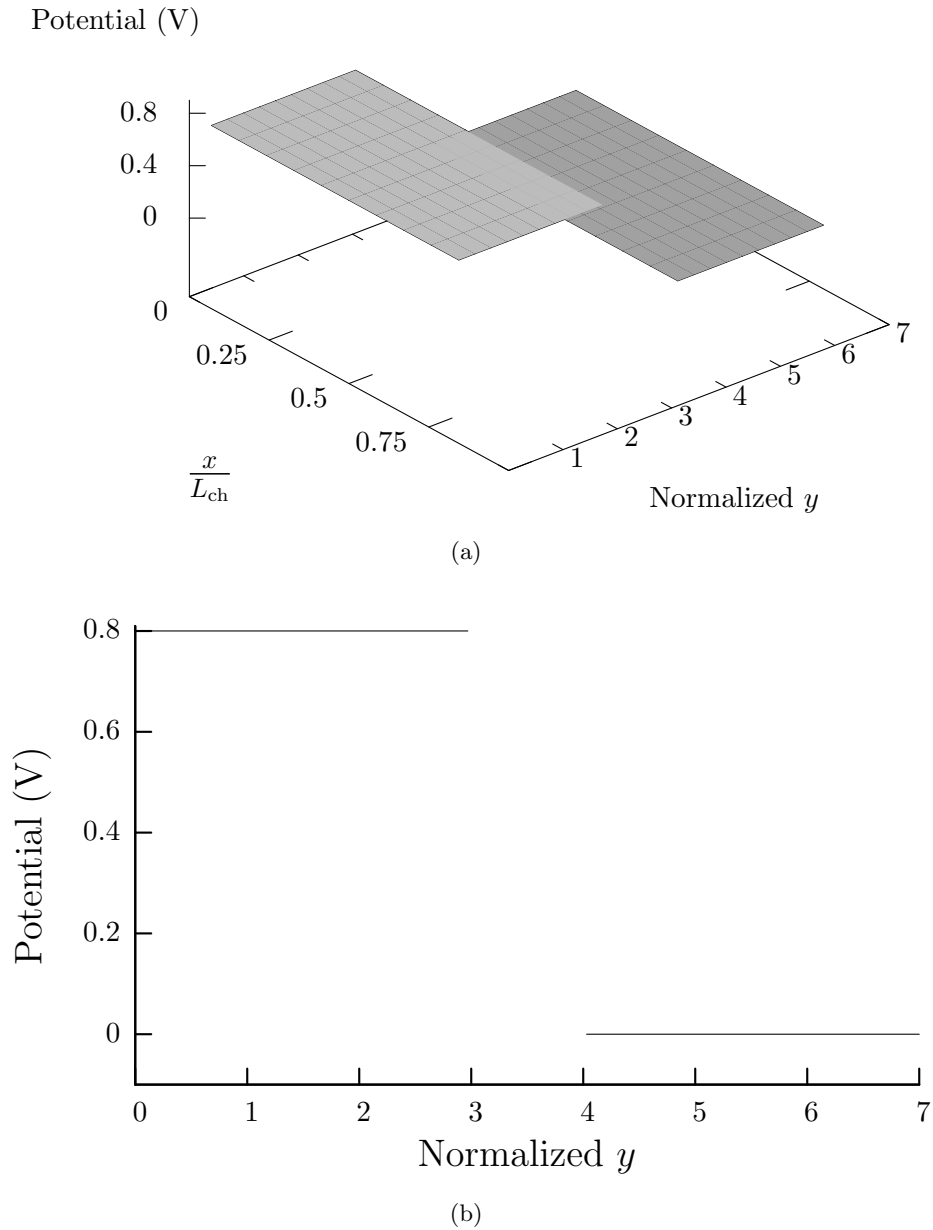


Figure 7.25: The solid phase potential in the PEM fuel cell. The y direction has been normalized such that the cathode gas flow channel corresponds to ($0 \leq y \leq 1$), the cathode electrode backing layer corresponds to ($1 \leq y \leq 2$), the cathode catalyst layer corresponds to ($2 \leq y \leq 3$), the polymer electrolyte layer corresponds to ($3 \leq y \leq 4$), the anode catalyst layer corresponds to ($4 \leq y \leq 5$), the anode electrode backing layer corresponds to ($5 \leq y \leq 6$), and the anode gas flow channel corresponds to ($6 \leq y \leq 7$). The (a) two-dimensional distribution and the (b) one-dimensional distribution at $x/L_{ch} = 0.5$ are shown.

7.6.6 Hydronium Transport

Hydronium ions are transported in the liquid filled pores of the polymer electrolyte and the ionic current density can be defined as

$$\mathbf{J}_e = \epsilon_{\ell,e} \mathcal{F} \mathcal{N}_{\ell,e}^{\text{H}_3\text{O}^+},$$

where $\mathcal{N}_{\ell,e}^{\text{H}_3\text{O}^+}$ is the molar flux of hydronium. As with the solid phase, the y -component of the ionic current density is much larger than the x -component and the current density distribution is one-dimensional. Figure 7.26 shows the y -component of the electronic current density within the catalyst and polymer electrolyte layers. The three dimensional ionic current density distribution is illustrated in Figure 7.26(a) and the ionic current density at a constant x value of $x/L_{\text{ch}} = 0.5$ is shown in Figure 7.26(b). The electrolyte is only present in the catalyst and polymer electrolyte layers, resulting in a zero ionic current density at the electrode backing/catalyst layer interfaces. In the polymer electrolyte layer, the ionic current density is constant with a value of -220 A/m^2 . Electro-neutrality results in [105]

$$\nabla \cdot \mathbf{J}_s + \nabla \cdot \mathbf{J}_e = 0. \quad (7.32)$$

Therefore, the gradients for the electronic and ionic current densities are mirror images, with the magnitude of the gradient being larger in the anode catalyst layer than in the cathode catalyst layer.

The distribution of potential in the electrolyte of the anode and cathode catalyst layers and polymer electrolyte is shown in Figure 7.27. Figure 7.27(a) illustrates the distribution of potential in the x and y directions, while the distribution for a x value of $x/L_{\text{ch}} = 0.5$ is shown in Figure 7.27(b). The potential in the electrolyte is lowest in the cathode catalyst layer near the cathode electrode backing/catalyst layer interface. The potential increases within the cathode catalyst layer and reaches a maximum near the cathode catalyst layer/polymer electrolyte layer

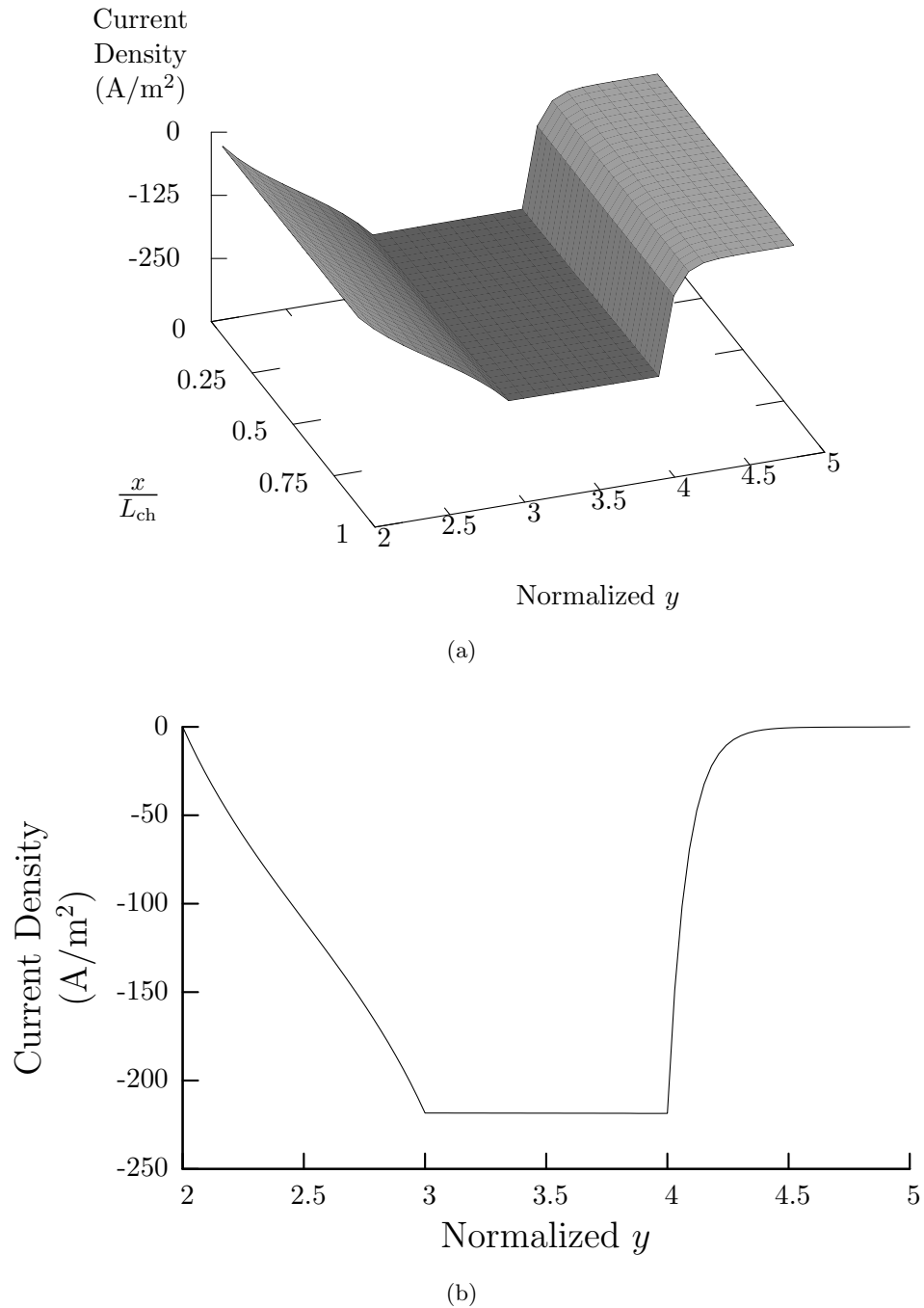


Figure 7.26: The y -component of ionic current density in the PEM fuel cell. The y direction has been normalized such that the cathode catalyst layer corresponds to ($2 \leq y \leq 3$), the polymer electrolyte layer corresponds to ($3 \leq y \leq 4$), and the anode catalyst layer corresponds to ($4 \leq y \leq 5$). The (a) two-dimensional distribution and the (b) one-dimensional distribution at $x/L_{\text{ch}} = 0.5$ are shown.

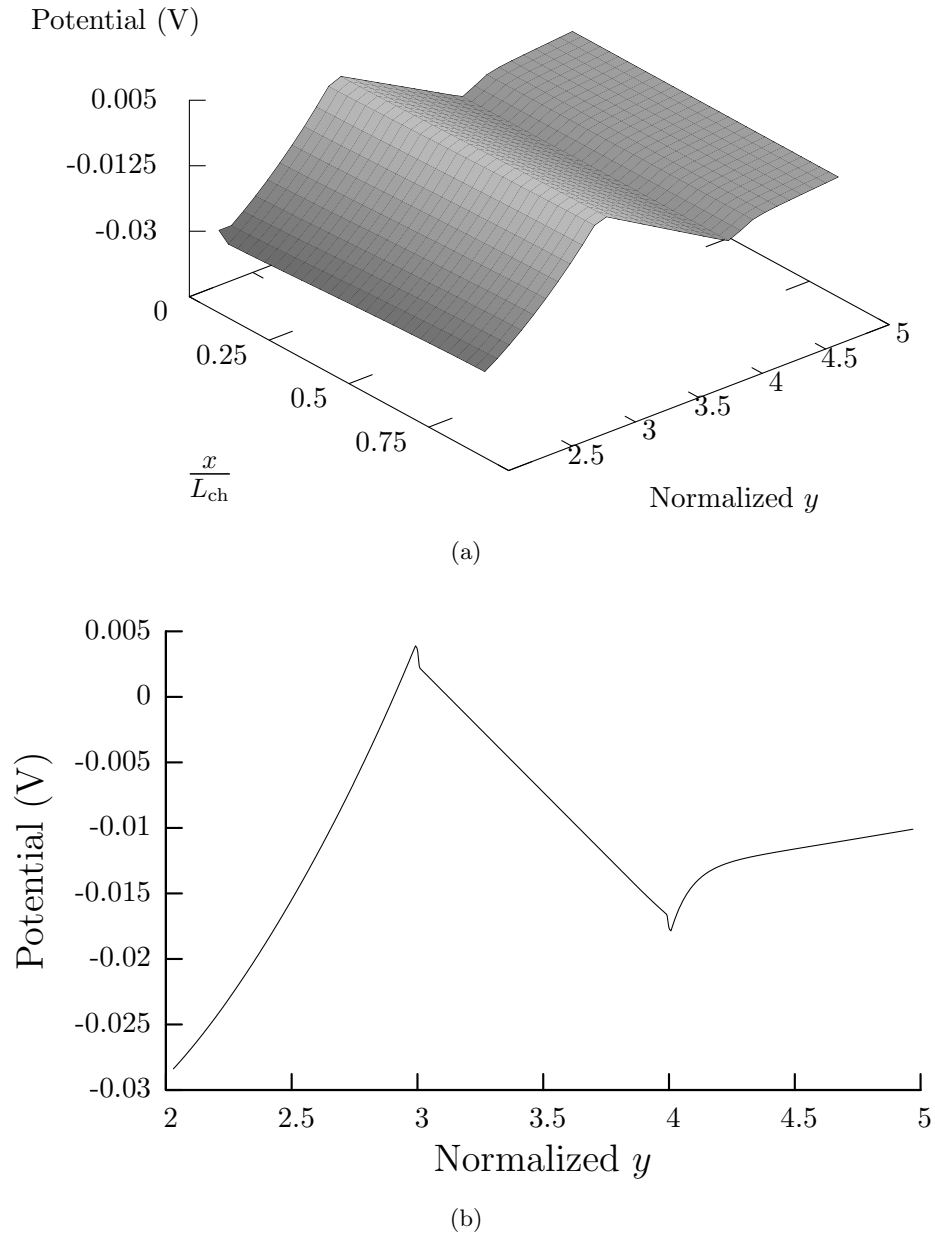


Figure 7.27: The electrolyte potential in the catalyst and polymer electrolyte layers. The y direction has been normalized such that the cathode catalyst layer corresponds to ($2 \leq y \leq 3$), the polymer electrolyte layer corresponds to ($3 \leq y \leq 4$), and the anode catalyst layer corresponds to ($4 \leq y \leq 5$). The (a) two-dimensional distribution and the (b) one-dimensional distribution at $x/L_{ch} = 0.5$ are shown.

interface. In the polymer electrolyte layer, the potential decreases until it reaches a local minimum in the anode catalyst layer, near the polymer electrolyte/anode catalyst layer interface. The electrolyte potential within the anode catalyst layer increases from the local minimum near the polymer electrolyte/anode catalyst layer to the constant value in the anode gas flow channel.

Comparing the membrane activity distribution shown in Figure 7.23 and the electrolyte potential distribution shown in Figure 7.27, the potential and activity distributions are similar. In the mathematical model presented in this thesis, the ionic current density is a function of both potential and water mole fraction gradient with Equation (6.25). Therefore, the potential gradient is a function of the current density and water mole fraction gradient in the electrolyte:

$$\nabla\Phi_e = -\frac{\mathbf{J}_e - \frac{\epsilon_{\ell,e}\hat{\mathcal{D}}_{\text{H}_2\text{O}}^{\text{H}_3\text{O}^+}}{\mathcal{F}}\nabla x_{\ell,e}^{\text{H}_2\text{O}}}{\frac{\epsilon_{\ell,e}|\hat{\mathcal{D}}_{\text{H}_3\text{O}^+}^{\text{H}_3\text{O}^+}|}{\mathcal{F}}}, \quad (7.33)$$

where $\hat{\mathcal{D}}_{\text{H}_2\text{O}}^{\text{H}_3\text{O}^+}$ is positive, $\hat{\mathcal{D}}_{\text{H}_3\text{O}^+}^{\text{H}_3\text{O}^+}$ is negative, and the water mole fraction gradient is proportional to the membrane activity. Using Equation (7.33), the electrolyte potential distribution, shown in Figure 7.27, can be explained.

In the cathode catalyst layer, the ionic current density is negative. The membrane activity gradient, as shown in Figure 7.23, is positive and since the membrane activity is proportional to the water mole fraction in the electrolyte, the gradient of water mole fraction in the electrolyte is also positive. Hence, from Equation (7.33), the potential gradient in the electrolyte is positive. In the polymer electrolyte layer and in the catalyst layers near the catalyst/polymer electrolyte layer interfaces, the membrane activity and water mole fraction gradients become negative. The mole fraction gradient term is greater than the current density term in Equation (7.33) and the electrolyte potential gradient in Figure 7.27 becomes negative. Other than near the polymer electrolyte layer interface, the ionic current density in the anode catalyst layer is zero, as shown in Figure 7.26. Thus, from Equation (7.33), the potential gradient becomes proportional to the water mole fraction gradient. Since the membrane activity gradient is positive, the gradients of water mole fraction

and potential in the electrolyte are also positive in the anode catalyst layer.

Therefore, the potential distribution in the electrolyte is heavily influenced by the water content through the mole fraction gradient term in Equation (7.33). The ionic current density appears to have little effect, such that

$$\nabla\Phi_e \propto \nabla x_{\ell,e}^{\text{H}_2\text{O}}.$$

This result differs significantly from other modeling studies that use the Springer membrane model [26]. The model of Springer *et al.* [26] uses the Ohm's law relationship of Equation (6.22) and ignores the effect of concentration gradient on ionic transport:

$$\nabla\Phi_e \propto -\mathbf{J}_e.$$

The potential gradient obtained with the Springer model would be always positive, since the ionic current density is negative in the catalyst and polymer electrolyte layers. Therefore, because the Springer model neglects the effect of concentration gradients, the predicted voltage loss associated with ionic transport in the electrolyte would be larger for the Springer model than the membrane model presented in this thesis.

7.6.7 Catalyst Layer Reactions

The reaction rates for the anode and cathode catalyst layers are represented by Equation (4.64) for the anode catalyst layer and Equation (3.82) for the cathode catalyst layer. The production and consumption of hydrogen, oxygen, water, electrons and hydronium are proportional to the reaction rate, which has units of mole/m² · s and represents the molar production of electrons per unit area of catalyst. The distribution of the reaction rate within the catalyst layers is influenced by magnitude of the reaction rate constants, such as exchange current density and Tafel slope, and the resistance to mass transport for the reactants.

Figure 7.28 shows the distribution of the reaction rate in the cathode catalyst layer. The two-dimensional distribution and the reaction rate at $x/L_{\text{ch}} = 0.5$ are illustrated in Figures 7.28(a) and 7.28(b), respectively. The reaction rate is negative because electrons are consumed in the cathode catalyst layer. The magnitude of the reaction rate is highest near the electrode backing/catalyst layer and catalyst layer/polymer electrolyte layer interfaces. A higher oxygen concentration increases the magnitude of the reaction rate and from Figure 7.18, the highest oxygen concentration in the cathode catalyst layer is near the electrode backing/catalyst layer interface; hence, the magnitude of the reaction rate in the catalyst layer reaches a maximum at the interface with the electrode backing layer. Resistance to hydronium ion transport is responsible for the increase in reaction rate magnitude at the catalyst layer/polymer electrolyte interface. Since the hydronium ions enter the cathode catalyst layer from the polymer electrolyte layer, the resistance to hydronium transport is lowest near the catalyst layer/polymer electrolyte layer interface and increases with distance from the interface. Thus, the reaction rate is highest where resistance to oxygen transport is lowest, at the electrode backing layer interface, and where the resistance to hydronium ion transport is lowest, at the polymer electrolyte layer interface. The distribution of reaction rate in the cathode catalyst layer is due to resistance to both oxygen and hydronium transport.

The reaction rate distribution in the anode catalyst layer is significantly different than the distribution in the cathode catalyst layer. The reaction rate in the anode catalyst layer is illustrated in Figure 7.29. Figure 7.29(a) shows the reaction rate for both the x and y directions, while Figure 7.29(b) shows the reaction rate for $x/L_{\text{ch}} = 0.5$. Because electrons are produced in the anode catalyst layer, the reaction rate is positive. The reaction rate is zero in most of the anode catalyst layer, showing a large increase near the polymer electrolyte/anode catalyst layer interface. Unlike the cathode catalyst layer where oxygen transport is through diffusion, hydrogen transport is through convection and the concentration of hydrogen increases within the anode catalyst layer. Therefore, the main mechanism that limits the rate of reaction in the anode catalyst layer is resistance to hydronium ion transport, as indicated by the distribution shown in Figure 7.29. The reaction rate distribution is more uniform in the cathode catalyst layer than in the anode catalyst

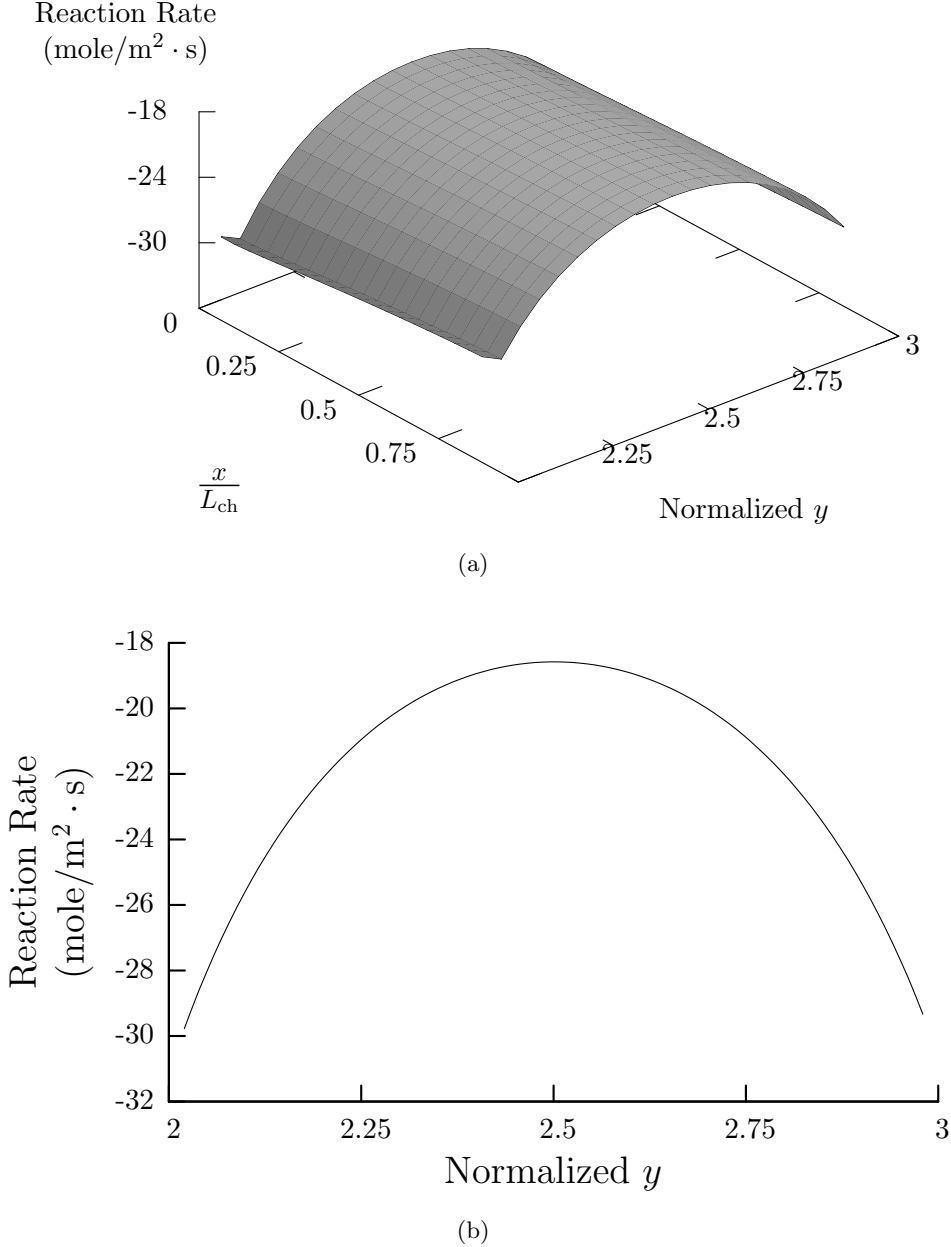


Figure 7.28: The reaction rate in the cathode catalyst layer. The y direction has been normalized such that the cathode catalyst layer corresponds to $(2 \leq y \leq 3)$. The (a) two-dimensional distribution and the (b) one-dimensional distribution at $x/L_{ch} = 0.5$ are shown.

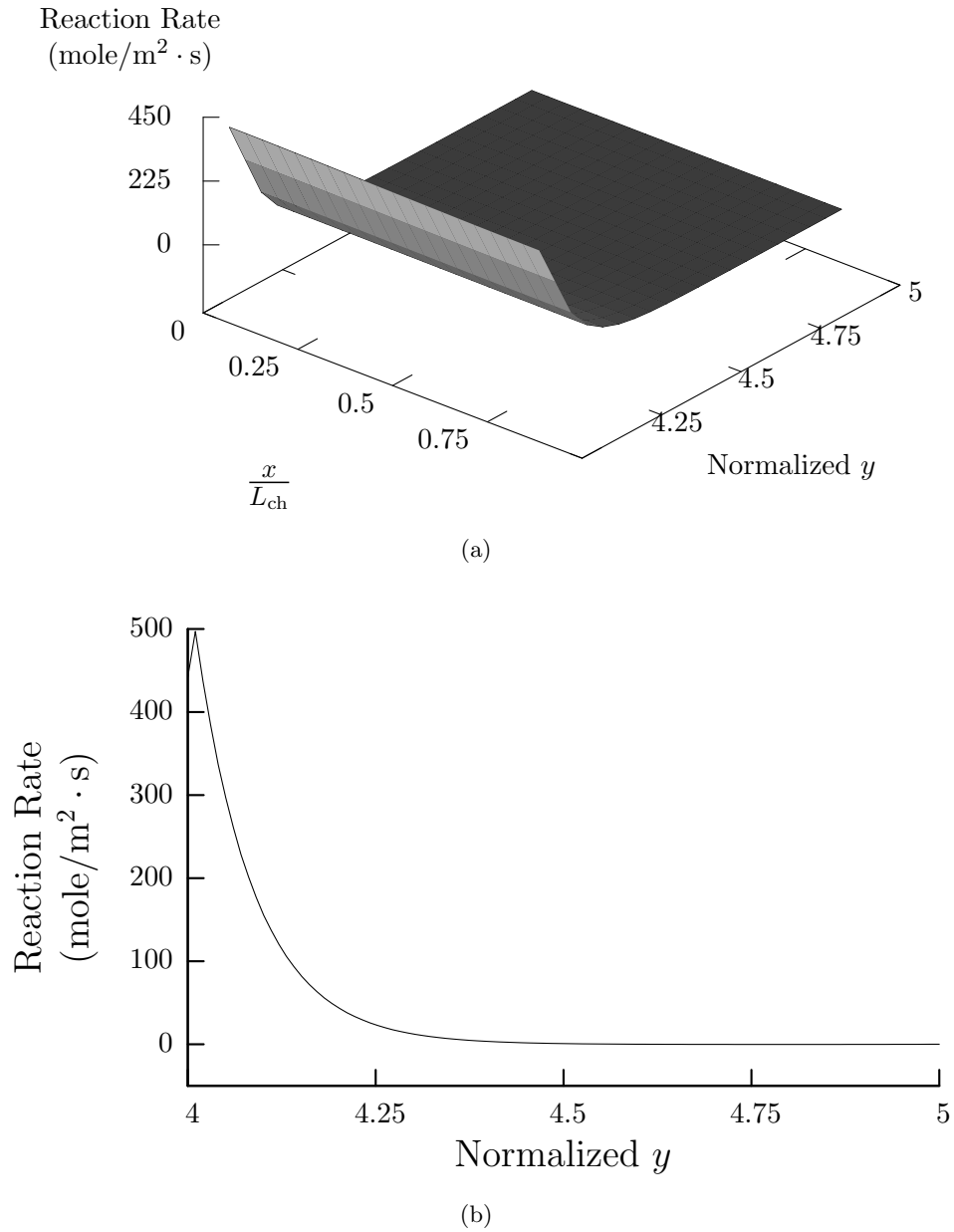


Figure 7.29: The reaction rate in the anode catalyst layer. The y direction has been normalized such that the anode catalyst layer corresponds to ($4 \leq y \leq 5$). The (a) two-dimensional distribution and the (b) one-dimensional distribution at $x/L_{ch} = 0.5$ are shown.

layer. This is caused by the differences in exchange current density. The anode exchange current density is approximately six orders of magnitude larger than the cathode exchange current density. Thus, the anode reaction requires a much smaller reaction area than the cathode reaction.

7.6.8 Effect of Channel Length

The results shown in the previous sections show little variations along the channel length and the profiles of concentration, current density, and potential are one-dimensional across the MEA. This is due to the short length of the channel, 1×10^{-3} m, used in the previous sections. However, if a cell with a longer channel length is simulated, then two-dimensional effects are more evident, particularly for the water content of the electrolyte and current density. The effect of channel length of membrane activity and current density are illustrated in this section by simulating cells with channel lengths of 1×10^{-2} m and 1×10^{-1} m.

For the simulations used in this section, the boundary conditions are illustrated in Figure 7.30. The boundary conditions are similar to the ones illustrated in Figure 7.2, but the flow configuration is different. The flow configuration is counter-flow, whereby the anode and cathode inlets are on the opposite sides of the fuel cell. Fully humidified hydrogen enters the anode gas flow channel, while fully humidified air enters the inlet of the cathode gas flow channel. The cell voltage is 0.8 V while the cell temperature is set to 343 K.

The design parameters are listed in Table 7.6. Most of the design parameters used in this section are similar to the ones used in the previous sections, which are listed in Table 7.4. However, two different channel lengths, 1×10^{-2} and 1×10^{-1} m, are used. As well, both positive and negative channel extensions are employed, with lengths of 1×10^{-2} m.

The grid is illustrated in Figure 7.31. The difference between the grid used in this section and the grid of Figure 7.4 is the presence of the anode and cathode minus extensions. These extensions reduce the effect of the boundary conditions on the numerical solution of the PEM fuel cell. The number of control volumes used for the grid illustrated in Figure 7.31 are listed in Table 7.7.

The length of the channel affects the water content in the polymer electrolyte layer. Figure 7.32

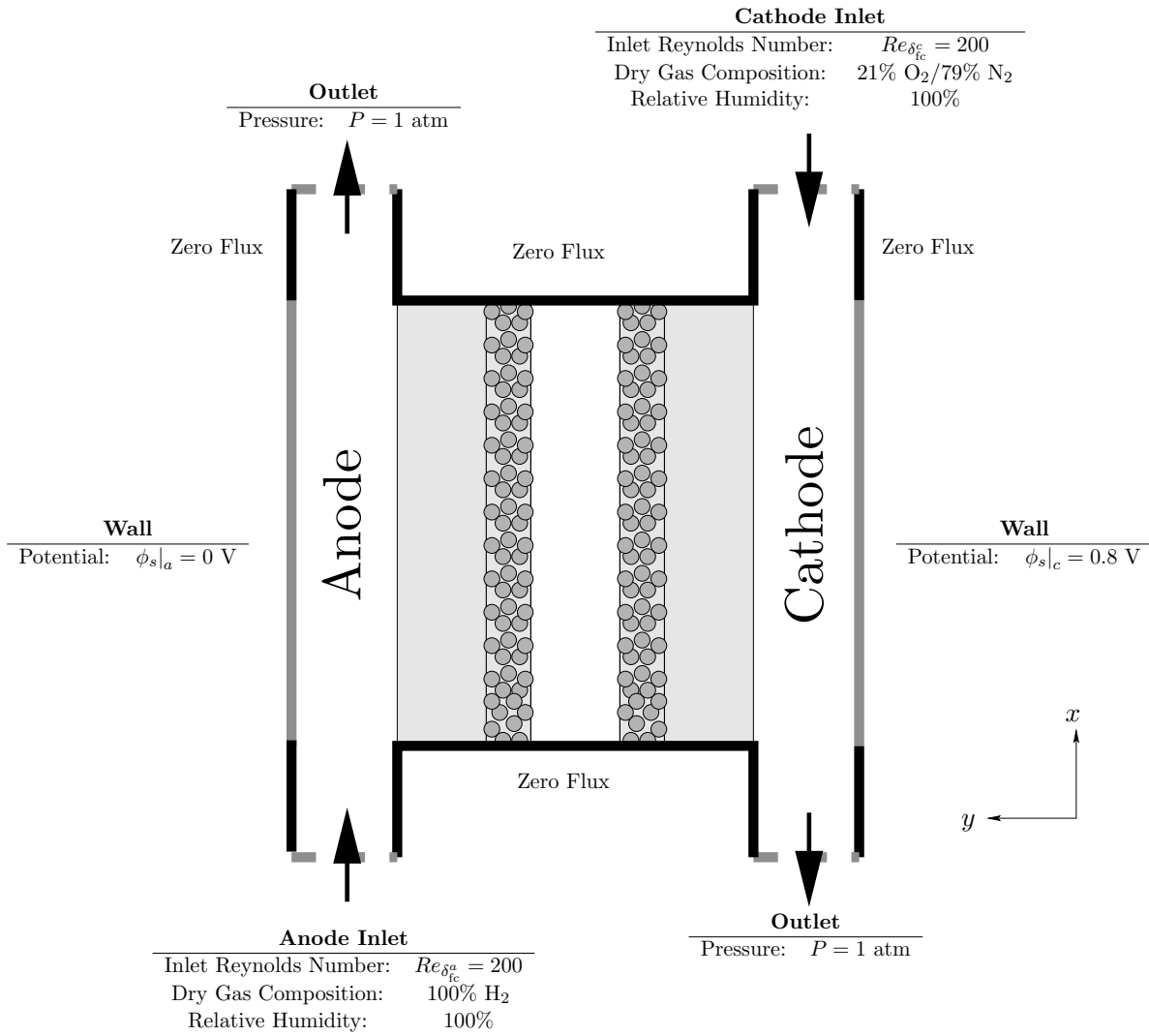


Figure 7.30: The boundary conditions used for examining the effect of channel length.

Table 7.6: The design parameters used for illustrating two-dimensional effects.

Layer	Parameter	Value
Gas Flow Channel	δ_{fc}	1×10^{-3} m
Electrode Backing Layer	δ_{eb}	2.03×10^{-4} m
	ϵ_g	0.5
	K	1.76×10^{-11} m
Catalyst Layer	δ_{cl}	2.55×10^{-5} m
	ϵ_g	0.1
	ϵ_e	0.1
	K	1.76×10^{-11} m
	m_{Pt}	1 mg/cm ²
	f_{Pt}	0.2
Polymer Electrolyte Layer	δ_{cl}	1.64×10^{-4} m
Channel Length	L_{ch}	1×10^{-2} m, 1×10^{-1} m
Anode and Cathode Extensions	L_{plus}, L_{minus}	1×10^{-2} m

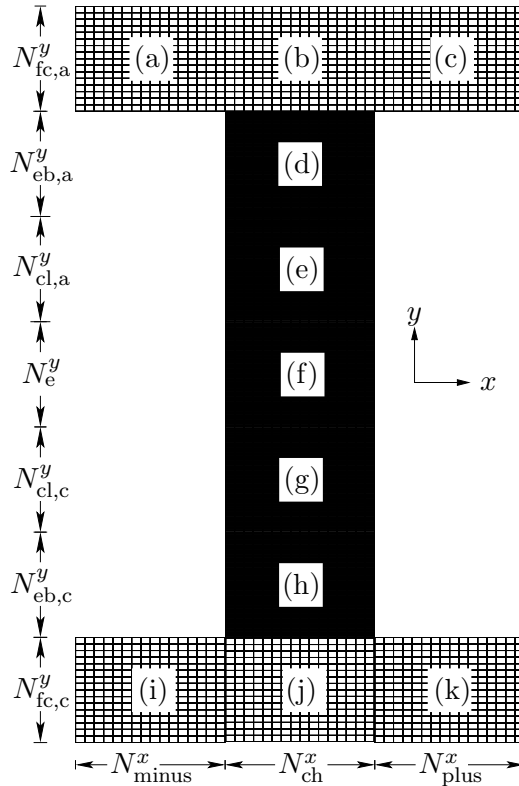


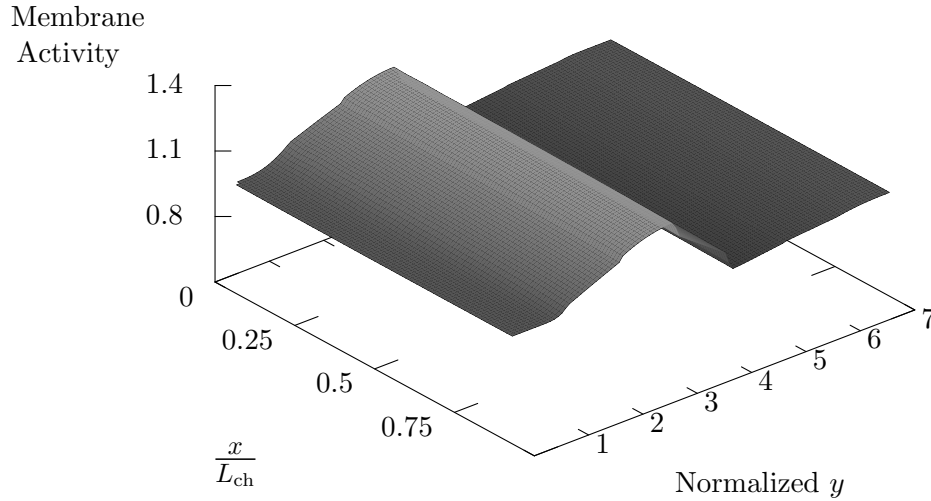
Figure 7.31: The mesh used for the comparison between the mathematical model and experimental data. The regions are the (a) anode minus extension, (b) anode gas flow channel, (c) anode plus extension, (d) anode electrode backing layer, (e) anode catalyst layer, (f) polymer electrolyte layer, (g) cathode catalyst layer, (h) cathode electrode backing layer, (i) cathode minus extension, (j) cathode gas flow channel, (k) cathode plus extension. Note that the figure is not drawn to scale.

Table 7.7: The number of control volumes used for illustrating two-dimensional effects.

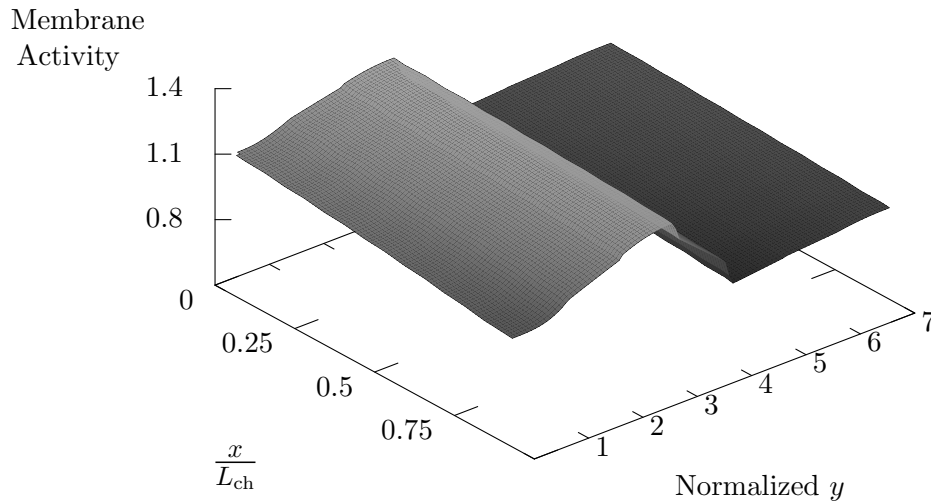
Number of y direction control volumes	$N_{fc,a}^y = N_{fc,c}^y = 16$ $N_{eb,a}^y = N_{eb,c}^y = N_{cl,a}^y = N_{cl,c}^y = N_{e,c}^y = 32$
Number of x direction control volumes	$N_{ch}^x = N_{plus}^x = N_{minus}^x = 16$

shows the membrane activity in a PEM fuel cell. The membrane activity for a cell with channel lengths of 1×10^{-2} m and 1×10^{-1} m are illustrated in Figures 7.32(a) and 7.32(b), respectively. The anode gas flow channel inlet is located at $x/L_{ch} = 0$, while the inlet for the cathode gas flow channel is at $x/L_{ch} = 1$. For both channel lengths, the membrane activity in the cathode channel decreases as x increases; the cathode gas stream gains water as it travels from the inlet, at $x/L_{ch} = 1$, to the outlet at $x/L_{ch} = 0$. The membrane activity in the anode channel also decreases as x increases, with the anode gas stream losing water as it flows from the inlet, at $x/L_{ch} = 0$, to the outlet at $x/L_{ch} = 1$.

Comparing Figures 7.32(a) and 7.32(b), the minimum membrane activity is lower and the maximum membrane activity is higher for the channel length of 1×10^{-1} m than for the 1×10^{-2} m channel. The difference in membrane activity between the two channel lengths can be more clearly seen in Figure 7.33. Figure 7.33 shows the membrane activity for the y -direction of the PEM fuel cell for x/L_{ch} values of 0, 0.5 and 1. The membrane activity for the fuel cell with a channel length of 1×10^{-2} m is illustrated in Figure 7.33(a), while Figure 7.33(b) shows the membrane activity for a channel length of 1×10^{-1} m. At the anode inlet and cathode outlet, $x/L_{ch} = 0$, the membrane activity is highest, while at the anode outlet and cathode inlet, the membrane activity is the lowest. For the channel length of 1×10^{-2} m, the profiles of membrane activity across the flow channels and MEA at the three x/L_{ch} locations are similar. However, for the longer flow channel of 1×10^{-1} m, the profiles at the three x/L_{ch} values are significantly different from each other. The greater variation between the profiles is due to the water transport from the anode to the cathode. With a longer channel length, more water is transferred from the anode to the cathode; hence, the



(a)



(b)

Figure 7.32: The membrane activity in the PEM fuel cell with a channel length of (a) 1×10^{-2} m and (b) 1×10^{-1} m. The y direction has been normalized such that the cathode gas flow channel corresponds to ($0 \leq y \leq 1$), the cathode electrode backing layer corresponds to ($1 \leq y \leq 2$), the cathode catalyst layer corresponds to ($2 \leq y \leq 3$), the polymer electrolyte layer corresponds to ($3 \leq y \leq 4$), the anode catalyst layer corresponds to ($4 \leq y \leq 5$), the anode electrode backing layer corresponds to ($5 \leq y \leq 6$), and the anode gas flow channel corresponds to ($6 \leq y \leq 7$).

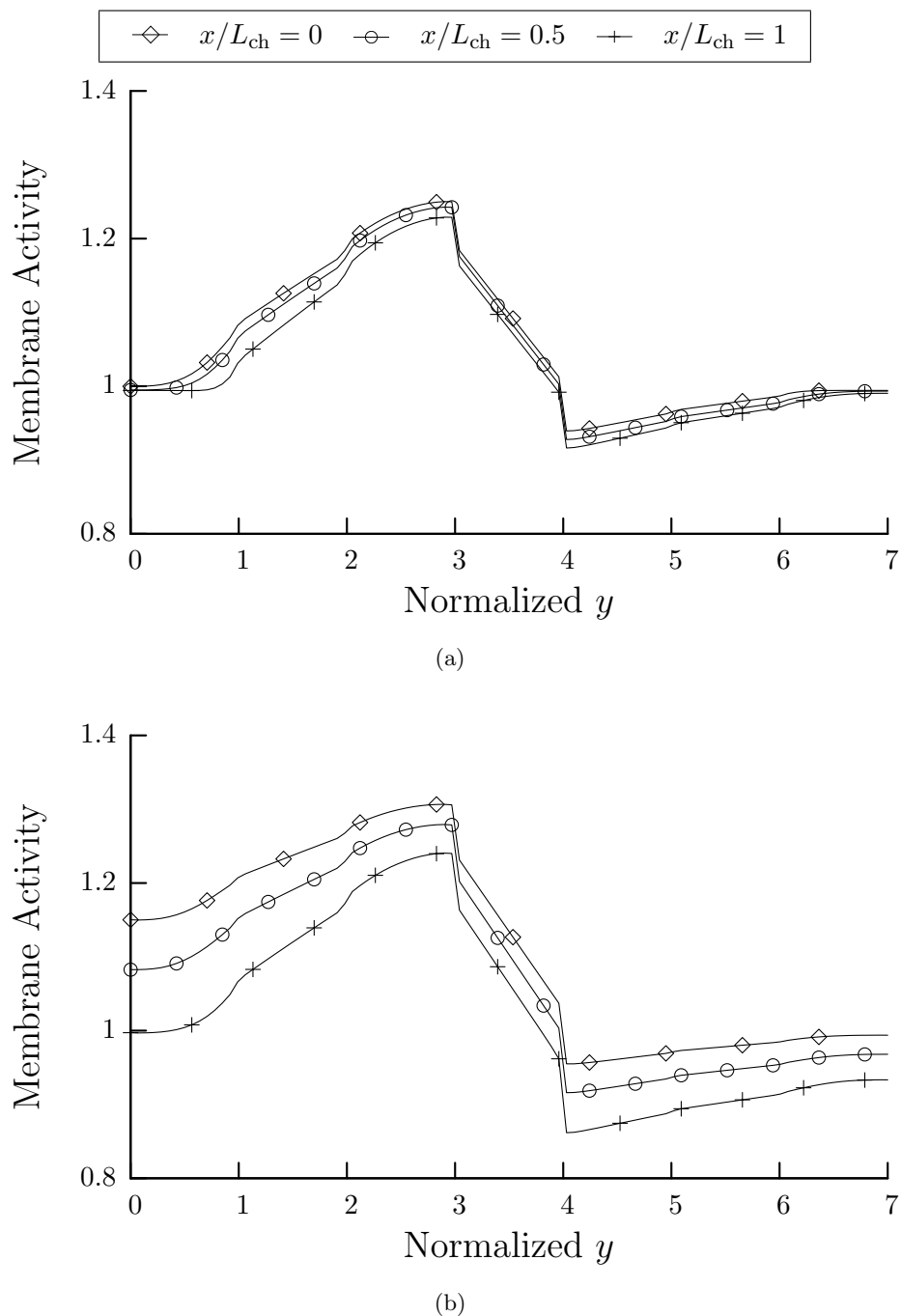


Figure 7.33: The membrane activity in the PEM fuel cell with a channel length of (a) 1×10^{-2} m and (b) 1×10^{-1} m at $x/L_{ch} = 0, 0.5$ and 1 . The y direction has been normalized such that the cathode gas flow channel corresponds to $(0 \leq y \leq 1)$, the cathode electrode backing layer corresponds to $(1 \leq y \leq 2)$, the cathode catalyst layer corresponds to $(2 \leq y \leq 3)$, the polymer electrolyte layer corresponds to $(3 \leq y \leq 4)$, the anode catalyst layer corresponds to $(4 \leq y \leq 5)$, the anode electrode backing layer corresponds to $(5 \leq y \leq 6)$, and the anode gas flow channel corresponds to $(6 \leq y \leq 7)$.

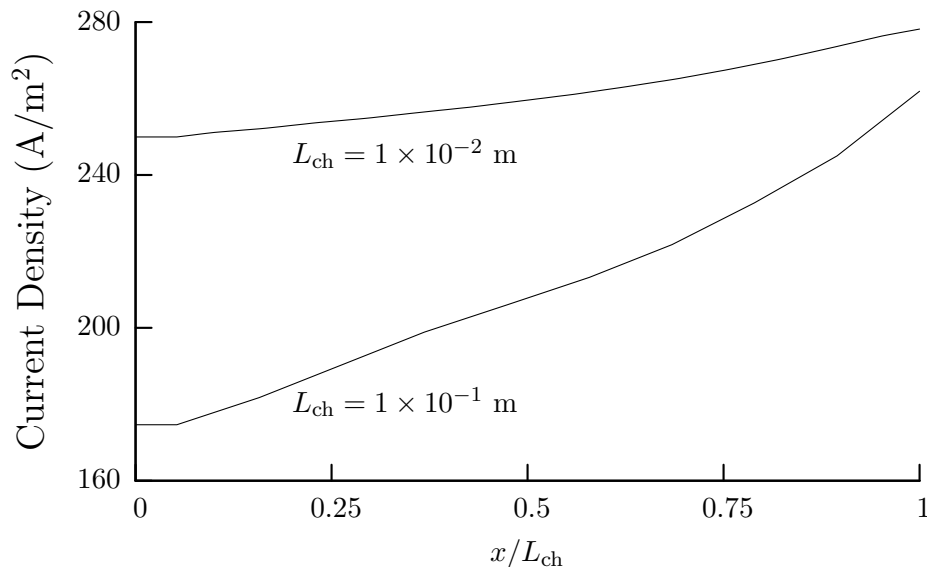


Figure 7.34: The magnitude of the y-direction current density at the external boundary of the cathode bipolar plate ($y = 0$).

maximum membrane activity in the cathode catalyst layer is larger for the longer channel length. As well, the minimum membrane activity, in the anode catalyst layer, is smaller for the longer channel length. Therefore, both water flooding and membrane dehydration are more significant for longer channel lengths.

The difference in membrane activity between the two channel lengths results in different current density profiles, as illustrated in Figure 7.34. For the shorter channel length, the current density is more uniform along the channel length. As well, the average current density is higher for the $1 \times 10^{-2} m$ channel than for the $1 \times 10^{-1} m$ channel; the average current density is $261 A/m^2$ for the $1 \times 10^{-2} m$ channel length and $210 A/m^2$ for the longer channel length of $1 \times 10^{-1} m$. Thus, the smaller fuel cell has a larger power density than the larger fuel cell. This result illustrates the difficulty of scaling small cell designs to larger cells. The transport phenomena in small cells can be approximated one-dimensionally; however, two-dimensional effects are significant for larger cells. Therefore, practical sized cells can not be designed by scaling-up small cells.

7.7 Summary

The numerical solution of the simplified formulation was used to illustrate transport phenomena in a PEM fuel cell. First, however, the numerical model developed in this thesis research was validated against another CFD code. Also, the number of control volumes required for a grid independent solution were determined, as well as the appropriate value of the convergence criteria. In addition, the predicted current density from the numerical model of this thesis research was compared against published, experimental PEM fuel cell performance data.

The transport of the bulk gas phase, hydrogen, oxygen, water, electrons, and hydronium was examined. The direction for the bulk flow of the gas phase in the membrane electrode assembly was always from the anode to the cathode side of the cell. Thus, a net mass transfer occurred from the anode side to the cathode side of the fuel cell. This convective gas flow aided the transport of hydrogen from the anode gas flow channel to the reaction sites in the anode catalyst layer. However, the bulk gas phase flow acted to hinder the transport of oxygen from the cathode gas flow channels to the cathode catalyst layer. As a result, the concentration of hydrogen increased in the anode catalyst layer, but decreased in the cathode catalyst layer.

Water was transported in both the gas phase and as a liquid phase in the polymer electrolyte. Due to the electro-chemical reactions, water was consumed in the anode catalyst layer and produced in the cathode catalyst layer. Some of the water produced in the cathode catalyst layer traveled through the polymer electrolyte layer to react in the anode catalyst layer. However, because the resistance to mass transfer was lower in the gas phase than in the electrolyte, the majority of the water required for the anode reaction was drawn from the anode gas flow channels. Likewise, the majority of the water produced in the cathode catalyst layer was exhausted through the cathode gas flow channels. As a result, the relative humidity in the cathode side of the fuel cell exceeded 100%, indicating that water flooding would occur. In the anode catalyst layer, the relative humidity in the gas phase was below 100%, indicating that membrane dehydration occurred. Thus, performance problems due to both excess water in the cathode and insufficient water in the anode could plague

CHAPTER 7. RESULTS AND DISCUSSION

a PEM fuel cell simultaneously.

The conductivity of the solid phase was high, resulting in no significant voltage losses due to electrical resistance. The potential distribution in the electrolyte was highly influenced by the water content; thus, hydronium transport due to concentration gradients was significant. Both reactant gas and hydronium transport affected the reaction rate distribution in the cathode catalyst layer. In the anode catalyst layer, however, the reaction rate was limited solely by ion transport, since hydrogen transport was aided by convection.

The length of the gas flow channel affected the water content of the electrolyte and gas stream, as well as the current density. A longer channel resulted in both more flooding and electrolyte dehydration, and thus reduced the average current density of the fuel cell.

Chapter 8

Summary and Future Work

This thesis presented a consistent, systematic, and comprehensive general formulation for a PEM fuel cell. Simplifying assumptions were applied to the general formulation in order to obtain a numerical solution. The results from the numerical solution illustrated physical phenomena that occur within the PEM fuel cell. The simplified mathematical model used the Generalized Stefan-Maxwell equations to describe water and ion transport in the polymer electrolyte. The use of these equations to describe transport in the electrolyte was novel, since most, published, PEM fuel cell models employ semi-empirical equations to describe ion and water transport in the electrolyte.

A PEM fuel cell consists of several distinct layers, or regions, and within each layer, several physical processes occur. In the anode and cathode bipolar plates, fluid flow occurs in the gas flow channels while current flows in the solid portion of the bipolar plate. The anode and cathode electrode backing layers are characterized by fluid flow in porous media. Positive ions and water flow in the pores of the acidic polymer electrolyte layer. The catalyst layers combine the fluid flow characteristics of the electrode backing and polymer electrolyte layers. As well, the electro-chemical reactions that convert the chemical energy of hydrogen and oxygen into electrical energy, heat and water occur within the catalyst layers: oxygen reduction occurs in the cathode catalyst layer while hydrogen oxidation occurs in the anode catalyst layer. The processes in the layers are coupled and due to the thinness of the layers, direction measurements of quantities that can characterize these

CHAPTER 8. SUMMARY AND FUTURE WORK

processes, such as temperature or concentration, is impossible. Therefore, mathematical modeling is used to provide insight on the physical phenomena occurring within a PEM fuel cell. Several mathematical models currently exist in the published literature. These models tend to concentrate on modeling phenomena in the membrane electrode assembly, or on modeling the fluid flow in the gas flow channels.

The general formulation of this thesis research was derived by considering the fuel cell to be composed of several co-existing phases. These phases included a multi-component gas phase that included hydrogen, oxygen, water, nitrogen, carbon dioxide or carbon monoxide; liquid phase consisting of water that exists in the gas flow channels, electrode backing and catalyst layers; solid phase that is the solid matrix in the catalyst and electrode backing layers, as well as the solid of the bipolar plate; and a liquid phase consisting of water and hydronium ions in the pores of the polymer electrolyte. The conservation of mass, momentum and energy was applied to each phase, although only the conservation of species, for electrons, and energy apply to the solid phase. The phases interact with each other and this interaction was captured by volume-averaging the conservation equations of each phase. The volume-averaging procedure resulted in the addition of interfacial source terms to the conservation of mass, momentum, species and energy of each phase. These interfacial source terms represented the interactions between the phases and expressions for these terms were required in order to solve the governing equations.

The general governing equations were simplified by assuming that the fuel cell was isothermal and operating in steady-state. Also, the polymer electrolyte was assumed impervious to the gas phase, the anode fuel was assumed to be free of carbon monoxide, and liquid water was considered to exist only in the gas phase or the liquid in the pores of the polymer electrolyte. Thus, the conservation of energy did not need to be solved and constitutive equations for two-phase, gas-liquid flow were not required for solution. The transport of liquid water and hydronium in the pores of the electrolyte were modeled with the Generalized Stefan-Maxwell equations. The use of these equations in a PEM fuel cell model was unique, since most modeling studies use semi-empirical equations to describe ion and water transport.

CHAPTER 8. SUMMARY AND FUTURE WORK

The simplified mathematical model was solved numerically for a two-dimensional geometry using a finite volume, SIMPLE algorithm, which was written in the computer language of C++ as part of the thesis research. The independent variables included the gas phase x - and y -component velocities; the gas phase pressure; the partial density of the gas phase hydrogen, oxygen, water and nitrogen; and the potentials in the solid and electrolyte. The water transport in the polymer electrolyte was coupled to the gas phase water transport by assuming local equilibrium between the water in the gas phase and the water in the electrolyte pores.

Since the model for water and ion transport in the electrolyte used by this thesis was unique, values for the diffusion coefficients in the Generalized Stefan-Maxwell equations were not available from the published literature. The values for the diffusion coefficients were obtained using experimental water diffusion and conductivity data for Nafion from the published literature. The electrolyte model of this thesis was compared to the common semi-empirical model used by other PEM fuel cell models in the published literature. The electrolyte model of this thesis reduced to the semi-empirical model if no water concentration gradients existed within the polymer electrolyte membrane; thus, the semi-empirical model neglected the effect of concentration gradients on ionic transport. The effect of neglecting this effect was discovered to be significant and would result in the semi-empirical model under-estimating the current flow in the electrolyte if the water content of the anode side of the electrolyte was less than the cathode side.

The numerical solution of the mathematical model highlighted many of the processes that occurred within a PEM fuel cell. Examining the flow of the gas phase yielded that a net transfer of mass occurred between the anode and cathode sides of the fuel cell due to hydronium transport from the anode to the cathode. The net mass transfer resulted in a convective flow direction in the catalyst and electrode backing layers that was from the anode to the cathode. The convective flow aided the transport of hydrogen in the anode electrode backing and catalyst layers. As well, the nature of the electro-chemical reactions, in which hydrogen and water were removed from the gas phase at a ratio of 1:2, resulted in the hydrogen concentration increasing in the catalyst layers even though it was being consumed. The convective flow hindered oxygen transport in the cathode and

CHAPTER 8. SUMMARY AND FUTURE WORK

the main mechanism of oxygen transport was diffusion.

Hydrogen transport was confined to the anode side of the fuel cell, while oxygen transport occurred only in the cathode side. However, water transport was continuous across all regions of the fuel cell because water was present in the gas phase as well as the electrolyte. Water was consumed in the anode catalyst layer and produced in the cathode catalyst layer. Since the resistance to water transport was lower in the gas phase than in the electrolyte, most of the water consumed in the anode catalyst layer was obtained from the anode gas flow channel, while most of the water produced in the cathode catalyst layer exited the fuel cell via the cathode gas flow channel. However, some of the water produced in the cathode catalyst layer near the catalyst layer/polymer electrolyte interface traveled through the polymer electrolyte layer to participate in the anode reaction. The relative humidity in the gas phase on the cathode side of the cell was greater than 100%, indicating that liquid water formation would occur if it was included in the model. On the anode side of the cell, the relative humidity was below 100% in the catalyst layers even though the flow in the anode gas flow channel was fully humidified. Thus, these simulations suggested that both liquid water flooding and membrane dehydration could occur simultaneously.

The potential in the solid phase was nearly constant in the anode and cathode sides of the fuel cell due to the high conductivity of the solid phase. The potential in the electrolyte was influenced more by the water content of the electrolyte than the current density. Thus, electrolyte models should include the effect of concentration gradients on ion transport, since this effect was found to be significant.

The reaction rate distributions in the anode and cathode catalyst layers indicated the relative importance of different processes to the conversion of chemical energy to electrical energy in the fuel cell. In the cathode catalyst layer, both reactant gas transport and ion transport influenced the reaction rate. However, in the anode side of the fuel cell, the reaction rate was limited solely by ion transport, since hydrogen transport was aided by convection.

The length of the flow channel affected the water content in the gas phase and electrolyte. A longer channel resulted in both more flooding and more electrolyte dehydration. As a result, the

CHAPTER 8. SUMMARY AND FUTURE WORK

performance of a fuel cell decreased when the channel length increased.

The results of this thesis research suggest several areas of future research. Since simulations showed that the cathode side of the fuel cell would have a relative humidity of greater than 100%, two-phase, liquid-gas flow can not be neglected and should be incorporated into the mathematical model. Also, the fuel cell reactions are exothermic and the transport of the heat of reaction from the catalyst layers out of the fuel cell is a significant problem, especially at operating conditions that produce high current densities. Therefore, the isothermal assumption should be discarded and the conservation of energy equation added to the mathematical model. As well, practical gas flow channel configurations, such as the serpentine pattern, are three-dimensional; thus, the numerical solution should include three dimensions. Finally, the numerical solution presented in this thesis was limited to small cells because the time to achieve a converged solution was long. In order to simulate fuel cells of practical size, a more efficient solver than the one currently used should be employed and the numerical solution should be re-written in order to take advantage of parallel computing methods.

References

- [1] U.S. Department of Energy. Hydrogen, fuel cells & infrastructure technologies program: Multi-year research. 2005.
- [2] N. Zamel and X. Li. Life cycle analysis of vehicles powered by a fuel cell and by internal combustion engine for Canada. *Journal of Power Sources*, 155(2):297–310, 2006.
- [3] X. Li. *Principles of Fuel Cells*. Taylor & Francis, New York, 2005.
- [4] M. Warshay, P. Prokopius, M. Le, and G. Voecks. The NASA fuel cell upgrade program for the space shuttle orbiter. *Proceedings of the Intersociety Energy Conversion Engineering Conference*, pages 228–231, 1997.
- [5] Ballard Power Systems. Ballard fuel cell power module 902. Available at: http://www.ballard.com/be_a_customer/spec_sheets, Accessed August 30, 2006.
- [6] T. Ralph, G. Hards, J. Keating, S. Campbell, D. Wilkinson, M. Davis, J. St-Pierre, and M. Johnson. Low cost electrodes for proton exchange membrane fuel cells. Performance in single cells and Ballard stacks. *Journal of the Electrochemical Society*, 144(11):3845–3857, 1997.
- [7] R. Bellows, E. Marucchi-Soos, and D. Buckley. Analysis of reaction kinetics for carbon monoxide and carbon dioxide on polycrystalline platinum relative to fuel cell operation. *Industrial & Engineering Chemistry Research*, 35(4):1235–1242, 1996.
- [8] X. Li and I. Sabir. Review of bipolar plates in PEM fuel cells: Flow-field designs. *International Journal of Hydrogen Energy*, 30(4):359–3571, 2005.
- [9] T. Fuller and J. Newman. Water and thermal management in solid-polymer-electrolyte fuel cells. *Journal of the Electrochemical Society*, 140(5):1218–1225, 1993.
- [10] D. Watkins. Research, development and demonstration of solid polymer fuel cell systems. In L. Blomen and M. Mugerwa (eds.), *Fuel Cell Systems*, pages 493–530. Plenum Press, New York, 1993.
- [11] C. Marr and X. Li. An engineering model of proton exchange membrane fuel cell performance. *ARI*, 50:190–200, 1998.
- [12] J. Baschuk and X. Li. Carbon monoxide poisoning of proton exchange membrane fuel cells. *International Journal of Energy Research*, 25(8):695–713, 2001.

REFERENCES

- [13] S. Gottesfeld and J. Pafford. A new approach to the problem of carbon monoxide poisoning in fuel cells operating at low temperatures. *Journal of the Electrochemical Society*, 135(10):2651–2652, 1988.
- [14] J. Baschuk and X. Li. Modelling of polymer electrolyte membrane fuel cells with variable degrees of water flooding. *Journal of Power Sources*, 86(1-2):181–196, 2000.
- [15] J. Baschuk and X. Li. A general formulation for a mathematical PEM fuel cell model. *Journal of Power Sources*, 142(1-2):134–153, 2005.
- [16] J. Kim, S.-M. Lee, S. Srinivasan, and C. Chamberlin. Modeling of proton exchange membrane fuel cell performance with an empirical equation. *Journal of the Electrochemical Society*, 142(8):2670–2674, 1995.
- [17] G. Squadrito, G. Maggio, and E. Passalacqua. An empirical equation for polymer electrolyte fuel cell (PEFC) behavior. *Journal of Applied Electrochemistry*, 29(12):1449–1455, 1999.
- [18] J. Amphlett, R. Baumert, R. Mann, B. Peppley, P. Roberge, and T. Harris. Performance modeling of the Ballard Mark IV solid polymer electrolyte fuel cell I. Mechanistic model development. *Journal of the Electrochemical Society*, 142(1):1–8, 1995.
- [19] J. Amphlett, R. Baumert, R. Mann, B. Peppley, P. Roberge, and T. Harris. Performance modeling of the Ballard Mark IV solid polymer electrolyte fuel cell II. Empirical model development. *Journal of the Electrochemical Society*, 142(1):9–15, 1995.
- [20] A. Rodrigues, J. Amphlett, R. Mann, B. Peppley, and P. Roberge. Carbon monoxide poisoning of proton-exchange-membrane fuel cells. *Proceedings of the Intersociety Energy Conversion Engineering Conference*, pages 768–773, 1997.
- [21] M. Fowler, R. Mann, J. Amphlett, B. Peppley, and P. Roberge. Incorporation of voltage degradation into a generalised steady state electrochemical model for a PEM fuel cell. *Journal of Power Sources*, 106(1-2):274–283, 2002.
- [22] R. Jinnouchi and K. Okazaki. Molecular dynamics study of transport phenomena in perfluorosulfonate ionomer membranes for polymer electrolyte fuel cells. *International Journal of Environmental Studies*, 150(1):E66–E73, 2003.
- [23] T. Li, A. Wlaschin, and P. Balbuena. Theoretical studies of proton transfer in water and model polymer electrolyte systems. *Industrial and Engineering Chemistry Research*, 40(22):4789–4800, 2001.
- [24] D. Bernardi and M. Verbrugge. Mathematical model of a gas diffusion electrode bonded to a polymer electrolyte. *AIChE Journal*, 37(8):1151–1163, 1991.
- [25] D. Bernardi and M. Verbrugge. A mathematical model of the solid-polymer-electrolyte fuel cell. *Journal of the Electrochemical Society*, 139(9):2477–2491, 1992.
- [26] T. Springer, T. Zawodzinski, and S. Gottesfeld. Polymer electrolyte fuel cell model. *Journal of the Electrochemical Society*, 138(8):2334–2342, 1991.

REFERENCES

- [27] T. Springer, M. Wilson, and S. Gottesfeld. Modeling and experimental diagnostics in polymer electrolyte fuel cells. *Journal of the Electrochemical Society*, 140(12):3513–3526, 1993.
- [28] K. Weisbrod, S. Grot, and N. Vanderborgh. Through-the-electrode model of a proton exchange membrane fuel cell. *Proceedings of the First International Symposium on Proton Conduction Membrane Fuel Cells I*, pages 152–166, 1995.
- [29] F. Gloaguen and R. Durand. Simulations of PEFC cathodes: an effectiveness factor approach. *Journal of Applied Electrochemistry*, 27(9):1029–1035, 1997.
- [30] M. Eikerling and A. Kornyshev. Modelling the performance of the cathode catalyst layer of polymer electrolyte fuel cells. *Journal of Electroanalytical Chemistry*, 453(1-2):89–106, 1998.
- [31] L. Pisani, G. Murgia, M. Valentini, and B. D’Aguanno. A working model of polymer electrolyte fuel cells comparisons between theory and experiments. *Journal of the Electrochemical Society*, 149(7):A898–A904, 2002.
- [32] H. Chu, C. Yeh, and F. Chen. Effects of porosity change of gas diffuser on performance of proton exchange membrane fuel cell. *Journal of Power Sources*, 123(1):1–9, 2003.
- [33] J.-T. Wang and R. Savinell. Simulation studies on the fuel electrode of a $H_2 - O_2$ polymer electrolyte fuel cell. *Electrochimica Acta*, 37(15):2737–2745, 1992.
- [34] H. Dhar, L. Christner, and A. Kush. Nature of CO adsorption during H_2 oxidation in relation to modeling for CO poisoning of a fuel cell anode. *Journal of the Electrochemical Society*, 134(12):3021–3026, 1987.
- [35] T. Springer, T. Zawodzinski, and S. Gottesfeld. Modeling of polymer electrolyte fuel cell performance with reformat feed streams: effects of low levels of CO in hydrogen. In S. Srinivasan, J. McBreen, A. Khandkar, and V. Tilak (eds.), *Electrode Materials and Processes for Energy Conversion and Storage IV*, pages 15–24. The Electrochemical Society, Inc., Pennington, 1997.
- [36] S. Chan, S. Goh, and S. Jiang. A mathematical model of polymer electrolyte fuel cell with anode CO kinetics. *Electrochimica Acta*, 48(13):1905–1919, 2003.
- [37] J. Baschuk and X. Li. Modelling CO poisoning and O_2 bleeding in a PEM fuel cell anode. Accepted to the *International Journal of Energy Research*, 2003.
- [38] D. Bevers, M. Wöhr, K. Yasuda, and K. Ogura. Simulation of a polymer electrolyte fuel cell electrode. *Journal of Applied Electrochemistry*, 27(11):1254–1264, 1997.
- [39] M. Wöhr, K. Bolwin, W. Schnurnberger, M. Fischer, W. Neubrand, and G. Eigenberger. Dynamic modelling and simulation of a polymer membrane fuel cell including mass transport limitation. *International Journal of Hydrogen Energy*, 23(3):213–218, 1998.
- [40] A. Rowe and X. Li. Mathematical modeling of proton exchange membrane fuel cells. *Journal of Power Sources*, 102(1-2):82–96, 2001.
- [41] T. Nguyen and R. White. A water and heat management model for proton-exchange-membrane fuel cells. *Journal of the Electrochemical Society*, 140(8):2178–2186, 1993.

REFERENCES

- [42] D. Thirumalai and R. White. Mathematical modeling of proton-exchange-membrane-fuel-cell stacks. *Journal of the Electrochemical Society*, 144(5):1717–1723, 1997.
- [43] J. Yi and T. Nguyen. An along-the-channel model for proton exchange membrane fuel cells. *Journal of the Electrochemical Society*, 145(4):1149–1159, 1998.
- [44] H. van Bussel, F. Koene, and R. Mallant. Dynamic model of solid polymer fuel cell water management. *Journal of Power Sources*, 71(1-2):218–222, 1998.
- [45] T. Springer, T. Rockward, T. Zawodzinski, and S. Gottesfeld. Model for polymer electrolyte fuel cell operation on reformat feed. Effects of CO, H₂ dilution, and high fuel utilization. *Journal of the Electrochemical Society*, 148(1):A11–A23, 2001.
- [46] D. Singh, D. Lu, and N. Djilali. A two-dimensional analysis of mass transport in proton exchange membrane fuel cells. *International Journal of Engineering Science*, 37(4):431–452, 1999.
- [47] A. Kazim, H. Liu, and P. Forges. Modelling of performance of PEM fuel cells with conventional and interdigitated flow fields. *Journal of Applied Electrochemistry*, 29(12):1409–1416, 1999.
- [48] R. Bradean, K. Promislow, and B. Wetton. Transport phenomena in the porous cathode of a proton exchange membrane fuel cell. *Numerical Heat Transfer; Part A: Applications*, 42(1-2):121–138, 2002.
- [49] W. He, J. Yi, and T. Nguyen. Two-phase flow model of the cathode of PEM fuel cells using interdigitated flow fields. *AIChE Journal*, 46(10):2053–2064, 2000.
- [50] D. Natarajan and T. Nguyen. A two-dimensional, two-phase, multicomponent, transient model for the cathode of a proton exchange membrane fuel cell using conventional gas distributors. *Journal of the Electrochemical Society*, 148(12):A1324–A1335, 2001.
- [51] D. Natarajan and T. Nguyen. Three-dimensional effects of liquid water flooding in the cathode of a PEM fuel cell. *Journal of Power Sources*, 115(1):66–80, 2003.
- [52] V. Gurau, H. Liu, and S. Kakac. Two-dimensional model for proton exchange membrane fuel cells. *AIChE Journal*, 44(11):2410–2422, 1998.
- [53] T. Zhou and H. Liu. 3-D model of proton exchange membrane fuel cells. *American Society of Mechanical Engineers, Heat Transfer Division, (Publication) HTD*, 366(1):43–49, 2000.
- [54] L. You and H. Liu. A two-phase and multi-component model for the cathode of PEM fuel cells. *American Society of Mechanical Engineers, Heat Transfer Division, (Publication) HTD*, 369(4):325–334, 2001.
- [55] S. Shimpalee, S. Dutta, W. Lee, and J. V. Zee. Effect of humidity on PEM fuel cell performance part II-numerical simulation. *American Society of Mechanical Engineers, Heat Transfer Division, (Publication) HTD*, 364(1):367–374, 1999.
- [56] S. Shimpalee and S. Dutta. Numerical prediction of temperature distribution in PEM fuel cells. *Numerical Heat Transfer; Part A: Applications*, 38(2):111–128, 2000.

REFERENCES

- [57] S. Shimpalee, W. Lee, J. V. Zee, and H. Naseri-Neshat. Predicting the transient response of a serpentine flow-field PEMFC I: Excess to normal fuel and air. *Journal of Power Sources*, 156(2):355–368, 2006.
- [58] S. Shimpalee, W. Lee, J. V. Zee, and H. Naseri-Neshat. Predicting the transient response of a serpentine flow-field PEMFC II: Normal to minimal fuel and air. *Journal of Power Sources*, 156(2):369–374, 2006.
- [59] S. Shimpalee, S. Dutta, and J. Zee. Numerical prediction of local temperature and current density in a PEM fuel cell. *American Society of Mechanical Engineers, Heat Transfer Division, (Publication) HTD*, 366(1):1–9, 2000.
- [60] C. Wang, Z. Wang, and Y. Pan. Two-phase phase transport in proton exchange membrane fuel cells. *American Society of Mechanical Engineers, Heat Transfer Division, (Publication) HTD*, 364(1):351–357, 1999.
- [61] S. Um, C. Wang, and K. Chen. Computational fluid dynamics modeling of proton exchange membrane fuel cells. *Journal of the Electrochemical Society*, 147(12):4485–4493, 2000.
- [62] Y. Wang and C. Wang. Modeling polymer electrolyte fuel cells with large density and velocity changes. *Journal of the Electrochemical Society*, 152(2):A445–A453, 2005.
- [63] Y. Wang and C. Wang. Ultra large-scale simulation of polymer electrolyte fuel cells. *Journal of Power Sources*, 153(1):130–135, 2006.
- [64] A. Kulikovskiy. Quasi-3d modeling of water transport in polymer electrolyte fuel cells. *Journal of the Electrochemical Society*, 150(11):A1432–A1439, 2003.
- [65] S. Mazumder and J. Cole. Rigorous 3-d mathematical modeling of PEM fuel cells ii. model predications with liquid water transport. *Journal of the Electrochemical Society*, 150(11):A1510–A1517, 2003.
- [66] S. Lister, J. Pharoah, G. McLean, and N. Djilali. Computational analysis of heat and mass transfer in a micro-structured PEMFC cathode. *Journal of Power Sources*, 156(2):334–344, 2006.
- [67] N. Siegel, M. Ellis, D. Nelson, and M. von Spakovsky. Single domain PEMFC model based on agglomerate catalyst geometry. *Journal of Power Sources*, 115(1):81–89, 2003.
- [68] J. Jang, W. Yan, and C. Shih. Numerical study of reactant gas transport phenomena and cell performance of proton exchange membrane fuel cells. *Journal of Power Sources*, 156(2):244–252, 2006.
- [69] T. Jen, T. Yan, and S. Chan. Chemical reacting transport phenomena in a PEM fuel cell. *International Journal of Heat and Mass Transfer*, 46(22):4157–4168, 2003.
- [70] A. Kumar and R. Reddy. Modeling of polymer electrolyte membrane fuel cell with metal foam in the flow-field of the bipolar/end plates. *Journal of Power Sources*, 114(1):54–62, 2003.

REFERENCES

- [71] T. Berning, D. Lu, and N. Djilali. Three-dimensional computational analysis of transport phenomena in a PEM fuel cell. *Journal of Power Sources*, 106(1-2):284–294, 2002.
- [72] Y. Ferng, C. Sun, and A. Su. Numerical simulation of thermal-hydraulic characteristics in a proton exchange membrane fuel cell. *International Journal of Energy Research*, 27(5):495–511, 2003.
- [73] J. Stockie. Modeling hydrophobicity in a porous fuel cell electrode. Presented at CFCD II, April 19-25, Banff International Research Station, Banff, Alberta, Canada, 2003.
- [74] E. Scattergood and E. Lightfoot. Diffusional interaction in an ion-exchange membrane. *Transactions of the Faraday Society*, 64:1135–1146, 1968.
- [75] M. Ishii. *Thermo-Fluid Dynamic Theory of Two-Phase Flow*. Eyrolles, Paris, 1975.
- [76] T. Gierke and W. Hsu. The cluster-network model of ion clustering in perfluorosulfonated membranes. In A. Eisenberg and H. Yeager (eds.), *Perfluorinated Ionomer Membranes*, ACS Symposium Series 180, pages 283–307. American Chemical Society, Washington, U.S.A, 1982.
- [77] Z. Ogumi, T. Kuroe, and Z. Takehara. Gas permeation in SPE method II. Oxygen and hydrogen permeation through Nafion. *Journal of the Electrochemical Society*, 132(11):2601–2605, 1985.
- [78] T. Thampan, S. Malhotra, H. Tang, and R. Datta. Modeling of conductive transport in proton-exchange membranes for fuel cells. *Journal of the Electrochemical Society*, 147(9):3242–3250, 2000.
- [79] T. Zawodzinski, T. Springer, F. Uribe, and S. Gottesfeld. Characterization of polymer electrolytes for fuel cell applications. *Solid State Ionics*, 60(1-3):199–211, 1993.
- [80] Y. Bultel, P. Ozil, and R. Durand. Modelling the mode of operation of PEMFC electrodes at the particle level: influence of ohmic drop within the active layer on electrode performance. *Journal of Applied Electrochemistry*, 28(3):269–276, 1998.
- [81] K. Kuo. *Principles of Combustion*. Wiley, New York, 1986.
- [82] S. Whitaker. Flow in porous media I: a theoretical derivation of Darcy’s law. *Transport in Porous Media*, 1(1):3–25, 1986.
- [83] M. Kaviany. *Principles of Heat Transfer in Porous Media (2nd Edition)*. Springer, New York, 1995.
- [84] R. Bird, W. Stewart, and E. Lightfoot. *Transport Phenomena (2nd Edition)*. Wiley, New York, 2002.
- [85] M. Kimble and N. Vanderborgh. Reactant gas flow fields in advanced PEM fuel cell designs. *Proceedings of the Intersociety Energy Conversion Engineering Conference*, pages 3.413–3.417, 1992.
- [86] F. Boyer. A theoretical and numerical model for the study of incompressible mixture flows. *Computers and Fluids*, 31(1):41–68, 2002.

REFERENCES

- [87] C. Wang. Multiphase flow and heat transfer in porous media. *Advances in Heat Transfer*, 30:93–196, 1997.
- [88] K. Vafai and C. Tien. Boundary and inertia effects on flow and heat transfer in porous media. *International Journal of Heat and Mass Transfer*, 24(2):195–203, 1981.
- [89] A. Adamson. *Physical Chemistry of Surfaces (5th Edition)*. Wiley, New York, 1990.
- [90] P. Ustohal, F. Stauffer, and T. Dracos. Measurement and modeling of hydraulic characteristics of unsaturated porous media with mixed wettability. *Journal of Contaminant Hydrology*, 33(1-2):5–37, 1998.
- [91] N. Morrow. Capillary pressure correlations for uniformly wetted porous media. *Journal of Canadian Petroleum Technology*, 15(4):49–69, 1976.
- [92] A. Demond and P. Roberts. Effect of interfacial forces on two-phase capillary pressure-saturation relationships. *Water Resources Research*, 27(3):423–437, 1991.
- [93] J. Chen, J. Hopmans, and M. Grismer. Parameter estimation of two-fluid capillary pressure-saturation and permeability functions. *Advances in Water Resources*, 22(5):479–493, 1999.
- [94] G. Karimi and X. Li. Electroosmotic flow through polymer electrolyte membranes in PEM fuel cells. *Journal of Power Sources*, 140(1):1–11, 2005.
- [95] K. Vetter. *Electrochemical Kinetics*. Academic Press, New York, 1967.
- [96] P. Stonehart and P. Ross. The commonality of surface processes in electrocatalysis and gas-phase heterogeneous catalysis. *Catalysis Reviews-Science and Engineering*, 12(1):1–35, 1975.
- [97] A. de Bevedelievre, J. de Bevedelievre, and J. Clavilier. Electrochemical oxidation of adsorbed carbon monoxide on platinum spherical single crystals. Effect of anion adsorption. *Journal of Electroanalytical Chemistry and Interfacial Electrochemistry*, 294(1-2):97–110, 1990.
- [98] S. Gilman. The mechanism of electrochemical oxidation of carbon monoxide and methanol on platinum II. The “reactant pair” mechanism for electrochemical oxidation of carbon monoxide and methanol. *Journal of the Electrochemical Society*, 68(1):70–80, 1964.
- [99] W. Vogel, J. Lundquist, P. Ross, and P. Stonehart. Reaction pathways and poisons-II. The rate controlling step for electrochemical oxidation of hydrogen on Pt in acid and poisoning of the reaction by CO. *Electrochimica Acta*, 20(1):79–93, 1975.
- [100] T. Engel and G. Ertle. Oxidation of carbon monoxide. In D. King and D. Woodruff (eds.), *The Chemical Physics of Solid Substances and Heterogeneous Catalysis Volume 4: Fundamental Studies of Heterogeneous Catalysis*, pages 73–93. Elsevier, Amsterdam, 1982.
- [101] H. Ikeda, J. Sato, and F. Williams. Surface kinetics for catalytic combustion of hydrogen-air mixtures on platinum at atmospheric pressure in stagnation flows. *Surface Science*, 326(1-2):11–26, 1995.

REFERENCES

- [102] P. Norton. The hydrogen-oxygen reaction on metal surfaces. In D. King and D. Woodruff (eds.), *The Chemical Physics of Solid Substances and Heterogeneous Catalysis Volume 4: Fundamental Studies of Heterogeneous Catalysis*, pages 27–72. Elsevier, Amsterdam, 1982.
- [103] E. Gileadi, E. Kirowa-Eisner, and J. Penciner. *Interfacial Electrochemistry: An Experimental Approach*. Addison-Wesley, Boston, 1975.
- [104] A. Parthasarathy, S. Srinivasan, A. Appleby, and C. Martin. Temperature dependence of the electrode kinetics of oxygen reduction at the platinum/Nafion interface - a microelectrode investigation. *Journal of the Electrochemical Society*, 139(9):2530–2537, 1992.
- [105] J. Newman. *Electrochemical Systems (2nd Edition)*. Prentice-Hall, New Jersey, 1991.
- [106] G. Castellan. *Physical Chemistry*. Addison-Wesley, Boston, 1983.
- [107] D. Lide. *CRC Handbook of Chemistry and Physics (83rd Edition)*. CRC Press, Boca Raton, 2002.
- [108] A. Rowe. *Mathematical modeling of proton exchange membrane fuel cells*. Master’s thesis, University of Victoria, 1997.
- [109] G. Maggio, V. Recupero, and C. Mantegazza. Modelling of temperature distribution in a solid polymer electrolyte fuel cell stack. *Journal of Power Sources*, 62(2):167–174, 1996.
- [110] X. Li, I. Sabir, and J. Park. A flow channel design procedure for PEM fuel cells with effective water removal. Submitted to the *Journal of Power Sources*, 2006.
- [111] B. Poling, J. Prausnitz, J. O’Connell, and R. Reid. *The properties of gases and liquids (5th Edition)*. McGraw-Hill, New York, 2001.
- [112] K. Sutton and P. Gnoffo. Multi-component diffusion with application to computational aerothermodynamics. *7th AIAA/ASME Joint Thermophysics and Heat Transfer Conference*, (AIAA 98-2575), 1998.
- [113] D. Trim. *Calculus*. Prentice-Hall, New York, 1993.
- [114] K. Vafai and S. Kim. Fluid mechanics of the interface region between a porous medium and a fluid layer. An exact solution. *International Journal of Heat and Fluid Flow*, 11(3):254–256, 1990.
- [115] P. Futerko and I. Hsing. Thermodynamics of water vapor uptake in perfluorosulfonic acid membranes. *Journal of the Electrochemical Society*, 146(6):2049–2053, 1999.
- [116] J. Prausnitz, R. Lichtenthaler, and E. Azevedo. *Molecular Thermodynamics of Fluid-Phase Equilibria*. Prentice-Hall, New Jersey, 1999.
- [117] J. Hinatsu, M. Mizuhata, and H. Takenaka. Water uptake of perfluorosulfonic acid membranes from liquid water and water vapor. *Journal of the Electrochemical Society*, 141(6):1493–1498, 1994.

REFERENCES

- [118] S. Turns. *An Introduction to Combustion: Concepts and Applications*. McGraw-Hill, New York, 1996.
- [119] J. Baschuk and X. Li. Mathematical model of a PEM fuel cell incorporating O₂ poisoning and O₂ (air) bleeding. *International Journal of Global Energy Issues*, 20(3):245–276, 2003.
- [120] J. Ferziger and M. Perić. *Computational Methods for Fluid Dynamics*. Springer, New York, 1999.
- [121] W. Press, S. Teukolsky, W. Vetterling, and B. Flannery. *Numerical Recipes in C: The Art of Scientific Computing*. Cambridge University Press, Cambridge, 1992.
- [122] S. Motupally, A. Becker, and J. Weidner. Diffusion of water in Nafion 115 membranes. *Journal of the Electrochemical Society*, 147(9):3171–3177, 2000.
- [123] T. Zawodzinski, M. Neeman, L. Sillerud, and S. Gottesfeld. Determination of water diffusion coefficients in perfluorosulfonate ionomer membranes. *The Journal of Physical Chemistry*, 95(15):6040–6044, 1991.
- [124] Y. Sone, P. Ekdunge, and D. Simonsson. Proton conductivity of nafion 117 as measured by a four electrode ac impedance method. *Journal of the Electrochemical Society*, 143(4):1254–1259, 1996.
- [125] B. Mahan and R. Myers. *University Chemistry: Fourth Edition*. The Benjamin/Cummings Publishing Company, Inc., Menlo Park, California, 1987.
- [126] A. Mughal and X. Li. Experimental diagnostics of PEM fuel cells. *International Journal of Environmental Studies*, 63(4):377–389, 2006.
- [127] A. Mughal. Experimental diagnostics of PEM fuel cells. M.A.Sc Project Report, Department of Mechanical Engineering, University of Waterloo, 2004.
- [128] E-TEK. Gas diffusion electrodes and catalyst materials catalogue. 1995.
- [129] J. Park and X. Li. An experimental and numerical investigation on the cross flow through gas diffusion layer in a pem fuel cell with a serpentine flow channel. Submitted to the Journal of Power Sources, 2006.
- [130] F. White. *Viscous Fluid Flow (2nd Edition)*. McGraw-Hill, New York, 1991.